Optimisation of the Photocatalytic Activity of Defect-Pyrochlores, especially in Visible Light

Dissertation

zur Erlangung des akademischen Grades

"*doctor rerum naturalium*"

(Dr. rer. nat)

eingereicht an der

Fakultät für Biologie, Chemie und Geowissenschaften

der Universität Bayreuth

von

Morten Weiß, M. Sc.

geboren in Alsfeld

Bayreuth, den 11. Januar 2021

Die vorliegende Arbeit wurde in der Zeit von September 2016 bis Oktober 2018 am Physikalisch-Chemischen Institut der Justus-Liebig-Universität Gießen und von Oktober 2018 bis Mai 2020 am Lehrstuhl für Physikalische Chemie III unter Betreuung von Herrn Prof. Dr. Marschall der Universität Bayreuth angefertigt.

Vollständiger Abdruck der von der Fakultät für Biologie, Chemie und Geowissenschaften der Universität Bayreuth genehmigten Dissertation zur Erlangung des akademischen Grades eines Doktors der Naturwissenschaften (Dr. rer. Nat).

Dissertation eingereicht am: 17.06.2020

Zulassung durch die Promotionskommission: 01.07.2020

Wissenschaftliches Kolloquium: 23.11.2020

Amtierender Dekan: Prof. Dr. Matthias Breuning

Prüfungsausschuss:

Prof. Dr. Roland Marschall (Gutachter)

Prof. Dr. Josef Breu (Gutachter)

Prof. Dr. Georg Papastavrou (Vorsitz)

Prof. Dr. Matthias Breuning

Danksagung

Danken möchte ich meinem Betreuer Prof. Dr. Roland Marschall für die Möglichkeit der Promotion in seinen Arbeitsgruppen, für die langjährige Unterstützung und vor allem für die große Freiheit bei der Wahl meiner Forschungsthemen, die er mir gewährte.

Mein besonderer Dank gilt Prof. Dr. Josef Breu, der freundlicherweise das Zweitgutachten für diese Arbeit übernommen hat.

Bei Prof. Dr. Bernd Smarsly möchte ich mich für die langjährige Integration in seine Arbeitsgruppe und die hilfreichen Diskussionen bedanken

Mein Dank gilt auch Prof Dr. Thomas Bredow für die Durchführung von theoretischen Berechnungen für $KTaWO_6$ und $Sn_{0.5}TaWO_6$.

Diese Arbeit wäre nicht möglich gewesen ohne die Hilfe vieler Kollegen, die mir verschiedenste Messmethoden beigebracht oder Messungen für mich durchgeführt haben. Mein Dank gilt Dr. Jana Timm, Sebastian Werner, Kevin Turke und Jonas Jungmann für die Durchführung sämtlicher Physisorptions-Messungen. Außerdem vielen Dank an Huber Wörner für TGA-MS Mesungen. Bei Dr. Kristin Kirchberg möchte ich mich für die Aufnahme von TEM Bildern bedanken. Ganz besonderer Dank gebührt Anja Hofmann für zahlreiche REM Aufnahmen und EDX Messungen, außerdem danke ich ihr für ihre Mitarbeit bei Transiente-Absorptions-Messungen. Bei Dr. Sabine Rosenfeldt bedanke ich mich für ihre Hilfe und Gesellschaft bei XPS Messungen. Aus der Arbeitsgruppe von Prof. Dr. Jürgen Janek danke ich Dr. Bjoern Luerßen für seine Hilfe mit *in situ* XRD Messungen, bei Dr. Boris Mogwitz und Dr. Klaus Peppler für ihre Hilfe bei REM und EDX Messungen und bei Dr. Joachim Sann und Felix Walther für XPS Messungen. Bei Dr. Gerald Hörner bedanke ich mich für die Durchführung und Auswertung von SQUID Messungen.

Außerdem möchte ich mich bei den Mitarbeitern der wissenschaftlichen Werkstätten und der Chemikalienausgabe der Universität Gießen, insbesondere Anja Beneckenstein, Hans-Jürgen Wolf, Harald Weigand, Eike Santowski, Mario Dauber und Harry Heidt und seine Mitarbeiter für die langjährige Hilfe, die viele Experimente erst möglich gemacht haben.

Weiterer Dank gebührt jenen Studenten, die ich während ihrer Forschungsarbeiten unterstützen durfte und die mir geholfen haben: Deborah Wegstein, Thomas Kasper für die Vorarbeiten von $CsM_xW_{2-x}O_6$ Verbindungen und Benedikt Wirth, der die Synthesebedingungen von Tellurhaltigen Defekt-Pyrochloren gefunden und optimiert hat.

Für die Finanzierung meiner Stelle im Rahmen des Emmy-Noether-Programms danke ich der Deutschen Forschungsgemeinschaft.

Bedanken möchte ich mich bei Jonas Jungmann für die alltägliche Hilfe im Labor. Mein besonderer Dank gilt auch Dr. Jana Timm für ihre Hilfe und Ratschläge während der Promotionszeit. Bedanken möchte ich mich natürlich auch bei meinen Kollegen Kristin, Anja, Sebastian, Andre, Giuli, Natalia, Christopher, Michael und allen anderen der Arbeitsgruppen Marschall und Smarsly, sowie meinen Korrekturlesern Sabina Kaiser, Dr. Marian Weiß, Dr. Kristin Kirchberg und Anja Hofmann.

Zu guter Letzt möchte ich mich bei meinen Eltern und meiner Familie für die Unterstützung über all die Jahre bedanken.

Table of Contents

Abstract

The present thesis concerns itself with optimising the photocatalytic activity of quaternary metal oxides with defect-pyrochlore structure. The cubic crystal structure offers manifold opportunities to change not only the optical properties – such as light absorbance and bandgap – but also the elemental composition without sacrificing the suitable band positions for overall water splitting.

Potassium tantalum tungsten oxide $KTaWO_6$ nanoparticles with adjustable crystallite sizes have been synthesised *via* hydrothermal reaction. It was discovered that water molecules can enter the crystal structure of $KTaWO_6$, which greatly facilitates the ion-exchange reaction of K^+ with Sn^{2+}. The combination of the $5s^2$ states of Sn^{2+} and water incorporation greatly reduces the bandgap of the ion-exchanged materials by up to 1.4 eV. However, these materials are quite prone to self-oxidation during illumination, followed by the leaching of Sn from the samples.

The possible range of elemental compositions of $CsM_xW_{2-x}O_6$ has been investigated, where the M^{n+} cation can be M^{5+}, M^{4+}, M^{3+} and even M^{2+}. For M^{n+} cations with d^0 or d^{10} electron configuration the influence on band structure is negligible and the photocatalytic activity is approximately comparable. For M^{n+} cations with only partially filled *d*-levels the optical properties vary drastically, although the lifetime of photogenerated charge carriers is presumably diminished.

The different A cations in alkaline metal niobium tellurium oxides $ANbTeO_6$ with A = K^+, Rb^+ and Cs^+ result in different defect concentrations and a distorted crystal structure. The defects cause visible light absorbance of various magnitudes, but neither the bandgap of 3.4 eV nor the charge carrier concentration are changing. UV light irradiation results in the reduction of surface species to metallic tellurium and subvalent niobium compounds and in changed defect concentrations.

Kurzfassung

Die vorliegende Arbeit handelt von der Optimierung der photokatalytischen Aktivität von quaternären Metalloxiden mit Defekt-Pyrochlorstruktur. Die kubische Kristallstruktur bietet vielfältige Möglichkeiten, um nicht nur die optischen Eigenschaften wie Licht-Absorption und Bandlücke, sondern auch die elementare Zusammensetzung zu variieren, ohne dabei die für Wasserspaltung geeigneten Bandpositionen zu beeinträchtigen.

Kaliumtantalwolframat $KTaWO_6$ Nanopartikel mit einstellbaren Kristallit-Größen wurden mittels Hydrothermalmethode synthetisiert. Es hat sich gezeigt, dass Wassermoleküle in die Kristallstruktur eingebaut werden können, was den Ionen-Austausch von K^+ gegen Sn^{2+} erheblich verbessert. Die Kombination aus den $5s^2$ Zuständen von Sn^{2+} und der Einbau von Wasser reduziert die Bandlücke der Ionen-ausgetauschten Materialien um bis zu 1,4 eV. Allerdings sind diese Materialien anfällig für Selbst-Oxidation während Bestrahlung, gefolgt vom Auswaschen von Sn aus den Proben.

Die mögliche Bandbreite an elementaren Zusammensetzungen von $CsM_xW_{2-x}O_6$ wurde untersucht, wobei das M^{n+}-Kation entweder M^{5+}, M^{4+}, M^{3+} oder sogar M^{2+} sein kann. Für M^{n+}-Kationen mit d^0- oder d^{10}-Elektronenkonfiguration ist der Einfluss auf Bandstruktur vernachlässigbar und die photokatalytische Aktivität ist annähernd vergleichbar. Für M^{n+}-Kationen mit nur teilweise gefüllten *d*-Zuständen ändern sich die optischen Eigenschaften drastisch, allerdings verringert sich vermutlich die Lebenszeit der photoangeregten Ladungsträger.

Die unterschiedlichen A Kationen in Alkalimetall-Niob-Telluroxiden $ANbTeO_6$ mit A = K^+, Rb^+ und Cs^+ resultieren in unterschiedlichen Defekt-Konzentrationen und einer verzerrten Kristallstruktur. Die Defekte verursachen die Absorption sichtbaren Lichtes unterschiedlichen Ausmaßes, jedoch ändern sich weder die Bandlücke von 3.4 eV noch die Ladungsträgerkonzentration. Die Bestrahlung mit UV-Licht resultiert sowohl in einer Reduktion von Oberflächen-Spezies zu metallischem Tellur und niedervalenten Niob-Verbindungen als auch in geänderten Defektkonzentrationen.

1 Introduction

1.1 Motivation

The quest for a clean and sustainable energy source is arguably one of the most important aims of contemporary research.[1] The combination of a rising population growth with an ever-increasing demand for energy will require a significant rise in world energy production in the decades to come. It is expected that the yearly energy consumption will more than double from 18.5 TWy y^{-1} nowadays to approximately 27 TWy y^{-1} in 2050.[2] The most important energy source today is the combustion of fossil fuels such as coal, oil and natural gas. Doing so results in the release of carbon dioxide (CO_2) into the atmosphere, which ultimately increases the global average temperature. Global warming will cause dire ramifications, *e.g.* the rise of sea levels, thawing of permafrost grounds and socioeconomic implications such conflicts about resources.

Solar energy is a highly promising energy source with a yearly energy potential of 23000 TWy.[2] Due to the intermittency of solar irradiation the energy needs to be converted into a storable form, *e. g.* chemical fuels. Since the discovery from Fujishima and Honda in 1972, photocatalysis has been considered as a viable pathway to convert solar energy into chemical fuels.[3] The bandgaps of many oxide semiconductors such as titanium(IV) oxide TiO_2 – which is arguably the most investigated photocatalyst – only allow the absorption in the ultraviolet (UV) region of the solar spectrum, which is severely restricting their large-scale application in solar fuel generation.[4] Other photocatalysts, such as bismuth vanadate $BiVO_4$ or iron-based oxides, have lower bandgaps, therefore utilising a larger amount of solar light. However, other factors are limiting their practical application: charge recombination is the limiting factor for $BiVO_4$;[5] whereas the disadvantages of iron oxide based photocatalysts are high recombination and poor charge carrier diffusion lengths.[6]

Pyrochlores are oxidic materials with the general formula $A_2M_2O_6X$, where A can be an alkaline, earth-alkaline or even a rare-earth metal, while M is generally a transition metal and X can be O^{2-}, OH^-, F^- or S^{2-}.[7] Vacancies in the structure result in the formation of AM_2X_6 compounds that have first been reported by Babel *et al.* and have later been called defect-pyrochlores.[8] The M cation may consist of two identical ions, but also of two different metal cations. Both occupy the same crystallographic positions, which give pyrochlores and defect-pyrochlores a wide range of possible elemental compositions.[9–15] The first photocatalytic application by Ikeda *et al.* using $AMWO_6$ (A = Rb^+, Cs^+ and M = Nb^{5+}, Ta^{5+}) was reported in 2004,[16] however, the large bandgaps of 3.6 eV and 3.8 eV are limiting their photocatalytic prospects.

The research group around Kudo has used the incorporation of Sn^{2+} *via* ion exchange to greatly diminish the bandgaps of layered titanates, niobates and tantalates and have shown photocatalytic evolution of hydrogen and oxygen with visible light irradiation in the presence of sacrificial agents.[17,18] This experimental pathway to extend the absorbance into the visible part of the solar spectrum can also be applied to defect-pyrochlores.[19] Another way to increase the visible light absorption of defect-pyrochlores is the incorporation of M^{n+} cations with partially occupied *d* states.[20] The substitution of W^{6+} with Te^{6+} can also be used to obtain compounds that absorb visible light.[21]

1.2 Aims of this Work

The results presented in this thesis can roughly be divided in three different parts.

The aim of the first part is the attempt to synthesise a defect-pyrochlore for photocatalytic hydrogen evolution in visible light, using the ion exchange with Sn^{2+}-ions as described above. For that reason a hydrothermal synthesis route for $CsTaWO_6$ nanoparticles[22] is adapted to $KTaWO_6$, since the hydrophilicity of $KTaWO_6$ has turned out to be beneficial for ion exchange. The influences of temperature, time and ammonia concentration are being discussed, especially with regards to tailoring the crystallite size. The ability of $KTaWO_6$ to incorporate water molecules into the crystal structure is thoroughly investigated. The synthesised nanoparticles emerging from the Sn^{2+} ion exchange are analysed – especially their optical properties and the phase purity following the exchange reaction. The degree of hydrophilicity of the exchanged samples was also researched and has been published in *Nanoscale* in 2018.[23] Theoretical calculations have been employed to study the effect of the ion exchange and the incorporation of the water molecules upon the band structure and optical properties. In order to optimise the ion exchange procedure, a wide range of Sn^{2+} precursors and solvents have been employed to investigate the effect of exchange conditions upon the properties and composition of the samples afterwards. The ion exchanged samples have been used in photocatalytic hydrogen evolution experiments in simulated solar and ultraviolet light. Post-catalytic measurements have been performed to examine the stability of these samples. This has been published in *Chemistry: A European Journal* in 2018.[24]

The second part concerns itself with exploring the compositional possibilities of $CsM_xW_{2-x}O_6$, where M^{n+} can be M^{5+}, M^{4+}, M^{3+} and even M^{2+}. A systematic investigation concerning the formation and stability in a temperature range from 500-900 °C is performed. All samples are investigated towards possible derivations and/or disturbances from the ideal structure. The

influence of M^{n+} on the bandgap and band level is analysed, as is the impact on photocatalytic hydrogen evolution and overall water splitting.

The third part is the synthesis and characterisation of $ANbTeO_6$ with A = K^+, Rb^+, Cs^+. $KTaTeO_6$ has a reported bandgap of 2.5 eV,[25] which seems to be promising for photocatalysis in visible light. The influence of A on crystal structure, band structure and photocatalytic activity is investigated. This has been published in *Inorganic Chemistry* in 2020.[26]

2 Theoretical Background

2.1 The Future of Energy Supply and Demand

The approaching change of global climate is arguably the biggest challenge in the future of humanity. The main reason for the rise of global temperature is the change of atmospheric composition, especially the increasing concentration of greenhouse gases, such as carbon dioxide CO_2, methane CH_4 and nitrous oxides NO_x.[27] This concentration increase is of anthropogenic provenance, mainly by the combustion of fossil fuels. Of these gases, CO_2 has by far the most impact on global climate, causing approximately 25 % of the greenhouse effect.[27] The correlation between the aberration of annual mean global temperature and CO_2 concentration is depicted in Figure 2.1, displaying the interrelation of increasing CO_2 concentration with rising temperature.

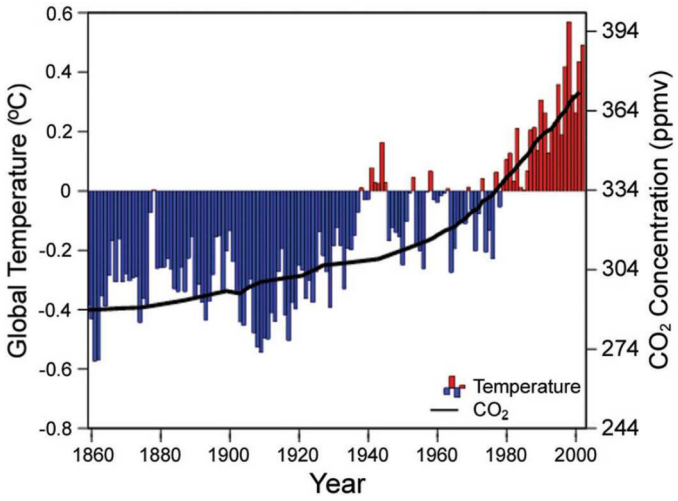

Figure 2.1: Correlation of aberration from annual mean global temperature and atmospheric CO_2 concentration in parts per million by volume (ppmv).[27] Reprinted with permission from The American Association for the Advancement of Science.

The rise of global temperature is projected to have catastrophic ramifications such as rising sea-levels due to the melting of glacial, arctic and antarctic ice sheets, resulting in the flooding of low-lying islands and regions or more frequent droughts and heat waves.[27]

The obvious consequence is that the rise of global temperature needs to be limited, which will only be possible if CO_2 emissions are decreased. However, fossil fuels are the major energy source for both worldwide primary energy and electricity. The present share of renewable energies (including hydroelectricity) is rather low with 10.8 % for primary energy consumption (Figure 2.2, left). However, renewable energies already make up 25.1 % of electricity generation (Figure 2.2, right).[28]

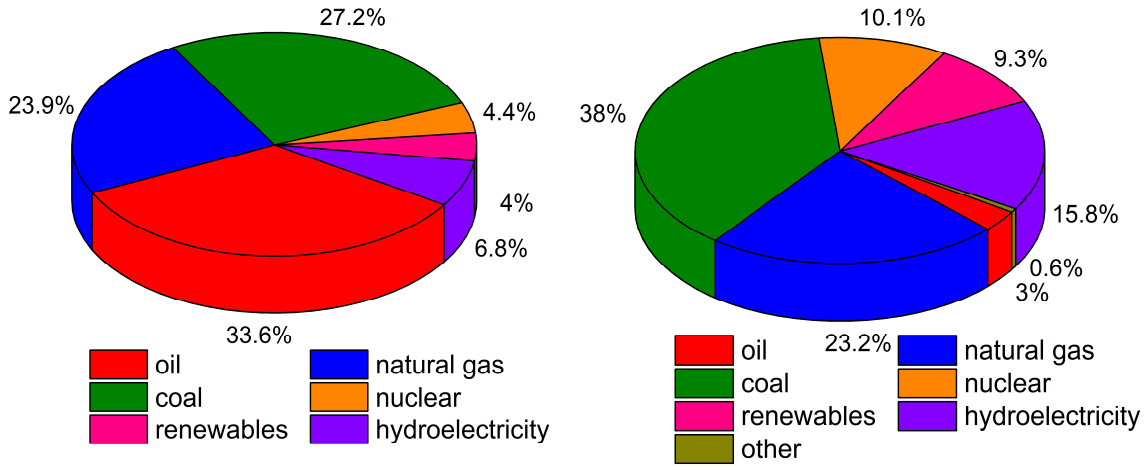

Figure 2.2: World primary energy consumption (left) and world electricity generation (right) for 2018. Data taken from BP Statistical Review of World Energy 2019.[28]

Besides their contribution to climate change, fossil fuels only have limited reserves – which also applies for nuclear energy. Even if the reserves are projected to last several decades:[2] making a transition to a sustainable energy supply is unavoidable. Although there are several potential renewable energy sources, their potential is vastly different. By far the biggest potential energy source is solar energy with a yearly potential of 23000 TWy, which would be enough to satisfy the world energy demand of approximately 18.4 TWy in 2018 more than a thousand times.[2,28] Solar energy, however, is not stable but succumbs to fluctuations, which are diurnal, seasonal, depending on weather and geographical latitude.

Hence, it is necessary to find a way to buffer solar derived energy for use during night, overcast days and winter. Moreover, energy needs not only to be stored, but also transported to regions with low solar irradiance such as in the polar circles, and then consumed on demand. While there are several energy carriers, their storable amount of energy and their power are vastly different (Figure 2.3). Flywheels and super capacitors possess high power, however, their specific energy is too low to store large amounts. While batteries have a far larger specific energy, it is still approximately three orders of magnitude less than that of chemical fuels, such as methanol or petrol. Besides their unparalleled energy density, chemical fuels are relatively easy to transport over larger distances using already existing infrastructure and are storable for at least several months. However, they are mostly carbon based, resulting in the release of CO_2 into the atmosphere upon combustion.

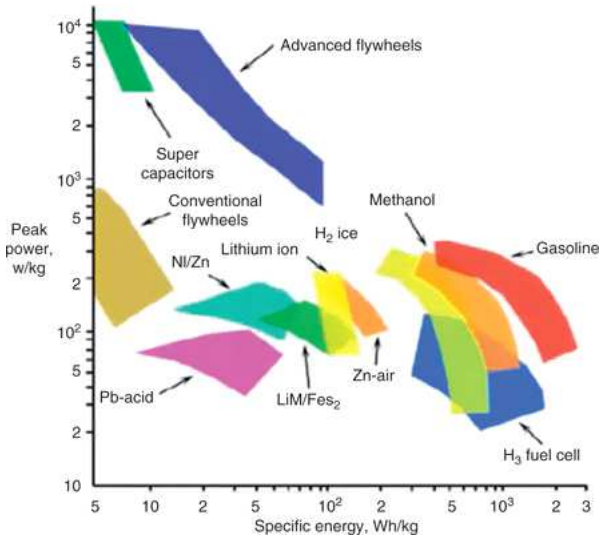

Figure 2.3: Ragone plot of different energy carriers[29]. Reprinted with permission from Elsevier.

An exception is hydrogen, which forms water upon combustion in combination with oxygen from the air. This reaction can also be done electrochemically in fuel cells to directly generate electrical energy. While hydrogen is conventionally produced using steam reforming of methane, it can also be produced from photocatalytic water splitting or from a combination of a photovoltaic device coupled with an electrolyser.[30] Water is an abundant and convenient source for hydrogen and oxygen is already a component of air or can be released into the atmosphere without any difficulties, respectively. Both reaction pathways can be combined into a way of storing energy in hydrogen, providing an overall carbon free cycle (Figure 2.4).

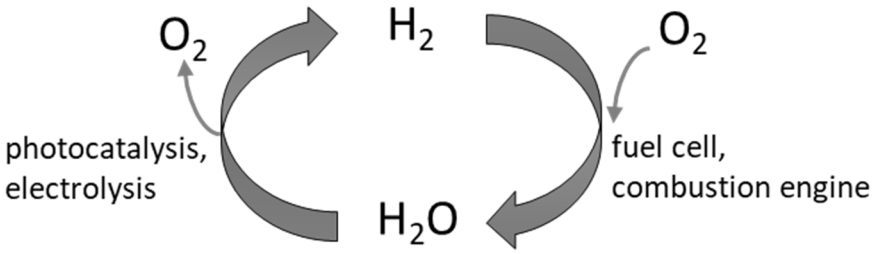

Figure 2.4: Scheme of a possible cycle using hydrogen as energy carrier.

Hydrogen is not only an energy carrier, but also an important reactant in several important processes, *e. g.* the Haber-Bosch process, which is important in the manufacture of fertilisers needed in global food supply.[31] An overview of the possible usages of hydrogen is depicted in Figure 2.5.

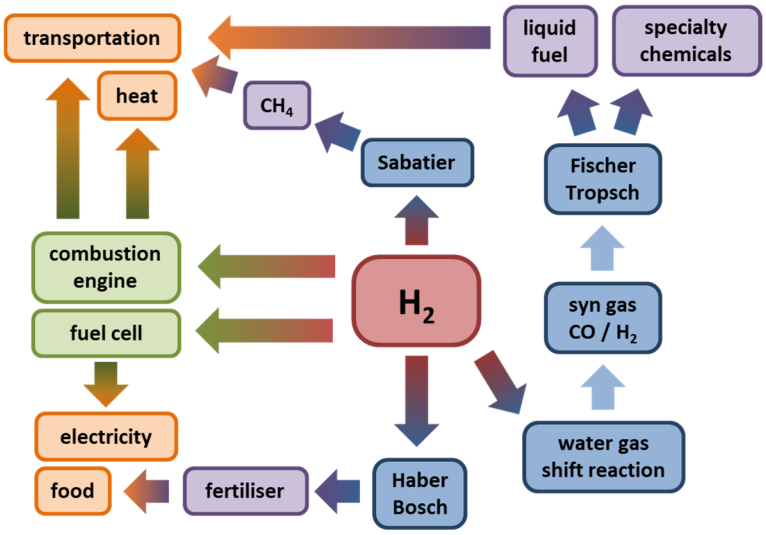

Figure 2.5: Scheme of the possibilities of hydrogen usage, adapted from van de Krol *et al.*[31] Chemical processes are depicted in blue, chemical products in purple, general goods in orange and other technologies in green.

Due to the global importance of hydrogen a sustainable production pathway will be necessary. The change of global climate and its dire consequences will also force the abandonment of fossil fuels, therefore requiring an alternative to steam reforming. Hydrogen production *via* solar energy has the potential to become the foundation of future energy supply. Photocatalysis is a promising way to directly generate hydrogen from solar irradiation.

2.2 Photocatalysis

In general, photocatalysis can be considered as a catalytic reaction that can only occur if the catalyst (C) is first activated by light irradiation ($h\nu$). The activated catalyst (C*) is then able to catalyse the reaction of a substrate (S) to a product (P). After the reaction the catalyst relaxes back to the ground state and can be again activated by light (Figure 2.6).

There is a difference in literature between photosynthetic and photocatalytic reactions, based on the change of Gibbs energy ΔG during the reaction.[32] Photosynthetic reactions use the light's energy to drive endergonic reactions such as the splitting of water molecules into the elements (P_2). Photocatalytic reactions, however, are exergonic (P_1); an example for this kind of reaction would be the decomposition of organic pollutants in waste water.

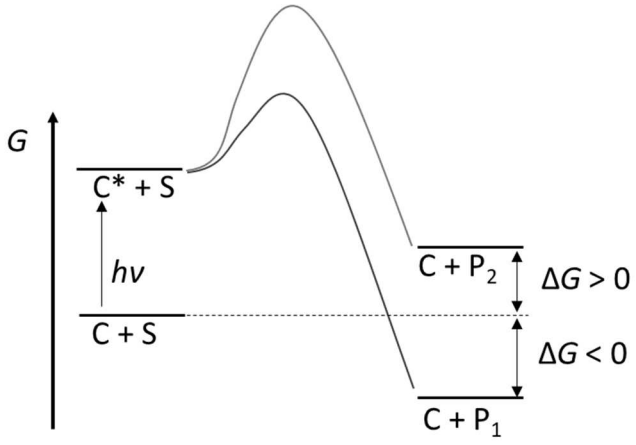

Figure 2.6: Reaction scheme of a photocatalytic reaction.

As in thermal catalysis, photocatalysis can be performed homogeneously or heterogeneously. In a homogeneous reaction, the photocatalyst and substrate are located in the same phase, a typical example would be transition metal complexes in a liquid solvent. In heterogeneous photocatalysis, the solid photocatalyst is either dispersed in a liquid reaction medium or fixed on a substrate, which is immersed in the reaction medium. Electrically conductive substrates are typically used in photoelectrochemistry.

2.2.1 The Fundamentals of Semiconductors

n-type and p-type Semiconductors

The electronic structure of semiconductors consists of a valence band (VB), formed by fully occupied states, and a conduction band (CB) consisting of fully unoccupied states. The energy difference between those two bands is called the bandgap energy E_g. Normally no states are located within the bandgap. If E_g is larger than 4-5 eV, the semiconductor becomes an insulator, while in metals both VB and CB are overlapping. The Fermi level E_F is the energy state with an occupation probability of 0.5; for an intrinsic semiconductor it is located in the middle of the bandgap.

Semiconductors can be divided in three different kinds, depending on their majority charge carriers: intrinsic, n-type and p-type (Figure 2.7). Intrinsic semiconductors – such as pure silicon – possess only poor electric conductivity. It is possible to adjust the electrical conductivity by doping with atoms of a different valence than those of the pristine semiconductor. Doping with elements with higher valence introduces surplus electrons, which then are the majority charge carriers creating an n-type semiconductor. Doping with an element of lower valence

introduces an electron hole resulting in a p-type semiconductor. The introduction of additional states in the vicinity of the conduction band for an n-type semiconductor results in a shift of the Fermi level towards the CB, while the Fermi level of a p-type semiconductor is shifting towards the VB (Figure 2.7).

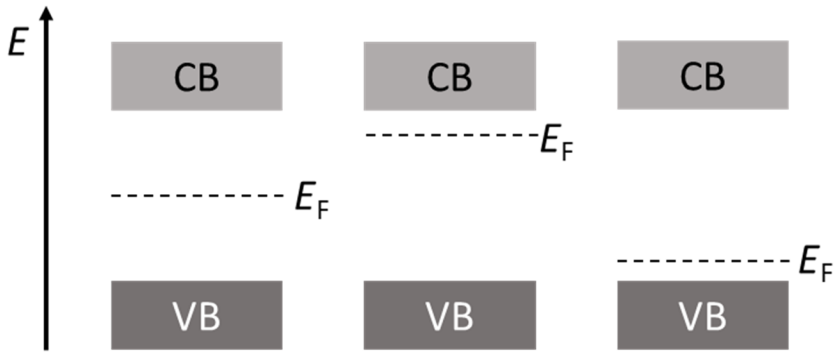

Figure 2.7: Scheme displaying the three different kinds of semiconductors; intrinsic (left), n-type (middle) and p-type (right).

For metal oxides, the formation of n- or p-type behaviour is the result of a divergence from the ideal stoichiometry due to defects within the crystal lattice, *e. g.* vacancies. For a binary metal oxide MO there are two possibilities of vacancies: either cation vacancies V_M – written in Kröger-Vink notation – (formula 2.1) or oxygen vacancies V_O (formula 2.2).[33]

$$\frac{1}{2}O_2 \rightarrow V_M'' + 2\,h^{\cdot} + O_O \qquad (2.1)$$

$$O_O \rightarrow V_O^{\cdot\cdot} + 2\,e' + \frac{1}{2}O_2 \qquad (2.2)$$

The defect formation reaction with lower formation energy will be more dominant and thus determine the type of semiconductor.[33] Most commonly used photocatalysts, such as TiO_2, WO_3, Fe_2O_3 and $BiVO_4$, are n-type semiconductors due to oxygen defects;[6,34] some p-type semiconductors are CuO[33], Cu_2O[35] and $CaFe_2O_4$[36].

Direct and Indirect Transitions

Apart from their majority charge carriers, semiconductors can also be distinguished between those with direct and indirect transitions. Both valence and conduction bands are not flat but curved at different points of the *k*-vector, which is directly proportional to the crystal momentum. If both VB maximum and CB minimum are located at the same *k*-vector (Figure 2.8, left), a direct transition may occur and the resulting electron-hole-pair is formed at the same value

of *k*. A direct transition only requires a photon energy larger than the bandgap, thus both excitation and recombination are highly probable. An indirect transition occurs when the CB minimum and the VB maximum are located at different *k*-values. The transition not only requires a photon energy larger than the bandgap, but also the momentum between the two different k-values in the form of a phonon. The indirect transition – in the form of both excitation and recombination – is therefore less probable than a direct transition.

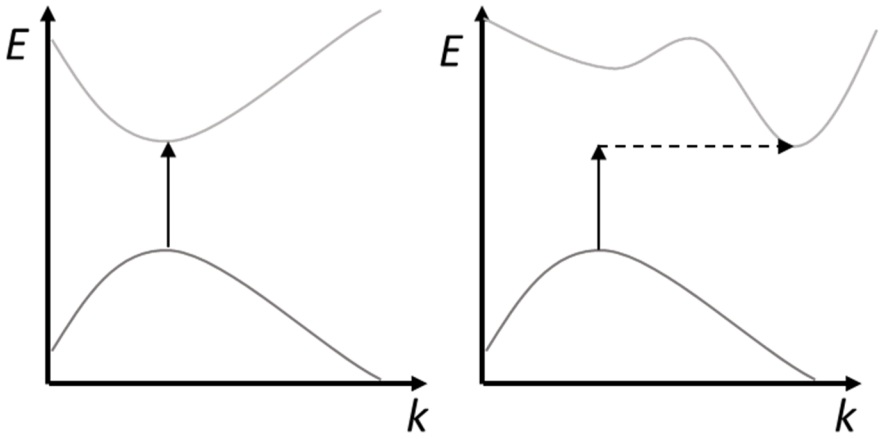

Figure 2.8: Scheme of a direct (left) and indirect (right) transition.

2.2.2 The Mechanism of Photocatalysis

A photocatalytic reaction can be divided in different steps according to their consecutive chronological order; the whole process is depicted in Figure 2.9. The first step is the absorption of a photon: for this, the photon energy *hv* has to be larger than the bandgap energy E_g of the semiconductor. An electron e^- is elevated to the conduction band, while an electron hole h^+ remains in the valence band.

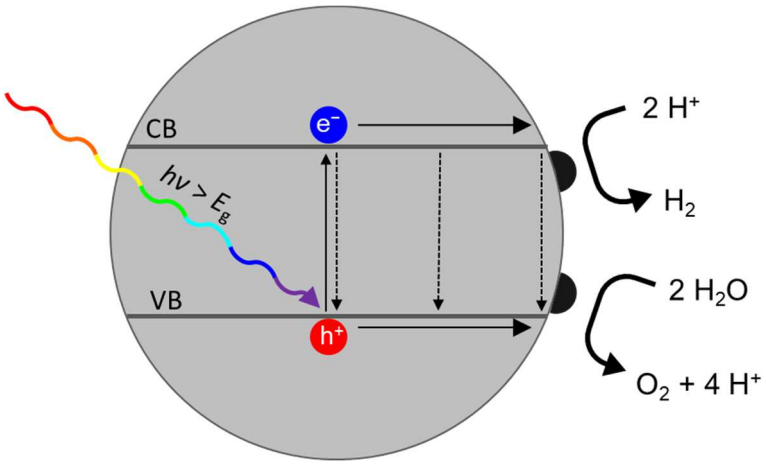

Figure 2.9: Scheme of a photocatalytic reaction using the example of water splitting.

The majority of the formed electron-hole-pairs undergo recombination, which can occur either radiatively in the form of photoluminescence or non-radiatively, whereat the energy is converted into heat by phonons.

The charge carries formed by photoexcitation can subsequently diffuse to the surface. On their way they can be subject to bulk recombination; this may happen at point defects or grain boundaries. Even if the charge carriers arrive at the surface, they can undergo surface recombination. A prominent example would be $BiVO_4$, whose photocurrent is limited by surface recombination.[5] The electrons and holes on the surface can perform reductive or oxidative half-reactions with adsorbed compounds. In the case of water splitting, the protons are reduced to hydrogen (formula 2.3), and water is oxidised to oxygen (formula 2.4).

$$2\ H^+ + 2\ e^- \rightarrow H_2\uparrow \tag{2.3}$$

$$2\ H_2O + 4\ h^+ \rightarrow O_2\uparrow + 4\ H^+ \tag{2.4}$$

The overall water splitting reaction is the combination of formulas 2.3 and 2.4. In a final step the newly formed reaction products are desorbed from the surface.

$$2\ H_2O \xrightarrow{4\ h\nu} 2\ H_2\uparrow + O_2\uparrow \tag{2.5}$$

Recombination is evidently bad for photocatalysis, since the charge carriers will not exist anymore afterwards. Several strategies have been developed to prevent recombination. One is the use of sacrificial agents: these react rapidly with only one kind of charge carriers, omitting the other charge carriers, which now have nothing to recombine with anymore. Depending on the type of half reaction, the redox potential of the sacrificial agent needs to be at higher or lower potential than the band potential of the semiconductor. Another strategy consists of using co-catalysts: these are small metal or metal oxide particles on the surface of the photocatalyst, where electrons or holes will be accumulated. The use of sacrificial agents and co-catalysts will be discussed in detail in sections 2.2.4 and 2.2.5, respectively. A third method to prevent recombination is the combination of two or even more photocatalytic materials with different band positions.[37,38] Here, the charge carriers are spatially separated on the different materials, thus preventing recombination.

2.2.3 The Requirements of a Photocatalyst

An efficient photocatalyst has several requirements, some of which are contradictory to each other.

Since the first step of a photocatalytic reactions is the absorption of light, a small bandgap would be beneficial. However, in case of a single material photocatalyst the bandgap has to

be at least equal to the Gibbs Energy of the catalysed reaction; for water splitting this would be 1.23 eV or 237 kJ mol^{-1}. Additionally, an overpotential is often necessary for a sufficient reaction rate and in case of gas evolution reactions, resulting in a suitable bandgap of approximately 2 eV.

Besides the bandgap, the energetic positions of VB and CB need to match the redox potentials of both half-reactions. The CB minimum needs to be at a more negative potential than the reduction half-reaction, while the VB maximum needs to be at a more positive potential than the potential of the oxidation half-reaction. For water splitting, this implies that the conduction band minimum needs to be at a more negative potential than 0 V (vs. normal hydrogen electrode (NHE)) and that the valence band maximum needs to be at a more positive potential than 1.23 V (vs. NHE). A larger potential difference between band potential and redox potential would result in a larger driving force for the respective half-reaction. It would also result in a larger bandgap, therefore limiting the light absorption.

The photocatalyst has to be stable in the (usually aqueous) reaction medium and during light irradiation. Otherwise, the photogenerated charge carriers may react irreversibly with the atoms of the photocatalyst. The performance of *e.g.* α-$SnWO_4$ is limited by surface oxidation to SnO_2 during illumination, creating a barrier layer between photogenerated holes and the electrolyte.[39] Metal sulphides possess smaller bandgaps than metal oxides due to the higher valence band. However, they are prone to photocorrosion, resulting in the oxidation of the sulphide anions.[40]

Another important characteristic of photocatalysts is their crystallinity, which is usually tantamount with a lack of defects. A high crystallinity is considered superior since defects can serve as recombination centres for charge carriers,[41] but different kinds of defects may have different influences on the photocatalytic activity. Wang *et al*. found that the purposeful creation of copper vacancies in CuO increases the photocurrent, whereas oxygen vacancies decrease the photocurrent.[33] If defects are created non-specifically, *e. g.* by ball milling, the photocatalytic activity will decrease and cannot be restored completely by annealing at high temperatures to repair defects.[42] The influence of defects also varies according to the reaction. The influence of crystallinity seems to be minor in photocatalytic hydrogen evolution by β-Ga_2O_3 in the presence of methanol as a sacrificial agent, but significant in the overall water splitting reaction.[41]

One important aspect of photocatalyst materials is also their surface area. Since photocatalytic reactions occur on the surface of the photocatalyst, it can be assumed that a higher surface area results in a higher photocatalytic activity. While this assumption is generally true for photocatalytic reactions, exceptions may occur.[32] For example, larger WO_3 particles are more active in water oxidation than smaller particles, since the higher surface areas of the smaller

particles result in increased surface recombination.[43] The surface of a semiconductor can be considered as a defect and surface states may act as trap states for photogenerated charge carriers. Photosynthetic reactions such as overall water splitting are usually restricted by mobility of the charge carriers and mass transport if the half-reactions are spatially separated.[32] For β-Ga_2O_3 it has been observed that the activity in water splitting seems to be a compromise between surface area and crystallinity.[41] Trying to achieve high surface area and high crystallinity simultaneously is normally difficult, since a high crystallinity is generally achieved by annealing at high temperatures. This will result in small surface areas, since surfaces are inherently less energetically favourable. On the other hand, synthesis techniques yielding high surface areas usually result in higher defect concentrations.

The morphology has an additional influence, since different exposed crystal facets may possess varying activity. The difference in surface energy causes electrons and holes to accumulate on different facets resulting in spatial separation, thus preventing recombination.[44]

2.2.4 The Role of Sacrificial Agents

Sacrificial agents are chemicals that react rapidly with either electrons or holes. Which reaction happens depends on the redox potential of the sacrificial agent in question and the band potential of VB or CB. Since only one kind of charge carriers is consumed by the sacrificial agent, the other kind of charge carriers cannot recombine anymore, thus elongating their lifetime and chance to react.

Hole scavengers or sacrificial electron donors are typically small organic molecules; alcohols – especially methanol – are the most commonly used hole scavengers.[45] Methanol molecules react rapidly with photogenerated holes: this results in the formation of α-hydroxymethyl radical (formula 2.6).

$$CH_3OH + h^+_{VB} \rightarrow {}^{\bullet}CH_2OH + H^+ \qquad (2.6)$$

In the absence of oxygen the highly reactive radical injects one electron into the conduction band in a process called (photo)current doubling (formula 2.7).[45]

$$^{\bullet}CH_2OH \rightarrow H_2CO + H^+ + e^-_{CB} \qquad (2.7)$$

The formed formaldehyde molecule is able to react analogue to formic acid, which can be further oxidised to carbon dioxide.

On the other side, the most commonly used sacrificial electron acceptor is silver nitrate. Silver ions react with photogenerated electrons resulting in the reductive photodeposition of metallic silver on the photocatalyst surface (formula 2.8).

$$Ag^+ + e^-_{CB} \rightarrow Ag\downarrow \quad (2.8)$$

The severe disadvantage of this method is the blockage of active sites on the surface of the photocatalyst by the deposition of metallic silver. Furthermore, it changes the light absorption of the system and silver nanoparticles may be catalytically active on their own.[45] Additionally, it has been suggested that Ag^+ ions in solution may be further oxidised to Ag^{2+}, which could form peroxides in solution, resulting in additional oxygen formation upon oxidation.[45] Silver ion solutions are also sensitive to halide impurities, which would result in precipitation of insoluble silver salts.

2.2.5 The Role of Co-Catalysts

Co-catalysts are small metal or metal oxide nanoparticles that have been deposited on the surface of the photocatalyst to enhance their activity. This enhancement results from two different effects; one is that co-catalysts lower the necessary over-potential for hydrogen or oxygen evolution reactions. This is especially important on the oxygen evolution reaction, since the formation of an oxygen molecule requires the transfer of four holes and the removal of four protons making it the limiting step in overall water splitting.[46] The second effect is the enhancement of charge carrier separation. Photogenerated charge carriers are transferred to the co-catalyst. Since a single co-catalyst only promotes one half-reaction the charge carriers are spatially separated. The efficiency of charge carrier transfer is dependent on the energy difference between photocatalyst and co-catalyst.[46] It has been found, for example, that cobalt phosphate on $BiVO_4$ is supressing surface recombination and is not enhancing kinetics.[5]

Typical co-catalysts for hydrogen evolution are noble metals, such as Pt or Rh, whereas noble metal oxides, especially RuO_2 and IrO_2, are typically used for oxygen evolution.[46]

While several methods of co-catalyst depositions – *e.g.* impregnation or electrodeposition – exist, *in situ* photodeposition offers several advantages such as the homogeneous distribution or the avoidance of an extra step. It is also possible to deposit reduction and oxidation co-catalysts on different facets using photodeposition.[47] However, there are no reports of a generally superior method – probably due to the wide range of experimental differences.[48]

A widely used co-catalyst system for water splitting is Rh/Cr_2O_3. The high activity of the system, consisting of a Rh core and a Cr_2O_3 shell, is explained by Maeda *et al.*: Cr_2O_3 prevents the

back reaction of evolved hydrogen and oxygen on the Rh surface.[49,50] However, results from Busser *et al.* imply that Cr_2O_3 acts as a co-catalyst for oxygen evolution in water splitting with CuO_x-Cr_2O_3/Ga_2O_3 and that a core/shell system is unlikely. Simultaneous deposition of both Rh and Cr_2O_3 and deposition of first Cr_2O_3 and then CuO_x results in a more active system than the consecutive deposition of CuO_x and Cr_2O_3.[51] It has also been found that pure Cr_2O_3 and Cr_2O_3/Rh are more active than Rh/Cr_2O_3 in overall water splitting with $Ba_5Ta_4O_{15}$, further implying that Cr_2O_3 functions also as an oxygen evolution co-catalyst and that the formation of a Rh/Cr_2O_3 core/shell system is not necessary.[52]

2.2.6 Bandgap Engineering

The photocatalytic solar-to-hydrogen efficiency of a semiconductor is directly linked to the size of the bandgap, *i. e.* the amount of light that can be absorbed. Most commonly used photocatalysts, consisting of d^0 and d^{10} metal ions, possess large bandgaps.[53] Consequently, these materials can only absorb UV light. The UV light is only a minor part of the solar spectrum since ozone O_3 and oxygen are able to absorb UV light. The solar spectrum before and after 1.5 air masses is depicted in Figure 2.10; the difference mainly results from absorption by IR-active species, especially CO_2 and water. Defect-pyrochlores with a high bandgap – *e.g.* $CsTaWO_6$ with 3.6 eV – only absorb in the minor UV part of the solar spectrum. Lowering the bandgap to increase the amount of absorbable light is a highly promising way to enhance photocatalytic activity.

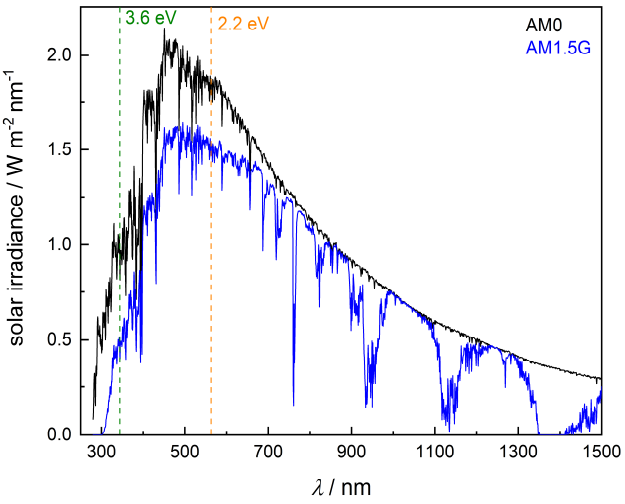

Figure 2.10: Solar light before entering earth´s atmosphere (AM0, black) and after 1.5 air masses (AM1.5G, blue). The dashed lines represent bandgaps of 3.6 eV (green) and 2.2 eV (orange).

Decreasing the bandgap can be achieved by either adjusting the VB or the CB. In most metal oxide semiconductors the VB is formed by O 2*p* states and the CB consists of metal ion *d* states.[53] However, since the CB minima in most photocatalytic materials are only slightly more negative than the hydrogen evolution potential, shifting the CB minimum to a more positive potential could easily make the material unable to evolve hydrogen. In contrast, the VB maximum is located at highly positive potentials for most metal oxide semiconductors, which makes the shift of the VB to more negative potentials more promising.[54]

To shift the VB to less positive potentials it is necessary to introduce occupied states at energies above the original VB. These occupied states can either be introduced by doping with transition metal ions, main group metal ions or non-metals. Doping TiO_2 with different transition metal ions results in visible light absorption, since the t_{2g} states of the doping metal ions create an occupied level in the bandgap or on top of the VB.[55] Doping may increase or decrease the photocatalytic activity, depending on the dopant and its concentration. Decrease can occur due to transition metal ions acting as recombination centres.[56] Additionally, the influence of the dopant may also change depending on the exact crystal lattice site. By doping $SrTiO_3$ with Cr-cations Wang *et al*. found much higher activity for Cr^{3+} on the Sr^{2+} site than for Cr^{3+} and Cr^{6+} on the Ti^{4+} site, since the unoccupied Cr^{6+} states act as trapping states below the potential for hydrogen evolution.[57] The ion exchange from K^+ to Cu^{2+} in $CuNbTeO_6$ with defect-pyrochlore crystal structure resulted also in the formation of a mid-gap state, which acts as recombination centre.[58]

The reason for the smaller bandgap of $NiNb_2O_6$ as compared to $SrNb_2O_6$ – 3.1 eV compared to 3.7 eV – is the split of the *d* states of octahedrally coordinated Ni^{2+}.[53] The filled *d* states are around 1 V more negative than the O 2*p* states, whereas the unoccupied *d* states are approximately 5.5 V above the O 2*p* states. The transition from the filled Ni *d* states to the Nb *d* state conduction band at –0.7 V results in the smaller bandgap energy.

The optical properties of tungstates with the general formula MWO_4 (M^{2+} = Mg^{2+}, Mn^{2+}, Co^{2+}, Ni^{2+}, Cu^{2+} and Zn^{2+}) are highly dependent on the M^{2+} cation.[20] All compounds crystallise in the wolframite structure with the exception of $CuWO_4$, which is triclinic due to a Jahn-Teller distortion. M^{2+} cations with a closed electron shell, *i.e.* Mg^{2+} (d^0) and Zn^{2+} (d^{10}), result in bandgaps of 4.06 eV and 3.95 eV (Figure 2.11), while M^{2+} cations with only partially filled *d* levels – Mn^{2+} (d^5), Co^{2+} (d^7), Ni^{2+} (d^8) and Cu^{2+} (d^9) – have far lower bandgaps of 2.72 eV, 2.67 eV, 2.99 eV and 2.31 eV, respectively.

This is because the 3*d* levels of the transition metal cations are located above the O 2*p* levels, thus lowering the bandgap energy. The calculated excitation energy from O 2*p* levels to the

W 5*d* levels would be 3.7 eV for $MnWO_4$, a similar value as for $MgWO_4$ and $ZnWO_4$. Also visible are *d*-*d* transitions that appear as broad bands at higher wavelengths than the excitation from valence to conduction band.

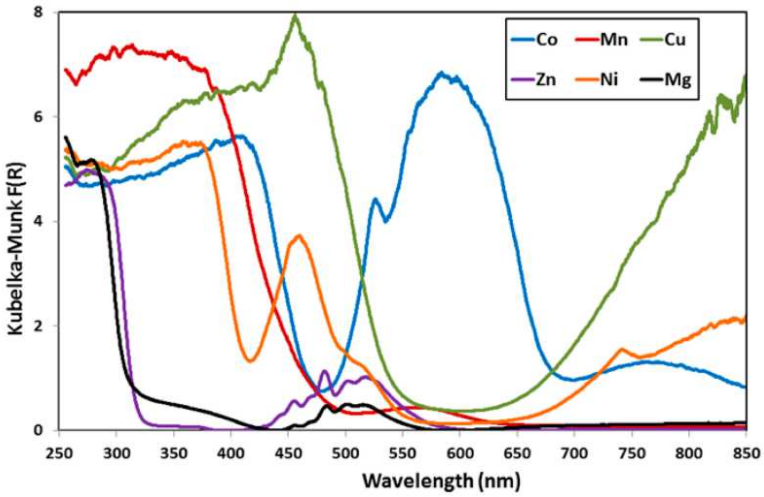

Figure 2.11: Kubelka-Munk absorption spectra of MWO_4 compounds.[20] Reprinted with permission from the American Chemical Society.

An alternative is the use of main group metal cations with d^{10} or $d^{10}s^2$ electron configuration. By substitution of Al^{3+} – which has no *d* electron states – with Ga^{3+} with d^{10} electron configuration, it is possible to adjust the position of the CB and therefore the size of the bandgap of $AgAl_{1-x}Ga_xO_2$ between 2.2 eV and 2.8 eV.[59]

In 2008 the research group around Kudo reported a bandgap decrease of 0.7-1.2 eV in layered titanates and niobates after ion exchange of K^+ against Sn^{2+}.[18] These samples have been photocatalytically active in visible light in the presence of sacrificial agents and co-catalysts. However, Kudo and his colleagues also observed a decrease in activity and an enlarged bandgap after photocatalytic experiments in $Sn^{2+}/K_4Nb_6O_{17}$, which is attributed to the oxidation of Sn^{2+} to Sn^{4+} by photogenerated holes. The oxidation was also observed in $Sn^{2+}/KTiNbO_5$, which became inactive after several hours and also showed a shift of the absorption edge towards smaller wavelengths after photocatalytic experiments.[18]

In the same year the research group around Kudo also published the synthesis of SnM_2O_6 and $Sn_2M_2O_7$ (M = Nb, Ta) by solid state synthesis.[17] Calculations showed that the valence bands of $Sn_2Ta_2O_7$, $SnNb_2O_6$ and $SnTa_2O_6$ consist of Sn 5*s* and O 2*p* states, whereas the Sn 5*s* states constitute the upper and lower part of the valence band (Figure 2.12).

The calculated bandgap of $Sn_2Ta_2O_7$ is approximately 1 eV smaller than that of $Ca_2Ta_2O_7$, since the CB is narrower without the contribution by the Sn 5*s* states. XPS measurements of

the Sn precursors also revealed the presence of Sn^{4+} states, which are located beneath the CB and act as electron traps.[17]

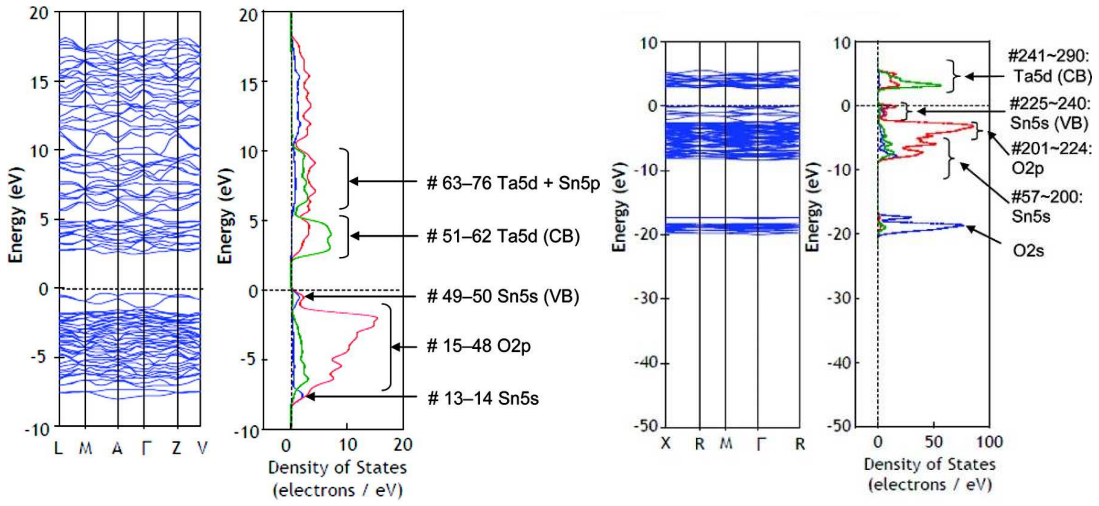

Figure 2.12: Electronic band structures and densities of states of $SnTa_2O_6$ (left) and $Sn_2Ta_2O_7$ (right).[17] Reprinted with permission from the American Chemical Society.

The bandgap decrease upon incorporation has also been observed in stannous tungstate $SnWO_4$, which manifests in two polymorphs: orthorhombic α-$SnWO_4$ as the low temperature form and β-$SnWO_4$, which is stable at temperatures above 670 °C and can be obtained by quenching after calcination.[60] The VB consists of Sn 5*s* and O 2*p* states, in which the Sn 5*s* states form the upper and lower part of the VB (Figure 2.13). The shorter W–O bond length in β-$SnWO_4$ increases the crystal field splitting, resulting in a larger calculated bandgap. The measured optical bandgaps are 1.64 eV for α-$SnWO_4$ and 2.68 eV for β-$SnWO_4$.

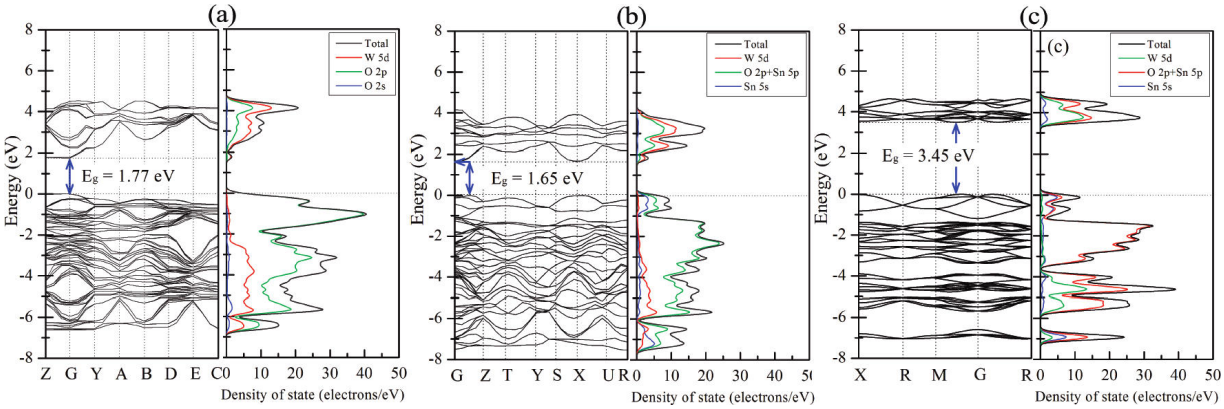

Figure 2.13: Electronic band structures of monoclinic WO_3 (left), orthorhombic α-$SnWO_4$ (middle) and cubic β-$SnWO_4$.[60] Reprinted with permission from the American Chemical Society.

XPS measurements also revealed the presence of Sn^{4+} for both polymorphs, indicating a general instability of Sn^{2+} containing metal oxides. Both polymorphs showed higher activity in photocatalytic dye degradation than WO_3; additionally, β-$SnWO_4$ showed hydrogen evolution under visible light irradiation with methanol as a sacrificial agent.

Boltersdorf *et al.* reported a bandgap decrease of 1.3 eV upon ion exchange up to a Sn^{2+} content of 17.7 % for $Na_{2-2x}Sn_xTa_{4-y}Nb_yO_{11}$ solid solutions.[61] Their samples also showed hydrogen evolution with platinum as co-catalyst and methanol as sacrificial agent under UV irradiation. The same group also reported the synthesis of Sn_2TiO_4 with a bandgap of approximately 1.6 eV; their samples were active in both sacrificial hydrogen and oxygen evolution in UV and visible light.[62] However, for some samples the hydrogen evolution seems to stop after some hours. Additionally, XP spectra also reveal a significant part of Sn^{4+}, apparently unnoticed by the authors.

Conductivity measurements on epitaxial $SnNb_2O_6$ thin films showed high resistivities.[63] Calculations showed low formation energies for oxygen vacancies $V_O^{\cdot\cdot}$ and tin(IV)-on-niobium(V)-sites $Sn_{Nb}^{'}$ defects, resulting in low charge carrier concentrations and thus low conductivity (Figure 2.14).

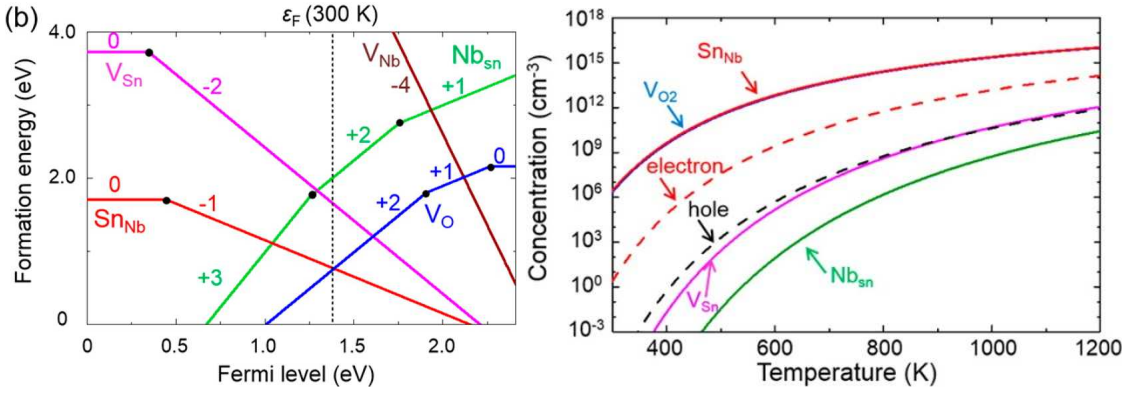

Figure 2.14: Calculated formation energies of defects (left) and calculated concentrations of defects and carriers in $SnNb_2O_6$ at different temperatures (right).[63] Reprinted with permission from the American Chemical Society.

The first Sn^{2+} incorporation into a defect-pyrochlore was reported in 2009 by Uma *et al.*[19] $KSbWO_6$, $KTaWO_6$ and $H_2Sb_2O_6$ have been used as base material in an ion exchange with aqueous $SnCl_2$ solution, which resulted in a bandgap reduction of 0.9-1.6 eV. The photocatalytic activity had been investigated by degradation of methyl orange in visible light. The defect-pyrochlores $KTi_{0.5}W_{1.5}O_6$ and $KTi_{0.5}Te_{1.5}O_6$ have also been used in similar ion exchange reactions and employed in dye degradation.[64,65] While dye degradation is relatively easy to per-

form, it should not be performed to evaluate photocatalytic activity in visible light, since photocatalytic degradation may happen parallel to sensitisation.[66] Sn^{2+}-doped $KNbWO_6$ has also been used in photocatalytic carbon dioxide reduction.[67] $Sn_2Sb_2O_7$ with pyrochlore structure has been synthesised *via* ion exchange starting from antimonic acid and was found to be active in sacrificial hydrogen evolution in visible light.[68] The photocatalytic activity decreases if the tin content is increased beyond that of stoichiometric $Sn_2Sb_2O_7$, which is attributed to defects within the crystal lattice.[69]

A similar absorption edge shift to higher wavelengths as with Sn^{2+} has also been observed upon Bi^{3+} and Pb^{2+} incorporation, however, the shift is of smaller magnitude compared to Sn^{2+}.[70,71]

Another method to diminish the bandgap is doping with non-metals on oxygen sites, especially nitrogen or sulphur. $CsTaWO_6$ has been doped with nitrogen by annealing in an ammonia flow at high temperatures, resulting in a bandgap decrease of 1.4 eV even though the nitrogen content was relatively low with approximately 0.3 wt%.[72] The reason for the bandgap diminishment is the hybridisation of N 2*p* states with the O 2*p* states that form the VB. It was also shown that doping $CsTaWO_6$ with single N atoms would only result in a calculated bandgap decrease of approximately 0.3 eV. However, doping with higher nitrogen concentrations would result in the formation of N–N clusters.[73] The electron transition from the N–N π^* states of these clusters into the CB results in a bandgap of 1.6 eV, which is fairly close to the experimental value. Additionally, nitrogen doping also results in the formation of oxygen vacancies. Doping with sulphur and co-doping with both nitrogen and sulphur in $CsTaWO_6$ also results in a decreased bandgap.[74] Doping with sulphur results in a downward shift of the CB consisting of S 3*p* and 3*d* states.[75] Moreover, co-doping with nitrogen and sulphur also promotes the separation of charge carriers.

Other strategies to enhance the absorption of visible light include the use of metal nanoparticles for their surface plasmon resonance or sensitisation of a photocatalyst with dyes. Since these strategies are not employed in this thesis, their explanation will be succinct. Small noble metal nanoparticles – especially gold and silver – show absorption of visible light, due to their surface plasmon resonance. These particles are dispersed on the surface of photocatalyst and the photogenerated charge carriers are separated at the interface between noble metal particle and semiconductor.[76] A similar approach is used in dye sensitisation. A highly absorbing dye is adsorbed on the surface of the semiconductor. The photogenerated electrons will be transferred from the dye to the semiconductor and eventually to a co-catalyst for the actual photocatalytic reaction. The oxidised dye is then regenerated by a redox mediator or an oxidation co-catalyst.[77]

2.3 Defect-Pyrochlores

Pyrochlores are cubic minerals with the general formula $A_2M_2O_6X$ and a wide range of possible compositions. A and M are typically rare-earth or transition metals and X can be an additional O^{2-}, OH^- or F^- anion. Defect-pyrochlores lack one A cation and the additional X anion, resulting in the general formula $AM_xM'_{2-x}O_6$. Here, A is a monovalent cation, while M and M' can be transition or main group metal cations.

2.3.1 The Defect-Pyrochlore Crystal Structure

Defect-pyrochlores crystallise in the cubic space group with the Hermann-Mauguin symbol $Fd\bar{3}m$ (number 227). The structure consists of corner-sharing MO_6 and $M'O_6$ octahedra, which form channels with a hexagonal cross section (Figure 2.15). In these channels the A cations are located and loosely coordinated eightfold by oxygen atoms of the octahedra. The metal cations M and M' both occupy the same crystallographic 16c (0, 0, 0) Wyckoff positions and are statistically distributed; this solid solution structure is a key advantage of the defect-pyrochlore structure. By changing the ratio of M to M' it is possible to change the valence of M, which allows a wide range of elemental compositions with the general formulas $AM_1M'_1O_6$ for M^{5+},[12–14,78,79] $AM_{0.5}M'_{1.5}O_6$ for M^{4+},[11,15,80] $AM_{0.33}M'_{1.67}O_6$ for M^{3+},[9,15,81,82] and $AM_{0.25}M'_{1.75}O_6$ for M^{2+}[15]. M' is a hexavalent cation, which can be Mo^{6+}, Te^{6+} or W^{6+}. Oxygen atoms are located at a 48f (x, 0.125, 0.125) Wyckoff position. The number of formula units per unit cell is eight.

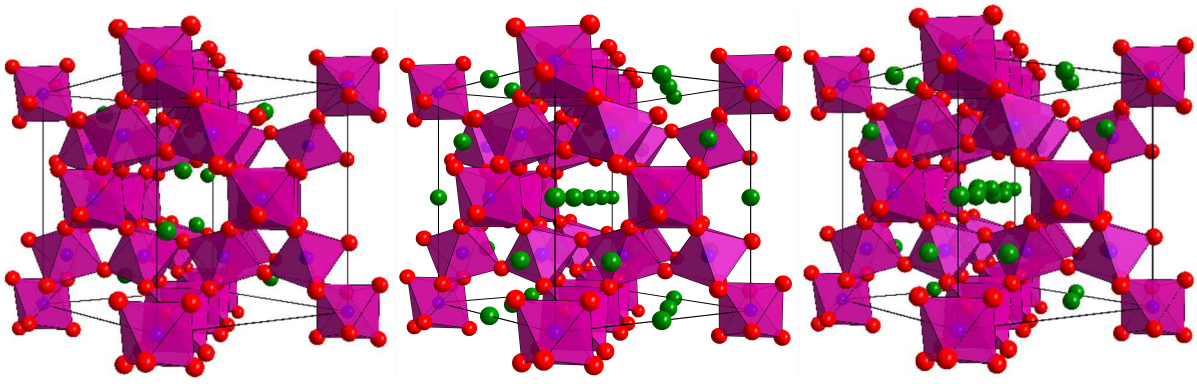

Figure 2.15: Crystal structure of defect-pyrochlores; A cations are shown at different Wyckoff positions: 8b (left), 16d (middle) or 32e (right). A cations are depicted in green, M and M‘ cations in blue and O anions in red.

The exact positions of the A cations depend on size and nature of the cations and are disputed in the literature – especially for K^+. In generally, three different Wyckoff positions are possible: 8b (0.375, 0.375, 0.375) (fully occupied), 16d (0.5, 0.5, 0.5) (half occupied) and 32e (x, x, x)

(one quarter occupied).[83] While Cs^+ has been located at 8b[14,82,84,85] or 32e[80,81], Rb^+ has also been located either at 8b[14] or at 32e[82], whereas K^+ has been located at 8b[8], 16d[14] or at 32e[82,85–87]. Due to the larger electron polarizability Tl^+ is also located at 32e.[14] The A cations are only loosely coordinated and can easily be exchanged.[88,89] The sodium compounds $NaTaWO_6$ and $NaTaMoO_6$ are orthorhombic, presumably due to the smaller size of Na^+.[90] The lithium compounds $LiNbWO_6$ and $LiTaWO_6$ are not defect-pyrochlores, but crystallise in a layered structure.[91] However, Li^+ and Na^+ containing defect-pyrochlores can be obtained by ion exchange.[92] Defect-pyrochlores with A = H^+ or NH^{4+} can also be prepared by ion exchange and are proton conducting.[93–96]

X-ray diffraction on $CsNbMoO_6$ and $CsTaMoO_6$ single-crystals revealed a distortion of the MO_6-octahedra along the [111] direction, resulting in the non-centrosymmetric $F\bar{4}3m$ space group.[78] Disorder has also been found in $RbNbWO_6$, in which the WO_6 octahedra consists of three different W-O distances.[97] *In-situ* XRD with synchrotron radiation revealed that $CsTaWO_6$ becomes orthorhombic at pressures above 5.9 GPa and monoclinic above 15.7 GPa.[98] It is also argued that the phase transformation to orthorhombic indicates a tetragonal distortion of the cubic crystal structure at normal pressure, however, no results to undermine this assumption are shown.

A mixed valence defect-pyrochlore CsW_2O_6 – or rather $CsW^{5+}W^{6+}O_6$ – was first described in 1993 by Cava *et al.* and has been investigated for superconductivity.[99–101]

2.3.2 Water Incorporation

Insertion of water molecules into K^+ containing defect-pyrochlores has first been claimed in 1967, but not investigated.[8] Neutron diffraction of $KNbWO_6 \cdot 0.69\ D_2O$ revealed that both K^+ and D_2O occupy 32e positions and that the distances between K^+ and the D_2O oxygen atoms are indeed shorter than the distances between K^+ and the oxygen atoms of the framework octahedra.[102] The displacement of K^+ from ideal 8b and 16d sites takes place to avoid close distances to two water molecules.

Recent neutron diffraction experiments confirmed the existence of water molecules in $KNbWO_6$, but not in $KSbWO_6$ and $KNbTeO_6$.[87] The O atoms of water are located at 32e sites and the H atoms at 96g. The large atomic displacement parameters of 2.8 $Å^2$ and 15 $Å^2$, respectively, indicate the labile nature of the water molecules. The incorporation of water into

$KNbWO_6$ was found to be reversible with a nominal formula of $KNbWO_6 \cdot 1.17\ H_2O$. The octahedra in all three compounds are axially distorted, but the M/M'–O distances are equal. The more covalent nature of the main group elements Sb and Te is reported to be responsible for smaller M/M'–O–M/M' angles and shorter M/M'–O distances and thus smaller unit cells as compared to $KNbWO_6$.

The diffusion of water molecules in $KNbWO_6 \cdot H_2O$ has been found to be pseudo-two-dimensional, which has been ascribed to the [110] direction of the channels.[103] The reported activation energy for diffusion is between 36-43 kJ mol^{-1} and suggests van der Waals interactions.[103]

While $RbNbWO_6$ does not incorporate water molecules at ambient conditions, high-pressure XRD measurements performed with monochromatic synchrotron radiation revealed water incorporation at pressures above 3.47 GPa.[83] The Rb^+ atoms move from 8b to 32e positions – with water molecules also residing on 32e positions. The shift of Rb^+ atoms results in shorter Rb–O distances; in order to compensate for this the unit cell expands. When the pressure is released, the Rb^+ atoms shift back to 8b positions and water molecules are expelled from the unit cell. $KNbWO_6 \cdot H_2O$ shows only an expected decrease of unit cell volume and no change in reflection intensity. Water incorporation at high pressures has also been observed for NH_4NbWO_6.[83,104]

Ion exchange in hydrothermal conditions has been used to dope $KNbWO_6$ with Eu^{3+} to achieve luminescence; the presence of water molecules quenches the luminescence.[89] Water incorporation increases the local symmetry of Eu^{3+}, resulting in a less likely electric dipole transition.[105] Interaction between Eu^{3+} and the O atom of water results in the splitting of spin-up Eu 4*f* states: the unoccupied states are moved 0.3 eV above the VB maximum, thus reducing the bandgap (Figure 2.16); the spin-down states do not change position.[105] The occupied O 2*p* states of water are raised above the VB maximum. Additionally, the presence of water molecules increases the formation energy of oxygen vacancies.

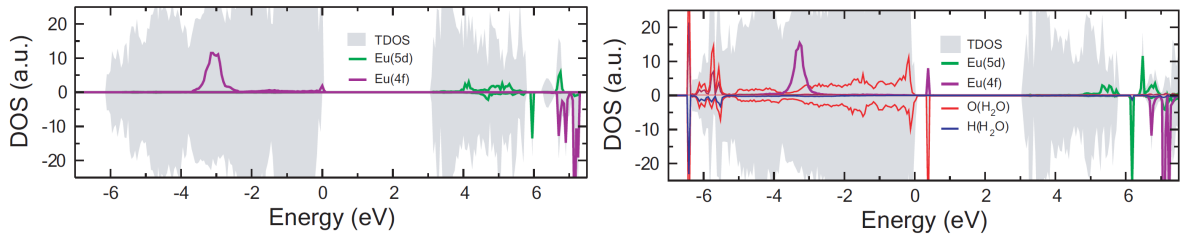

Figure 2.16: Partial DOS for anhydrous (left) and hydrous (right) Eu^{3+} doped $KNbWO_6$.[105]

2.3.3 Tellurium containing Defect-Pyrochlores

The tellurium defect-pyrochlores $AVTeO_6$ (A = K^+, Rb^+, and Cs^+) are reported as either greenish-grey (K^+ and $Rb^{+)}$ or beige (Cs^+) powders that decompose above 550 °C.[21] The corresponding antimony compounds $ASbTeO_6$ (A = K^+, Rb^+, Ag^+, Cs^+ and Tl^+) require higher temperatures (700-750 °C) to be synthesised.[10] The electric conductivities of $ATi_{0.5}Te_{1.5}O_6$ (A = K^+, Rb^+, Cs^+ and Tl^+) are similar with slightly lower values for Rb^+; the conductivity is reported to be a mixture of ionic and electronic parts.[11] Additionally, a linear correlation between the unit cell parameter and the ionic radii of A and between the unit cell parameter and the ionic radii of M (Ti^{4+}, Zr^{4+}, Hf^{4+}) and M' (Te^{6+} and W^{6+}) was found.

Combined X-ray and neutron diffraction of $KSbTeO_6$ revealed that K^+ occupies a 32e Wyckoff position that is indistinguishable within the experimental error – and therefore equivalent – to an 8a site.[106] The octahedra are axially distorted, but the Sb/Te–O distances are equal. However, both 8b and 32e positions of K^+ were found for $KNbTeO_6$.[87,107] High temperature measurements of $KNbTeO_6$ showed a phase transition above 870 °C and a starting decomposition above 935 °C.[107]

A range of $CsM_xTe_{2-x}O_6$ compounds with M^{2+}, M^{3+} and M^{4+} have been synthesised using a solid state reaction by Siritanon *et al.*[15] A linear correlation between the ionic radii of M and the unit cell parameter could be found. Electric conductivity could be detected in some of these compounds; temperature dependence of conductivity and Seebeck coefficients indicate n-type semiconducting behaviour. All compounds are reported as coloured black; reduced Te^{6+} is suspected being the reason. This reduction results in occupied Te 5*s* states, which are located beneath the conduction band. The conductivity of some samples can be explained by mixing of M states with the Te 5*s* conduction band. Neutron diffraction of $CsAl_xTe_{2-x}O_6$ indicated fully occupied O sites for x = 0.24-0.45 values, which precludes a significant share of O vacancies.[108]

$CsMn_xTe_{2-x}O_6$ defect-pyrochlores with x = 0.15-0.43 have been synthesised with the intent to create a mixed valence Te oxide for electronic conductivity.[109] X-Ray absorption near edge spectroscopy (XANES) measurements showed that Mn is mainly incorporated as Mn^{3+} with Mn^{4+} also present if x > 0.33. XANES measurements also revealed a decrease of Te^{4+} with increasing Mn content, indicating that Mn^{3+} replaces Te^{4+}. The energy levels for the Te 5*s* states have been found to be different with Te^{4+} 5*s* in the valence band maximum and Te^{6+} 5*s* states contributing to the conduction band minimum. This splitting of the Te 5*s* band is attributed to a local distortion of the crystal lattice resulting in a longer Te^{4+}–O bond.

2.3.4 Defect-Pyrochlores in Photocatalysis

The first photocatalytic application of a defect-pyrochlore – namely $AMWO_6$ ($A = Rb^+$, Cs^+ and $M = Nb^{5+}$, Ta^{5+}) – was published in 2004 by Ikeda *et al.*[16] Overall water splitting was achieved by loading with NiO_x as a co-catalyst and reduced pressure; irradiation was done with a high power ultra-high pressure mercury lamp. Significant efforts were invested in doping defect-pyrochlores with nitrogen for visible light adsorption;[64,72–75,110,111] these are depicted in section 2.2.6. Substituting Ta^{5+} with Nb^{5+} in $CsTaWO_6$ changes neither crystal nor band structure; however, $CsTaWO_6$ exhibits surface Lewis-base sites, which $CsNbWO_6$ does not.[112] The substitution of W^{6+} with Mo^{6+} in $CsTaWO_6$ was also investigated.[112] The bandgap of $CsTaMoO_6$ is only 2.9 eV, compared to 3.6 eV for $CsTaWO_6$; the reason for this diminishment is a shift of the CB to more positive potentials. Due to the more positive potential, Mo^{6+} containing defect-pyrochlores are not able to evolve hydrogen anymore. Therefore, defect-pyrochlores with Mo^{6+} are excluded from this work. Ball-milling of $CsTaWO_6$ results in a higher surface area, but also creates surface defects, which decreases the photocatalytic activity.[113]

Several strategies have been employed to increase the surface area of $CsTaWO_6$. Weller *et al.* developed a hydrothermal synthesis that yields adjustable, single-crystalline nanoparticles between 8-30 nm.[22] The highest hydrogen evolution rates were found for intermediate particles with 13 nm size, showing that a high surface area does not correlate directly to photocatalytic activity. The reasons for the lower activity of smaller nanoparticles – and therefore higher surface areas – were the larger bandgap due to quantum confinement effects and a stronger agglomeration. Synthesis of highly mesoporous $CsTaWO_6$ *via* hard-templating or evaporation-induced self-assembly showed that the photocatalytic activity depends on pore diameter and pore size distribution rather than simply a high surface area.[114,115] Large pores and a broad pore size distribution seem to facilitate mass transport of solvent and sacrificial agent into the porous structure. Mesoporous $CsTaWO_6$ with a highly ordered 3D gyroidal pore structure with large mesopores showed considerably higher activity than non-ordered $CsTaWO_6$ with a higher surface area.[116] The large mesopores and the ordered pore structure with interconnected pores is favourably for mass transport and is not impaired by capillary forces or pore-blocking.

Tellurium containing defect-pyrochlores have only rarely been used in photocatalysis. $KM_xTe_{2-x}O_6$ ($M = Al^{3+}$, Cr^{3+}, Fe^{3+}, Ti^{4+}) have only been employed in dye degradation using a tungsten lamp; the reported bandgaps are 2.09 eV, 1.25 eV, 1.92 eV and 2.97 eV, respectively.[65,117] $KTaTeO_6$ and Ag^+ doped $KTaTeO_6$ with reported bandgaps of 2.47 eV and 2.14 eV have been used in the degradation of methyl violet and sacrificial hydrogen evolution in direct solar light.[25] $KNbTeO_6$ has been ion exchanged with Sn^{2+}, Ag^+ and Cu^{2+} to increase the visible

light absorption and used in dye degradation.[58] The bandgap of KNbTeO6 has been reported as 3.38 eV; the reported yellow colour of the sample has not been explained so far.

2.4 Nanostructuring

At first glance, nanostructuring of photocatalytic materials seems to be beneficial, since the small dimensions are resulting in larger surface areas and smaller diffusion lengths of photogenerated charge carriers. The absolute possible surface area of a non-porous sample directly depends on the particle size. The theoretical surface area of non-agglomerated, spherical and non-porous $KTaWO_6$ nanoparticles decreases rapidly from approximately 200 $m^2\ g^{-1}$ for particles with a diameter of 5 nm to 10 $m^2\ g^{-1}$ for particles 100 nm in diameter (Figure 2.17). The surface-area-to-volume ratio is also rapidly decreasing and is only larger than unity for particles smaller than 6 nm.

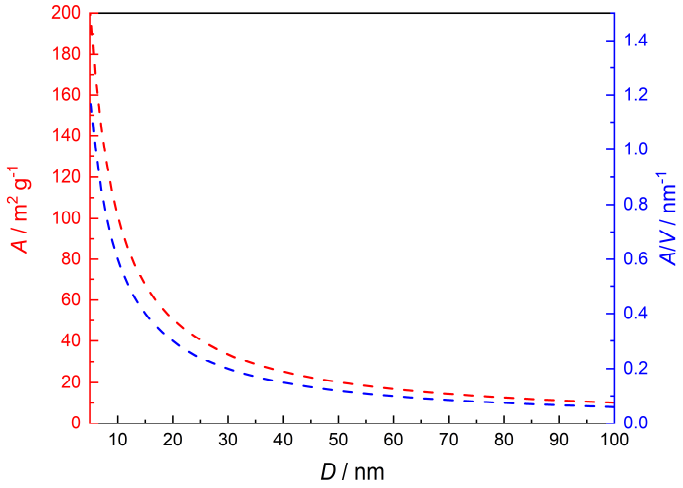

Figure 2.17: Theoretical surface area *A* (red) and surface-area-to-volume ratio *A*/*V* (blue) of non-agglomerated, spherical and non-porous $KTaWO_6$ nanoparticles with particle diameter *D*.

However, a larger surface area also enhances surface recombination (section 2.2.3), which may end up decreasing the photocatalytic activity. Moreover, the comparatively low temperatures used in the syntheses of materials with high surface areas usually results in a higher number of unhealed defects, thus increasing bulk recombination of charge carriers.

Another advantage of nanostructuring is to compensate for the generally limited diffusion length of photogenerated charge carriers. The optimum particle size would be twice the mean diffusion length of photogenerated charge carriers. If the diameter of an ideally spherical particle is more than twice as large as the diffusion length, not all generated charge carriers will

reach the surface. On the other hand, if the particles become too small, the number of photo-generated charge carriers will be reduced. In addition, the quantum size effect will result in a larger bandgap and the larger surface area will result in increased surface recombination. However, small nanoparticles are often single-crystalline in nature, thereby avoiding recombination at grain boundaries. For $CsTaWO_6$ the optimum particle size has been determined to be around 13 nm.[22]

Nanostructured materials can either be synthesised top-down or bottom-up. Top-down syntheses start from a bulk material that is reduced in its size; possible methods are ball milling or etching. Bottom-up syntheses are starting from smaller building blocks, such as molecules or ionic compounds. These precursors are then dissolved; depending on the concentration either nucleation or particle growth will occur. Possible synthesis approaches are hydrothermal or solvothermal treatment, sol-gel synthesis, microwave-assisted synthesis, electrospinning or the use of ionic liquids.[22,36,118–120]

Instead of dense particles, the formation of porous materials can also be used to achieve high surface areas either by soft or hard templating. In soft templating a scaffold is formed *in-situ* from structure directing agents, such as ionic surfactants or polymers. The metal ion precursors are first hydrolysed and then condensed; removal of the structure directing agents can be achieved by either combustion or extraction.[116,121] In hard templating a rigid, mesoporous scaffold is infiltrated with a metal ion precursor solution, followed by annealing to obtain the desired metal oxide; the scaffold can either be removed with combustion or etching.[114,122]

2.4.1 Sol-Gel Synthesis

As described in section 2.3.1 above, the defect-pyrochlore structure is a solid solution, in which M and M' are statistically distributed. Conventional solid state reaction requires the diffusion of solids, which requires high temperatures and long annealing times and even then may not result in an ideal distribution of M and M' atoms. For that reason an aqueous sol-gel synthesis developed by Schwertmann *et al*. was employed.[113] The metal ion precursors are dissolved in water, which results in a homogeneous mixture. Chelate ligands are added to prevent the precipitation of the metal ion precursors. In this work citric acid and ethylenediaminetetraacetic acid (EDTA) are used. Chelate ligands are also necessary to ensure the presence of isolated tungsten ions in solution, since the used tungsten precursors – ammonium para tungsten oxide and ammonium meta tungsten oxide – tend to form polyoxometalates in solution (Figure 2.18). Since EDTA is insoluble in water, the pH is first increased with ammonium hydroxide solution until dissolution of the chelate ligands. The pH is then decreased with nitric acid to 4-5, since

many metal ions form insoluble hydroxides and oxides at basic pH values. Additionally, hydrogen peroxide is added to stabilise the highest oxidation state of the metal precursor salts.

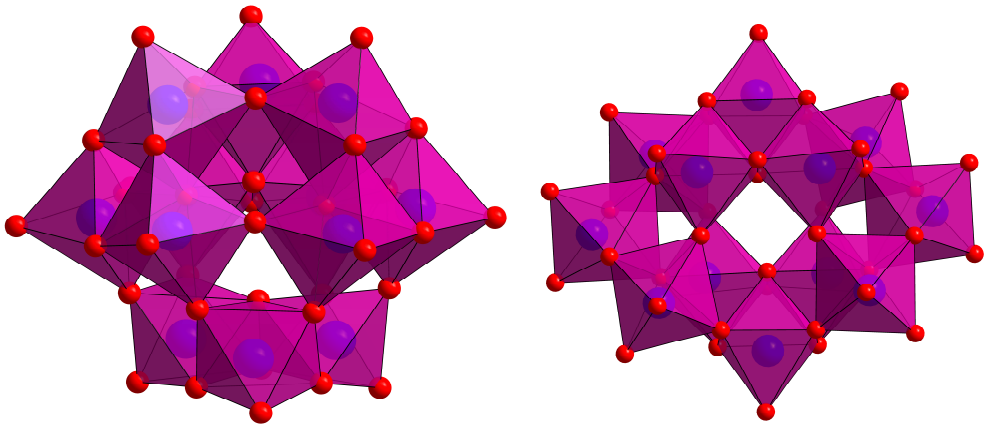

Figure 2.18: Crystal structures of the metatungstate cluster $W_{12}O_{40}$ with the α-Keggin structure (left) and the paratungstate cluster $W_{12}O_{42}$ (right). Tungsten atoms are depicted in blue and oxygen atoms in red. Modelled with the crystal structure information published by Juelsholt *et al.*[123]

During the synthesis the solvent is evaporated, resulting in an increasing concentration of metal cations and in the formation of a viscous solution with weakly interconnected metal complexes.[124] The next step is pyrolysis in air, whereas the chelate ligands are combusted. The nitrate ions from metal ion precursors and nitric acid act as oxidant, which in combination with the organic ligands as fuel typically results in a rapid, self-propagating combustion reaction.[125] This process is enhanced by the initial addition of ammonia: ammonia in combination with nitric acid leads to the formation of ammonium nitrate, which decomposes to nitrous oxides and oxygen accelerating the reaction.[124] Due to the high amount of chelate ligands, carbon remains in the pyrolysed solid.[125] The final step of the synthesis is annealing in air atmosphere in order to remove the carbon and to crystallise the metal oxide. The annealing temperature and time necessary for the formation of a highly crystalline metal oxide may be lower than for a solid state reaction due to the homogenous mixture of the reactants.[124]

2.4.2 Hydrothermal Synthesis

A hydrothermal synthesis is performed in a closed vessel filled with water at temperatures above 100 °C and pressures above 1 bar(a). High temperature and elevated pressure have a significant influence on the physical properties of water, such as density, viscosity and dielectric constant. The decreasing dielectric constant changes the solubility of the precursors, while the decreasing viscosity results in a higher mobility.[126] Due to these conditions, the addition

of chelate ligands is not necessary as opposed to the sol-gel synthesis detailed above ‘(section 2.4.1). The hydrothermal synthesis used in this work is adapted from a synthesis of Weller *et al*.[22] The addition of ammonia or urea – which is subsequently hydrolysed to ammonia – is necessary to ensure the solubility of Ta^{5+} ions, since the $Ta(OEt)_5$ precursor hydrolyses rapidly in water. Ammonia can be easily removed after the reaction by washing with water.

However, one disadvantage is the incomplete reaction: EDX measurements have shown a surplus of Ta in $CsTaWO_6$.[22] This has been attributed to amorphous tantalum oxide, which is insoluble in water as opposed to caesium nitrate and ammonium tungstate. In addition, TGA-MS measurements have revealed the presence of nitrate ions that have not been removed by washing. The presence of nitrates is problematic, since light irradiation results in the formation on nitrate radicals, which may undergo other reactions.[127]

3 Experimental Procedure

3.1 Used Chemicals

All chemicals – except solvents – used in this work are listed in Table 3.1 and have been used without further purification. Potassium carbonate sesquihydrate and potassium nitrate have been dried at 80 °C for several days in advance in order to get rid of adsorbed water.

Table 3.1: List of all used chemicals.

chemical	purity	supplier
aluminium(III) nitrate nonahydrate	99 %	Acros Organics
ammonium meta tungsten oxide hydrate		Alfa Aesar
ammonium metavanadate	99 %	Alfa Aesar
ammonium niobate(V) oxalate hydrate	99.99 %	Aldrich
ammonium para tungsten oxide	99.99%	Alfa Aesar
antimony(III) acetate	97 %	Alfa Aesar
bismuth(III) citrate	99.99 %	Aldrich
caesium carbonate	99.9 %	Alfa Aesar
caesium nitrate	99.8 %	Alfa Aesar
chromium(III) nitrate nonahydrate	99 %	Acros Organics
citric acid monohydrate		Alfa Aesar, Bernd Kraft
cobalt(II) nitrate hexahydrate	99 %	abcr
copper(II) nitrate trihydrate	99-104 %	Sigma-Aldrich
ethylenediamine	98 %	Th. Geyer
ethylenediaminetetraacetic acid	99.4 %	Alfa Aesar
gallium(III) nitrate hydrate	99.9 %	Alfa Aesar
germanium(IV) ethoxide	99.99 %	abcr
hafnium(IV) ethoxide	99.9 %	Alfa Aesar
hydrogen peroxide	30 %	Fisher Scientific
indium(III) nitrate hydrate	99.99 %	Alfa Aesar
iron(III) nitrate nonahydrate	99 %	Acros Organics
lanthanum(III) nitrate hexahydrate	99.999 %	Acros Organics
magnesium(II) nitrate hexahydrate	99 %	Acros Organics
manganese(II) nitrate tetrahydrate	97 %	Sigma-Aldrich
nickel(II) nitrate hexahydrate	99.999 %	Aldrich
niobium(V) oxide	99.99 %	H. C. Starck
potassium carbonate	99 %	Acros Organics
potassium carbonate sesquihydrate	98 %	ORG Laborchemie
potassium chromate	99.9 %	Alfa Aesar
potassium nitrate	99%, 99%	Grüssing, Acros Organics

chemical	purity	supplier
potassium hydroxide		Bernd Kraft
rubidium carbonate	98 %	Alfa Aesar
scandium(III) nitrate hydrate	99.9 %	Alfa Aesar
Sicapent®		Merck
sodium carbonate	99.5 %	Sigma-Aldrich
sodium hexachlororhodate(III)		Aldrich
sodium sulphate anhydrous	99 %	J. T. Baker, Carl Roth
tantalum(IV) ethoxide	99.999%	Alfa Aesar,
	99.99%	abcr
tantalum(V) oxide	99.99 %	Acros Organics,
	99.98 %	H. C. Starck
tellurium(IV) oxide	99.99 %	Alfa Aesar
telluric acid (ortho)	99 %	Sigma-aldrich
tin(II) acetate		Aldrich
tin(II) bromide		Aldrich
tin(II) chloride dihydrate		Fisher Scientific
tin(II) iodide		Alfa Aesar
tin(II) oxalate	98%	Aldrich
tin(II) oxide		Merck
tin(II) sulfate	99%	Carl Roth
tin(IV) acetate		Alfa Aesar
titanium(IV) n-propoxide	98 %	Aldrich
tungsten(VI) oxide	99.9	Chem Pur
yttrium(III) acetate tetrahydrate	95 %	abcr
zinc(II) nitrate hexahydrate	99 %	Carl Roth
zirconium(IV) ethoxide	99 %	abcr

3.2 Hydrothermal Synthesis of $KTaWO_6$ Nanoparticles

$KTaWO_6$ nanoparticles have been synthesizes by adapting a previously published synthesis by Weller *et al.*[22]

For every synthesis 61 mg KNO_3 have been dissolved while stirring in a Teflon vessel using a mixture of water and 25 % aqueous ammonia solution; the total volume was always 17 mL. After dissolution of KNO_3, 147 mg ammonium para tungsten oxide were added, followed by 2.5 mL of 0.24 mol L^{-1} solution of tantalum(V) ethoxide in ethanol. Stirring was continued for 10 minutes; afterwards the Teflon vessel was placed into a steel autoclave (4744 general purpose acid digestion vessel from Parr Instrument Company) and placed in a drying furnace.

Both temperature and duration of the heat treatment were varied. Following the hydrothermal treatment, the resulting powder was retrieved by centrifugation, washed with water and ethanol and dried at 80 °C.

One control experiment was performed without addition of ammonia, one with 1 mL of ethylenediamine and one with 825 mg KOH instead.

Ion exchange of $KTaWO_6$ Nanoparticles

For ion exchange about 150 mg $KTaWO_6$ were added to an aqueous solution of tin(II) sulphate in 5 mL water. The molar amount of tin(II) sulphate was calculated for total ion exchange towards $Sn_{0.5}TaWO_6$; no excess has been used. The mixture was then shaken for 24 h at room temperature. Samples have been centrifuged, washed with water and dried at 80 °C.

Direct synthesis of $Sn_{0.5}TaWO_6$

The direct synthesis of $Sn_{0.5}TaWO_6$ was attempted *via* solid-state reaction and hydrothermal treatment. For the solid-state reaction 65 mg tin(II) oxide SnO, 212 mg tantalum(V) oxide Ta_2O_5 and 223 mg tungsten(VI) oxide WO_3 were ground in an agate mortar and annealed at 700 °C for 10 h in an argon flow of 100 sccm. The heating rate was 5 °C min^{-1}; heating-up and cooling down was also done in argon.

For the hydrothermal treatment, 65 mg $SnCl_2 \cdot 2\ H_2O$ and 147 mg ammonium para tungsten oxide were dissolved in 16 mL water and 1 mL 25 % ammonia solution. 0.15 mL $Ta(OEt)_5$ in 2.4 mL EtOH – resulting in a concentration of 0.24 mol L^{-1} – were added and stirring was continued for 10 minutes. Hydrothermal treatment was performed at 150 °C for 12 h in a stainless steel autoclave with a Teflon inlet (see above for details). Following the hydrothermal treatment, the resulting powder was retrieved by centrifugation, washed with water and ethanol and dried at 80 °C.

Analysis of Water Influence

For analysing the water influence on $KTaWO_6$ and $Sn_xK_{1-2x}TaWO_6$ a sample synthesised at 150 °C for 12 h in 25 % ammonia was chosen. Both samples were dried in a vacuum furnace at 150 °C in the presence of Sicapent®, which is phosphorous pentoxide on an inert carrier material with an indicator. Saturation with water has been achieved by placing the sample next to a vessel filled with water on a heating plate at 50 °C overnight. A glass dome was placed over vessel and sample to ensure an atmosphere saturated with water vapour.

Additional quantification of tin content

The elemental composition of ion exchanged samples was additionally determined by titrating the amount of the non exchanged Sn^{2+} remaining in solution. 60 mg $KTaWO_6$ (0.12 mmol) were ion exchanged with 13 mg tin(II) sulphate (0.06 mmol) in 10 mL water and shaken for 24 hours. The samples were subsequently retrieved by centrifugation and washed twice with 10 mL water. The supernatant and the washing water were then combined; 50 µL sulphuric acid were added and titrated with aqueous $KMNO_4$ solution (0.001 mol L^{-1}). The concentration of the $KMnO_4$ solution was checked by titrating against a known sodium oxalate concentration (0.01 mol L^{-1}).

3.3 Investigation of Ion Exchange Conditions

$KTaWO_6$ base material has been prepared by solid state synthesis.[112] A stoichiometric 0.5:0.5:1 mixture of 415 mg K_2CO_3, 1326 mg Ta_2O_5 and 1391 mg WO_3 has been ground in an agate mortar and calcined at 810 °C for 18 h in air. The heating rate was set to 5 °C min^{-1}. For ion exchange, 200 mg $KTaWO_6$ (0.4 mmol) have been added to 0.2 mmol of a Sn^{2+} precursor in the respective solvent and shaken for 24 h at room temperature (Table 3.2). Afterwards, the samples have been centrifuged, washed thrice in the respective solvent and dried at 80 °C. The sample exchanged in 1 mol L^{-1} hydrochloric acid was washed in water to remove chloride ions. Samples washed in dimethylsulfoxide (DMSO) were additionally washed in acetone to enable drying at lower temperatures.

Table 3.2: Overview of used ion exchange reactions.

Sn^{2+} precursor	mass / mg	solvent	volume / mL
$SnSO_4$	43	water	5
$Sn(OAc)_2$	47	water	5
$Sn(OAc)_2$	47	acetic acid	5
$Sn(OAc)_2$	47	methanol	5
$Sn(OAc)_2$	47	DMSO	5
SnC_2O_4	41	water	5
$SnCl_2 \cdot 2\ H_2O$	45	1 mol L^{-1} HCl	5
$SnCl_2 \cdot 2\ H_2O$	45	ethanol	5
$SnBr_2$	48	acetone	10
$SnBr_2$	48	DMSO	10
SnI_2	75	chloroform	10
SnI_2	75	toluene	10

3.4 Synthesis of $CsM_xW_{2-x}O_6$ Materials

$CsM_xW_{2-x}O_6$ materials have been prepared following a sol-gel synthesis published by Schwertmann *et al.*[113]

For the synthesis of 2 g $CsM_xW_{2-x}O_6$ thrice the molar amount of citric acid hydrate and twice the molar amount of EDTA were added to 120 mL water. Ammonia solution was added until both solids were completely dissolved. The solution was acidified with nitric acid until a pH of 4-5 was achieved; subsequently 10 mL 30 % hydrogen peroxide were added. The adding of hydrogen peroxide was omitted if M^{n+} is Co^{2+} or Mn^{2+} to prevent oxidation to Co^{3+} and disproportionation of hydrogen peroxide, respectively. Next, $CsNO_3$ was added and – after its dissolution – the solution was heated to 95 °C. During heating the M-precursor was added. Titanium(IV) n-propoxide, germanium(IV) ethoxide and tantalum(IV) ethoxide have been added dropwise as a 0.24 mol L^{-1} solution in ethanol; all other precursors have been added pure and at once. Following the complete dissolution of the M-precursor, ammonium tungsten oxide was added. Ammonium para tungsten oxide was used for M^{5+}, M^{4+} and M^{3+}, while for M^{2+} ammonium meta tungsten oxide was used due to the better solubility. The solution was concentrated to approximately 20 mL and then transferred into a porcelain bowl, which was placed into a heating mantle (Winkler) and heated to 350 °C. As a result of the reaction a black solid remained, which was subsequently ground into a powder and calcined at temperatures from 500-900 °C for 10 h in air; the heating rate was set to 5 °C min^{-1}. The exact amounts can be seen in Table 3.3 to Table 3.7.

Table 3.3: Necessary amounts for the synthesis of 2 g $CsM_{0.25}W_{1.75}O_6$.

M =	**Mg^{2+}**	**Mn^{2+}**	**Co^{2+}**	**Ni^{2+}**	**Cu^{2+}**	**Zn^{2+}**
$CsNO_3$ / mg	700	691	690	690	688	688
$M(NO_3)_2 \cdot n\ H_2O$ / mg	230	222	257	257	213	262
n =	6	4	6	6	3	6
$(NH_4)_6W_{12}O_{39}\ H_2O$ / mg	1549	1528	1525	1525	1522	1521
EDTA / g	2.10	2.07	2.07	2.07	2.06	2.06
citric acid / g	2.26	2.23	2.23	2.23	2.23	2.22

Table 3.4: Necessary amounts for the synthesis of 2 g $CsM_{0.33}W_{1.67}O_6$.

M =	Al^{3+}	Sc^{3+}	Cr^{3+}	Fe^{3+}	Ga^{3+}	In^{3+}	La^{3+}
$CsNO_3$ / mg	716	708	705	704	698	680	670
$M(NO_3)_3 \cdot n\ H_2O$	460	302	483	486	327	371	496
n =	9	1	9	9	1	1	6
$(NH_4)_{10}W_{12}O_{41}$ / mg	1565	1548	1541	1538	1522	1482	1462
EDTA / g	2.15	2.12	2.12	2.11	2.09	2.04	2.01
citric acid / g	2.32	2.29	2.28	2.28	2.26	2.20	2.17

Table 3.5: Necessary amounts for the synthesis of 2 g $CsM_{0.33}W_{1.67}O_6$.

M =	Y^{3+}	Sb^{3+}	Bi^{3+}
$CsNO_3$	690	677	644
$M(OAc)_3$ / mg	399	346	-
bismuth(III) citrate / mg	-	-	439
$(NH_4)_{10}W_{12}O_{41}$ / mg	1505	1476	1408
EDTA / g	2.07	2.03	1.93
citric acid / g	2.23	2.19	2.08

Table 3.6: Necessary amounts for the synthesis of 2 g $CsM_{0.5}W_{1.5}O_6$.

M =	Ti^{4+}	Ge^{4+}	Zr^{4+}	Sn^{4+}	Hf^{4+}
$CsNO_3$ / mg	737	721	708	691	656
$M(R)_4$ / mg	538	467	493	629	604
R =	O^nPr	OEt	OEt	OAc	OEt
$(NH_4)_{10}W_{12}O_{41}$ / mg	1448	1414	1390	1357	1288
EDTA / g	2.21	2.16	2.12	2.07	1.97
citric acid / g	2.39	2.33	2.29	2.24	2.12

Table 3.7: Necessary amounts for the synthesis of 2 g $CsMWO_6$.

M =	V^{5+}	Nb^{5+}	Ta^{5+}
$CsNO_3$ / mg	841	771	657
M precursor	NH_4VO_3	$NH_4Nb(C_2O_4)_2O$	$Ta(OEt)_5$
mass of M precursor / mg	505	1198	1369
$(NH_4)_{10}W_{12}O_{41}$ / mg	1100	1009	859
EDTA / g	2.52	2.31	1.97
citric acid / g	2.72	2.49	2.12

3.5 Synthesis of $ANbTeO_6$ Materials

All $ANbTeO_6$ samples have been synthesised *via* solid state reaction. Stoichiometric amounts of the precursors have been mixed in an agate mortar. The exact amounts are shown in Table 3.8. Annealing was performed at 700 °C for 10 h in air atmosphere with a heating rate of 5 °C min^{-1}; after cooling the samples were ground again.

Table 3.8: Necessary precursor amounts for the synthesis of 2 g $ANbTeO_6$.

A =	**Na^+**	**K^+**	**Rb^+**	**Cs^+**
A_2CO_3 / mg	312	389	575	725
Nb_2O_5 / mg	783	747	661	592
TeO_2 / mg	940	898	794	710

Above synthesis (for A = K^+, Rb^+, Cs^+) was also performed in a pure oxygen flow of 75 sccm oxygen instead of air. The used amounts were a quarter of those depicted in Table 3.8 (equivalent to 500 mg $ANbTeO_6$). Temperature, time and heating rates were identical to those described above.

As a control experiment, the standard synthesis – in air – has also been performed with a Te^{6+}-precursor, the exact amounts can be seen in Table 3.9.

Table 3.9: Necessary precursor amounts for the synthesis of 500 mg $ANbTeO_6$.

A =	**K**	**Rb**	**Cs**
A_2CO_3 / mg	97	144	181
Nb_2O_5 / mg	187	165	148
$Te(OH)_6$ / mg	323	286	255

3.6 Theoretical Calculations

The electronic structures of $Sn_{0.5}TaWO_6$ and $KTaWO_6$ have been calculated at hybrid density-functional level with the PW1PW method.[128] The Hartree-Fock exchange was reduced from 20 % to 14 % to improve the accuracy for electronic bandgaps.[129] Calculations were conducted with CRYSTAL17.[130] The following basis sets have been used; ECP28MDF with modified Def2-QVZPP basis sets for Sn,[131] all electron pob-TZVP for K and O,[132] and effective core potentials ECP60MWBand modified basis sets for Ta and W.[133]

4 Characterisation Techniques

4.1 X-Ray Powder Diffraction

X-Ray Diffraction (XRD) patterns were recorded either on a Malvern PANalytical X'Pert Pro with a X`Celerator detector or a Malvern PANalytical Empyrean with a Pixcel 1D detector. Measurements were performed in Bragg-Brentano geometry and with Cu K_α radiation with wavelengths λ of 1.54056 Å and 1.54439 Å. The incident divergence slit was fixed to ½° to achieve a constant irradiated sample volume.

$KTaWO_6$ nanoparticles were measured with a step size of 0.033°; measurements to analyse the water uptake were performed with a step time of 0.039°. A special sample holder with a polycarbonate dome DHS 1100 by Anton Paar was used to prevent exposure of the samples to ambient air. *In-situ* measurements were done in an Anton Paar XRK 900 reactor chamber with the same settings. Measurements were conducted every 50 °C up to a maximum temperature of 400 °C; the heating rate was 3 °C min^{-1} in air. To achieve a uniform temperature distribution within the reactor chamber the sample was equilibrated for 10 min at the desired temperature before beginning the measurement.

Samples prepared *via* solid state reaction or sol-gel synthesis were measured with step sizes of 0.017°, 0.026° or 0.066°. The larger step size was used for only investigating the phase purity and nor for Rietveld refinements.

Phase purity was determined by comparing with reference cards from the Crystallography Open Database (COD) or the Inorganic Crystal Structure Database (ICSD) using the software HighScore Plus (Malvern PANalytical). Theoretical diffraction patterns were calculated using the software Diamond 3.2c (Crystal Impact); based on the information published by Kuznetsova *et al.*[86] for $KTaWO_6$ and by Markin *et al.* for $CsM_xW_{2-x}O_6$[84] or with Vesta 3.4.4 with information published by Corrêa Jr. *et al.*[107] for $ANbTeO_6$.

The lattice constant *a* has been estimated for $KTaWO_6$ and $Sn_xK_{1-2x}TaWO_6$ with the method of McMaille, using HighScore Plus.

Crystallite sizes for $KTaWO_6$ nanoparticles were determined with the method of Stokes and Wilson using the integral breadth of a hkl reflection β_{hkl}.[134] First the Bragg angle θ is converted into radians and then the scattering vector S is calculated using formula 4.1.

$$S = \frac{2 \cdot \sin(\theta)}{\lambda} \tag{4.1}$$

Afterwards the diffraction intensity is plotted against S and β_{hkl} is calculated (formula 4.2) by determination of the reflection height H_{hkl} and the area A_{hkl} of the reflection.

$$\beta_{hkl} = \frac{A_{hkl}}{H_{hkl}} \tag{4.2}$$

The crystallite size L_{hkl} (formula 4.3) is inversely proportional to β_{hkl}. The obtained crystallite size is the volume averaged crystallite thickness perpendicular to the corresponding lattice plane.[134]

$$L_{hkl} = \frac{1}{\beta_{hkl}} \tag{4.3}$$

This method is only applicable for reflections that are well separated and do not overlap with any other reflection. In this work the (111), (004), (113) and (044) reflections have been used and averaged; the standard deviation is indicated as error bars in the respective figures.

Rietveld refinements

In a Rietveld refinement, a diffraction profile is calculated using an initial crystal structure model, which is then fitted to a measured diffraction profile using a non-linear least squares approach.[135] A variety of sample parameters, such as unit cell parameters, atom coordinates, atom occupancies, thermal displacement parameters, crystallite size, microstrain, preferred orientation or phase quantity, can be obtained using this method. However, Rietveld refinement is – as implied by its name – a structure refinement technique and thus requires an initial structure model. The quality of the results is therefore strongly dependent on the validity of the model. It is therefore impossible to elucidate an unknown structure using the Rietveld technique. Here, the information published by Markin *et al.*[84] and Corrêa Jr. *et al.*[107] was used to build initial models for Rietveld refinements for $CsM_xW_{2-x}O_6$ and $ANbTeO_6$, respectively.

The line broadening is not only dependent on the sample microstructure, but also on the resolution of the instrument. It is therefore necessary to measure a standard sample, in which line broadening effects – such as crystallite size or microstructure – are as minimised as possible to obtain a diffraction profile, whose line broadening is solely caused by the instrument. A high-purity $La^{11}B_6$ standard, Standard Reference Material 660c from the National Institute of Standards and Technologies (NIST), was used to obtain the instrumental resolution.

Rietveld Refinements were performed with the program FullProf.[136] The peak shape was fitted with a Thompson-Cox-Hastings Pseudo-Voigt function, which is a linear combination of Gaussian and Lorentzian functions.[137] The background was approximated by a 6-coefficient polynomial. The following sequence was used for Rietveld refinements:

1. Fitting of the background, the scale parameter (absolute intensity) and the zero parameter (instrumental 2θ offset) at the same time until convergence is achieved.

2. Fitting of the lattice constant *a*. The background, zero, scale and *a* have also been refined in every subsequent cycle.
3. Alternating refinement of the Gaussian parameters *U, X*, *W* and the Lorentzian parameters *X* and *Y*, starting with *Y*, until reaching an optimum. *X* and *W* were fixed to zero if the strain was also refined.
4. Contemporaneous refinement of isotropic thermal displacement parameters *B,* describing the thermal motion of atoms resulting in an attenuation of intensity. *B* values have been not refined if unreasonably large or negative values were calculated.
5. Refinement of atom coordinates *x, y, z*, only for values without integer fraction, *i. e. x* coordinate of oxygen.
6. Subsequent refinement of atomic occupancies.
7. Size estimation using an anisotropic Lorentzian size broadening (spherical harmonics) model with *K*00, *K*41, *K*61 and *K*81 parameters for the m3m Laue class.
8. Refinement of the anisotropic strain parameters Str1, Str2 and Str3. The additional strain parameters Str*i* (*i* = 4-8) were fixed to zero.

The quality of the refinement can be estimated by several *R*-factors. The most important of these factors is the weighted profile *R*-factor R_{wp} (refer to formula 4.4), which is minimised if the difference between the calculated intensity $y_{c,i}$ (at given 2θ angle of *i*) and the observed intensity $y_{o,i}$ (at given 2θ angle of *i*) becomes small.[138]

$$R_{wp}^2 = \frac{\sum_i w_i \left(y_{c,i} - y_{o,i}\right)^2}{\sum_i w_i y_{o,i}^2} \tag{4.4}$$

The weight w_i is equal to $1/\sigma[y_{o,i}]$, the standard uncertainty σ describes the measured variation of $y_{o,i}$. The expected *R* factor R_{exp} can be considered the smallest possible R_{wp} value.[138] Another important parameter is the so-called “goodness of fit” χ^2, which becomes unity for a perfect fit (formula 4.5).

$$\chi^2 = \frac{R_{wp}}{R_{exp}} \tag{4.5}$$

Given the problem of a high background potentially resulting in smaller χ^2 or R_{wp} values,[138] only background corrected *R* values are reported in this work.

The average crystallite size L_a and strain η are determined by FullProf by analysing the integral breadth of every reflection. The Gaussian part of the integral breadth is used to calculate strain, while the Lorentzian part is used to calculate the crystallite size.[139] The obtained parameters for crystallite size and strain η are averaged for all crystallographic directions; the standard deviation is plotted as error bars. Additionally, the error for the lattice constant *a* is only the

mathematical error; the “true” error also encompasses the experimental uncertainty and is larger, but difficult to quantify.

The obtained strain parameter η is derived from the line broadening that can be attributed neither to the instrumental resolution nor to size broadening. It stems from structural defects and cannot be traced back to the nature of the defect, *e.g.* dislocations, disorder, vacancies and so forth.[140] The strain calculated by FullProf is ¼ of the strain defined by Stokes and Wilson[141] and corresponds to the upper limit strain.

4.2 X-Ray Photoelectron Spectroscopy

X-ray photoelectron spectroscopy (XPS) measurements were conducted with a Physical Electronics PHI Versaprobe II Scanning ESCA Microprobe with a monochromatic Al K_α source with an X-ray power of 50 W, a beam voltage of 15 kV and a beam diameter of 200 µm. For detailed spectra the pass energy was set to 23.5 eV with a step time of 50 ms and a step size of 0.1 eV. For survey spectra the analyser pass energy was set to 187.85 eV with a step time of 50 ms and a step size of 0.2 eV.

The second used device was a Physical Electronics PHI VersaProbe III Scanning XPS Microprobe, also equipped with a monochromatic Al K_α source. The X-ray power was set to 25 W, a beam voltage of 15 kV and a beam diameter of 100 µm. Survey scans were performed with an analyser pass energy of 224 eV, a step size of 0.2 eV and a step time of 50 ms. Detailed spectra were recorded with a pass energy of 26 eV, a step size of 0.1 eV and a step time of 50 ms. For both devices an electron flood gun and slow-moving argon ions were used to prevent surface charging of the sample. Samples were sputter cleaned with argon ions at low energy to remove surface contaminations.

Data analysis was performed with CASA XPS 2.3.17 (Casa Software Ltd.). A Shirley background and GL(30) line shapes were used for peak fitting, which are a product of Gaussian and Lorentzian forms with a Lorentzian ratio of 30 %. Charge correction was performed by setting the C 1*s* signal to 284.8 eV.

All *p*, *d* and *f* levels – but not *s* levels – will be split into a peak doublet due to spin-orbit splitting. The area ratios for these peaks are identical for each *p*, *d* and *f*-level, respectively. The binding energy difference between both peaks depends on the element.

Chemical state analysis of atoms with unpaired electrons – especially first-row transition elements – is complicated by multiplet splitting. Coupling of the unpaired core electron created by

photoionization with another unpaired electron results in several possible final states, visible as multiple – but usually overlapping – peaks in the photoelectron spectra.

During XPS measurements Auger electrons can be emitted if the excited ion – caused by the incidental photoemission – relaxes and the relaxation energy is transferred to an electron which is subsequently ejected from the ion. The kinetic energy of the ejected electron is dependent on the kind of atom and its chemical state. Auger electrons can be distinguished from photoelectrons, since the kinetic energies of Auger electrons are independent of the initial X-ray photon energy.

The analysis of the chemical state of the sample can be further enhanced by combining photoelectron and Auger electron shifts. Wagner introduced the so-called Auger Parameter α, being the difference of the kinetic energies E_{kin} of the Auger electron and the energy of the photoelectron (formula 4.6).[142]

$$\alpha = E_{kin}(\text{Auger}) - E_{kin}(\text{photoelectron}) \quad (4.6)$$

Gaarenstroom and Winograd later used the sum of the kinetic energy of the Auger signal and the binding energy of the photoelectron signal $E_{binding}$,[143] resulting in the modified Auger parameter α' (formula 4.7). However, the word modified is usually omitted nowadays.[144]

$$\alpha' = \alpha + h\nu = E_{kin}(\text{Auger}) + E_{binding}(\text{photoelectron}) \quad (4.7)$$

The advantage of α' is the independence respective to the independent of the photon energy $h\nu$ and to surface charging. In this work, the Sn $M_4N_{45}N_{45}$ Auger transition and the Sn $3d_{5/2}$ photoelectron signal have been used to calculate the Auger parameter.

4.3 Energy Dispersive X-Ray Spectroscopy

The elemental composition was analysed by energy dispersive X-ray spectroscopy (EDX) using either a Zeiss Merlin field emission scanning electron microscope with an Oxford Instruments X-Max 50 mm² detector and an acceleration voltage of 10 kV or 15 kV or a Zeiss Leo 1530 with an Ultradry-EDX detector from Thermo Fisher Scientific and an acceleration voltage of 15 kV or 20 kV. For all samples several different spots were measured and averaged.

4.4 Diffuse Reflectance UV/vis Spectroscopy

Diffuse reflectance UV/vis spectroscopy was measured on a PerkinElmer Lambda 750 UV/VIS/NIR spectrometer, using a praying mantis mirror unit from Harrick. A spectralon tablet was used as a white standard and a step width of 1 nm was chosen. Diffuse reflectance spectra were converted into absorption spectra using the Kubelka-Munk function; Tauc-plots were used for bandgap estimation.[145]

4.5 Transient Absorption Spectroscopy

Transient absorption spectroscopy has been used to investigate the lifetime of excited states. The sample is first excited by a laser pulse – called pump – to generate electron-hole pairs; this excitation changes the absorption properties of the sample. For example, the conduction band of $CsTaWO_6$ consists of W 5*d* states. If an electron is raised into the conduction band by photoexcitation, a reduction of W^{6+} to W^{5+} happens. However, W^{5+} compounds are intensely blue coloured, which changes the absorption of the sample during the lifetime of the photo-generated charges. The absorption is then measured with a pulsed lamp called probe. The change in absorbance ΔOD is measured as a function of time at a specific wavelength (formula 4.8); I_0 is the probe intensity, whereas I_T is the intensity of pump and probe.

$$\Delta OD = \log \frac{I_0}{I_T} \tag{4.8}$$

Transient absorption measurements were performed with a LP980 spectrometer from Edinburgh Instruments. An EKSPLA NT340 laser was used to excite the samples; a xenon flash lamp was used as probe lamp. The laser wavelength was 266 nm wavelength for $CsM_xW_{2-x}O_6$ samples with bandgaps above 3 eV and 355 nm or 420 nm for samples with bandgaps below 3 eV. The finely powdered sample was measured in air atmosphere in diffuse reflection geometry. Measured signals were recorded with a Tektronix MDO3022 oscilloscope. The obtained curves are fitted with a one-phase (formula 4.9) exponential decay function:

$$\Delta OD = \Delta OD_{initial,\,1} \cdot e^{-t/\tau_1} + \Delta OD_{offset} \tag{4.9}$$

$\Delta OD_{initial}$ is the starting value at time $t = 0$, τ is the time constant and ΔOD_{offset} is an offset from the baseline and is usually close to zero.

4.6 Raman Spectroscopy

Raman-spectra were recorded with two different devices. One device was a Bruker Senterra, equipped with a 532 nm laser. The laser power was set to 2 mW, the resolution was set to 3-5 cm^{-1}. The second used device is a LabRAM 010 from Horiba Jobin Yvon with a 632 nm laser. The laser power was 11.5 mW.

All Raman spectra have been normalised; for $KTaWO_6$ nanoparticles the background was subtracted using the software OPUS 6.5 (Bruker Optik) if necessary.

4.7 Infrared Spectroscopy

Diffuse reflectance infrared Fourier transform (DRIFT) spectroscopy has been measured on a Bruker Alpha with a DRIFT module. A gold standard was used to measure background spectra; the resolution was set to 2 cm^{-1}. To investigate the water uptake of $KTaWO_6$ the device was purged with nitrogen beforehand. All spectra have been normalised; the background was removed using OPUS 6.5 (Bruker Optik) if necessary.

4.8 Scanning Electron Microscopy

Scanning electron microscopy (SEM) images were recorded with either a Zeiss Merlin field emission scanning electron microscope or a Zeiss Leo 1530. The acceleration voltage was set to 3 kV. Samples were coated with platinum using either an Edwards Scancoat Six or a Cressington sputter coater 208HR instrument prior to measuring. Samples were placed on a metal sample holder with double-sided carbon tape on top.

4.9 Transmission Electron Microscopy

Transmission electron microscopy (TEM) images were taken using a Philips CM30 with an acceleration voltage of 300 kV. Samples were dispersed in absolute ethanol and placed on a copper mesh grid with a carbon film.

4.10 Physisorption

The specific surface areas A_{BET} have been determined with the Brunauer-Emmett-Teller-model (BET) using the software ASiQwin (Quantachrome Instruments). For $KTaWO_6$ nanoparticles nitrogen was used as an adsorbate; measurements were done with a Quantachrome Quadrasorb evo gas adsorption station at 77 K. Samples were degassed at 150 °C for 6 h in vacuum prior to measuring.

Samples that have been synthesised with solid state or sol-gel methods usually exhibit only small surface areas due to the high calcination temperatures necessary. These samples have been measured with krypton as adsorbate, since krypton has a higher sensitivity for low surface areas compared to argon or nitrogen. The reason for this is the lower saturation pressure, resulting in fewer free molecules in the sample cell.[146] Krypton Physisorption measurements have been performed with a Quantachrome Autosorb iQ2 or an Anton Paar QuantaTec ASIQ-MP-MP-AG at 77 K. A cross section of 20.5 Å² has been used in data evaluation. $Sn_xK_{1-2x}TaWO_6$ samples have been degassed at 120 °C for approximately 10 hours, while $CsM_xW_{2-x}O_6$ and $ANbTeO_6$ samples have been degassed at 200 °C for 6.7 h.

Water vapour physisorption has also been measured with a Quantachrome Autosorb iQ2 at 293 K. $KTaWO_6$ has been degassed at 300 °C and at 150 °C for $Sn_xK_{1-2x}TaWO_6$. After the measurements, both samples have been evacuated again at 30 °C and measured anew.

4.11 Magnetic Measurements

Magnetic measurements were performed with a Quantum Design superconducting quantum interference device (SQUID) MPMS-XLSSQUID at a constant field strength of 5000 Oe and in a temperature range from 50-300K.

Samples were placed in a gelatine capsule held by a plastic straw. The raw data was corrected for the diamagnetism of the sample holder.

4.12 Dynamic Light Scattering and Zeta-Potentials

Dynamic light scattering (DLS) was measured on a Malvern PANalytical Zetasizer Nano ZS equipped with a 633 nm laser. $KTaWO_6$ nanoparticles were dispersed in water using ultrasonication. Measurements were performed at 25 °C and at an angle of 173°; the resolution was set to 300 size classes in the range of 0.4 nm to 10000 nm. Zeta-potentials were measured with the same device at a pH value of 6-7.

4.13 Thermogravimetric Analysis

Thermogravimetric analysis (TGA) was performed on a Netzsch STA PC/PG instrument from 25 °C to 800 °C with a heating rate of 2 °C min^{-1} in synthetic air. An attached mass spectrometer (MS) was used to detect evolving gases.

4.14 Photocatalytic Measurements

Two different gas analysis devices were used for photocatalytic measurements. A gas chromatograph (GC) was used when the anticipated photocatalytic activity was low, because of higher sensitivity for small hydrogen amounts. For other samples and especially for water splitting a mass spectrometer – with the advantages of online detection and high sensitivity for all gases – was used instead.

Gas evolution rates r have been calculated by transforming the relative concentration c_{rel} [%] into a molar rate with formula 4.10, assuming an ideal gas.

$$r = \frac{c}{100} \cdot \frac{p\,\dot{V}}{R\,T} \tag{4.10}$$

The pressure p in the reactor is 10^5 Pa, the volume flow $\dot{V}$ is 25 or 100 standard cubic centimetres per minute (sccm), R is the gas constant and T is the temperature of the gas flow, which is equal to room temperature. After photocatalysis all samples have been recovered by sedimentation and subsequent centrifugation for post-catalytic analysis.

4.14.1 Photocatalytic Measurements of $Sn_xK_{1-2x}TaWO_6$

For experiments with simulated solar light, 50 mg of every sample have been dispersed in a mixture of 135 mL water and 15 mL methanol with ultrasonication, filled into a homemade glass reactor with a quartz glass window on top and stirred with a magnetic stirrer. A constant temperature of 20 °C was maintained with a Lauda Proline RP845 thermostat. The reactor was purged with an argon 5.0 flow of 100 sccm using a Bronkhorst El-Flow Select mass flow controller. The flow was reduced to 25 sccm for measurements. Photodeposition of co-catalyst was performed by adding an aqueous Na_3RhCl_6 solution to achieve a loading of 0.05 wt%. A Newport Oriel Sol1A solar simulator with a 150 W Xe lamp and an integrated AM1.5G filter was used as a light source (Figure 4.1, left). The evolved gases were detected with a Shimadzu GC2014 gas chromatograph with a thermal conductivity detector (TCD) and a Restek ShinCarbon ST column. Argon was used as carrier and detector gas.

For measurements of $Sn_xK_{1-2x}TaWO_6$ samples in UV light 200 mg sample were dispersed in a mixture of 550 mL water and 50 mL methanol. The reactor is a homemade double-walled inner-irradiation-type reactor with a double-walled quartz glass inlet for its lamp. The reactor was stirred with a magnetic stirrer and cooled to 10 °C with a Lauda Proline RP845 thermostat. An iron doped mercury lamp – Z4 from Peschl Ultraviolet – was used for irradiation; its power was set to 350 W (Figure 4.1, right). Gas analysis and co-catalyst deposition were identical to those described above.

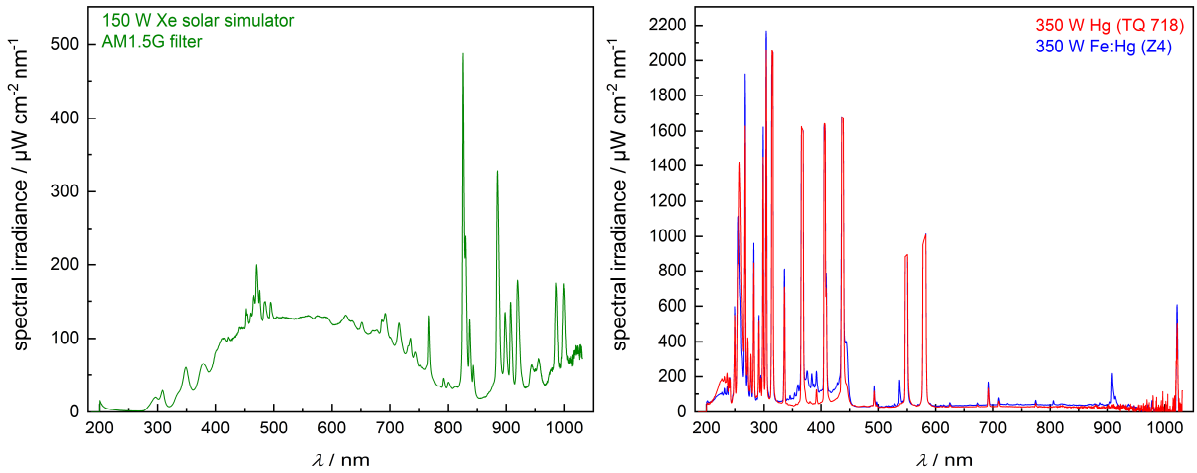

Figure 4.1: Spectra of the used solar simulator (left) and the Hg immersion lamps (right). Lamp spectra have been recorded with a Flame spectrometer from Ocean Optics.

4.14.2 Photocatalytic Measurements of $CsM_xW_{2-x}O_6$

$CsM_xW_{2-x}O_6$ samples with bandgaps above 3 eV were measured with the UV light irradiation setup described above. The used amount was 300 mg for all samples. A TQ718 mercury lamp from Peschl Ultraviolet was used for irradiation (Figure 4.1, right); the lamp power was set to 350 W. Due to the wide range of sample compositions with different molar masses, the co-catalyst amount was normalised to 3 µmol co-catalyst per mmol sample. After 2 h of irradiation the light was switched off and Na_2RhCl_6 was added; after 10 minutes the lamp was switched on again. After 4 h of irradiation the procedure was repeated with K_2CrO_4 instead. The evolved gases were detected with a Hiden Analytical HPR-20 Q/C mass spectrometer with an electron ionisation ion source; electron energy was set to 70 eV and filament current to 200 µA. The time for one measurement was approximately 30 s.

Some select samples – after having been washed and dried – were redispersed in 600 mL pure water for water splitting measurements. The lamp power was set to 500 W instead of 350 W. Due to the anticipated far smaller amounts of evolved gases, the measurement time was increased to approximately 60 s; additionally, the chamber pressure was increased from $1.5 \cdot 10^{-6}$ Torr to around $6 \cdot 10^{-6}$ Torr.

$CsM_xW_{2-x}O_6$ samples with bandgaps below 3 eV were measured with the simulated solar light setup described in section 4.13.1; measurement conditions were identical to those described there with the following exceptions: the sample amount was increased to 200 mg. The Rh amount was 3 µmol co-catalyst per mmol photocatalyst; the Rh precursor was added before the start of the measurement. A Lauda ECO RE 1050G thermostat was used to ensure a constant temperature of 20 °C.

Preparation of IrO_2 Co-catalyst

Since the amount of evolved gases during first water splitting experiments were rather minuscule, it was decided to use IrO_2 as an additional co-catalyst for oxygen evolution. IrO_2 was deposited once as colloidal nanoparticles and once photochemically. The deposited amount in both cases was also 3 µmol IrO_2 per mmol photocatalyst.

Colloidal IrO_2 nanoparticles were synthesised according to procedure of Zhao *et al.*[147] 54 mg K_2IrCl_6 were dissolved in 100 mL water; the pH was adjusted to 13 with NaOH. After stirring for 20 min at 90 °C the solution was cooled in an ice bath and the pH was adjusted to 1 with HNO_3; stirring continued for 90 min. The solution was stored at 4 °C. The photocatalyst sample was dispersed in 5 mL water and the necessary amount of IrO_2 nanoparticle dispersion was

added. After ultrasonication the dispersion was stirred in an oil bath heated to 90 °C until all solvent was evaporated.

Photodeposition of IrO_2 was performed according to Iwase *et al.*[148] The photocatalyst sample was dispersed in 600 mL 0.001 mol L^{-1} aqueous KNO_3 solution and filled into the UV irradiation reactor described in section 4.13.1. Other settings, such as cooling, lamp power and argon flow, are identical to those described in section 4.13.1. After photodeposition the sample was sedimented, washed, dried and used in water splitting experiments.

4.14.3 Photocatalytic Measurements of $ANbTeO_6$

$ANbTeO_6$ samples have been measured in simulated solar light and UV light. Measurements in simulated solar light have been conducted similar to those describes in section 4.13.1 with the following exceptions. A Lauda ECO RE 1050G thermostat was used instead to ensure a constant temperature of 20 °C. The deposited amount of co-catalyst was 3 µmol co-catalyst per mmol sample to ensure a comparable deposition with co-catalyst for the highly different molar masses of the samples.

Measurements in UV light are identical to those described in section 4.13.2. One series of samples was used for hydrogen evolution measurements in water/methanol with 3 µmol/mmol Rh. A second series of samples have first been used in the subsequent photodeposition of 3 µmol/mmol Rh/Cr_2O_3 in water/methanol, afterwards the washed and dried samples were re-dispersed in pure water for water splitting measurements. The lamp power was increased to 500 W for water splitting.

4.15 Mott-Schottky Analysis

If the surface of a semiconductor is in contact with an electrolyte solution, it will result in the equilibration of Fermi levels. This causes the band edges of the semiconductor to bend at the junction, leading to a migration of charge carriers and creating a depletion layer. Changing the Fermi level of the semiconductor artificially varies the magnitude of band bending and thus the width of the charge depletion layer. This changes the capacitance of the junction, which can be measured with impedance spectroscopy. The potential necessary to supress band bending is called flat band potential ϕ_{FB}, which is approximately equal to the CB for an n-type semiconductor. The flat band potential can be estimated using the Mott-Schottky-equation (formula 4.11).[149]

$$C^{-2} = \frac{2}{\epsilon\,\epsilon_0\,A^2\,e\,N_D}\left(\phi - \phi_{FB} - \frac{k_B\,T}{e}\right) \tag{4.11}$$

C represents the capacitance, ε the relative permittivity of the semiconductor, ε_0 the vacuum permittivity, A the area of the semiconductor in contact with the electrolyte, whereas e depicts the elementary charge, N_D the donor density, ϕ the applied potential, k_B the Boltzmann constant and T the absolute temperature.

Electrodes for $Sn_xK_{1-2x}TaWO_6$ samples were prepared by dispersing 30 mg sample in 500 µL absolute ethanol in an ultrasonic bath. The dispersion was drop casted onto a fluorine doped tin oxide (FTO) slide (20x30 mm, XOP Glass) and dried at room temperature. Electrodes for $CsM_xW_{2-x}O_6$ and $ANbTeO_6$ samples were made by spray coating. For this 100 mg of every sample were dispersed in 30 mL ethanol using ultrasonication. The dispersion was sprayed onto the electrode heated up to 250 °C using a commercially obtainable spray pistol at a nozzle to substrate distance of 150 mm, with an air pressure of 3 bar(g).

Afterwards, the electrode was contacted with conductive copper tape and mounted into a PECC-2 photoelectrochemical cell (Zahner Elektrik). A glass junction, filled with 3 mol L^{-1} NaCl solution, was used to protect the Ag/AgCl reference electrode. A 0.1 mol L^{-1} aqueous Na_2SO_4 solution with a pH value of 6.4 ($Sn_xK_{1-2x}TaWO_6$) or 5.2 ($CsM_xW_{2-x}O_6$ and $ANbTeO_6$) was used as electrolyte. A Zennium potentiostat (Zahner Elektrik) was used for all measurements. Mott-Schottky measurements were performed from positive to negative potentials with a step size of 50 mV; the used amplitude was 5 mV. The frequency was 100 Hz for $Sn_xK_{1-2x}TaWO_6$ samples and 1000 Hz for $CsM_xW_{2-x}O_6$ and $ANbTeO_6$ samples. The valid frequency range was determined by electrochemical impedance spectroscopy (EIS) measurements in a range from 10^6 or 10^5 Hz to 1 Hz. The used potential was 0.1 V, the amplitude 20 mV and the frequency 10^3 Hz. The logarithm of the frequency f was plotted against the logarithm of the negative imaginary part of the impedance Z_i. The frequency range at which the slope of the first derivative is approximately –1 can be used for Mott-Schottky measurements.

5 Sn^{2+} Ion Exchange for Visible Light Absorption

Introducing Sn^{2+} ions into a metal oxide can greatly reduce the bandgap of this material (see section 2.2.6). For defect-pyrochlores Sn^{2+} has usually been incorporated by ion exchange against K^+.[19,67] In a first ion exchange experiment $KTaWO_6$ and $CsTaWO_6$ nanoparticles – synthesised at identical conditions – have been stirred with 0.5 eq. $SnSO_4$ in water at room temperature. Following the ion exchange EDX measurements showed Sn/K and Sn/Cs ratios of 6.36 and 0.33, respectively. Assuming that the sum of Sn and K is 1, the corresponding chemical formulas would be $Sn_{0.46}K_{0.07}$ and $Sn_{0.20}Cs_{0.60}$; the degree of ion exchange is 92 % for $KTaWO_6$, but only 40 % for $CsTaWO_6$. The smaller size of K^+ compared to Cs^+ does not seem enough to explain this difference, especially since $KTaWO_6$ nanoparticles are larger compared to $CsTaWO_6$ (see section 5.2). Larger particles imply longer diffusion pathways, resulting in less ion exchange. Some K^+ containing defect-pyrochlores – especially $KNbWO_6$ – have been reported to incorporate water molecules into the hexagonal channels of the crystal structure (see section 2.3.2); whereas water incorporation has not been reported for Cs^+ containing defect-pyrochlores so far. These water molecules could facilitate the diffusion processes required for ion exchange.

5.1 Water Incorporation in $KTaWO_6$

The water incorporation in $KTaWO_6$ and $CsTaWO_6$ nanoparticles has been investigated with XRD measurements of dried and water vapour saturated samples (Figure 5.1). The patterns of $KTaWO_6$ show two distinctive differences: one is a shift in relative intensities of the (113) and (222) reflections, indicating a change of positions of the unit cell constituents upon water exposure. The other change is a shift towards higher diffraction angles, which is tantamount with a smaller lattice constant. Dry $KTaWO_6$ has a lattice constant of 10.418 Å, as compared to 10.482 Å for hydrated $KTaWO_6$. The broad reflection between 15-20° stems from a special sample holder with a polycarbonate dome on top to prevent sample exposure to ambient air. For $CsTaWO_6$ neither a change in relative intensities nor a shift in position is discernible, indicating no change of the crystal structure upon water exposure. The relative intensities – especially of the two main reflections at 30° – are also different for $KTaWO_6$ and $CsTaWO_6$, indicating that the atoms constituting the unit cell are located on different positions. Since the octahedral framework is rigid, it is likely that the alkaline metal cations are located on different crystallographic positions within the hexagonal channels. The reported positions for these cations are highly disputed in the literature (see section 2.3.1). The larger size of the Cs^+ with

1.67 Å than compared to K^+ with 1.38 Å (both values are for sixfold coordination) is the likely reason for water incorporation not happening for $CsTaWO_6$.[150]

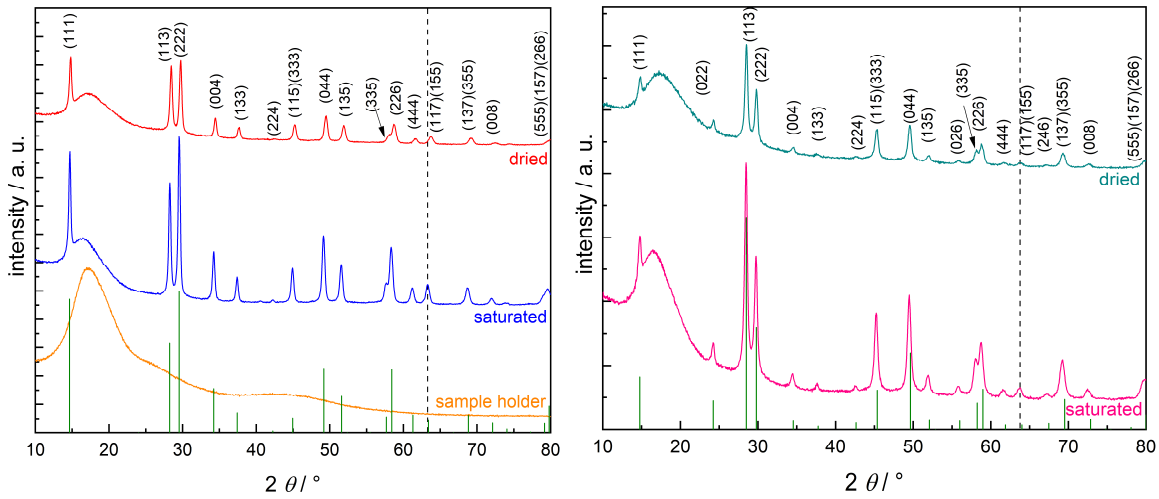

Figure 5.1: XRD patterns of dried and water vapour saturated $KTaWO_6$ (left) and $CsTaWO_6$ (right). Also displayed is a XRD pattern of the empty sample holder.

The changes in the crystal structure of $KTaWO_6$ have been investigated with temperature ϑ dependent *in-situ* XRD (Figure 5.2, left). During heating a gradual shift to higher diffraction angles is visible; the lattice constant *a* accordingly shows a sharp decrease until 150 °C and a second, less steep decrease between 300 °C and 350 °C (Figure 5.2, right). This two-step decrease could indicate a two-step dehydration process.

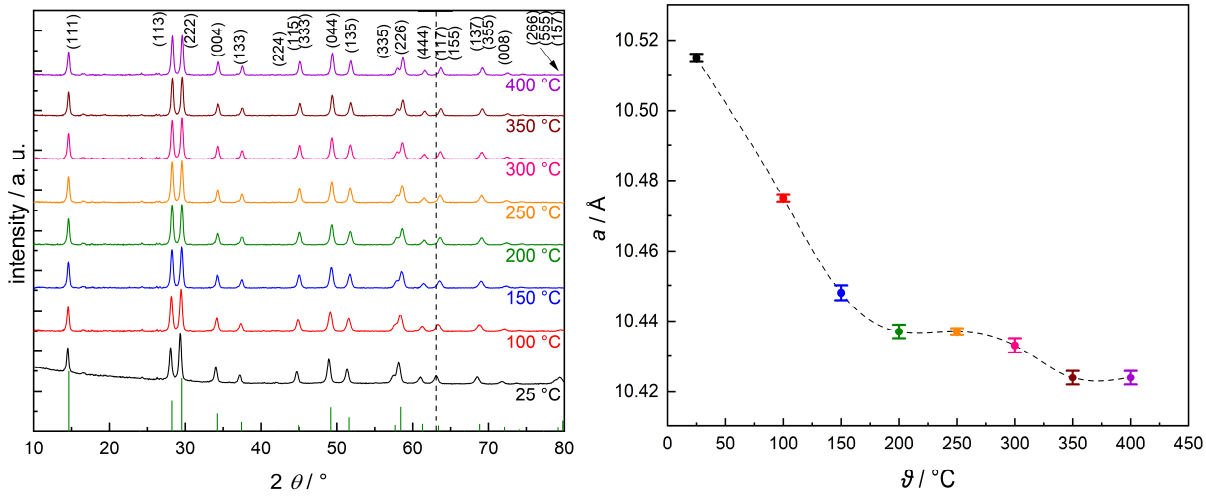

Figure 5.2: *In-situ* XRD patterns (left) of $KTaWO_6$ and corresponding lattice constants (right).

The (113) reflection increases, while the (222) reflection decreases during heating (Figure 5.3, left); these changes seem to be completed at 150-200 °C, which is in accordance with the

sharp decrease of the lattice constant described above. The relative diffraction intensities calculated for the three possible different K^+ Wyckoff positions also reveal a distinct intensity change for these two reflexes (Figure 5.3, right). By comparing with the experimental intensity change, it is possible to recognise a change in position from 16d or 32e to 8b during heating. Although the 32e position has two extra reflections compared to 16d, their intensities are too minuscule to distinguish between the 16d and 32e position. Rietveld refinements have been attempted but were not of sufficiently good quality to be used for analysis (Figure 10.1, appendix). These results are in accordance with neutron diffraction experiments, in which K^+ has been found to occupy a 32e position in hydrated $KNbWO_6$; the position of K^+ in anhydrous $KNbWO_6$ has also been found at an 32e position that is near the 8b position.[83,87]

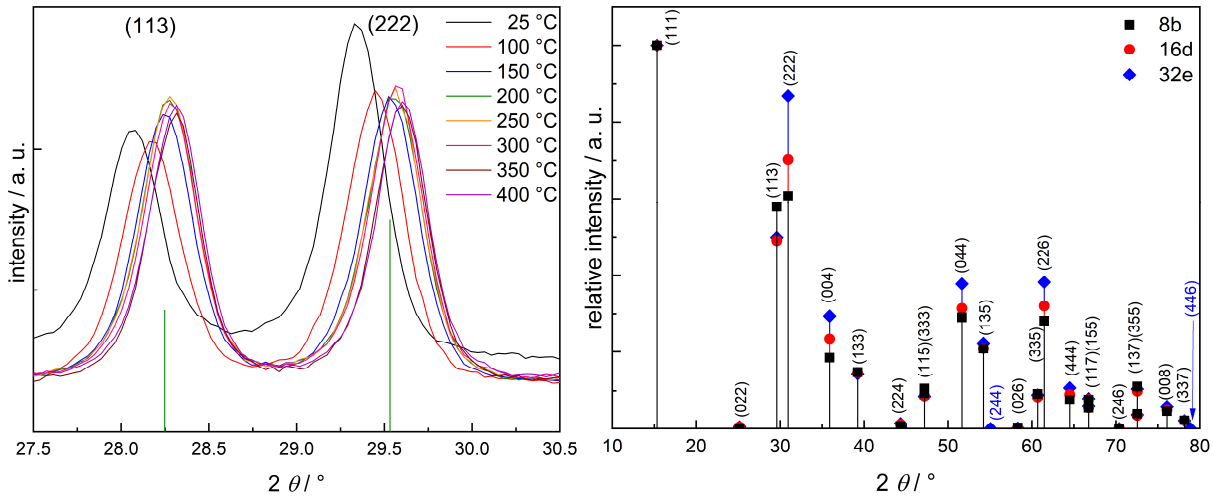

Figure 5.3: Magnification of the two main reflections (left) and calculated relative intensities (right).

The dynamics of water removal have been studied by TGA-MS; water loss occurs in two stages at 110 °C and 320 °C (Figure 5.4, left). These temperatures correspond well with the stepwise decrease of the lattice constant seen in *in-situ* XRD. The temperatures from TGA cannot be directly compared to those of *in-situ* XRD, since the temperature increase in TGA is continuous in contrast to the long equilibration and measuring times of *in-situ* XRD. The first water loss at 110 °C cannot belong purely to adsorbed surface water, but rather to a mixture of surface and crystal water: first, the dehydration of $KNbWO_6$ occurs between 100 °C and 150 °C; the dehydration of $KTaWO_6$ should therefore be in a similar temperature range.[87] Secondly, *in-situ* XRD showed a lattice constant decrease in the same temperature region and the loss of purely surface adsorbed water would not affect the crystal structure. The total amount of water lost corresponds to $KTaWO_6 \cdot 1.4\ H_2O$, which is similar to that reported for $KNbWO_6 \cdot 1.17\ H_2O$, but higher as the previously reported $KTaWO_6 \cdot 1\ H_2O$.[7,87] However, the nanoparticles shown here have a larger surface area and thus a larger amount of adsorbed surface water than particles synthesised by solid state reaction.

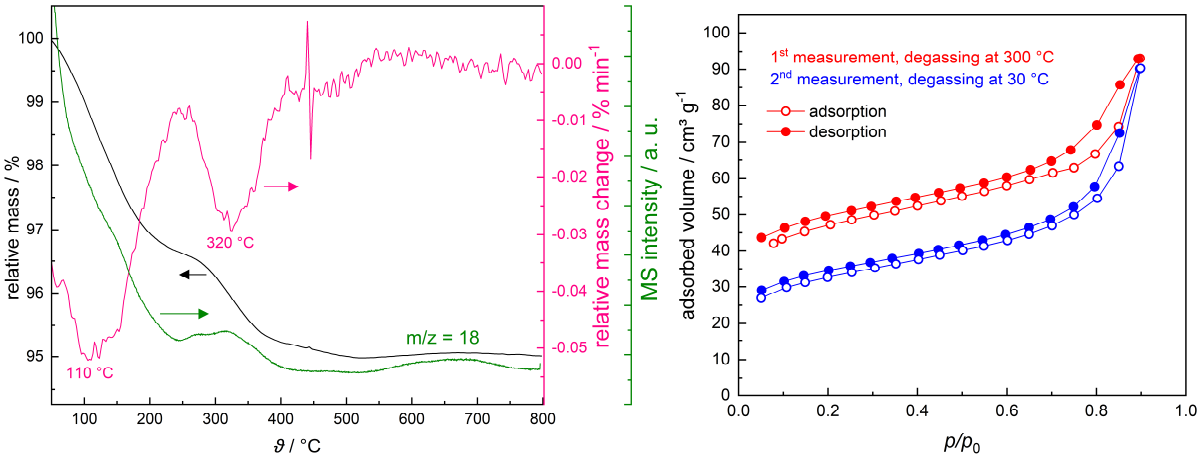

Figure 5.4: TGA-MS (left) and water vapour physisorption isotherms (right) of $KTaWO_6$.

An experimental differentiation between surface and crystal water could be observed with water vapour physisorption (Figure 5.4, right). The sample was first degassed at 300 °C to remove all water present in the sample (red curve); after the measurement was finished, the sample was again degassed at 30 °C to remove only surface adsorbed water (blue curve). During the first measurement the channels are filled with water, but not emptied by the subsequent degassing due to the temperature being too low. At the beginning of the second measurement the channels are already filled, which is the reason for the isotherm starting at lower values.

An attempt to study the timescale of water incorporation was done by DRIFT spectroscopy (Figure 5.5). $KTaWO_6$ shows several bands associated with water molecules; these are the bending mode at 1630 cm^{-1}, a combination of bending and vibration modes at 2150 cm^{-1} and 2050 cm^{-1}, a stretching mode at 3470 cm^{-1}, and a combination of bending and stretching modes at 5200 cm^{-1}.[151,152] All these bands are increasing with time, indicating a water uptake from ambient air. The sample seems to be saturated already after 30 min indicated by no further increase in the bands over time. The broad band at 3200 cm^{-1} can be assigned to surface hydroxyl groups and does not change over time. The bands at 1420 cm^{-1} belonging to residues of the nitrate precursor and the broad bands between 800-1100 cm^{-1} belonging to metal-oxygen bonds also remain constant with time.[22] The carbon dioxide bands at around 2350 cm^{-1} increase gradually, since the device was first purged with nitrogen and afterwards opened to ambient air to expose the sample to humidity.

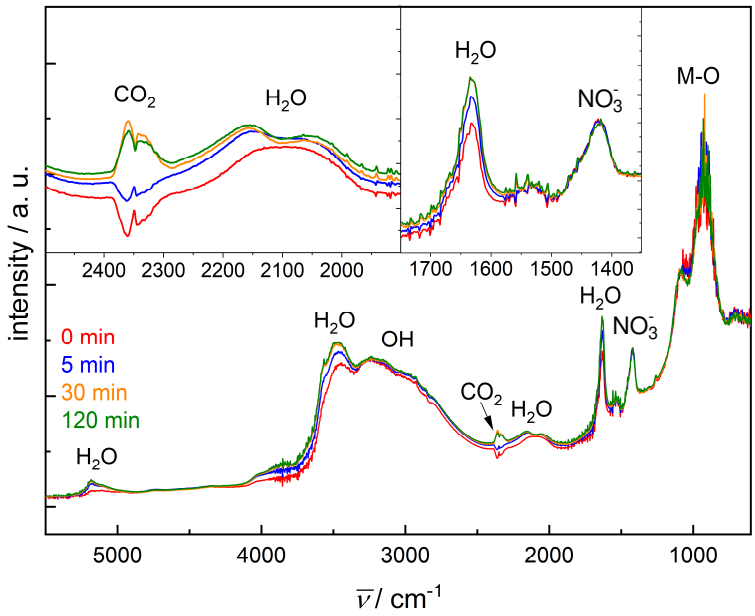

Figure 5.5: DRIFT spectra of initially dried $KTaWO_6$; the times in the legend specify the length of period the samples spent in ambient air prior to the beginning of the measurement.

To summarise, water molecules are able to enter the hexagonal channels of the defect-pyrochlore crystal structure of $KTaWO_6$, but not those of $CsTaWO_6$. Dehydration upon heating occurs in a two-step process, is fully completed at 350 °C and happens simultaneous with a contraction of the unit cell and a change in position of K^+ from 32e to an apparent 8b position. These water molecules are most likely the reason for ion exchange with Sn^{2+} performing better in $KTaWO_6$ than in $CsTaWO_6$. Subsequent experiments therefore focused on $KTaWO_6$ as base material for ion exchange.

5.2 Hydrothermal Synthesis of $KTaWO_6$ nanoparticles

Highly crystalline $CsTaWO_6$ nanoparticles can be prepared at low temperatures by hydrothermal treatment; the crystallite size can be adjusted by varying the amount of ammonia solution being added.[22] Since $KTaWO_6$ is better suited for ion exchange, it was attempted to use the same synthesis as for $CsTaWO_6$. Although, the synthesis results in phase pure and highly crystalline nanoparticles (Figure 5.6, left); the ammonia concentration has no discernible influence on the crystallite size (Figure 5.6, right). The mean crystallite size is around 19 ± 1 nm, only for very small amounts – that is 0.5 mL – of ammonia the size is minimal increased to 23 ± 2 nm. This is in contrast to $CsTaWO_6$ for which the crystallite sizes vary between 8 nm and 16 nm for similar ammonia concentrations.[22] Ammonia and water molecules are able to enter the hexagonal channels of $KTaWO_6$ but not those of $CsTaWO_6$; this could be a possible

reason for the size indifference of $KTaWO_6$. BET surface areas are between 26-37 $m^2\ g^{-1}$ (Figure 5.6, right). These values are smaller than the theoretically possible surface areas shown in section 2.4 (Figure 2.17), indicating that the samples consist of agglomerated particles.

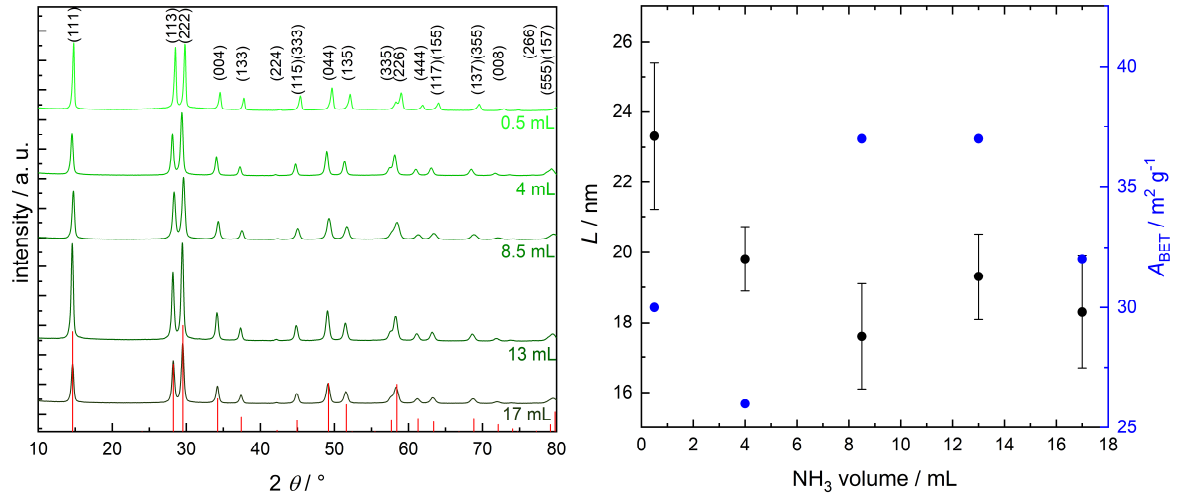

Figure 5.6: XRD patterns (left) and crystallite sizes and BET surface areas (right) of $KTaWO_6$ for different ammonia amounts; synthesis time and temperature were 12 h and 150 °C for all samples.

Raman spectroscopy also did not show any significant differences between these samples (Figure 5.7, left); labelling of these bands has been done according to Maczka *et al.*[153].The bandgaps of all five samples are virtually identical with values of 3.6 eV or 3.7 eV (Figure 5.7, right).

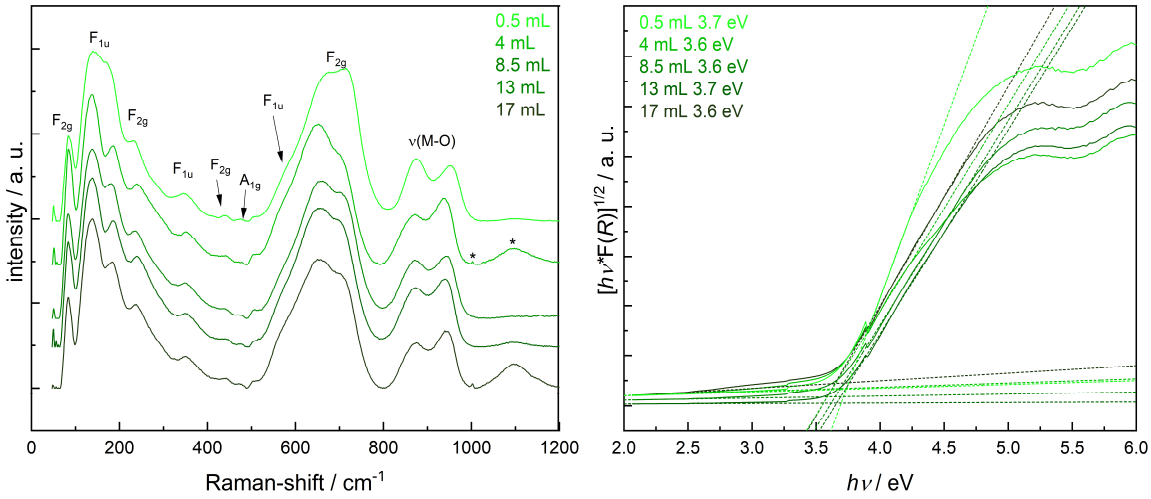

Figure 5.7: Raman spectra (left) and Tauc plots (right) of $KTaWO_6$ nanoparticles synthesised with different ammonia amounts; synthesis time and temperature were 12 h and 150 °C, respectively. Raman bands marked with an asterisk originate from the glass plate supporting the sample.

The addition of ammonia is necessary for the formation of $KTaWO_6$, if pure water is used in the synthesis only an amorphous product can be obtained (Figure 5.8). The addition of another amine-base such as ethylene diamine also results in an amorphous product. Hydrazine and hydroxyl amine may be more similar to ammonia – or rather less different to ammonia – than ethylene diamine; however, they have not been used due to their reactivity. Another base such as potassium hydroxide also results in the formation of phase pure $KTaWO_6$; the crystallite size is 23 ± 2 nm and the BET area 21 $m^2\ g^{-1}$, both values are similar to those obtained in the synthesis with ammonia. The addition of a base is therefore necessary for the synthesis of $KTaWO_6$. While potassium nitrate and ammonium tungstate are soluble in water, tantalum ethoxide rapidly hydrolyses and precipitates. Since potassium hydroxide is able to dissolve tantalum(V) oxide at elevated temperatures, it can be concluded that the addition of a base is necessary to dissolve the formed precipitate.[154]

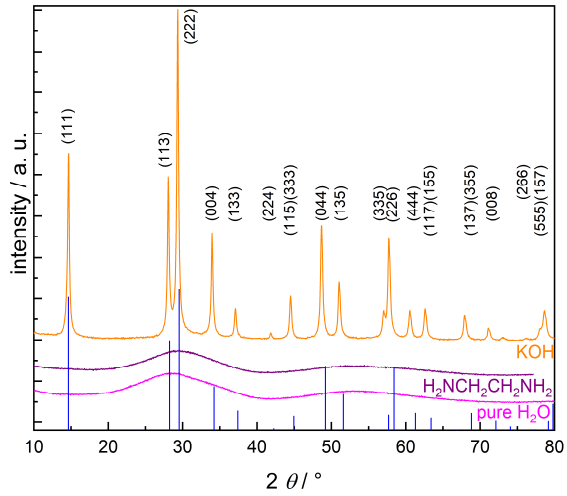

Figure 5.8: XRD patterns of $KTaWO_6$ with different additions instead of ammonia.

The synthesis temperature was lowered in an attempt to obtain smaller nanoparticles. The formation of $KTaWO_6$ is already possible at 105 °C; however, the increased background between 20-40° indicates the presence of an amorphous phase (Figure 5.9, left). At 120 °C the sample is fully crystalline; however, the crystallite size has increased from 15 ± 1 to 19 ± 1 nm (Figure 5.9, right). Increasing the temperature further does not change the crystallite size, but instead lowers the BET surface area. The likely reason is the growth of smaller particles due to Oswald ripening therefore decreasing the surface area, while the crystallite size remains constant within the experimental error. The surface areas for the 105 °C and the 120 °C sample are identical, while the crystallite sizes are not. The 105 °C sample is partly amorphous; the amorphous parts contribute to the surface area but not to the crystallite size.

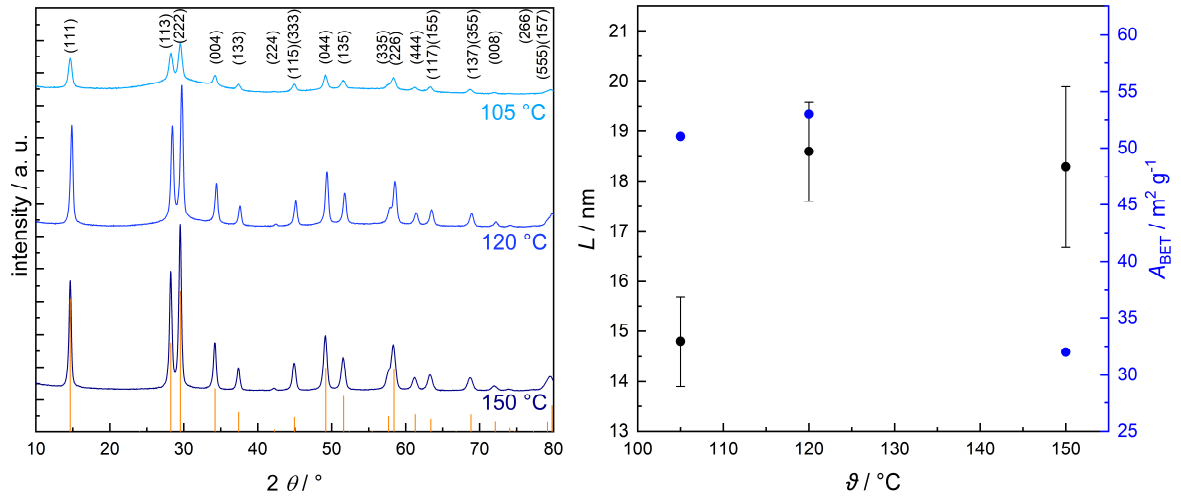

Figure 5.9: XRD patterns (left) and crystallite sizes and BET surface areas (right) of $KTaWO_6$ synthesised at different temperatures; time and ammonia amount were 12 h and 17 mL, respectively.

The Raman bands of the sample prepared at 150 °C are in some cases poorly defined due to the partially low crystallinity of the sample (Figure 5.10, left). For the samples prepared at 120 °C and 150 °C all Raman bands belong to modes of the defect-pyrochlore structure;

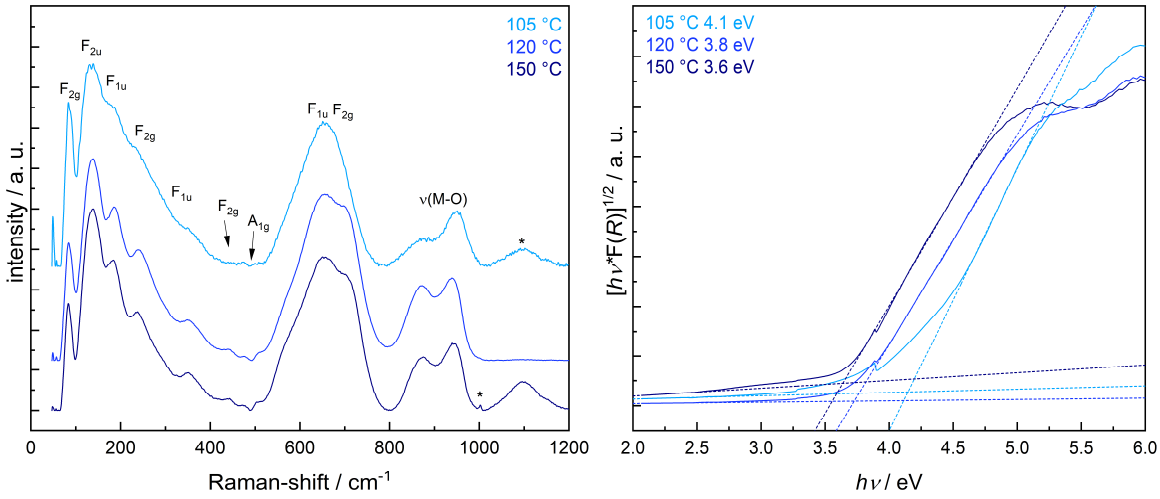

Figure 5.10: Raman spectra (left) and Tauc plots (right) of $KTaWO_6$ nanoparticles synthesised at different temperatures; time and ammonia amount were 12 h and 17 mL, respectively. Raman bands marked with an asterisk originate from the glass plate supporting the sample.

The optical bandgaps are decreasing with higher synthesis temperature (Figure 5.10, right). The sample prepared at 105 °C has a large bandgap of 4.1 eV and also the smallest crystallite size. Larger than normal bandgaps for small nanoparticles are oftentimes ascribed to the quantum size effect.[155] However, $CsTaWO_6$ nanoparticles which have shown a quantum size effect have been far smaller.[22] The larger bandgap of the sample prepared at 105 °C is likely a result

of the poor crystallinity and not due to the quantum size effect. The bandgaps of the other two sample match those reported in the literature for tungsten based defect-pyrochlores.[16,112]

The influence of synthesis time on crystallite sizes was also investigated. After 6 h $KTaWO_6$ has already been formed, but the sample is still partly amorphous (Figure 5.11, left); after 9 h no amorphous background is visible anymore. The crystallite size increases from 15 ± 1 nm at 6 h to 20 ± 1 nm at 18 h (Figure 5.11, right). The surface area of the partly amorphous sample is again smaller than expected for the small crystallite size. For all fully crystalline samples the surface area is slightly decreasing with increasing crystallite size.

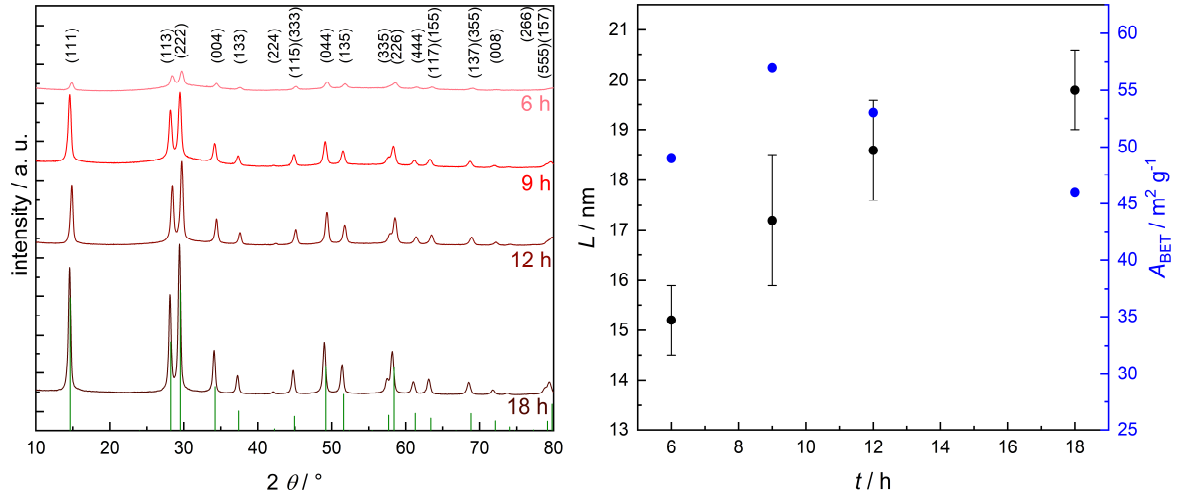

Figure 5.11: XRD patterns (left) and crystallite sizes and BET surface areas (right) of $KTaWO_6$ synthesised for different times; temperature and ammonia amount were 120 °C and 17 mL.

The phase purity of these samples is supported by Raman spectroscopy (Figure 5.12, left); all visible Raman bands can be assigned to the defect-pyrochlore structure.[86] The bandgaps of those samples synthesised at 6 h and 9 h are enlarged (Figure 5.12, right). This is likely due to the poorer crystallinity as compared to samples with longer synthesis times.

TEM images show mostly cubically-shaped particles for highly crystalline samples, whereas particles for a sample with amorphous parts are more irregularly shaped (Figure 5.13). Particles in this sample (upper right) also seem to be more agglomerated than in the other samples. The particles also seem to be single-crystalline in nature. For some samples lattice planes are visible and could be indexed to the (111) plane.

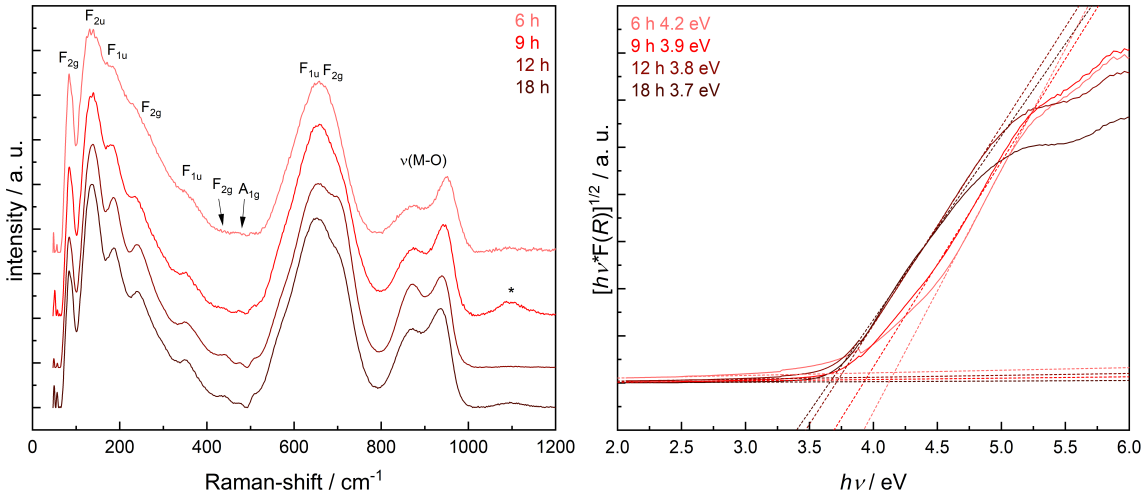

Figure 5.12: Raman spectra (left) and Tauc plots (right) of $KTaWO_6$ synthesised for different times; temperature and ammonia amount were 120 °C and 17 mL, respectively. Raman bands marked with an asterisk originate from the glass plate supporting the sample.

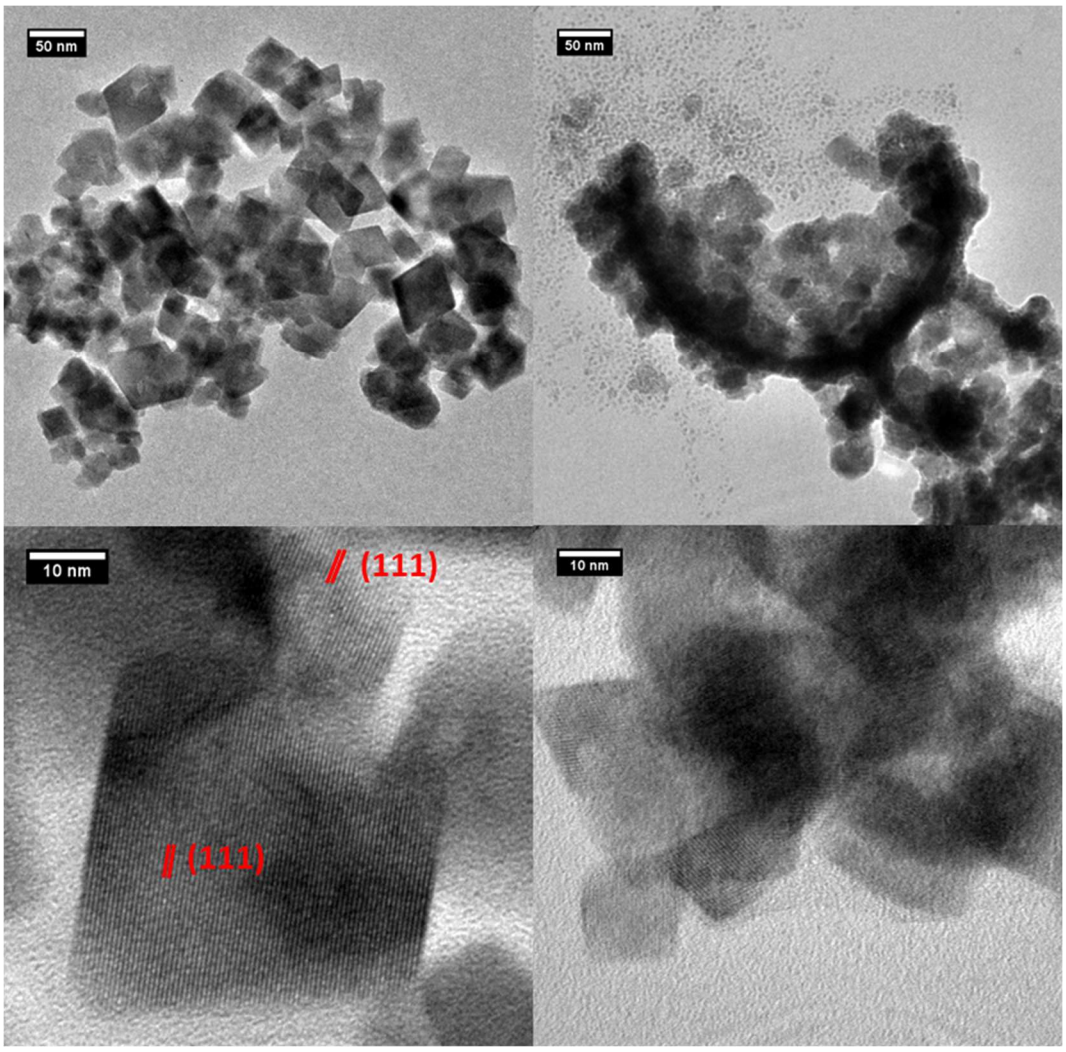

Figure 5.13: TEM images of $KTaWO_6$ nanoparticles synthesised at 150 °C and 12 h (upper left), 120 °C and 6 h (upper right), 120 °C and 12 h (lower left) and 120 °C and 18 h (lower right).

Photocatalysis requires the dispersion of the sample in a liquid medium, typically water. Dynamic light scattering (DLS) was used to investigate the particle size distribution of the samples dispersed in water (Figure 5.14). The measured particle sizes are far larger than the crystallite sizes and the particle sizes observed in TEM images, indicating the formation of agglomerates. Data analysis in DLS is based on the Einstein-Stokes equation – which is valid only for spherical particles – resulting in erroneous particle sizes for cubically shaped particles. Increasing the synthesis temperature decreases the mean particle size from 150 nm to 50 nm and also resulting in a rather narrow size distribution. Increasing the synthesis time also results in a slight decrease from 150 nm to 100 nm. Some samples also show a small amount of larger agglomerates between 250 nm and 500 nm. An increasing ammonia amount also results in smaller particles; however, the mean diameter for samples with an intermediate amount – that is 4-13 mL – is comparable (Figure 10.2, left, appendix).

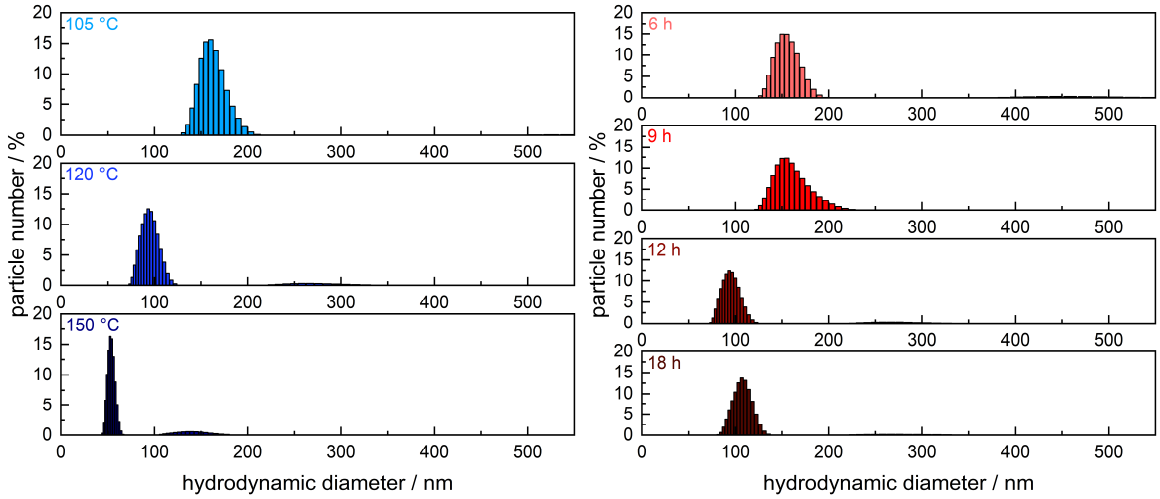

Figure 5.14: Particle size distributions measured by DLS for $KTaWO_6$ nanoparticles synthesised at different temperatures (left) and times (right).

The Zeta potential was measured to estimate the stability of the dispersion. The Zeta potential ranges between –30 mV and –45 mV – with one exception –, these values indicate a quite stable dispersion (Figure 5.15).

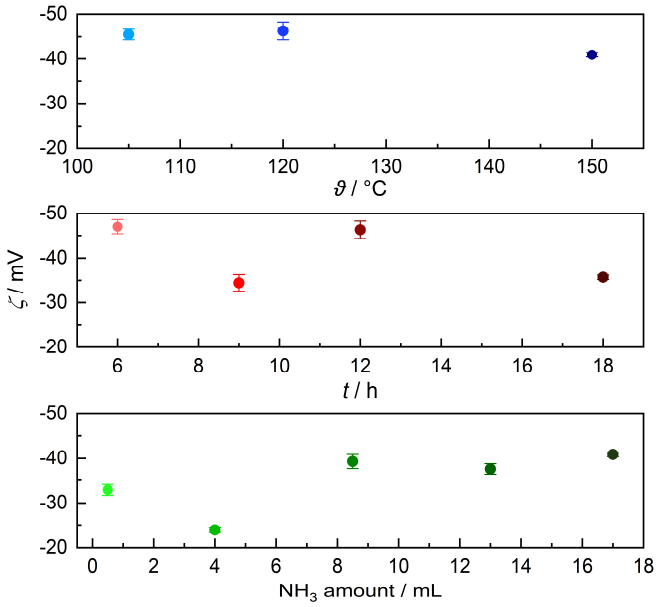

Figure 5.15: Measured Zeta potentials of all samples.

To summarise, phase-pure and single crystalline $KTaWO_6$ nanoparticles can be synthesised by hydrothermal treatment. The addition of ammonia (or another base) is necessary for the formation of $KTaWO_6$. The crystallite size can be slightly adjusted in the range from 15-20 nm by varying temperature and time of the hydrothermal treatment. However, if the temperature is too low or the time too short the obtained nanoparticles are still partly amorphous.

5.3 Sn^{2+} Ion Exchange in $KTaWO_6$

$KTaWO_6$ nanoparticles have been ion exchanged with 0.5 eq. $SnSO_4$ in water for 24 h at room temperature. The nominal reaction equation for complete ion exchange is written below (formula 5.1), however, no complete ion exchange could be achieved.

$$KTaWO_6 + \frac{1}{2}Sn^{2+}_{(aq)} \rightleftharpoons Sn_{0.5}TaWO_6 + K^{+}_{(aq)} \qquad (5.1)$$

For reasons of clarity and comprehensibility, only the results for one sample – synthesised for 12 h at 150 °C in 17 mL ammonia – are shown. The elemental composition following the ion exchange has been determined by EDX and is $Sn_{0.46}K_{0.07}TaWO_6$; chemical formulas are calculated with the assumption that the sum of Sn and K is one. Normalising the EDX results with respect to Ta = 1 instead would result in $Sn_{0.52}K_{0.08}Ta_1W_{0.48}O_{8.38}$. The values for Sn and K are similar for both calculations. The huge mismatch between Ta and W probably stems from the poor resolution of EDX spectroscopy and the strong overlap of the X-ray lines of Ta and W.[156]

Estimation of the Sn content by back-titrating the non-exchanged Sn^{2+} ions in solution results in $Sn_{0.47}K_xTaWO_6$. Due to the nonsensical values for Ta and W and the good agreement with the results from back-titration, the chemical formulas are calculated with the assumption that the sum of Sn and K is one.

The XRD pattern shows no impurities after ion exchange (Figure 5.16, left); however, the difference in relative intensities of the (113) and (222) reflections is increasing. This concurs with theoretical calculations that show an increase of the (222) reflection for $Sn_{0.5}TaWO_6$, which is an idealised model compound for complete ion exchange (Figure 5.16, right). The lattice constant of $Sn_{0.46}K_{0.07}TaWO_6$ is 10.454 Å, which is 0.03 Å smaller as compared to $KTaWO_6$. The reason being the smaller size of Sn^{2+} with a ionic radius of 1.22 Å as compared to K^+ with 1.51 Å (both values are for eightfold coordination, since a value for Sn^{2+} with sixfold coordination could not be found).[157]

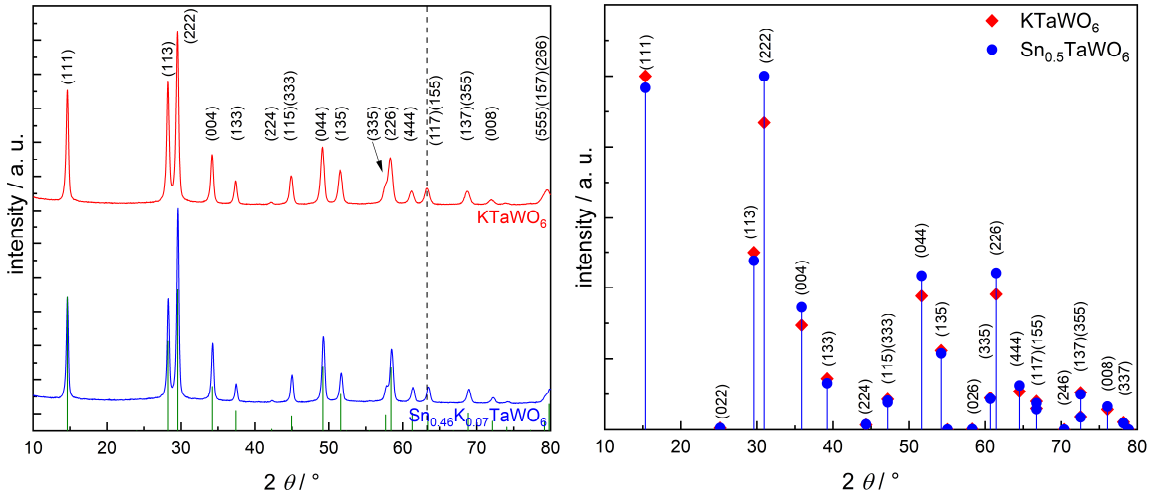

Figure 5.16: XRD pattern of $KTaWO_6$ and $Sn_{0.46}K_{0.07}TaWO_6$ (left) and calculated diffraction patterns for $KTaWO_6$ and $Sn_{0.5}TaWO_6$ (right).

The bandgap of $Sn_{0.46}K_{0.07}TaWO_6$ is 2.3 eV, which is a reduction of 1.3 eV compared to $KTaWO_6$ (Figure 5.17, left). The reason for this diminishment is the introduction of Sn 5*s* states; these are located at a less positive potential than the O 2*p* states forming the valence band in $KTaWO_6$ (Figure 5.17, right). The VB of $Sn_xK_{1-2x}TaWO_6$ consists of these Sn 5*s* states and is therefore located at less positive potentials than the VB of $KTaWO_6$; thus the lower bandgap for $Sn_xK_{1-2x}TaWO_6$.

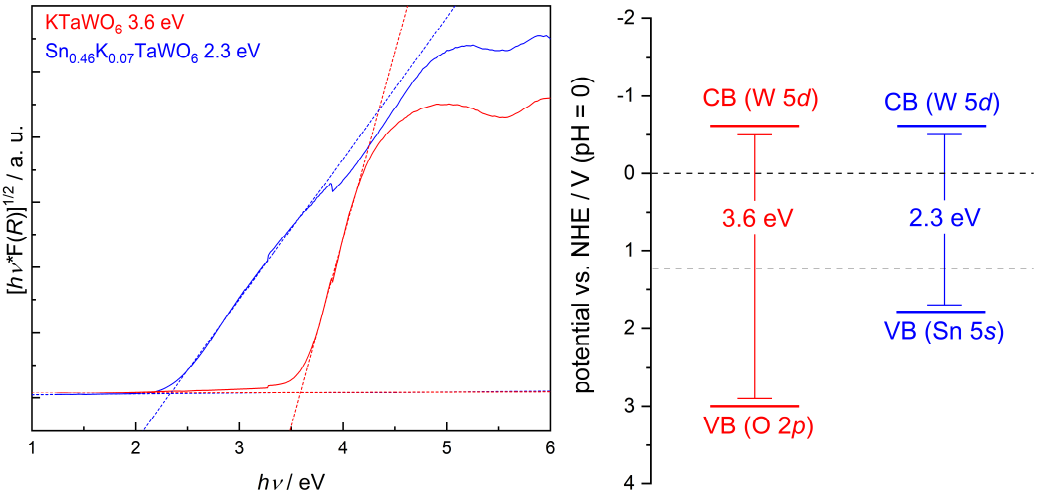

Figure 5.17: Tauc plots (left) and band scheme (right) of $KTaWO_6$ and $Sn_{0.46}K_{0.07}TaWO_6$.

Raman spectra show several differences after ion exchange (Figure 5.18); a F_{2g} and the A_{1g} mode (400-500 cm^{-1}) increase in intensity, whereas a F_{1u} and another F_{2g} mode (650-750 cm^{-1}) decrease. All four modes are attributed to stretching of the TaO_6/WO_6 octahedra.[92] Two K^+ are exchanged against one Sn^{2+}, which bisects the number of ions present in the hexagonal channels. Also Sn^{2+} does not necessarily occupy the same crystallographic position as K^+. This in turn changes the possibilities of the octahedra to stretch or to bend, thus changing the intensity of the Raman bands.

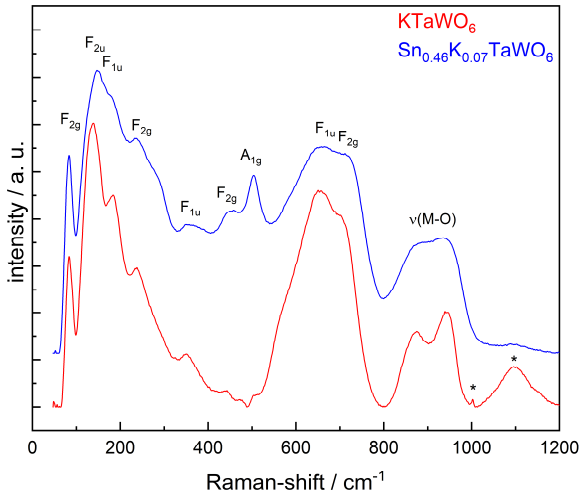

Figure 5.18: Raman spectra of $KTaWO_6$ and $Sn_{0.46}K_{0.07}TaWO_6$. Raman bands marked with an asterisk originate from the glass plate supporting the sample.

Attempts to directly synthesise $Sn_{0.5}TaWO_6$ by solid-state reaction in inert gas atmosphere were unsuccessful; a mixture of SnO_2, SnW_3O_9 and Ta_2O_5 was obtained instead (Figure 10.3, left, appendix). The presence of SnO_2 indicates a redox reaction between Sn^{2+} and W^{6+}. The

attempt to directly synthesise $Sn_{0.5}TaWO_6$ *via* hydrothermal treatment resulted in a mixture of SnO_2 and $TaWO_{5.5}$ (Figure 10.3, right, appendix), which also crystallises in the defect-pyrochlore crystal structure.[94] $Sn_{0.5}TaWO_6$ and $TaWO_{5.5}$ can be easily distinguished from each other due to their different lattice parameters and the different relative intensities of the (113) and (222) reflections at 29-30°.

The calculated band structure expectedly changes during ion exchange (Figure 5.19); the calculated bandgap decreases from 4.2 eV to 3.7 eV for complete ion exchange, which is 0.8 eV less than the experimental decrease. Moreover, the nature of the semiconductor itself changes during ion exchange. $KTaWO_6$ has an indirect transition from K_{VB} to Γ_{CB} (see arrow in Figure 5.19, upper left); $Sn_{0.5}TaWO_6$ in contrast is a direct semiconductor with a transition from K_{VB} to K_{CB} (see arrow in Figure 5.19, lower left). The projected density of states for $Sn_{0.5}TaWO_6$ (DOS) affirms the forming of the VB maximum by hybridisation of Sn and O states (Figure 5.19, right). The CB minimum on the other hand is composed of W states.

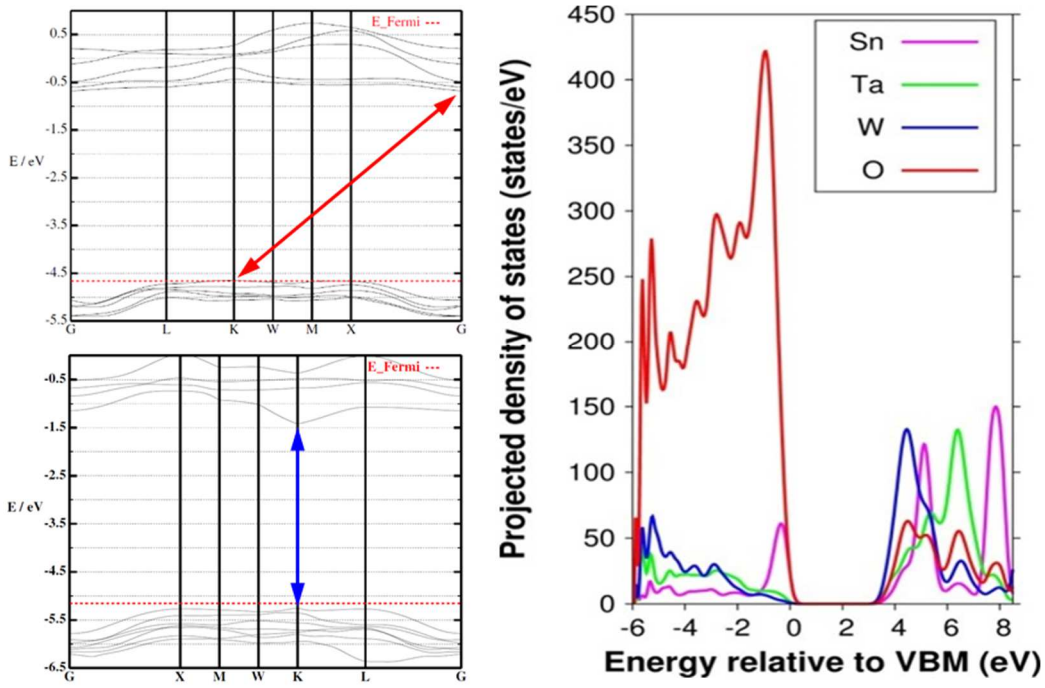

Figure 5.19: Band diagrams of $KTaWO_6$ (upper left) and $Sn_{0.5}TaWO_6$ (lower left) and projected density of states of $Sn_{0.5}TaWO_6$ (right); the arrows indicate the transition from valence to conduction band.

To summarise, ion exchange from K^+ to Sn^{2+} results in a bandgap diminishment of around 1.3 eV, since the newly introduced Sn 5*s* states are located at a less positive potential than the original valence band. The direct synthesis of $Sn_{0.5}TaWO_6$ is not possible, however, a

method to synthesise $TaWO_{5.5}$ at low temperatures *via* hydrothermal treatment was coincidentally found. During ion exchange a transition from indirect to direct semiconductor occurs. No impurities could be observed in the XRD pattern or in the Raman-spectrum.

5.4 Water Incorporation in $Sn_xK_{1-2x}TaWO_6$

The ion exchange from K^+ to Sn^{2+} is greatly facilitated by the incorporation of water molecules into the hexagonal channels of the crystal structure (see section 5.1).

Several experiments were conducted to investigate if the Sn^{2+} exchanged $Sn_xK_{1-2x}TaWO_6$ materials are also able to incorporate water molecules and to ascertain possible changes in the material properties. Water vapour saturated $Sn_{0.35}K_{0.30}TaWO_6$ shows a slight shift to smaller diffraction angles (Figure 5.20, left). The lattice constant increases from 10.416 Å to 10.455 Å upon saturation with water vapour; the increase is approximately half of the value than for $KTaWO_6$, which could also indicate a lower amount of incorporated water. No change of the relative intensities is discernible, leading to the assumption that the unit cell does not seem to change. Due to the inherent heat lability of $Sn_xK_{1-2x}TaWO_6$, no *in-situ* XRD measurements have been performed.

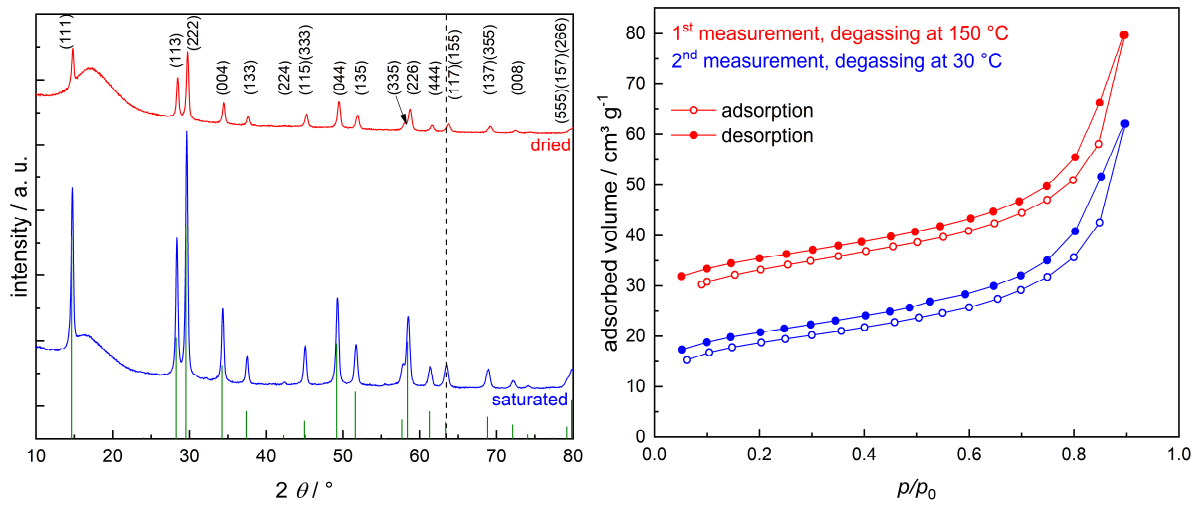

Figure 5.20: XRD patterns of dried and water vapour saturated $Sn_{0.35}K_{0.30}TaWO_6$ (left) and water vapour physisorption isotherms of $Sn_{0.35}K_{0.30}TaWO_6$ (right). The sample depicted in section 5.3 was decomposed since the initial degassing temperature of 300 °C was too high; therefore the degassing temperature was lowered to 150 °C and another sample was chosen for analysis.

In the first measurement, the water vapour physisorption isotherm starts at lower adsorbed volumes than for $KTaWO_6$, showing that the incorporated amount of water is indeed lower (Figure 5.20, right). The isotherm of the second measurement – indicating surface water – also starts at lower values, hinting that the surface of the nanoparticles also seems to change somewhat during ion exchange.

Thermogravimetric analysis reveals that water loss occurs at 170 °C, which is higher than for $KTaWO_6$ (Figure 5.21). The higher temperature is a sign that the water molecules seem to be more strongly bound in $Sn_{0.35}K_{0.30}TaWO_6$. Additionally, there is no second water loss at 320 °C compared to $KTaWO_6$, but a continuous loss of water with increasing temperatures. The determination of the exact amount of water is difficult since any mass changes at elevated temperatures could not only result from water loss but also from thermal decomposition.

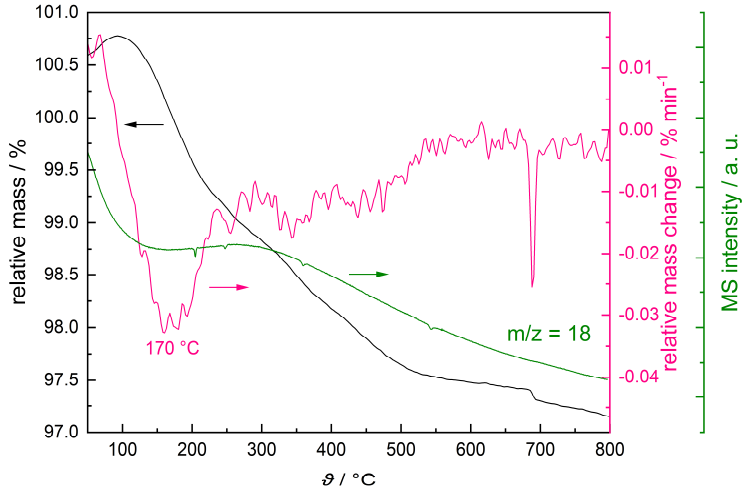

Figure 5.21: TGA-MS of $Sn_{0.35}K_{0.30}TaWO_6$.

Theoretical calculations for $Sn_{0.5}TaWO_6$ were performed to check if the water incorporation changes the electronic and optical properties; for that a single water molecule was added to the unit cell. The O atom of water is strongly coordinated to Sn^{2+}, with an O–Sn distance of 2.29 Å; this is rather close to the Sn–O distance of 2.2489 Å reported for tin(II) oxide SnO single crystals and indicates a strong bond.[158] This bond results in the splitting of Sn^{2+} states located close to the VB maximum (Figure 5.22, left); this has the effect that the electronic bandgap decreases from 3.66 eV to 3.31 eV. A similar state splitting has been observed for Eu^{3+} doped $KNbWO_6$ (see section 2.3.2).[105]

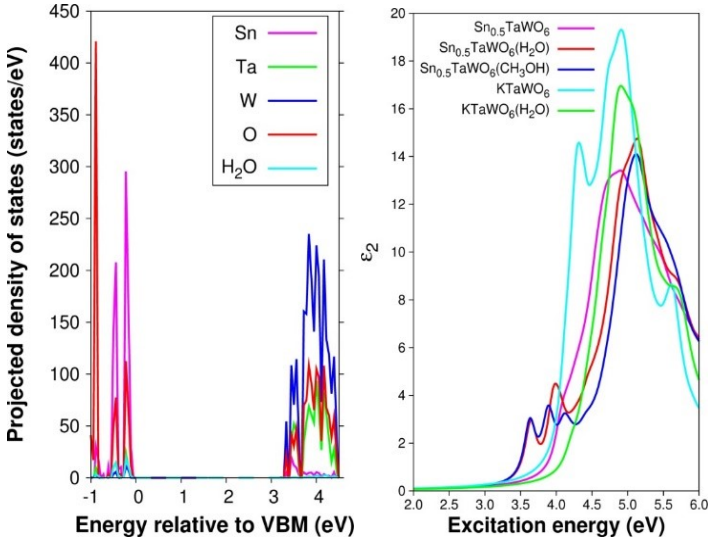

Figure 5.22: Projected density of states for $Sn_{0.5}TaWO_6 \cdot H_2O$ (left) and imaginary part of the dielectric function (right) for $KTaWO_6$ with and without incorporated water and $Sn_{0.5}TaWO_6$ with and without incorporated water or methanol.

The calculated optical spectra – in the form of the imaginary part of the dielectric function – show two low-lying excited states for water at 3.64 eV and 3.95 eV (Figure 5.22, right). The incorporation of methanol instead of water also results in these two states at 3.63 eV and 3.81 eV. The O atom of methanol also coordinates to Sn^{2+}, which results in the same state splitting effect as for water. Anhydrous $Sn_{0.5}TaWO_6$ has the lowest excited states at a higher energy of 4.04 eV. Adding a water molecule to $KTaWO_6$ increases the lowest excited states from 3.82 eV to 4.11 eV; additionally, the first absorption band between 4.0 eV and 4.5 eV is quenched. The larger O–K distance of 2.68 Å – as compared to the Sn–O distance of 2.29 Å – likely results in an enhanced ligand field, thus decreasing the bandgap from 4.87 eV to 4.27 eV.

Attempts to see these effects in measured absorption spectra were unsuccessful (Figure 10.4, appendix). The observed difference for $Sn_xK_{1-2x}TaWO_6$ is less than 2 nm and possibly a measuring artefact due to the height change occurring during the heat dissipation of the sample holder. To prevent damage to the sample holder, the drying temperature was far lower than for the other experiments in this section; it is possible that the temperature was too low to actually remove the water molecules from the sample.

To summarise, $Sn_xK_{1-2x}TaWO_6$ incorporates water molecules in lower amounts than $KTaWO_6$. Water physisorption isotherms also indicate a possible change of the surface properties after ion exchange. Calculations shows that the bandgap diminishment does not only result from the introduction of Sn^{2+}, but is a cooperative effect resulting from the introduction of Sn^{2+} and the incorporation of water or a similar guest molecule like methanol.

5.5 Optimisation of Ion Exchange

Previous reports concerning Sn^{2+} exchange typically used acidified $SnCl_2$ solutions as exchange reagent; in most cases the ion exchange was far from complete.[18,19,64,67,69] The actually used acid concentration – and thus the pH value – have been seldom reported. The pH is of utmost importance, since $SnCl_2$ hydrolyses to insoluble abhurite $Sn_{21}O_6Cl_{16}(OH)_{14}$ at pH values above 1.[159] Additionally, Cl^- is a known inhibitor of photocatalytic reactions.[160]

In order to find the optimal exchange reagent and solvent, a wide range of Sn^{2+} precursors in different solvents have been investigated. Special care has been taken to detect possible impurities resulting from ion exchange. The $KTaWO_6$ starting material is not composed of nanoparticles synthesised by hydrothermal treatment (as in sections 5.3 and 5.4), but of larger particles synthesised *via* solid state reaction (formula 5.2).

$$K_2CO_3 + Ta_2O_5 + 2\ WO_3 \rightarrow 2\ KTaWO_6 + CO_2 \uparrow \qquad (5.2)$$

The sample is phase pure and highly crystalline (Figure 5.23).

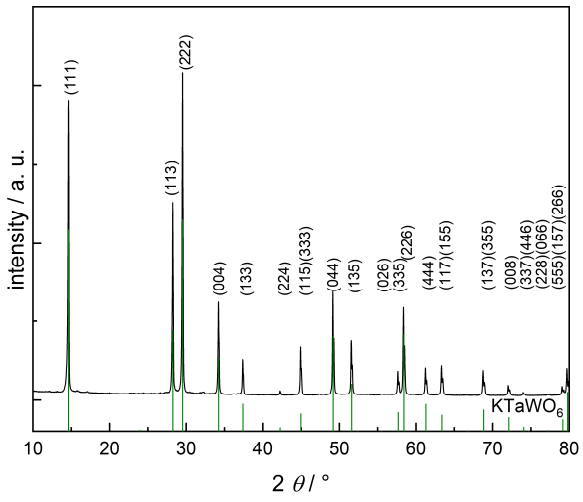

Figure 5.23: XRD pattern of $KTaWO_6$ synthesised *via* solid state reaction.

Water vapour physisorption isotherms of $KTaWO_6$ nanoparticles indicated a change of the surface after ion exchange (see section 5.4). In order to better elucidate such changes, larger particles were chosen in order to increase the differences between surface and bulk properties. The disadvantage of the larger particles is a generally worse ion exchange due to longer diffusion pathways. The crystallite size has not been estimated, since Rietveld refinement is not suitable for XRD patterns of $KTaWO_6$ due to the water incorporation and the reflections are too narrow for a reliable single reflection analysis. SEM images show irregularly formed particles with typical sizes between 100-200 nm (Figure 5.24).

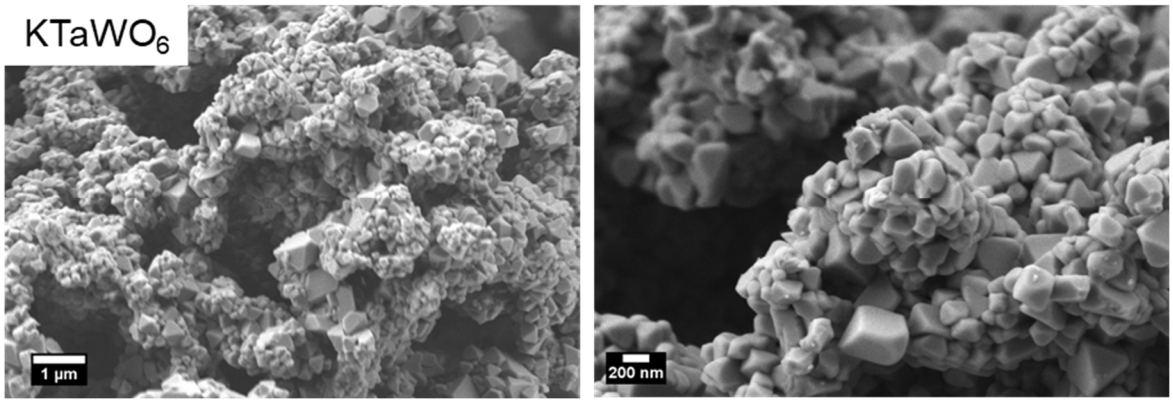

Figure 5.24: SEM images of $KTaWO_6$ synthesised *via* solid state reaction.

Ion exchange with $SnCl_2$ was performed in either 1 mol L^{-1} hydrochloric acid HCl – resulting in pH 0 – or in absolute ethanol EtOH to avoid hydrolysis. The elemental compositions of the samples after ion exchange have been measured by EDX spectroscopy and are $Sn_{0.08}K_{0.38}Ta_1W_{0.94}O_{4.86}$ (HCl) and $Sn_{0.14}K_{0.79}Ta_1W_{0.90}O_{4.74}Cl_{0.22}$ (EtOH) (normalised to Ta = 1), respectively. The low values for oxygen are most likely a result of the poor sensitivity of EDX spectroscopy for light elements and should not be interpreted as oxygen deficiency. The combined Sn and K content in the sample exchanged in HCl is too low for charge neutrality. It is possible that proton exchange (formula 5.3) happens as a side reaction.

$$KTaWO_6 + H_3O^+_{(aq.)} \rightleftharpoons HTaWO_6 + K^+_{(aq.)} + H_2O \qquad (5.3)$$

The theoretical elemental composition for a charge neutral compound would be $H_{0.46}Sn_{0.08}K_{0.38}Ta_1W_{0.94}O_{4.86}$; indicating that at lower pH values – and therefore higher proton concentrations – proton exchange is dominant compared to Sn^{2+} exchange. The sample exchanged in EtOH still contains a significant amount of Cl, even after several washing steps. The XRD pattern of this sample also shows a miniscule reflection (Figure 5.25, left, see arrow) that is not present in pristine $KTaWO_6$ or in the sample exchanged in HCl. For better readability, all samples in this section are labelled with the exchange agent and the used solvent, *e.g.* the sample that has been ion exchanged with $SnCl_2$ in EtOH is labelled "$SnCl_2$-EtOH". Since $KTaWO_6$ is an indirect semiconductor, whereas $Sn_{0.5}TaWO_6$ is a direct one and ion exchange only resulted in a partial exchange in all cases, bandgaps have been determined for both indirect and direct transitions. The indirect bandgaps are 2.7 eV and 2.3 eV (Figure 5.25, right), respectively, while the direct bandgaps are 3.1 eV and 2.8 eV (Figure 10.5, left, appendix).

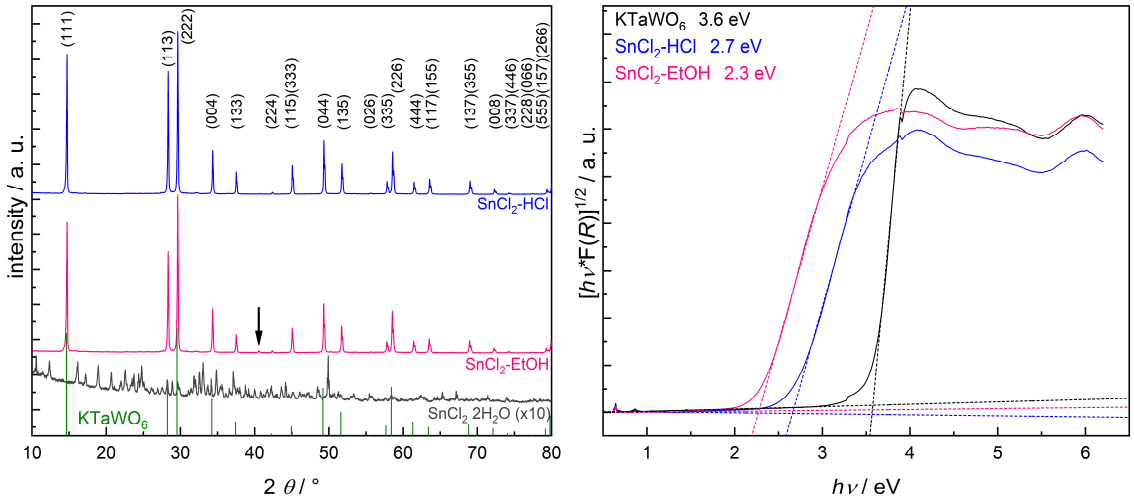

Figure 5.25: XRD patterns of $Sn_xK_{1-2x}TaWO_6$ and $SnCl_2 \cdot 2\ H_2O$ (left) and Tauc plots for indirect bandgaps for $KTaWO_6$ and $Sn_xK_{1-2x}TaWO_6$ exchanged with $SnCl_2$ (right).

Raman spectra do not show any impurities or residues of the exchange reagent after ion exchange (Figure 5.26, left). The Raman spectrum of $SnCl_2$-EtOH shows the increase in the F_{2g} and the A_{1g} modes (400-500 cm^{-1}), which has been observed for Sn^{2+} exchange (see section 4.3). The same is not visible for $SnCl_2$-HCl, probably due to the lower Sn^{2+} amount. DRIFT spectra show a new band at 1120 cm^{-1} after ion exchange that is most likely a Sn–O vibration (Figure 5.26, right). SEM images did not reveal any changes of the sample morphologies (Figure 10.6, appendix).

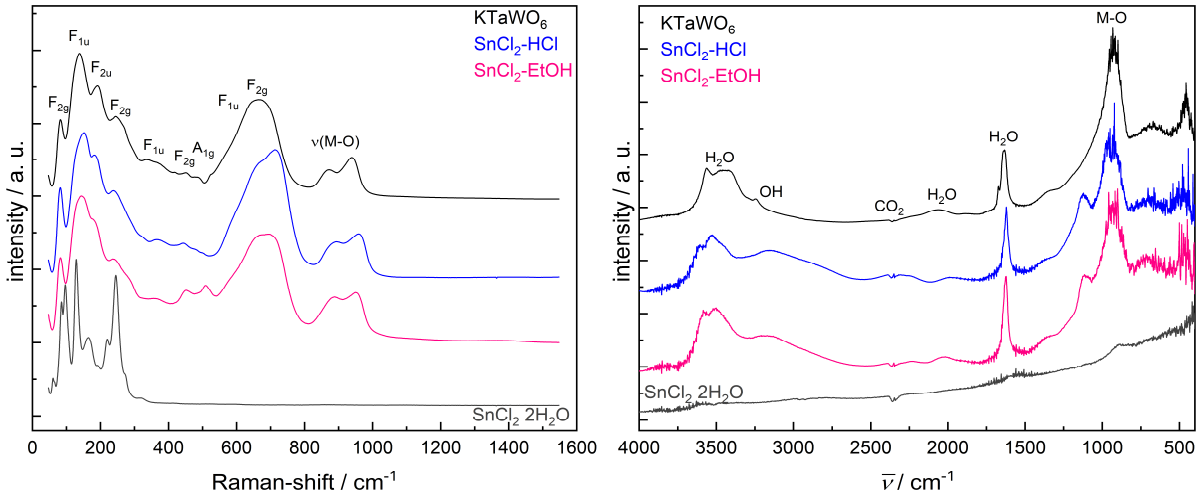

Figure 5.26: Raman spectra (left) and DRIFT spectra (right) of $KTaWO_6$, $Sn_xK_{1-2x}TaWO_6$ and $SnCl_2$.

Stannous bromide $SnBr_2$ and stannous iodide SnI_2 are soluble in organic solvents, which circumvent possible hydrolysis. The elemental compositions of these samples after ion exchange are $Sn_{0.06}K_{0.90}Ta_1W_{0.92}O_{4.49}Br_{0.27}$ ($SnBr_2$-acetone), $Sn_{0.02}K_{0.70}Ta_1W_{0.92}O_{4.20}$ ($SnBr_2$-

DMSO (dimethyl sulfoxide)), $Sn_{0.18}K_{1.02}Ta_1W_{0.96}O_{5.99}I_{0.41}$ (SnI_2-$CHCl_3$ (chloroform)) and $Sn_{0.27}K_{1.00}Ta_1W_{1.01}O_{7.05}I_{0.39}$ (SnI_2-toluene). Three of four samples still contain considerable amounts of halides. For these three samples impurities can be observed in the XRD patterns (Figure 5.27, left, see arrows). Moreover, ion exchange has been negligible, probably due to poor solubility of the exchange agents or the corresponding potassium salts. As a result of the poor exchange, the bandgaps have not been reduced (Figure 5.27, right and Figure 10.5, right, appendix); only a small shoulder from 2.5-3.5 eV is visible. Unlike water or methanol, the solvents used in this experiment are too large to enter the hexagonal channels and coordinate to Sn^{2+}, which is also necessary for bandgap diminishment (see section 5.4). Additionally, toluene and $CHCl_3$ lack the O atom necessary for coordination.

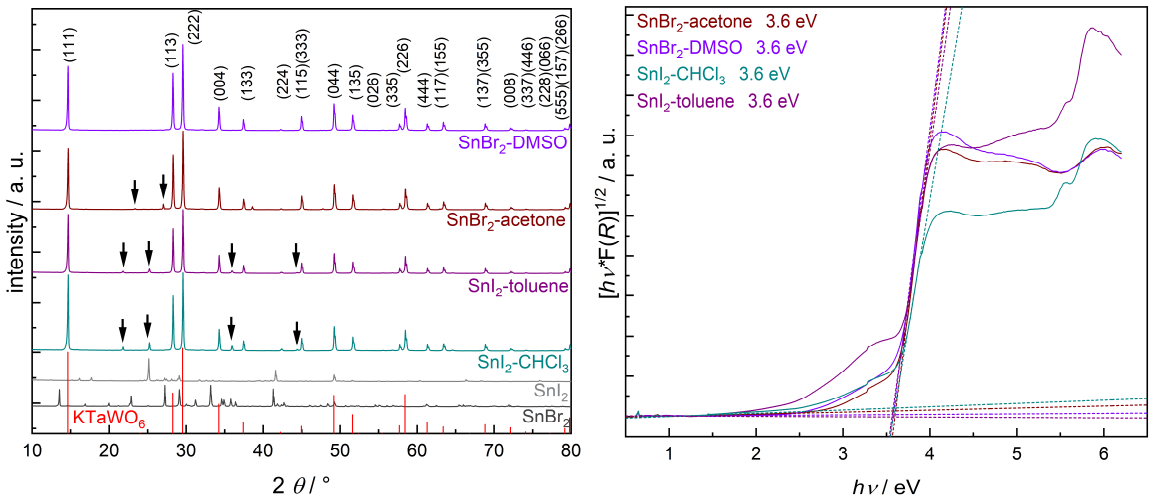

Figure 5.27: XRD patterns of $Sn_xK_{1-2x}TaWO_6$ and the exchange reagents (left) and Tauc plots for indirect bandgaps for $Sn_xK_{1-2x}TaWO_6$ exchanged with $SnBr_2$ or SnI_2 (right).

Raman spectra show no increase in the F_{2g} and the A_{1g} modes (400-500 cm^{-1}), also a sign of the poor ion exchange (Figure 5.28, left). DRIFT spectroscopy has a higher surface sensitivity, which is probably causing the supposed Sn–O vibration at 1130 cm^{-1} to be is visible, although no changes are visible in the Raman spectra.

SEM images of the SnI_2-toluene samples show small particles located on the larger $KTaWO_6$ particles; these are most likely residues of SnI_2 (Figure 5.29). SEM images for the other samples show no changes after ion exchange (Figure 10.7, appendix).

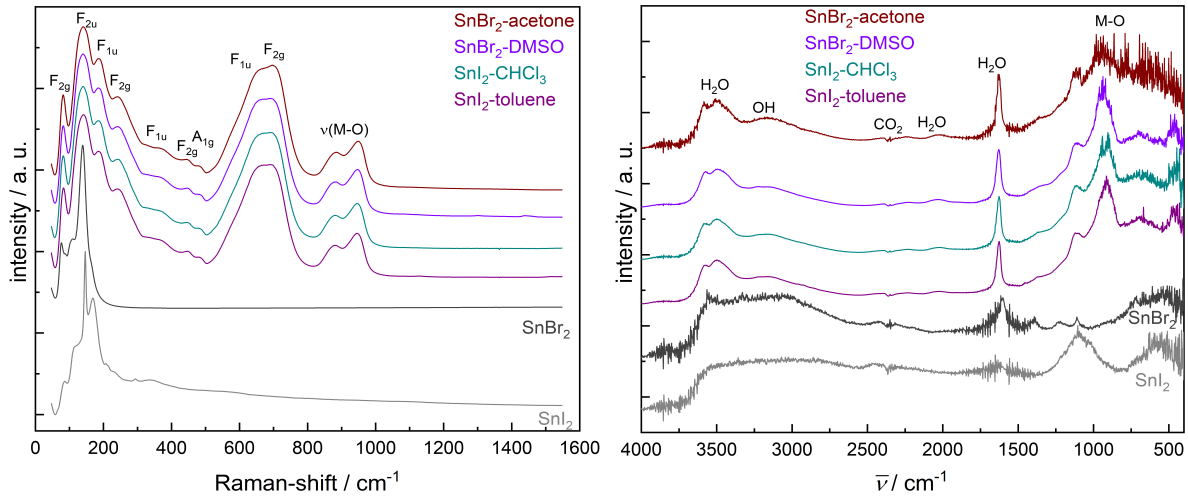

Figure 5.28: Raman spectra (left) and DRIFT spectra (right) of $Sn_xK_{1-2x}TaWO_6$, $SnBr_2$ and SnI_2.

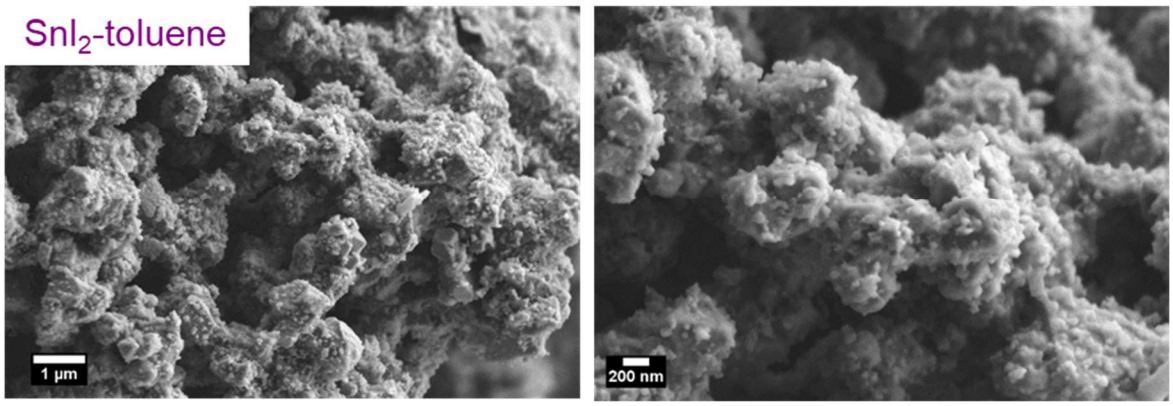

Figure 5.29: SEM images of the SnI_2-toluene sample.

Since using organic solvents does not result in diminished bandgaps, other exchange reagents in aqueous solution were considered. Stannous acetate $Sn(OAc)_2$ is especially of interest since photogenerated holes should decompose any OAc^- residues on the surface. The elemental composition – measured by EDX spectroscopy – of the sample exchanged in water ($Sn(OAc)_2$-H_2O) is $Sn_{1.06}K_{0.54}Ta_1W_{0.93}O_{6.38}$. The enormous Sn surplus results most likely from the contemporaneous hydrolysis of $Sn(OAc)_2$.[161] Exchanging the sample in glacial acetic acid also seems to result in proton exchange, since the measured composition $Sn_{0.09}K_{0.49}Ta_1W_{0.89}O_{4.67}$ is not sufficient for charge neutrality. The elemental compositions for the other two samples are $Sn_{0.18}K_{0.80}Ta_1W_{0.94}O_{4.88}$ ($Sn(OAc)_2$-DMSO) and $Sn_{0.08}K_{0.77}Ta_1W_{0.94}O_{4.88}$ ($Sn(OAc)_2$-MeOH). No impurities could be observed in the XRD patterns (Figure 5.30, left). The sample exchanged in DMSO does not show a reduced bandgap (Figure 5.30, right); the reasons for that have been explained above. The indirect bandgaps for the other samples are 2.2 eV (H_2O), 2.4 eV (MeOH) and 2.5 eV (HOAc). The MeOH sample proves that only a comparatively small amount

of Sn^{2+} is necessary for bandgap reduction. The direct bandgaps are slightly larger with 2.7 eV (H_2O), 3.0 eV (HOAc and MeOH both) and 3.8 eV (DMSO) (Figure 10.8, left, appendix).

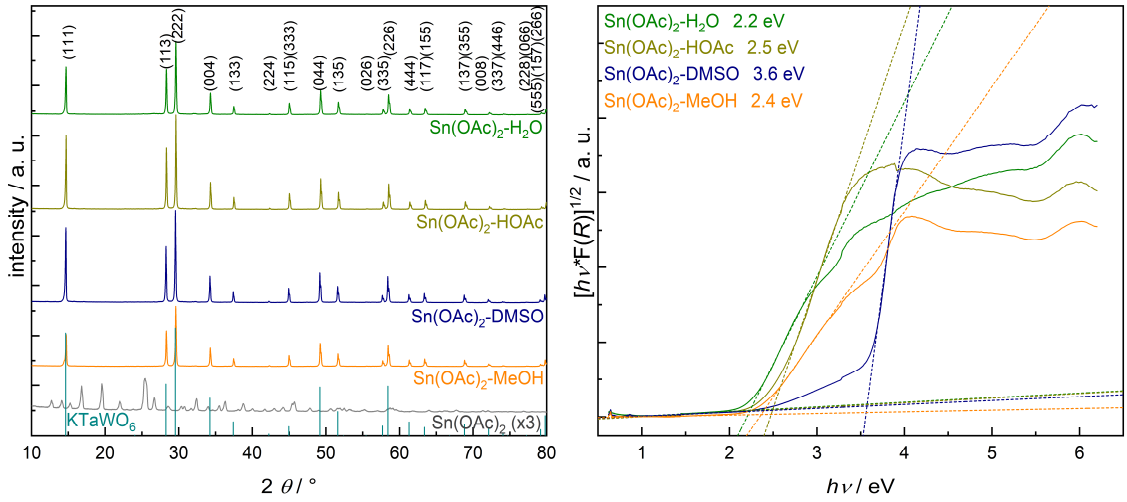

Figure 5.30: XRD patterns (left) and Tauc plots (right) of $Sn_xK_{1-2x}TaWO_6$ and $Sn(OAc)_2$.

Only the H_2O sample shows increased F_{2g} and A_{1g} Raman modes (Figure 5.31, left); probably due to it being the sample with the highest Sn^{2+} content. Raman bands of the exchange reagent could not be seen for any sample. DRIFT spectra show small bands around 1300 cm^{-1}, which could be residues of the exchange reagent (Figure 5.31 right).

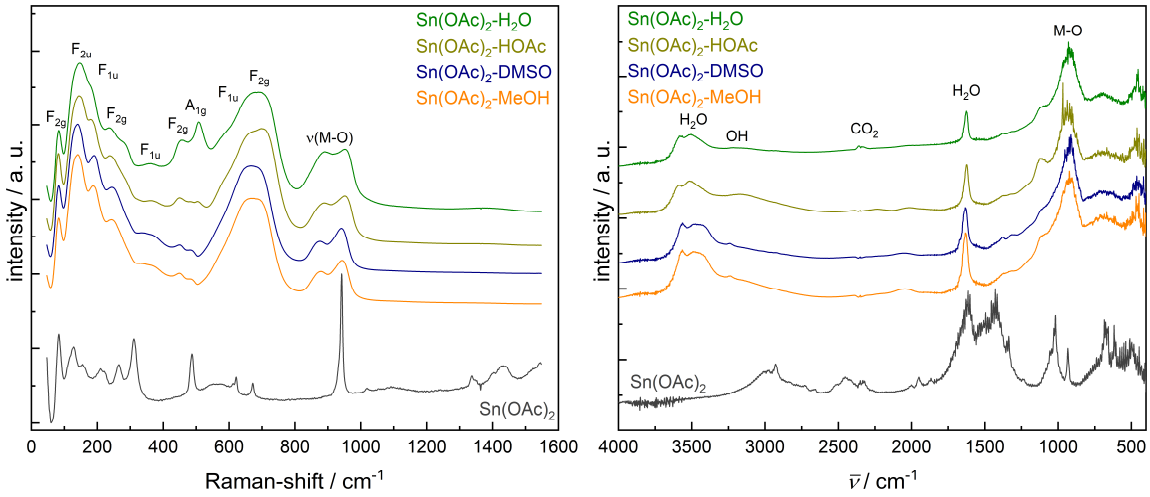

Figure 5.31: Raman spectra (left) and DRIFT spectra (right) of $Sn_xK_{1-2x}TaWO_6$ and $Sn(OAc)_2$.

SEM images for the H_2O and DMSO samples show smaller particles on top of the $Sn_xK_{1-2x}TaWO_6$ particles. These are probably hydrolysed tin compounds for the H_2O sample and remains of $Sn(OAc)_2$ for the DMSO sample (Figure 5.32). The other two samples – MeOH and HOAc – do not show any changes in morphology (Figure 10.9, appendix).

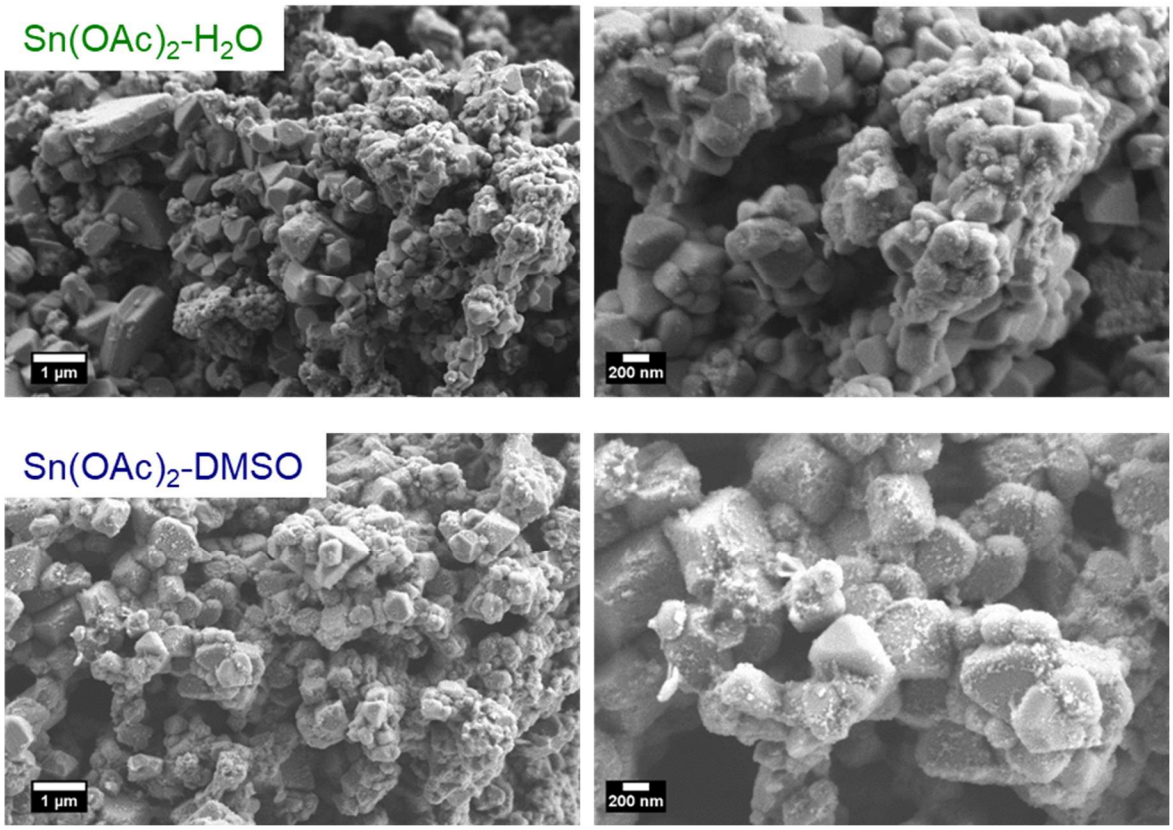

Figure 5.32: SEM images of the $Sn(OAc)_2$-H_2O (top) and $Sn(OAc)_2$-DMSO sample (bottom).

Due to the hydrolysis of $Sn(OAc)_2$ other Sn^{2+} salts were investigated; stannous sulphate $SnSO_4$ is reported to be stable at low pH values.[162] The elemental composition $Sn_{0.36}K_{0.45}Ta_1W_{0.96}O_{5.71}$ indicates a slight Sn surplus. However, no impurities are discernible in the XRD pattern (Figure 5.33, left). The indirect bandgap is 2.2 eV (Figure 5.33, right), while the direct one is 2.6 eV (Figure 10.8, right, appendix).

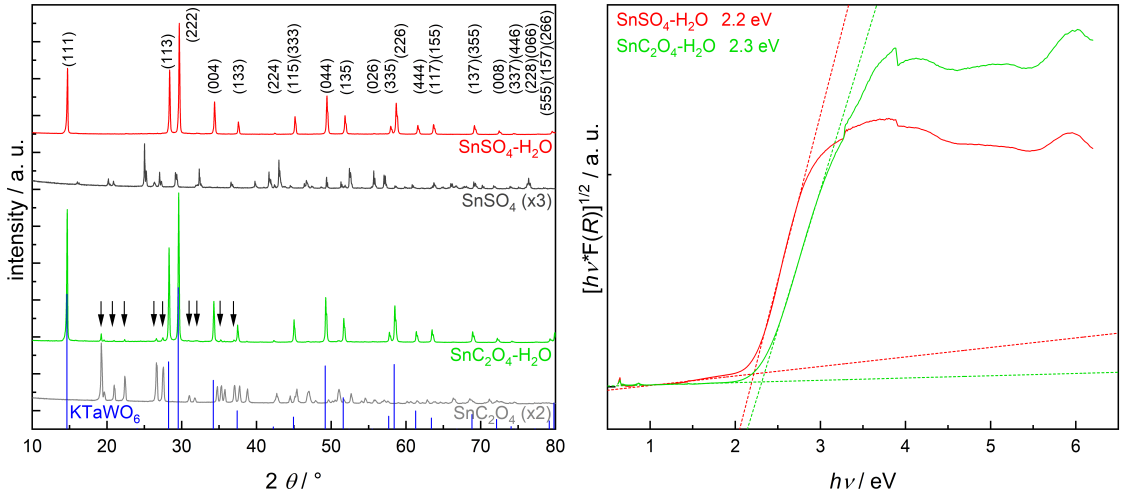

Figure 5.33: XRD patterns of $Sn_xK_{1-2x}TaWO_6$ and the exchange reagents (left) and Tauc plots for indirect bandgaps for $Sn_xK_{1-2x}TaWO_6$ exchanged with $SnSO_4$ or SnC_2O_4 (right).

The Raman spectra shows the increased F_{2g} and A_{1g} modes associated with high Sn^{2+} content (Figure 5.34, left); whereas the DRIFT spectra is unremarkable (Figure 5.34, right). SEM images also do not show any change in sample morphology (Figure 10.10, appendix).

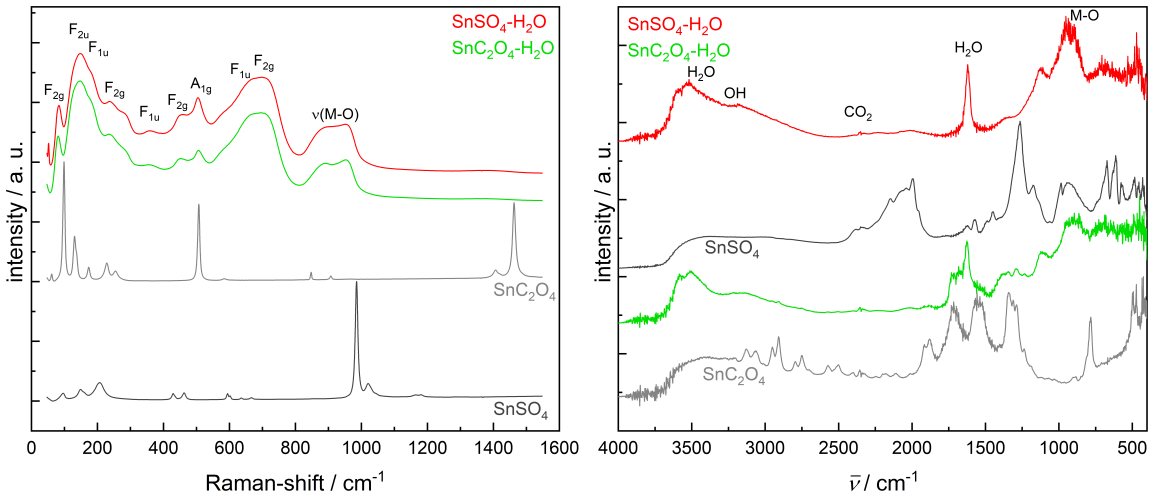

Figure 5.34: Raman spectra (left) and DRIFT spectra (right) of $Sn_xK_{1-2x}TaWO_6$, $SnSO_4$ and SnC_2O_4.

The last used exchange reagent is stannous oxalate SnC_2O_4 in water; the resulting sample has the elemental composition $Sn_{0.24}K_{0.57}Ta_1W_{0.84}O_{4.52}$. Residues of SnC_2O_4 are visible in the XRD pattern (Figure 5.33, left). The indirect bandgap is 2.3 eV (Figure 5.33, left), whereas the direct bandgap is 3.0 eV (Figure 10.8, right, appendix). Raman spectra again show increased F_{2g} and A_{1g} modes, but no SnC_2O_4 residues (Figure 5.34, left). However, DRIFT spectra show several bands originating from SnC_2O_4. Small particles can also be seen on the surface of the sample particles (Figure 5.35).

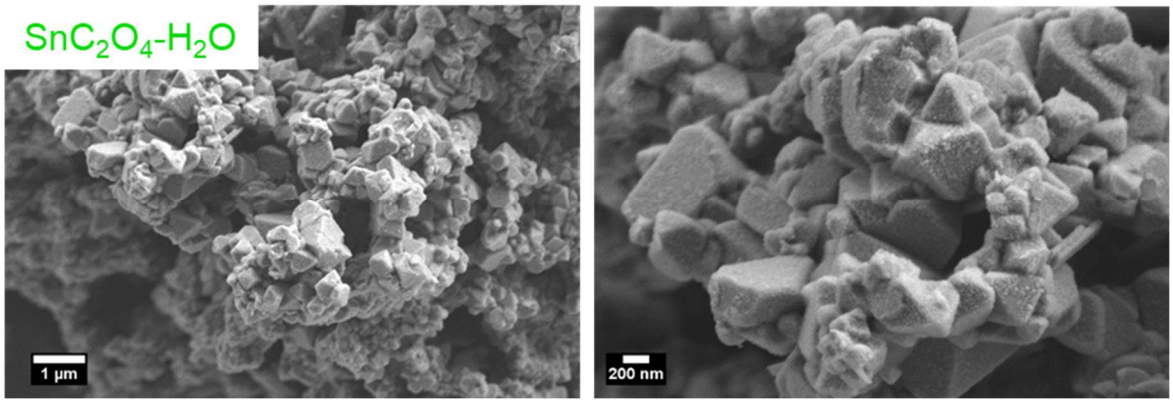

Figure 5.35: SEM images of the SnC_2O_4-H_2O sample.

Samples that were neither phase pure nor showed a bandgap reduction were omitted from further analysis and photocatalytic measurements. The $Sn(OAc)_2$-HOAc sample was also omitted, because of the proton exchange and having the same Sn content as the $Sn(OAc)_2$-MeOH sample.

Physisorption measurements with krypton resulted in similar BET surface areas of approximately 1 $m^2\ g^{-1}$, with the exception of the $Sn(OAc)_2$- H_2O sample with 4.3 $m^2\ g^{-1}$. The higher surface area might be a result from the hydrolysis and subsequent precipitation of $Sn(OAc)_2$.

In order to investigate possible changes to the surface of the samples and to determine the Sn oxidation state, XPS measurements were performed (Figure 10.11, left, appendix). The elemental compositions measured by EDX spectroscopy and XPS differ extensively; the reason is the different analysis depths of these methods. The two samples exchanged in water have a considerable surplus of Sn and O on the surface (Table 5.1), indicating a SnO_x and/or $Sn(OH)_y$ layer on top of the sample from the hydrolysis of the exchange reagent. A similar – but less severe – surface layer is present for the samples exchanged in HCl or MeOH. The sample exchanged with $SnSO_4$ also has sulphate residues on the surface. Moreover, the sample exchanged in HCl still shows traces of Cl^-, despite several washing steps.

Table 5.1: Elemental compositions of Sn^{2+} exchanged samples as measured by EDX spectroscopy and XPS (all values are normalised to Ta = 1).

sample	Sn	K	Ta	W	O	S	Cl	method
$SnSO_4$-H_2O	0.36	0.45	1	0.96	5.71			EDX
	5.67	0.19	1	0.96	22.78	0.67		XPS
$Sn(OAc)_2$-H_2O	1.06	0.54	1	0.93	6.38			EDX
	11.16	0.11	1	1.05	29.89			XPS
$SnCl_2$-HCl	0.08	0.38	1	0.94	4.86			EDX
	0.82	0.07	1	1.03	6.85		0.07	XPS
$Sn(OAc)_2$-MeOH	0.08	0.77	1	0.94	4.88			EDX
	1.78	0.64	1	1.02	11.22			XPS

The determination of the oxidation state of Sn is problematical, since the values for Sn(II) oxide SnO and Sn(IV) oxide SnO_2 given in the literature are not only close together, but also overlapping. The literature values for the Sn $3d_{5/2}$ signal of SnO range from 485.6-487.0 eV, whereas the range for SnO_2 is 486.2-488 eV (all values corrected for a C 1*s* signal at 284.8 eV).[163–166] All four samples show a symmetric signal in the overlapping region of SnO and SnO_2; the oxidation state is thus not unequivocally assignable (Figure 5.36, left). Fitting of the signals with one or two components results only in miniscule differences (Figure 10.11,

right, appendix). The Auger signals also shift with the chemical state of the sample. Although values reported in literature are less disperse as for the XPS values, an unambiguous assignment is still not possible (Figure 5.36, right).[167–172]

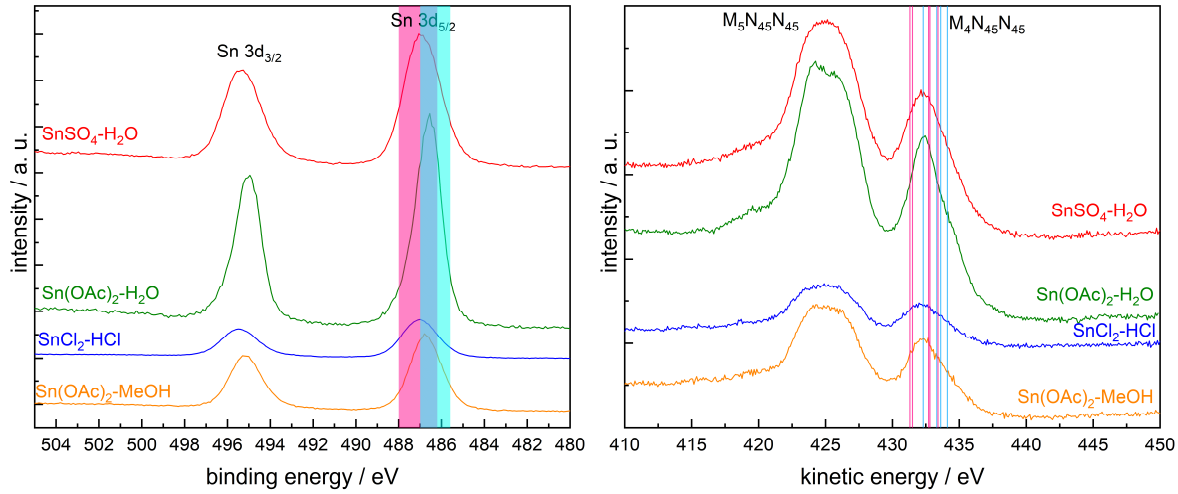

Figure 5.36: High resolution XPS of the Sn 3*d* region (left) and Sn Auger signals (right). The pink and cyan areas and lines emblematise values reported in literature for SnO and SnO_2, respectively.

For an unequivocal determination of the oxidation state, the Auger parameter for all four samples has been calculated and compared to values reported in literature (Figure 5.37).[142,167–174] All Sn on the surface of the four samples has been oxidised to Sn(IV); however, the bulk volume has to consist of Sn(II) to account for the bandgap reduction.

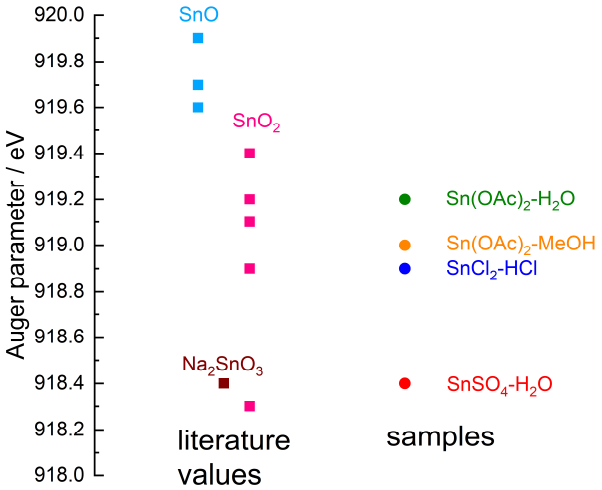

Figure 5.37: Literature values for the Sn Auger parameter ($3d_{5/2}$ + $M_4N_{45}N_{45}$) (left) and Auger parameters for all four samples.

To check if the Sn^{2+} exchanged samples are still suitable for photocatalytic hydrogen production, the flat band potential has been estimated *via* Mott-Schottky analysis (Figure 5.38, left). The flat band potentials of all four samples – and of $KTaWO_6$, which has been included as reference – are around –0.3 V and identical within the experimental uncertainty; indicating that the conduction band does not shift. The highly similar slope also suggests that the charge carrier density is not affected by Sn^{2+} exchange. By combining the flat band potential and the bandgaps measured by UV/vis spectroscopy it is possible to calculate the valence band maximum (Figure 5.38, right). The band positions of all four samples are suitable for water splitting.

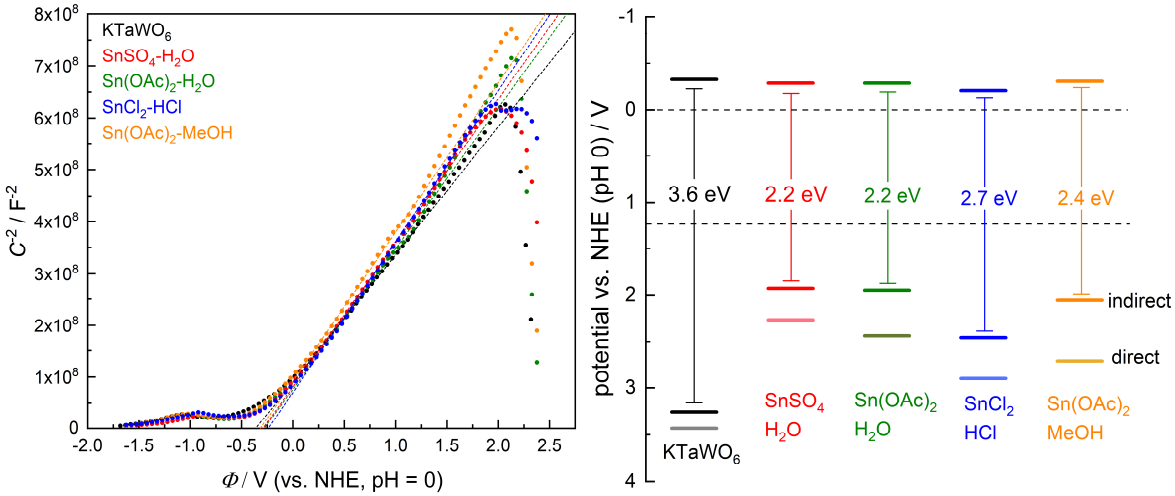

Figure 5.38: Mott-Schottky plots (left) and band schemes (right) for $KTaWO_6$ and the four $Sn_xK_{1-2x}TaWO_6$ samples. Displayed bandgaps are for an indirect transition; however, valence band maximum positions have been calculated for both indirect and direct transition. Dashed lines represent the redox potentials for water splitting.

To summarise, the Sn^{2+} ion exchange in water results in hydrolysis of Sn^{2+} and in the formation of a SnO_x layer on the sample surface. The hydrolysis is minimised in acidic media; however, proton exchange is favoured compared to Sn^{2+} exchange. The use of organic solvents only leads to negligible exchange and no bandgap reduction occurs. All samples consist of Sn(IV) on the surface.

5.6 Photocatalysis and Post Catalytic Analysis

Since the Sn^{2+} exchanged samples absorb visible light, photocatalytic hydrogen evolution experiments were performed in a water/methanol mixture in simulated solar light (Figure 5.39, left). However, only two samples evolved a small amount of hydrogen, which decreased to zero after a short time. This decrease indicates a decomposition of the respective samples,

therefore the hydrogen evolution cannot be considered photocatalytic. This is in contrast to the steady-state activity under UV irradiation, which is similar for all samples (Figure 5.39, right). Moreover, the activity of the two samples with the highest Sn content ($SnSO_4$-H_2O and $Sn(OAc)_2$-H_2O) – and therefore the biggest Sn^{4+} surface layers – is nearly identical to the activity of the $KTaWO_6$ starting material. Both the bandgap reduction and the Sn^{4+} surface layer seem to be irrelevant for photocatalyis in UV light irradiation. The sample exchanged in HCl – presumably also proton exchanged – shows the highest activity; proton exchange can increase the photocatalytic activity.[175] The reason for the $Sn(OAc)_2$-MeOH sample also showing a higher activity compared to the remaining three samples could not be explained.

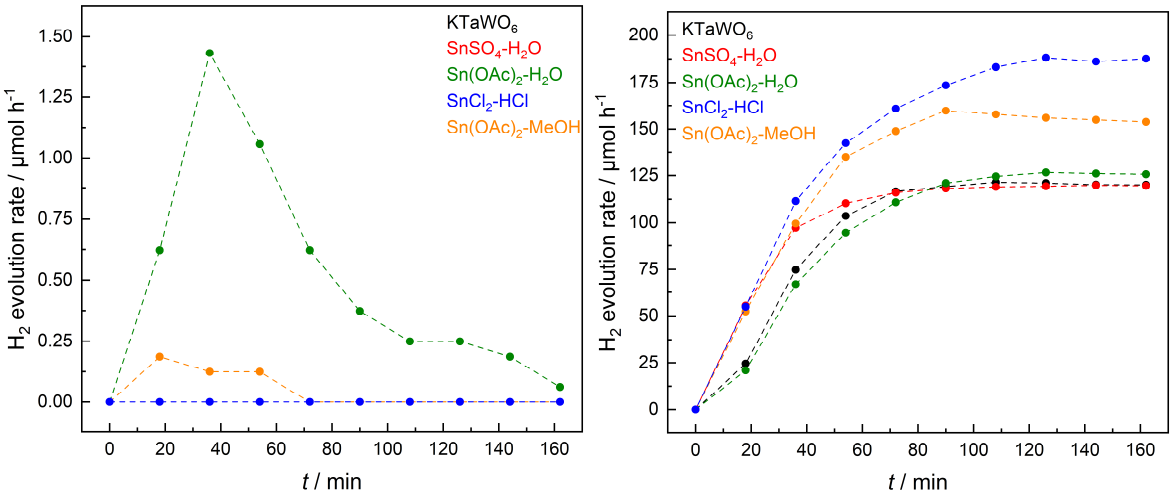

Figure 5.39: Hydrogen evolution rates of $KTaWO_6$ and the four $Sn_xK_{1-2x}TaWO_6$ samples in water/methanol under simulated solar light (left) and UV light irradiation (right); Na_3RhCl_6 was added as co-catalyst precursor before start of the irradiation.

In order to find the reason for the decomposition seen above and the non-activity in simulated solar light, all samples were recovered and analysed extensively. XRD patterns show no changes after simulated solar light irradiation; all samples are still phase pure and highly crystalline (Figure 5.40, left). The XRD patterns of the samples under UV light irradiation also show no changes (Figure 10.12, left, appendix).

Raman spectra show decreased F_{2g} and A_{1g} modes (400-500 cm^{-1}) for the $SnSO_4$-H_2O and $Sn(OAc)_2$-H_2O samples, indicating a lowered Sn content (Figure 5.40, right). The Raman spectra of the samples under UV light irradiation showed the same decrease (Figure 10.12, right, appendix).

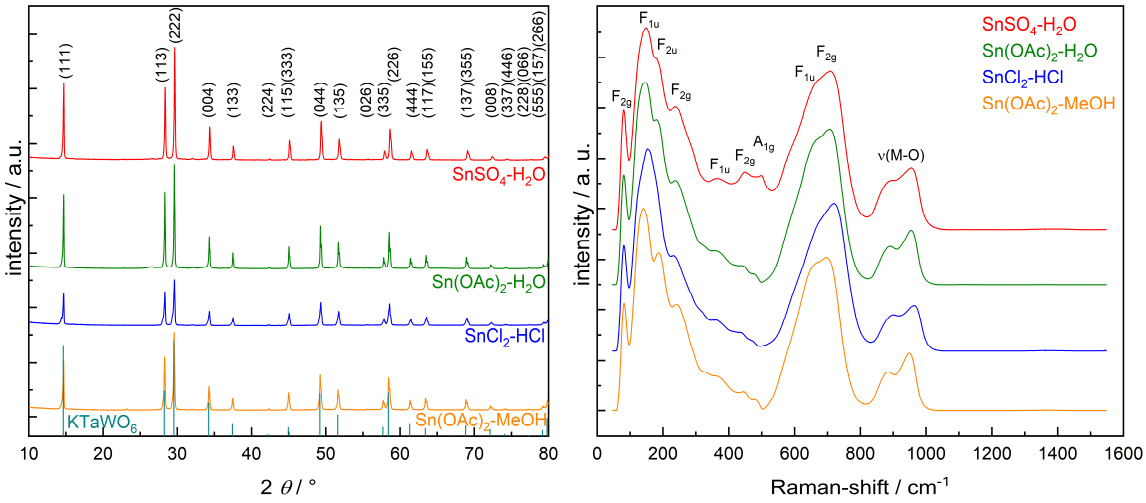

Figure 5.40: XRD patterns (left) and Raman spectra (right) of the samples after simulated solar light irradiation.

The elemental compositions show indeed a Sn loss for most samples after light irradiation (Table 5.2). The $Sn(OAc)_2$-H_2O sample – which evolved small amounts of hydrogen in simulated solar light – shows the highest Sn loss. The hydrogen evolution and the Sn loss can be explained by photoinduced self-oxidation of Sn^{2+} and subsequent dissolution of the emerging Sn^{4+} species. Oxidation of Sn^{2+} during light irradiation was also observed for α-$SnWO_4$.[39] However, the Sn content of the $SnSO_4$-H_2O sample has been increased afterwards; this is puzzling and cannot be explained. Measuring this sample anew resulted in the same trend (not shown).

Table 5.2: Elemental compositions measured by EDX spectroscopy before and after photocatalytic measurements (all values are normalised to Ta = 1).

sample	point of time	Sn	K	Ta	W	O
	before	0.36	0.45	1	0.96	5.71
$SnSO_4$-H_2O	after solar light	0.54	0.35	1	1.00	6.38
	after UV light	0.47	0.38	1	0.98	8.31
	before	1.06	0.54	1	0.93	6.38
$Sn(OAc)_2$-H_2O	after solar light	0.66	0.55	1	0.92	6.57
	after UV light	0.57	0.46	1	0.95	7.65
	before	0.08	0.38	1	0.94	4.86
$SnCl_2$-HCl	after solar light	0.06	0.42	1	0.95	4.90
	after UV light	0.05	0.40	1	0.95	5.58
	before	0.08	0.77	1	0.94	4.88
$Sn(OAc)_2$-MeOH	after solar light	0.06	0.56	1	0.95	5.24
	after UV light	0.10	0.56	1	0.73	6.17

A consequence of Sn^{2+} oxidation is a bandgap increase since water – or methanol – molecules cannot coordinate to Sn^{2+} anymore. All light irradiated samples show an increased bandgap and a decrease of visible light absorption (Figure 5.41), which explains why the samples are not photocatalytically active in simulated solar light.

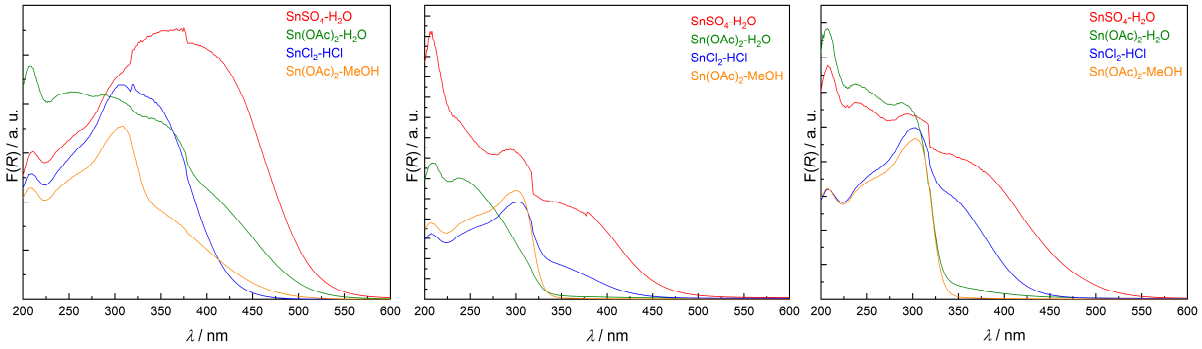

Figure 5.41: Kubelka-Munk absorption spectra before (left), after simulated solar light irradiation (middle) and after UV irradiation (right).

The bandgap increase is irrelevant for the photocatalysis in UV light, since the photon energy is high enough for the 3.6 eV transition from O 2*p* to W 5*d*, which is unaffected by Sn^{2+} oxidation. It is the same transition – with the same bandgap – as in $KTaWO_6$, which is why the photocatalytic activity of $KTaWO_6$ and the Sn^{2+} exchanged samples is so similar.

To summarise, although $Sn_xK_{1-2x}TaWO_6$ materials have bandgaps suitable for photocatalysis in visible light, the intrinsic susceptibility of Sn^{2+} towards (photo)oxidation makes them unsuitable for solar light photocatalysis.

6 Properties of $CsM_xW_{2-x}O_6$ and the Influence of the M^{n+} cation on Photocatalysis

A distinct advantage of the $CsM_xW_{2-x}O_6$ defect-pyrochlore structure is the wide range of possible elemental compositions. Since M^{n+} and W^{6+} occupy the same crystallographic position, it is possible to change the oxidation state of M^{n+} by simultaneously varying the amount of W^{6+} to retain charge neutrality. For example, if M^{n+} is a +V cation – such as Nb^{5+} or Ta^{5+} – the resulting formula would be $Cs_1M_1W_1O_6$, whereas a +IV cation would eventuate in the formula $Cs_1M_{0.5}W_{1.5}O_6$. This is also possible with +III and +II cations, resulting in the respective formulas $Cs_1M_{0.33}W_{1.67}O_6$ and $Cs_1M_{0.25}W_{1.75}O_6$. The CB may be formed mostly by W^{6+}, however states from M^{n+} are also involved (see also Figure 5.19). By changing M^{n+} it could be possible to change the potential of the CB minimum and therefore synthesise a semiconductor with a tailored CB minimum. However, the only systematic investigation of the correlation between M^{n+} and the photocatalytic activity was limited to $CsNbWO_6$ and $CsTaWO_6$.[112] Defect-pyrochlores with M^{n+} = Al^{3+}, Cr^{3+}, Fe^{3+} and Ti^{4+} have only been employed in dye degradation or as starting materials for Sn or N doping.[64,111,117] Moreover, literature reports on M^{2+} defect-pyrochlores are very scarce: $CsM_{0.25}Te_{1.75}O_6$ (M = Mg^{2+}, Ni^{2+} and Zn^{2+}) were investigated for their electronic conductivity, whereas only the lattice constant is known for $RbM_{0.25}W_{1.75}O_6$ (M = Mg^{2+}, Co^{2+}, Cu^{2+} and Zn^{2+}).[15,176] This chapter deals to begin with an investigation of a large number of novel and possible $CsM_xW_{2-x}O_6$ compounds, including a thorough characterisation of their material properties. Photocatalytic measurements are used to investigate a possible correlation between M^{n+} and the photocatalytic activity.

6.1 Investigating Possible M^{n+} Cations for Defect-Pyrochlore Tungstates

All $CsM_xW_{2-x}O_6$ materials in this section were synthesised with an aqueous sol-gel synthesis followed by combustion; the advantage of this synthesis strategy is the ideal mixture of all metal cations in the beginning (see section 2.4.1). After synthesis, the samples are calcined to remove carbon residues from EDTA and citric acid used in the synthesis and to ensure a thorough crystallisation. All samples have been calcined in a wide temperature range to investigate their thermal stability.

6.1.1 M^{n+} cations with oxidation state +V

Both $CsNbWO_6$ and $CsTaWO_6$ are phase pure in a wide temperature range from 500-900 °C (Figure 6.1). However a minimum temperature of usually 600 °C is necessary for the required removal of all carbon residues; samples calcined at only 500 °C or 550 °C are still tinged with grey. The reflections of $CsNbWO_6$ calcined at higher temperature are also narrower than those of $CsTaWO_6$; indicating that the crystallite growth may be different for each M^{n+} cation. The as synthesised (*as syn.*) $CsTaWO_6$ sample is already highly crystalline, whereas *as syn.* $CsNbWO_6$ is mainly amorphous. This difference may be explained by the different precursors: the Ta^{5+} precursor is Ta(V) ethoxide ($Ta(OEt)_5$) dissolved in ethanol; the Nb^{5+} precursor is ammonium niobate(V) oxalate $NH_4Nb(C_2O_4)_2O$. The ethanol is evaporated during synthesis, but the oxalate remains in solution and changes the oxidiser/fuel ratio thus influencing the combustion temperature and subsequently the crystallinity of the *as syn.* sample.

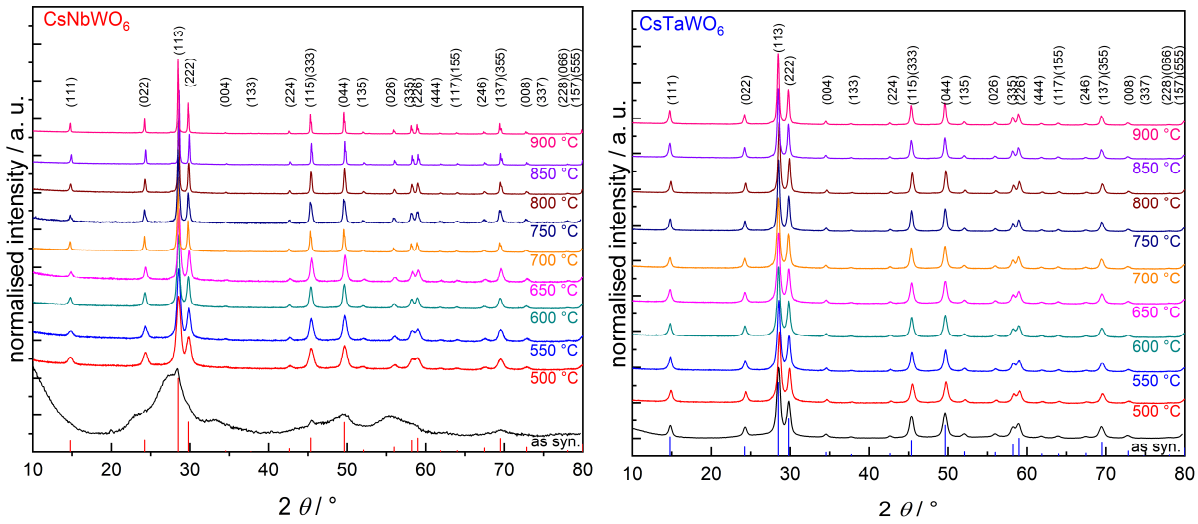

Figure 6.1: XRD patterns of $CsNbWO_6$ (left) and $CsTaWO_6$ (right). XRD patterns in this section have been normalised since calcined samples and as syn. samples have been measured with different settings, *i. e.* step size and time per step. The stated temperatures denote the calcination temperature; calcination duration was 10 h each. These are not *in-situ* XRD measurements since some samples reacted with the crucible material at higher temperatures.

All attempts to synthesise phase pure $CsVWO_6$ were unsuccessful (Figure 6.2, left). At temperatures above 800 °C the sample has been fused with the crucible; even at lower temperatures $CsVWO_6$ samples reacted with the crucible – independent of the crucible material (not shown). Attempts to synthesise $CsVWO_6$ by solid-state reaction were also unsuccessful (not shown). $CsSbWO_6$ can be obtained by solid-state reaction.[85] The sol-gel synthesis was, however, not attempted herein since antimony(V) oxide Sb_2O_5 is insoluble in water and antimony(V) chloride $SbCl_5$ decomposes upon heating.

6.1.2 M^{n+} cations with oxidation state +IV

$CsTi_{0.5}W_{1.5}O_6$ can be obtained phase pure starting from titanium(IV) n-propoxide $Ti(O^nPr)_4$ and is stable in the entire temperature range (Figure 6.2, right).

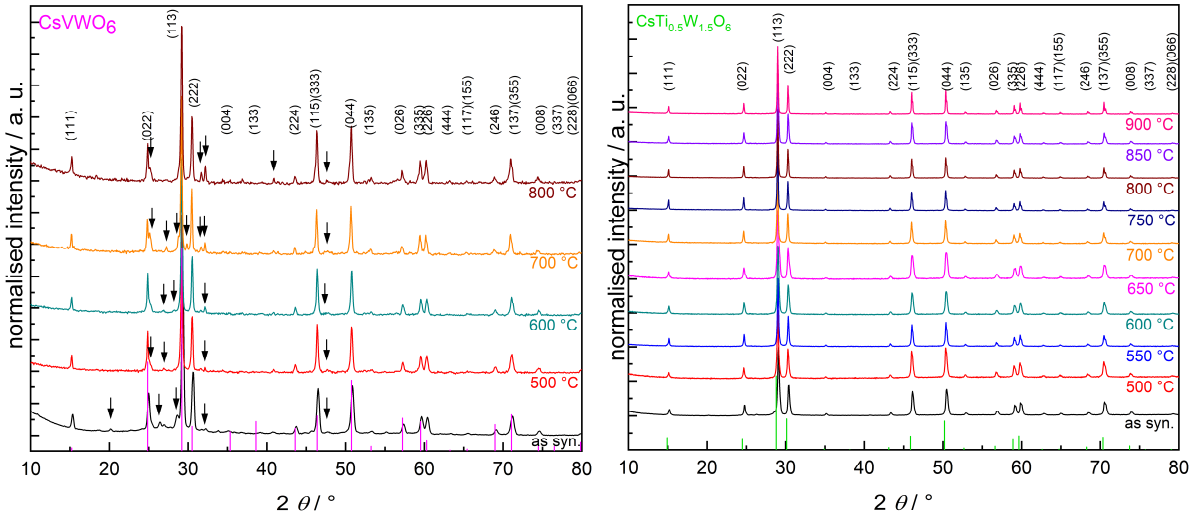

Figure 6.2: XRD patterns of $CsVWO_6$ (left) and $CsTi_{0.5}W_{1.5}O_6$ (right) calcined at different temperatures. Reflections belonging to impurities are marked with arrows.

On the other hand, $CsZr_{0.5}W_{1.5}O_6$ and $CsHf_{0.5}W_{1.5}O_6$ decompose at 800 °C and 650 °C, respectively (Figure 6.3). In the case of $CsHf_{0.5}W_{1.5}O_6$, reflections belonging to hafnium(IV) oxide HfO_2 can be observed. The emerging impurity for $CsZr_{0.5}W_{1.5}O_6$ could not be identified.

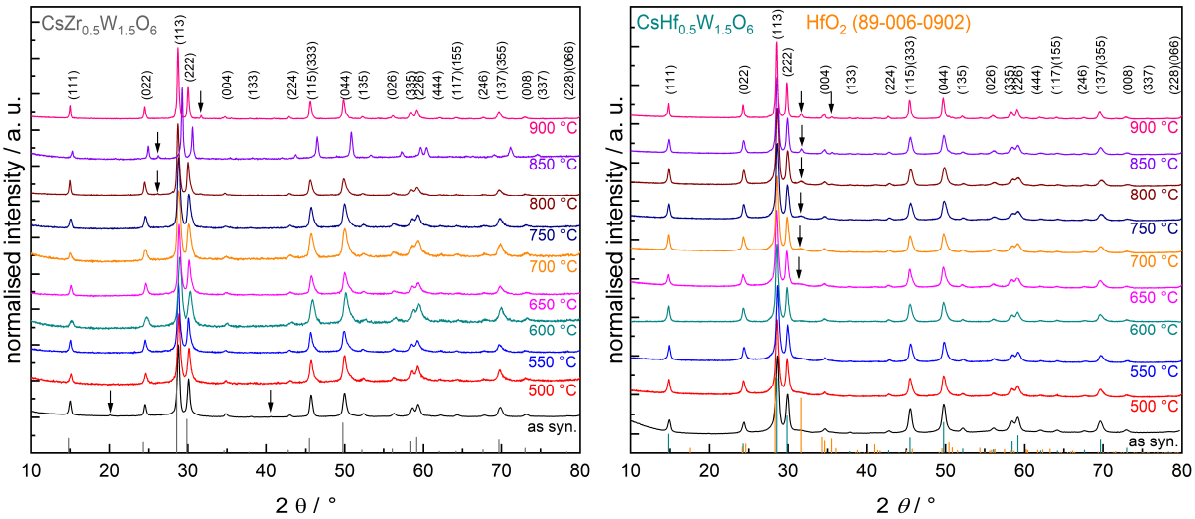

Figure 6.3: XRD patterns of $CsZr_{0.5}W_{1.5}O_6$ (left) and $CsHf_{0.5}W_{1.5}O_6$ (right) calcined at different temperatures. Reflections belonging to impurities are marked with arrows.

A similar decomposition – starting at even lower temperatures – can be observed for defect-pyrochlores with main group (+IV) cations, which are $CsGe_{0.5}W_{1.5}O_6$ and $CsSn_{0.5}W_{1.5}O_6$ (Figure 6.4). The decomposition product is in both cases the binary oxide germanium(IV) oxide GeO_2 and tin(IV) oxide SnO_2, respectively. Another, unidentified phase can be seen in the as syn. sample of $CsGe_{0.5}W_{1.5}O_6$. The only sample that shows no impurities in the XRD pattern is $CsGe_{0.5}W_{1.5}O_6$ calcined at 500 °C. However, due to the low temperature this sample still contains carbon residues and is tinged with grey (not shown).

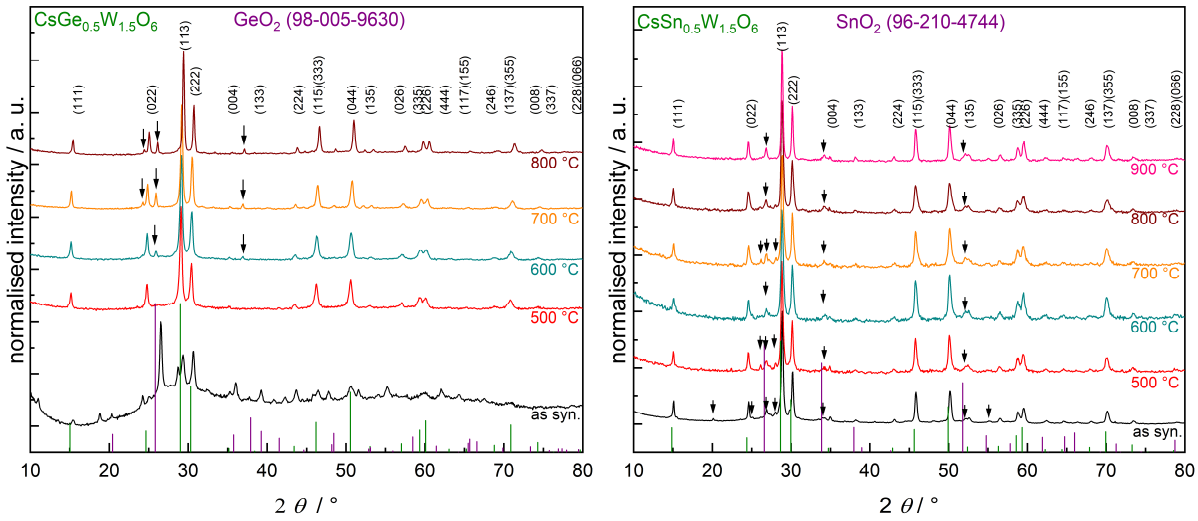

Figure 6.4: XRD patterns of $CsGe_{0.5}W_{1.5}O_6$ (left) and $CsSn_{0.5}W_{1.5}O_6$ (right) calcined at different temperatures. Reflections belonging to impurities are marked with arrows.

6.1.3 M^{n+} cations with oxidation state +III

The compounds $CsCr_{0.33}W_{1.67}O_6$ and $CsFe_{0.33}W_{1.67}O_6$ are phase pure directly after the synthesis and remain so for the entire temperature range (Figure 6.5).

This is in contrast to $CsSc_{0.33}W_{1.67}O_6$ in which an unidentified impurity phase is already present in the *as syn.* sample (Figure 6.6, left). The reflections belonging to this impurity are decreasing with increasing temperature; calcining at temperatures above 900 °C was not successful, since the sample has fused with the crucible (not shown). The reason why phase pure $CsSc_{0.33}W_{1.67}O_6$ could not be obtained is probably the larger ionic radius of Sc^{3+} with 0.745 Å as compared to W^{6+} with 0.60 Å (both values for sixfold coordination); since the $CsM_xW_{2-x}O_6$ solid solution structure requires comparatively equal ionic radii to be stable. [150]

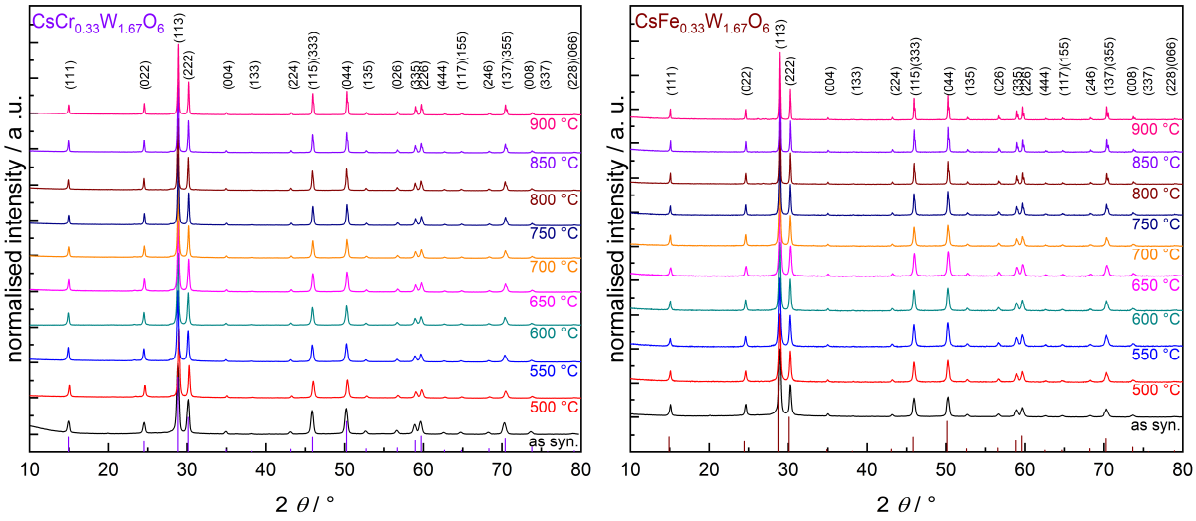

Figure 6.5: XRD patterns of $CsCr_{0.33}W_{1.67}O_6$ (left) and $CsFe_{0.33}W_{1.67}O_6$ (right) calcined at different temperatures.

Defect-pyrochlores with the hypothetical formulas $CsY_{0.33}W_{1.67}O_6$ and $CsLa_{0.33}W_{1.67}O_6$ could not be synthesised; instead only mixtures of several oxides were obtained (Figure 10.13, appendix). These defect-pyrochlores could probably not be synthesised due to the too large ionic radius of Y^{3+} with 0.900 Å and La^{3+} with 1.032 Å (both values for sixfold coordination).[150]

$CsAl_{0.33}W_{1.67}O_6$ shows an impurity phase in the *as syn.* sample, however, upon calcination this impurity phase disappears and $CsAl_{0.33}W_{1.67}O_6$ is phase pure until 900 °C (Figure 6.6, right).

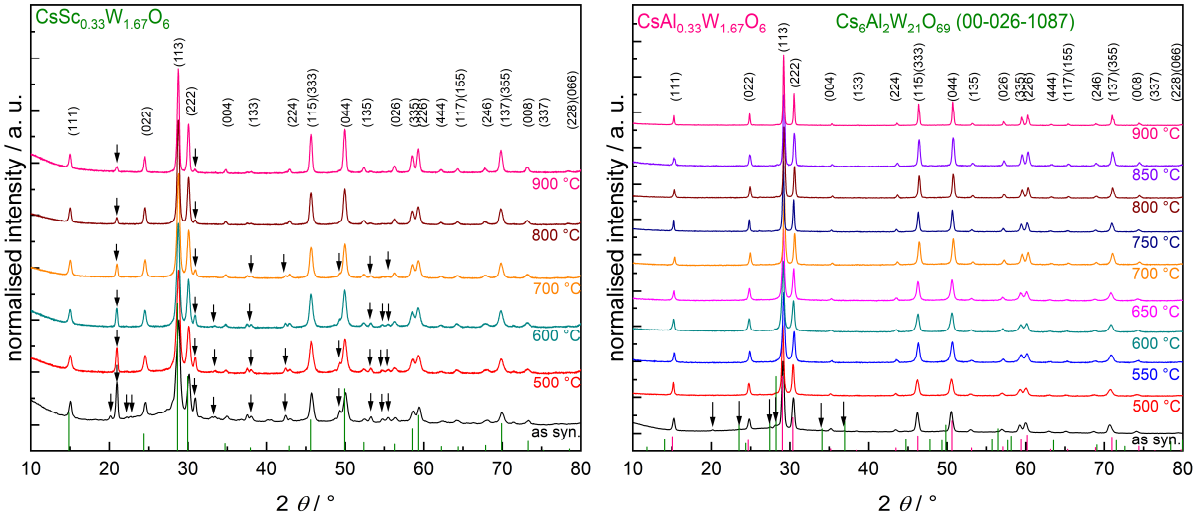

Figure 6.6: XRD patterns of $CsSc_{0.33}W_{1.67}O_6$ (left) and $CsAl_{0.33}W_{1.67}O_6$ (right) calcined at different temperatures. Reflections belonging to impurities are marked with arrows.

The same can be observed for $CsGa_{0.33}W_{1.67}O_6$; the *as syn.* sample shows an impurity phase, whereas all calcined samples are phase pure (Figure 6.7, left). All calcined samples of $CsIn_{0.33}W_{1.67}O_6$ are phase pure (Figure 6.7, right). The *as syn.* samples of most $CsM_xW_{2-x}O_6$

compounds are at least partly crystalline; however, the *as syn*. sample of $CsIn_{0.33}W_{1.67}O_6$ is fully amorphous. The reason for this could not be elucidated.

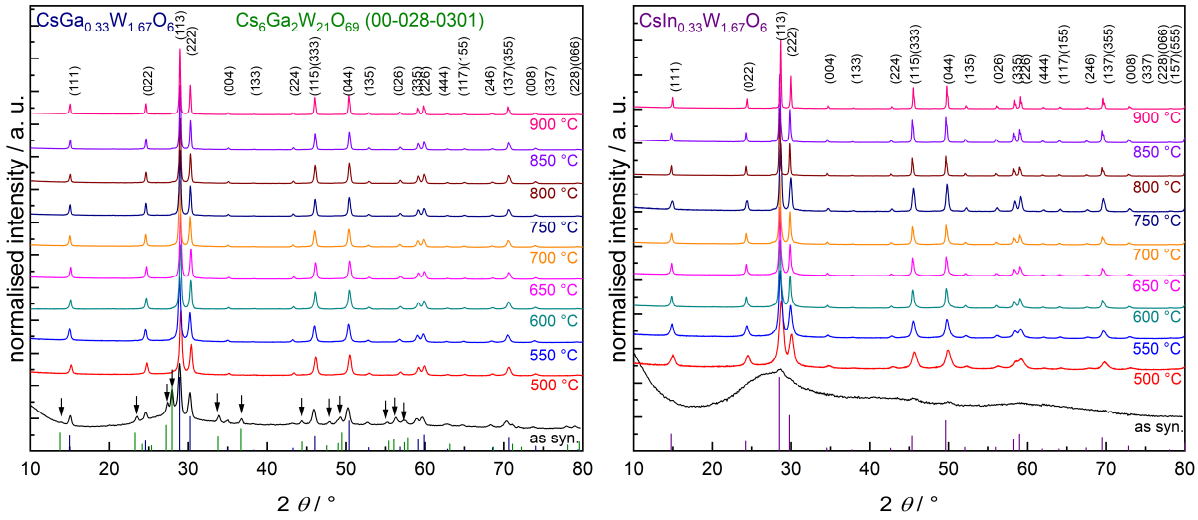

Figure 6.7: XRD patterns of $CsGa_{0.33}W_{1.67}O_6$ (left) and $CsIn_{0.33}W_{1.67}O_6$ (right) calcined at different temperatures. Reflections belonging to impurities are marked with arrows.

The XRD patterns of $CsSb_{0.33}W_{1.67}O_6$ exhibit several changes during the increase of the calcination temperature (Figure 6.8). The *as syn*. sample is largely amorphous. At temperatures above 600 °C, an impurity phase can be observed, which disappears again at a temperature of 800 °C. At 850 °C and 900 °C a second impurity phase appears. These changes are likely connected with the decomposition of antimony(III) oxide to antimony(III,V) oxide Sb_2O_4.[177]

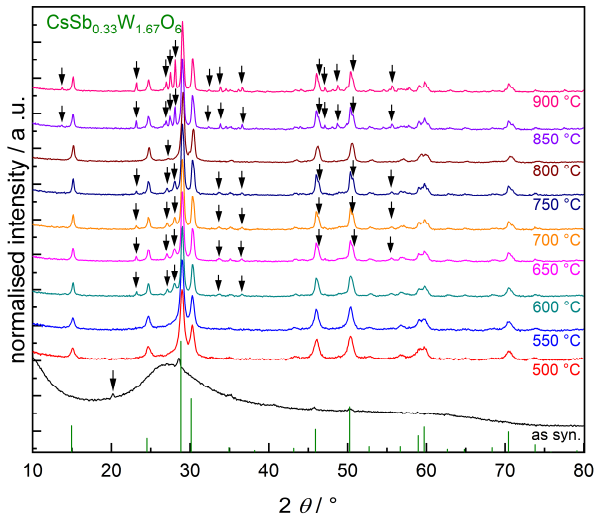

Figure 6.8: XRD pattern of $CsSb_{0.33}W_{1.67}O_6$ (right) calcined at different temperatures. Reflections belonging to impurities are marked with arrows.

The defect-pyrochlore $CsBi_{0.33}W_{1.67}O_6$ could not be synthesised; instead a mixture of oxides was obtained (Figure 10.14, appendix). The most likely reason for this may be the large size of Bi^{3+} with 1.03 Å compared to W^{6+} with 0.60 Å (both values for sixfold coordination).[150]

6.1.4 M^{n+} cations with oxidation state +II

The *as syn.* samples of $CsMg_{0.25}W_{1.75}O_6$ and $CsZn_{0.25}W_{1.75}O_6$ both show an impurity phase that disappears upon calcination (Figure 6.9). Both compounds remain phase pure in a temperature range from 500-900 °C.

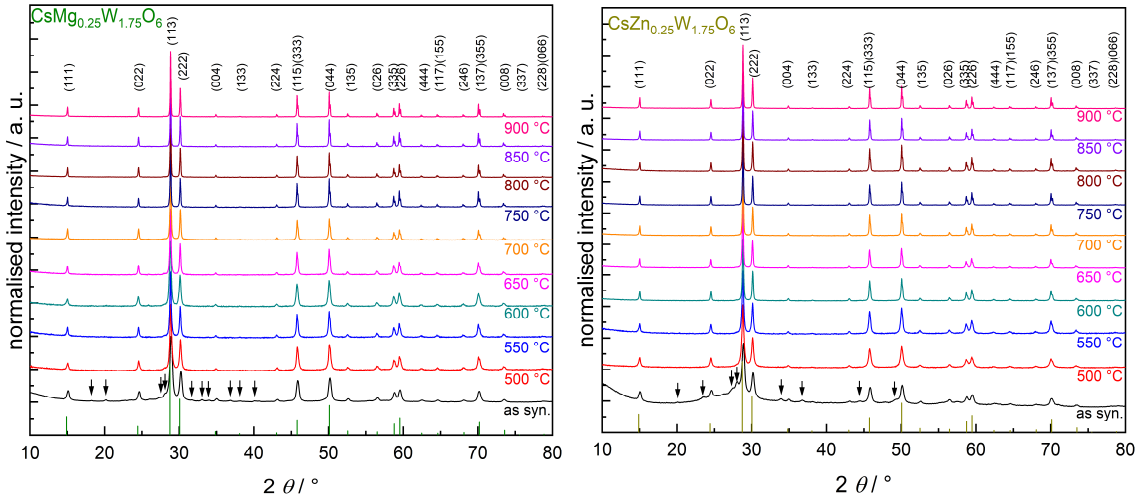

Figure 6.9: XRD patterns of $CsMg_{0.25}W_{1.75}O_6$ (left) and $CsZn_{0.25}W_{1.75}O_6$ (right) calcined at different temperatures. Reflections belonging to impurities are marked with arrows.

The same can be observed for $CsMn_{0.25}W_{1.75}O_6$ and $CsCo_{0.25}W_{1.75}O_6$ (Figure 6.10). Both *as syn.* samples show an impurity, whereas all calcined samples are phase pure.

$CsNi_{0.25}W_{1.75}O_6$ and $CsCu_{0.25}W_{1.75}O_6$ require at least 550 °C or 600 °C to become phase pure (Figure 6.11). The *as syn.* samples and samples calcined at too low temperatures show impurity phases.

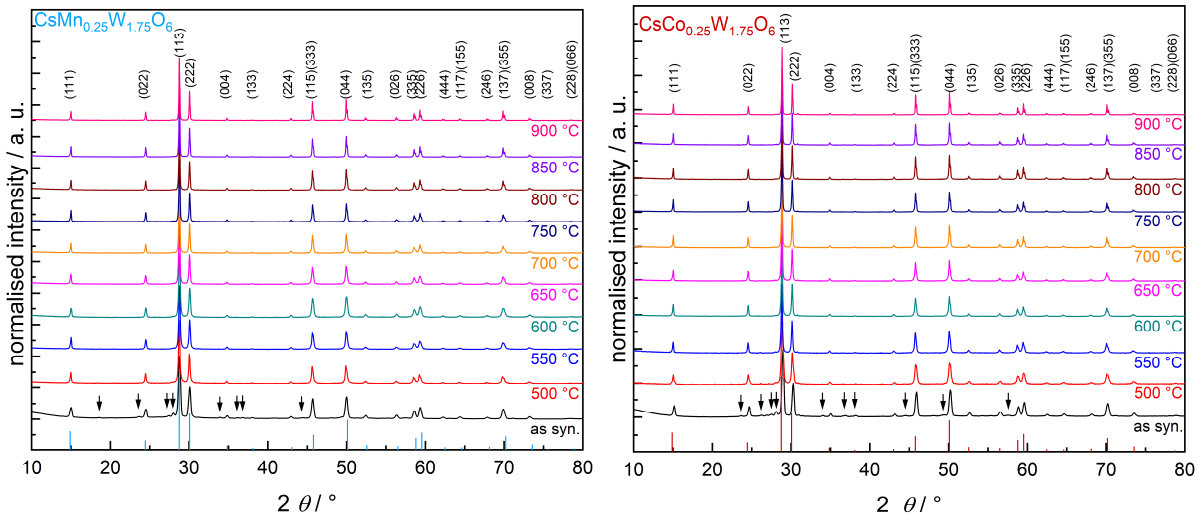

Figure 6.10: XRD patterns of $CsMn_{0.25}W_{1.75}O_6$ (left) and $CsCo_{0.25}W_{1.75}O_6$ (right) calcined at different temperatures. Reflections belonging to impurities are marked with arrows.

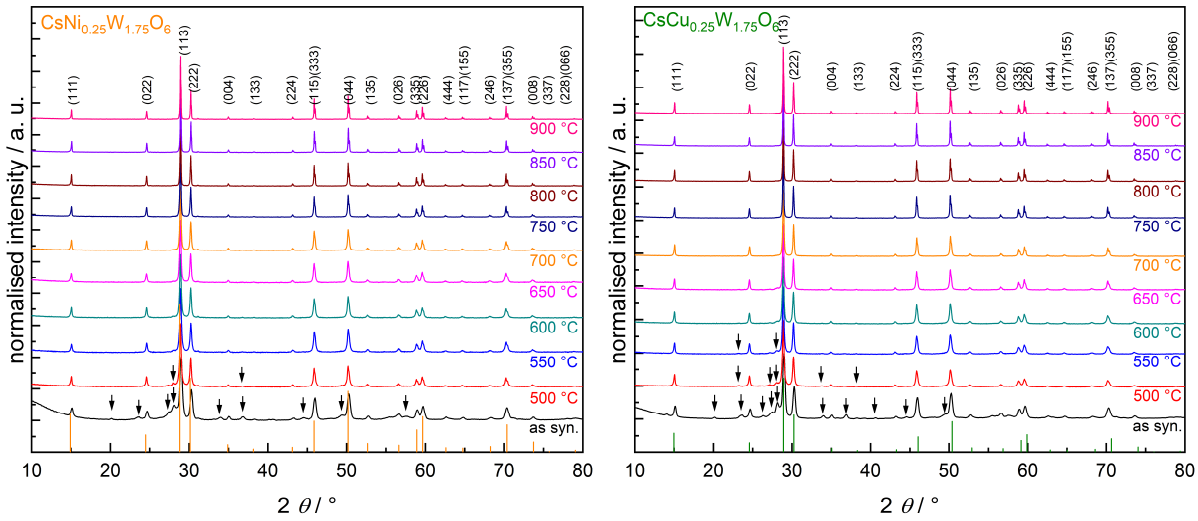

Figure 6.11: XRD patterns of $CsNi_{0.25}W_{1.75}O_6$ (left) and $CsCu_{0.25}W_{1.75}O_6$ (right) calcined at different temperatures. Reflections belonging to impurities are marked with arrows.

To summarise, 16 phase pure defect-pyrochlore tungstates with the general formula $CsM_xW_{2-x}O_6$ could be synthesised *via* an aqueous sol-gel route. The vast majority is stable up to 900 °C. The defect-pyrochlores $CsIn_{0.33}W_{1.67}O_6$ and $CsM_{0.25}W_{1.75}O_6$ (M^{n+} = Mg^{2+}, Mn^{2+}, Co^{+}, Ni^{2+}; Cu^{2+} and Zn^{2+}) have been synthesised for the first time ever. Five defect-pyrochlores with impurities could also be synthesised. If the M^{n+} cation is too large obtaining the defect-pyrochlore structure is not possible anymore. An overview of all possible $CsM_xW_{2-x}O_6$ defect-pyrochlores can be seen in Figure 6.12.

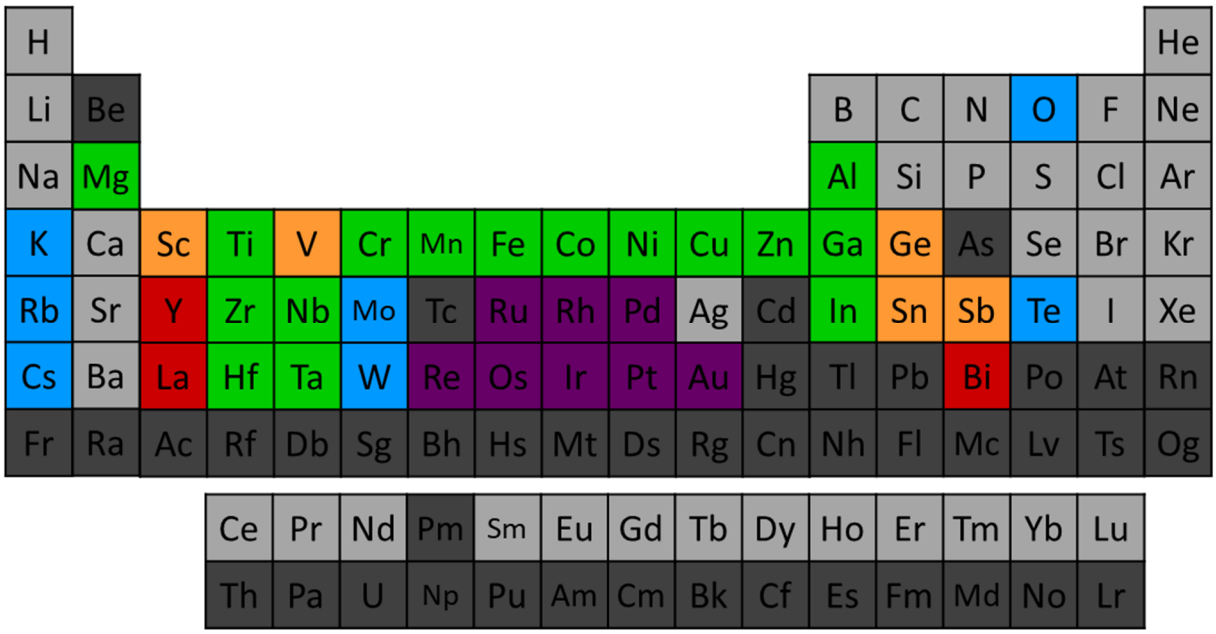

Figure 6.12: Periodic table depicting the possible elemental compositions of $CsM_xW_{2-x}O_6$ defect-pyrochlores. Green: phase pure defect-pyrochlores; orange: not phase pure defect-pyrochlore; red: no defect-pyrochlore could be synthesised; blue: structure components of defect-pyrochlores; purple: not attempted due to scarcity; light grey: not attempted due to incompatible ionic radius or chemistry; dark grey: not attempted due to toxicity and/or radioactivity.

6.2 In-Depth Structural Characterisation

For a more profound investigation regarding possible changes of the crystal structure with changing M^{n+} cations, Rietveld refinements of all phase pure $CsM_xW_{2-x}O_6$ compounds were performed (Figure 10.15 and Figure 10.16, appendix). The good agreement between calculated and measured patterns further confirms the defect-pyrochlore structure and the high crystallinity of all compounds. For a better comparison, all phase pure $CsM_xW_{2-x}O_6$ samples depicted in this section have been calcined at 800 °C for 10 h with the exception of $CsZr_{0.5}W_{1.5}O_6$ and $CsHf_{0.5}W_{1.5}O_6$, which have been calcined at 600 °C to avoid thermal composition.

A nearly linear correlation between the lattice constant and the ionic radius can be observed (Figure 6.13); an increasing size of M^{n+} results in a larger unit. A similar trend has previously been observed for the $CsM_{0.5}W_{1.5}O_6$ (M = Ti^{4+}, Zr^{4+}, Hf^{4+}) series.[11] In order to complete this correlation, the lattice constants of not phase pure $CsM_xW_{2-x}O_6$ compounds were also added; reflections belonging to impurities were excluded from the refinement if necessary (Figure 10.17, appendix)

However, this nearly linear trend has three exceptions: the lattice constant of $CsSb_{0.33}W_{1.67}O_6$ is nearly 0.1 Å smaller than that of $CsSc_{0.33}W_{1.67}O_6$, although the ionic radii of Sc^{3+} with 0.745 Å and Sb^{3+} with 0.76 Å are very similar.[150] The reason is probably the lone electron pair of Sb^{3+}. On the other hand, the lattice constants of $CsNbWO_6$ and $CsTaWO_6$ are comparatively large. The lattice constant of $KNbWO_6$ is even larger with 10.5068 Å, which has been ascribed to the presence of water molecules.[87] However, $CsTaWO_6$ does not incorporate water molecules (see section 5.1).

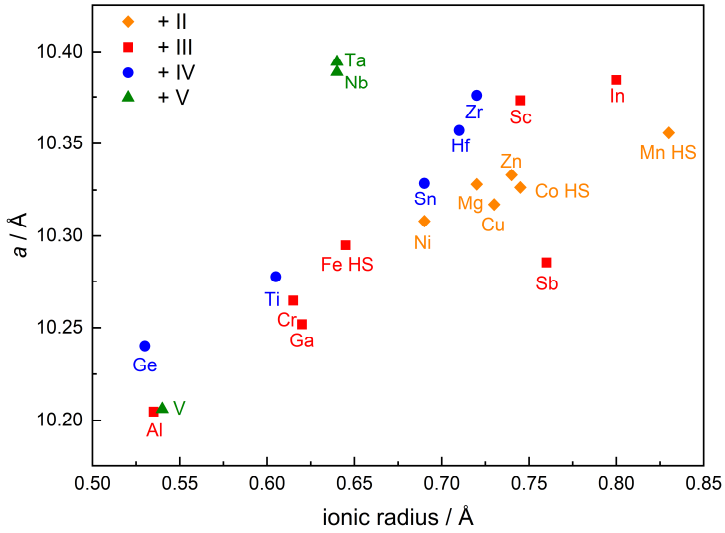

Figure 6.13: Correlation between lattice constant *a* and ionic radius. All ionic radii were taken from Shannon *et al.*[150] HS: high-spin

The above correlation is complicated by the fact that some M^{n+} cations – Mn^{2+}, Fe^{3+} and Co^{2+} – can exist in a high-spin and low-spin coordination, which changes the ionic radius. In order to ascertain the spin state, magnetic measurements have been performed.

SQUID measurements of $CsFe_{0.33}W_{1.67}O_6$ and $CsCo_{0.25}W_{1.75}O_6$ show a diamagnetic shape (Figure 6.14). Effective magnetic moments μ_{eff} were calculated with the molar mass of the entire unit cell, which consists of eight formula units. For $CsFe_{0.33}W_{1.67}O_6$ – which consists of unit cells with either two or three Fe atoms – calculations were performed with three Fe atoms per unit cell. For $CsFe_{0.33}W_{1.67}O_6$ the measured values match well with the estimated spin only value for high-spin d^5. $CsCo_{0.25}W_{1.75}O_6$ also confirms well for a high-spin d^7 configuration if partially quenched orbital angular momenta are taken into account. However, the linear shape of $CsMn_{0.25}W_{1.75}O_6$ could indicate a small amount of a ferromagnetic impurity, which could not be observed *via* XRD or Raman-spectroscopy (Figure 6.10 and Figure 6.20). The estimated spin only value for high-spin d^5 configuration is significantly lower than the measured values at room temperature and only match well at low temperatures.

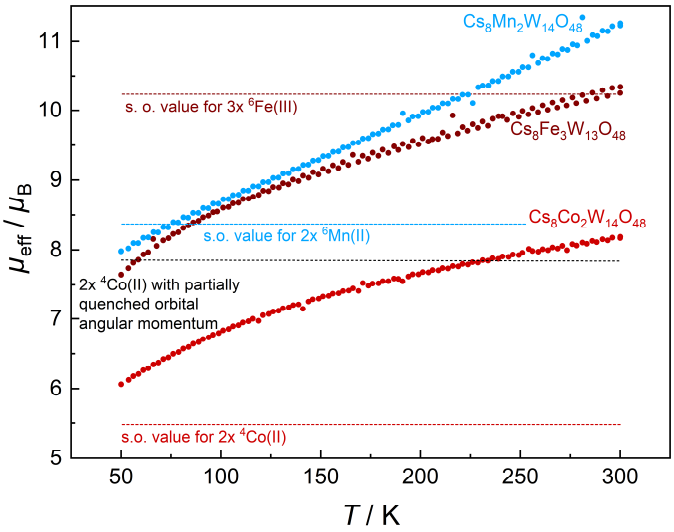

Figure 6.14: Effective magnetic moments μ_{eff} of $CsMn_{0.25}W_{1.75}O_6$, $CsFe_{0.33}W_{1.67}O_6$ and $CsCo_{0.25}W_{1.75}O_6$. Coloured dashed lines emblematise calculated spin only (s. o.) values, whereas the black value is calculated for a partially quenched orbital angular momentum, which is typical for a d^7 configuration.

The crystallite sizes of $CsM_xW_{2-x}O_6$ compounds with M^{2+} vary between 150 nm and 300 nm and are in most instances larger than for the other $CsM_xW_{2-x}O_6$ compounds (Figure 6.15, left). On the other hand $CsNbWO_6$ and especially $CsTaWO_6$ possess the smallest crystallite sizes. Overall no clear trend between crystallite size and M^{n+} can be discerned.

The strain of most samples is small with the exceptions of $CsZr_{0.5}W_{1.5}O_6$ and $CsHf_{0.5}W_{1.5}O_6$ (Figure 6.15, right). The reason for their larger strain is the lower calcination temperature, *i.e.* 600 °C instead of 800 °C.

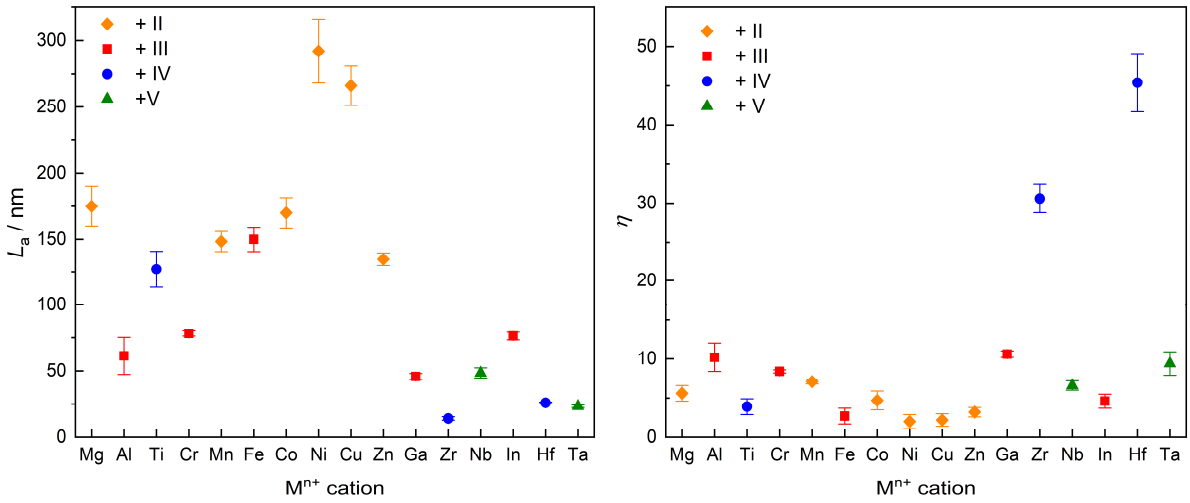

Figure 6.15: Correlation between crystallite size L_a and M^{n+} (left) and strain η and M^{n+} (right). Error bars indicate the standard deviation for all crystallographic directions and do not indicate an actual error.

At first glance the strain seems to be correlated with the ionic radius of M^{n+} (Figure 6.16, left); an increasing ionic radius of M^{n+} seems to result in a decreasing strain. However, a similar correlation can be observed between strain and crystallite size (Figure 6.16, right); smaller crystallites seem to be more strained. This could be explained by the generally higher curvature of smaller crystallites. Although both strain and crystallite size are derived from the reflection breadth, they are derived from different parts of the integral breadth (see section 4.1). To conclude, the (small) strain of the samples cannot certainly be ascribed to M^{n+}.

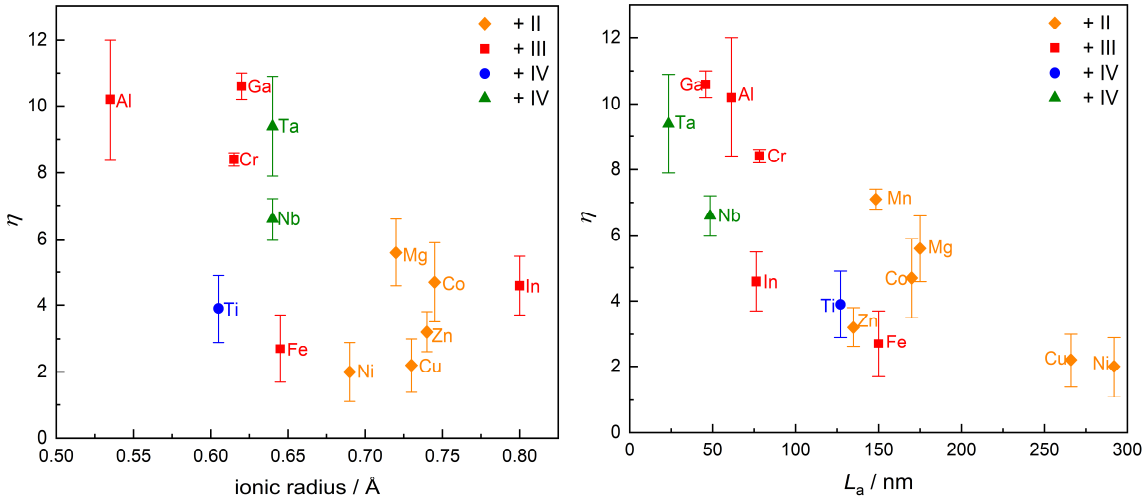

Figure 6.16: Correlation between strain η and ionic radius of M^{n+} (left) and between strain η and crystallite size L_a. Error bars indicate the standard deviation for all crystallographic directions and do not indicate an actual error. $CsZr_{0.5}W_{1.5}O_6$ and $CsHf_{0.5}W_{1.5}O_6$ have been omitted due to their different calcination temperature.

To investigate further if M^{n+} has a distorting influence on the crystal structure of $CsM_xW_{2-x}O_6$, the distance and angles of the refined structures have been evaluated. The M/W–O (centre–vertices of the octahedra) distance is fluctuating around a common value (Figure 6.17, left); the largest outlier has been found for Zr^{4+}, which can again be explained with the lower calcination temperature. The Cs–O distance is similar for most M^{n+}, but slightly increased for Nb^{5+}, In^{3+}, Hf^{4+} and Ta^{5+}. These are also the cations resulting in the largest lattice constants, thus increasing the Cs–O distance. The O–M/W–O angles (vertex–centre–vertex) are split in two due to the shift of the x-position of the oxygen atoms (Figure 6.17, right); whereas this angle of an ideal octahedra should be 90°. The magnitude of the distortion is similar for all M^{n+}, but slightly less for those four cations mentioned above.

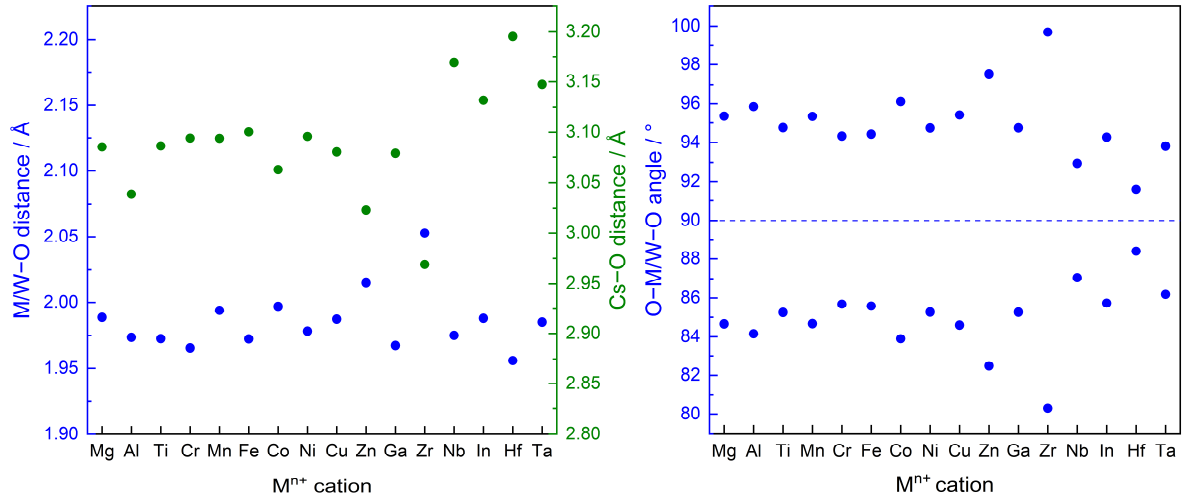

Figure 6.17: Distances (left) and angles (right) of the refined crystal structures. The dashed line emblematises the ideal angle.

Another consequence of the distortion is the occurrence of two different O–O distances within an octahedra (Figure 6.18, left); whereas the distances between the vertices of an ideal octahedra are all identical. The O–O distances and the difference between them are similar for most compounds, however, one distance is slightly increased for Nb^{5+}, In^{3+}, Hf^{4+} and Ta^{5+}. This again can be explained by the larger lattice constant, also resulting in a larger O–O distance.

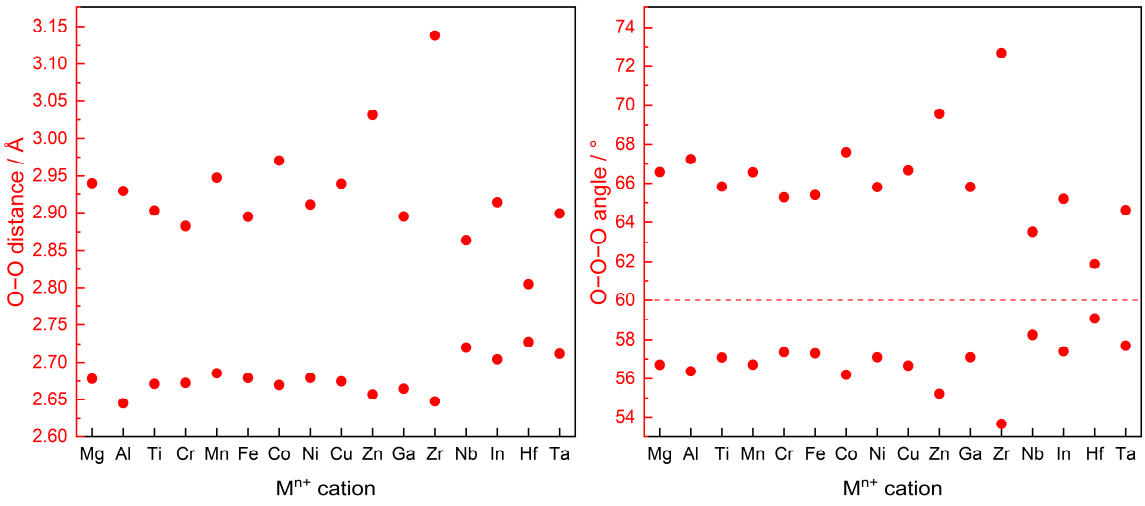

Figure 6.18: Distances (left) and angles (right) within a single octahedra of the refined crystal structures. The dashed line emblematises the ideal angle.

One distance is considerably increased for Zr^{4+}, which likely is a consequence of the lower calcination temperature; although Hf^{4+} - calcined at the same temperature – does not show an enlarged distance. The O–O–O angles (vertex–vertex–vertex) of one face are split into one dilated and two narrowed angles; the sum of all three equals 180°. The angles resulting for

most M^{n+} cations are similar with the exceptions of the five cations mentioned above (Figure 6.18, right).

Valuable insight into structural changes can also be gained from Raman spectroscopy. While most Raman bands of $CsM_xW_{2-x}O_6$ with M^{4+} and M^{5+} show only slight changes in band positions and relative intensities (Figure 6.19, left); the change of the bands between 800-1000 cm^{-1} is more pronounced. These Raman bands are stretching modes of shorter than normal M–O or W–O bonds, which are in turn caused by M^{n+} or W^{6+} vacancies in the centre of the octahedra.[153] M^{n+} (or W^{6+}) vacancies result in a rearrangement of the O^{2-} sublattice.[178] Since W^{6+} is present in all compounds, it is far more likely that the changes in the Raman modes are caused by M^{n+} vacancies. For $CsM_xW_{2-x}O_6$ with M^{2+} or M^{3+} the emergence of a third Raman band between 800-1000 cm^{-1} can be observed (Figure 6.19, right). This emergence could indicate a higher amount of vacancies resulting in a stronger rearrangement of the oxygen sublattice, which in turn results in shorter M–O or W–O bonds, whose vibration mode is the new third Raman band. Another difference can be seen in the Raman bands between 100-200 cm^{-1}; these are bending modes of the MO_6 and WO_6 octahedra coupled with the translational modes of Cs^+.[92] The intensity changes of the three Raman modes located in this region indicate that the bending of the octahedra changes with M^{n+}.

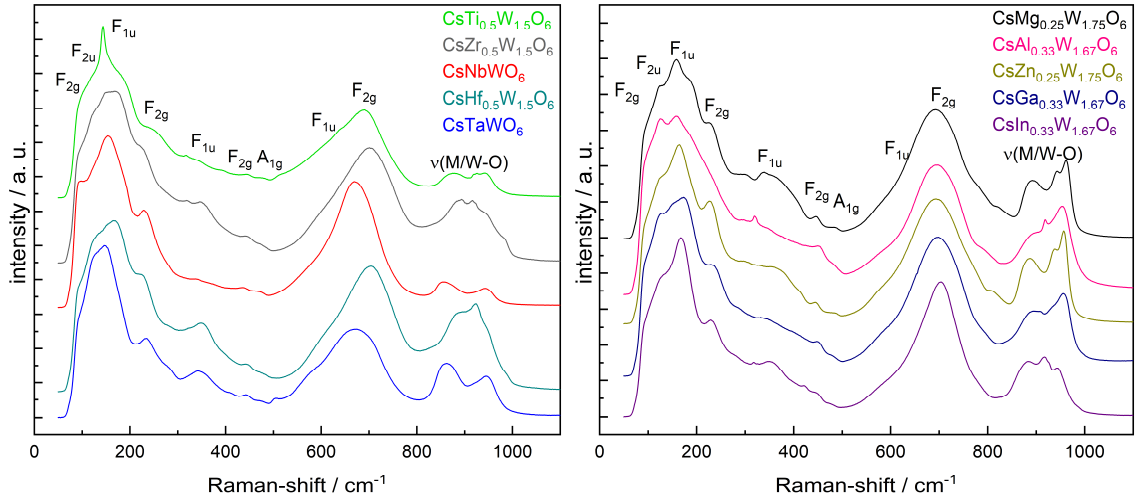

Figure 6.19: Raman spectra of $CsM_xW_{2-x}O_6$ compounds for M^{n+} with d^0 or d^{10} electron configuration.

The Raman spectra of $CsM_xW_{2-x}O_6$ compounds for M^{2+} with d^n electron configuration show some differences as compared to those with d^0 or d^{10} configuration (Figure 6.20). The Raman bands between 800-1000 cm^{-1} are increased, whereas the other Raman bands are broadening. This suggests a higher amount of vacancies and that the stretching and bending modes become less distinct.

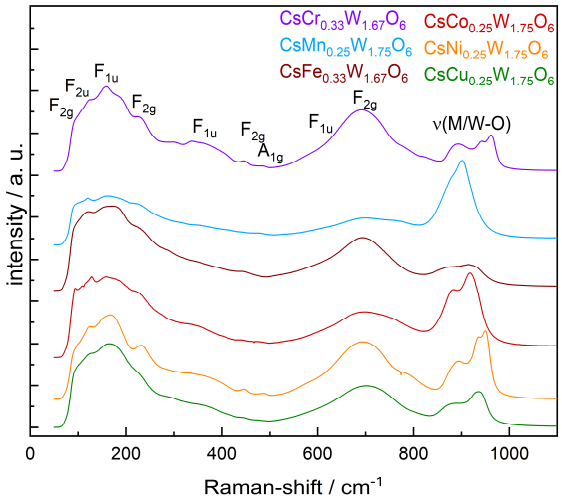

Figure 6.20: Raman spectra of $CsM_xW_{2-x}O_6$ compounds for M^{n+} with d^n electron configuration.

EDX spectroscopy measurements have been used to investigate the ratio of M/W. The measured ratio deviates somewhat from the theoretical values (Figure 6.21, left); however, the measured values lie below and above the theoretical values. Therefore no systematic deviation exists. By far the largest aberration is visible for Ta^{5+}, but Ta and W are adjacent elements in the periodic table and the X-ray lines are highly similar.[156] Combined with the relatively poor energy resolution of EDX spectroscopy this results in a large measurement error and explains the aberration. These measurements are additionally hindered by the low amount of M^{2+} and M^{3+} – corresponding to 2.8 at% and 3.7 at%, respectively – resulting in a larger error. The ratio of M/W depends on the oxidation state of M^{n+} (Figure 6.21, right); a lower oxidation state requires fewer M^{n+} and more W^{6+} atoms in the unit cell to retain charge neutrality.

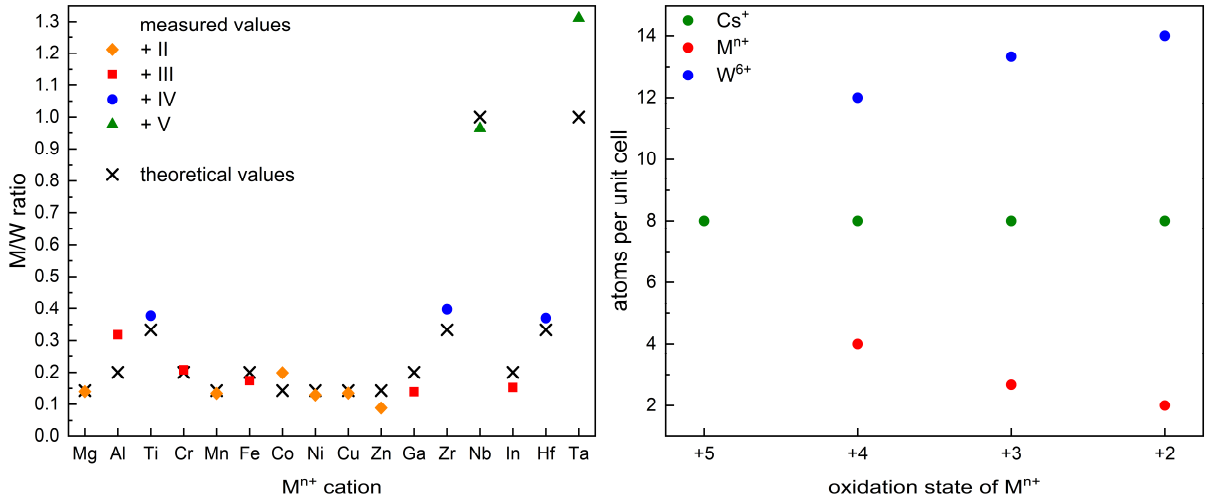

Figure 6.21: Ratio of M/W as measured by EDX spectroscopy for all $CsM_xW_{2-x}O_6$ compounds (left) and theoretical number of atoms per unit cell (right); the number of oxygen atoms – with constant 48 atoms per unit cell – is not depicted. Black crosses indicate theoretical values, coloured symbols denote measured values.

To summarise, the lattice constant of $CsM_xW_{2-x}O_6$ depends nearly linear on the ionic radius of M^{n+}. However, the ionic radius of M^{n+} does not seem to cause any strain on the different $CsM_xW_{2-x}O_6$ compounds. Additionally, the crystallite size is only marginally influenced by M^{n+}. While the octahedra in all $CsM_xW_{2-x}O_6$ compounds are distorted, the magnitude of the distortion is highly similar for all M^{n+}. Raman spectra indicate that $CsM_xW_{2-x}O_6$ compounds (M = Mn^{2+}, Co^{2+}, Ni^{2+} and Cu^{2+}) feature a higher amount of vacancies in the centre of the octahedra.

6.3 Morphological Characterisation

All samples show an inhomogeneous morphology (Figure 6.22; for SEM images of other samples see Figure 10.18 through Figure 10.21, appendix). Most samples consist of a mixture of well-formed octahedrally-shaped particles with a smooth surface and more irregular formed particles. The octahedrally-shaped particles exhibit edge lengths up to several hundred nm, whereas the irregularly formed particles are notably smaller. The overall morphology consists of large pores due to evolution of gases during the combustion reaction between nitrates and citric acid/EDTA.

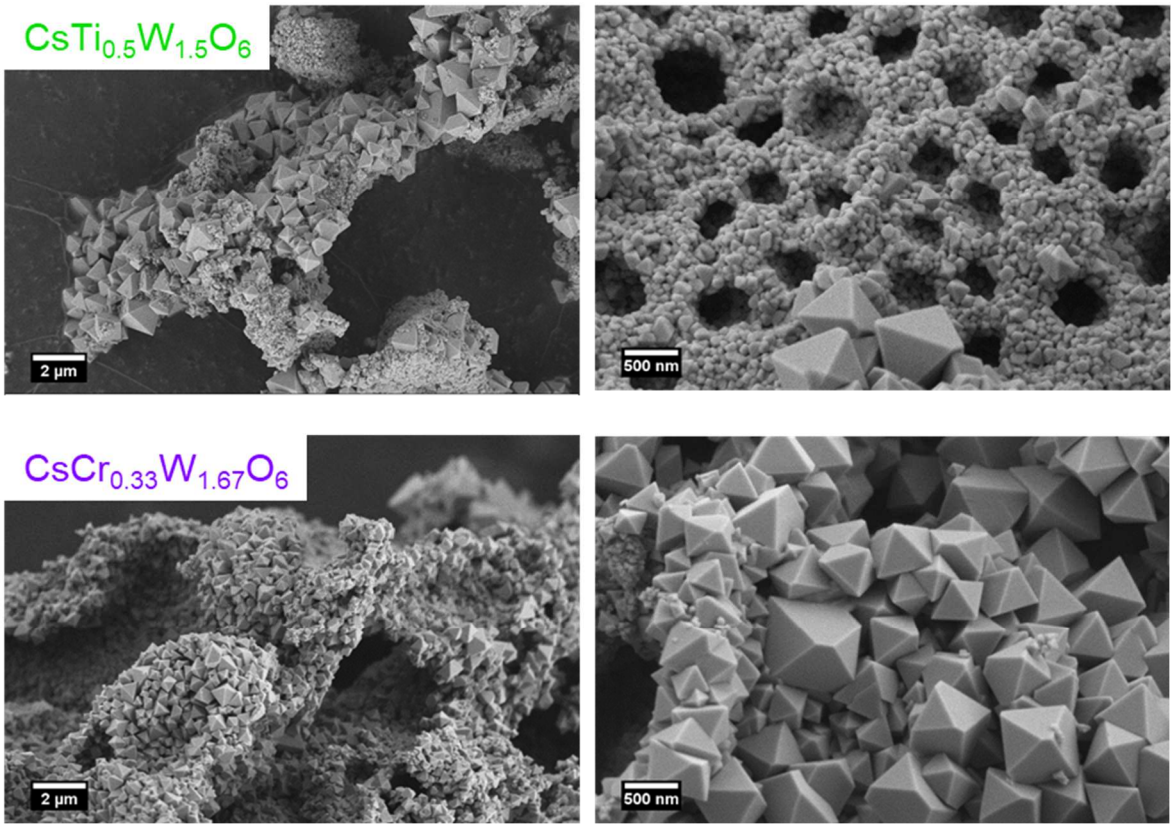

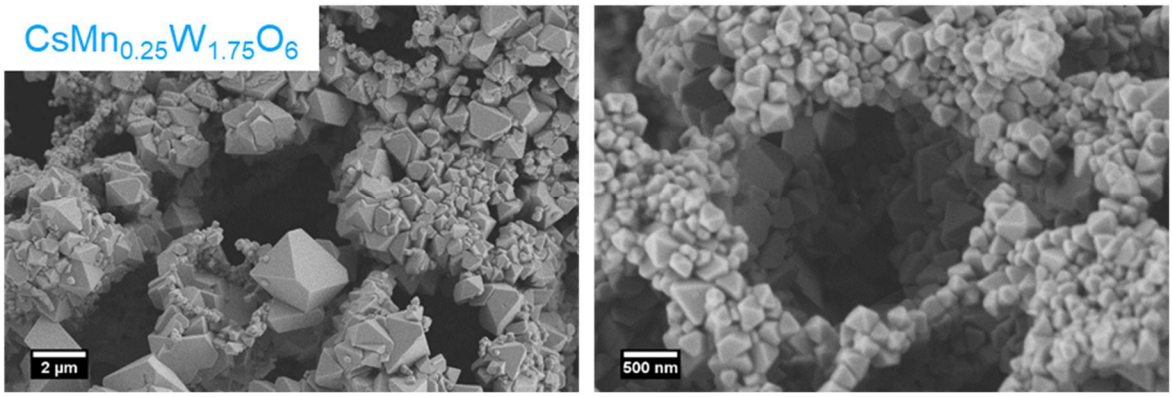

Figure 6.22: SEM images for selected $CsM_xW_{2-x}O_6$ samples.

A closer look at the octahedrally-shaped particles reveals a deviance from the ideal octahedral shape: the faces of these pseudo-octahedra are not all equilateral triangles (Figure 6.23). Whereas two opposing faces are triangles, the two faces between those can be considered as truncated triangles. The overall shape of the particles could be considered as truncated octahedra. However, non-truncated octahedrally-shaped particles can also be observed.

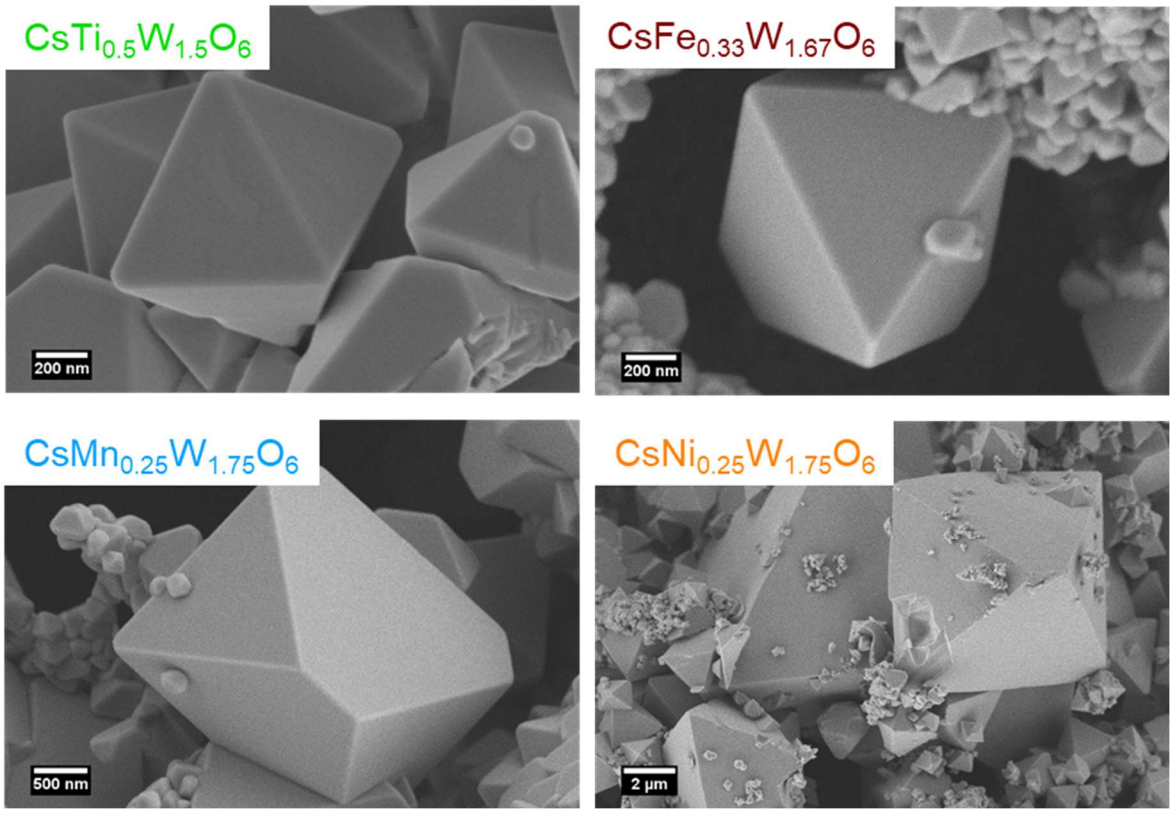

Figure 6.23: SEM particles of single particles of selected $CsM_xW_{2-x}O_6$ samples.

The BET surface areas have been determined by krypton physisorption and are between 1-2.5 $m^2\ g^{-1}$ for most samples (Figure 6.24). The surface areas for $CsM_xW_{2-x}O_6$ with M = Co^{2+} and Ni^{2+} are smaller – approximately 0.5 $m^2\ g^{-1}$ – but these two samples also exhibit the largest crystallite sizes between 250-300 nm and the largest particle sizes (Figure 6.15, left and Figure 10.20, appendix). On the other hand, $CsM_xW_{2-x}O_6$ with M = Nb^{5+}, Hf^{4+} and Ta^{4+} do not only consist of the smallest crystallites with sizes below 50 nm (Figure 6.15, left), SEM images also show that these samples exhibit the smallest particle sizes (Figure 10.18, appendix).

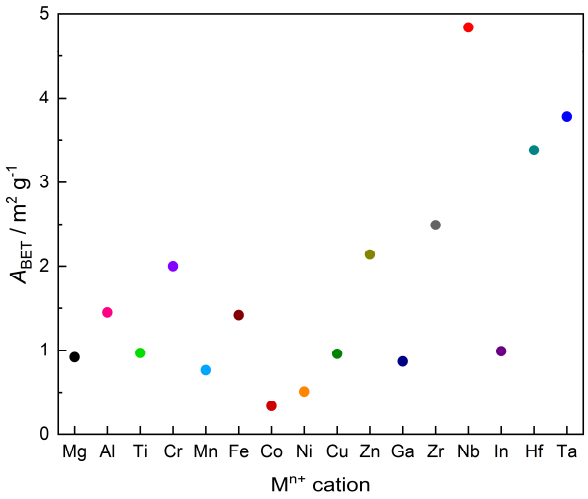

Figure 6.24: BET surface areas of $CsM_xW_{2-x}O_6$ samples.

To summarise, particle shapes and sizes are inhomogeneous: large, truncated octahedrally-shaped particles are mixed with smaller, irregular formed particles. The BET surface area of most samples is between 1-2.5 $m^2\ g^{-1}$.

6.4 Optical and Electronic Properties

The optical bandgap of all $CsM_xW_{2-x}O_6$ compounds in which M^{n+} has either a d^0 or a d^{10} electron configuration is 3.5 ± 0.1 eV (Figure 6.25); the deviation of 0.1 eV is within the experimental error. All compounds are white. This indicates that the transition from O 2*p* to W 5*d* is not affected by M^{n+} and that the CB minimum consists solely of W states.

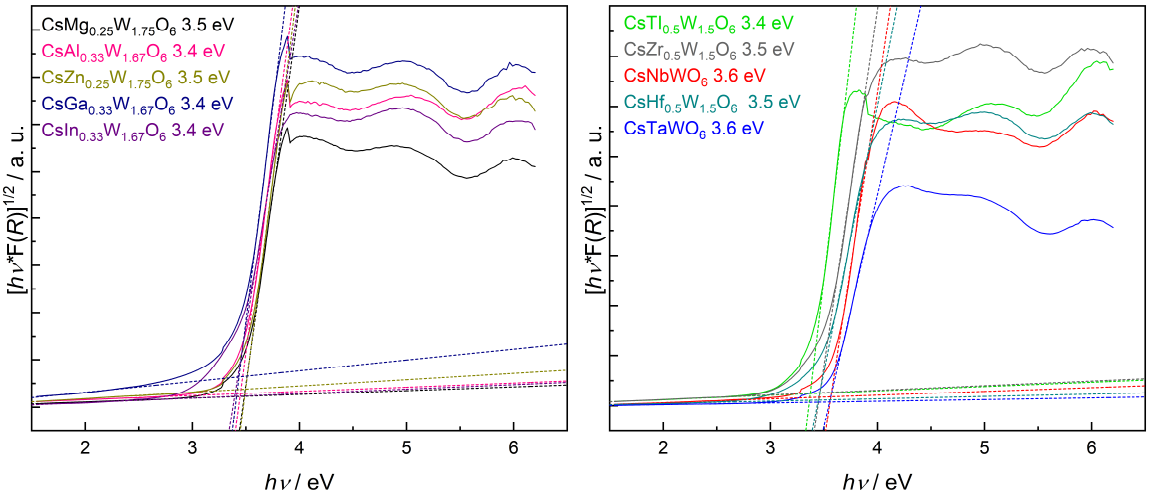

Figure 6.25: Tauc plots of $CsM_xW_{2-x}O_6$ for M^{n+} cations with d^0 or d^{10} electron configuration.

In contrast to that are the Tauc plots of $CsM_xW_{2-x}O_6$ in which M^{n+} has a d^n electron configuration, *i. e.* M^{n+} with partially filled *d* states (Figure 6.26, left). The determined bandgaps lie between 1.9 eV and 2.9 eV. The M^{n+} 3*d* states are either located above the O 2*p* levels and therefore raising the VB maximum or underneath the W 5*d* levels lowering the CB minimum. Besides the absorption edge most spectra exhibit discrete but broad absorption bands (Figure 6.26, right). These bands can be ascribed to *d*–*d* transitions of partially filled *d* states.[20] $CsMn_{0.25}W_{1.75}O_6$ is the only compound that does not exhibit these transitions; due to the d^5 high-spin configuration *d*–*d* transitions are spin forbidden.[20]

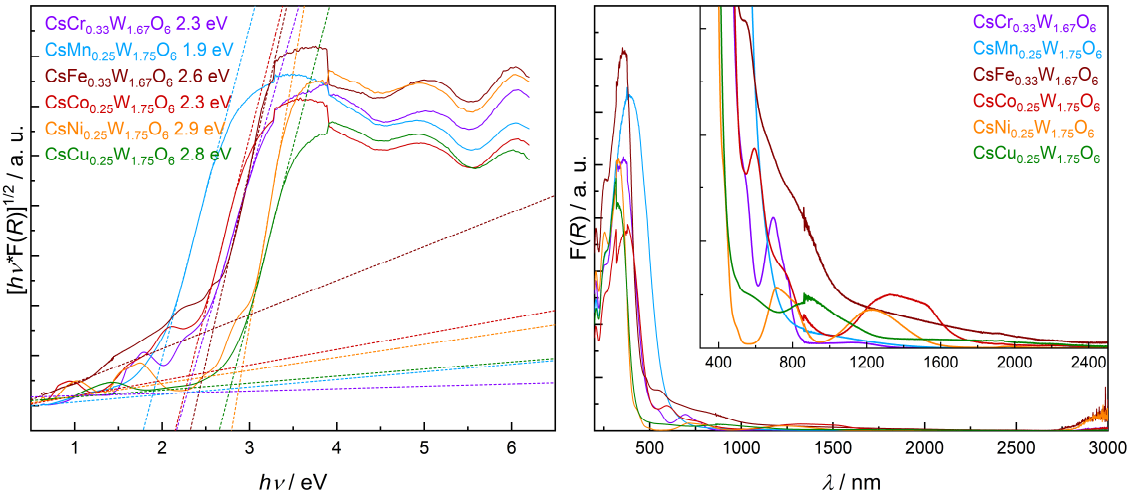

Figure 6.26: Tauc plots (left) and Kubelka-Munk absorption spectra (right) of $CsM_xW_{2-x}O_6$ for M^{n+} cations with d^n electron configuration.

The actual colours of the samples result from a combination of absorption edge and *d*–*d* transitions: $CsCr_{0.33}W_{1.67}O_6$ is light brown, $CsMn_{0.25}W_{1.75}O_6$ is dark red, $CsFe_{0.33}W_{1.67}O_6$ is greyish-

green, $CsCo_{0.25}W_{1.75}O_6$ is dark green, $CsNi_{0.25}W_{1.75}O_6$ is light yellow and $CsCu_{0.25}W_{1.75}O_6$ is green-greyish (Figure 6.27).

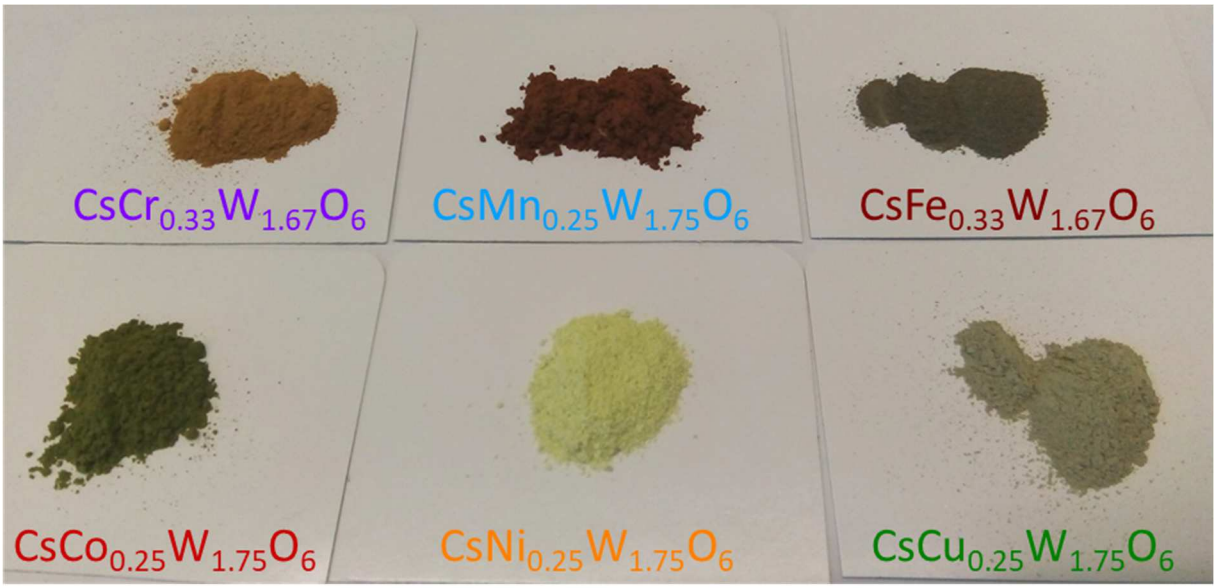

Figure 6.27: Picture of $CsM_xW_{2-x}O_6$ samples for M^{n+} cations with d^n electron configuration.

The flat band potentials have been estimated *via* Mott-Schottky analysis. The most Mott-Schottky plots of $CsM_xW_{2-x}O_6$ for M^{n+} with d^0 or d^{10} electron configuration are very similar (Figure 6.28). Not only is C^{-2} similar for most samples, but the slopes of the fitted lines are nearly identical. This indicates that the charge carrier density of these samples is also nearly identical – assuming that the relative permittivity and the exposed surface areas are also equal for all compounds. Most curves also show an aberration from the linear shape in the form of a downward bulge at 0.2 V, which could be surface states or an artefact from the electrode preparation by spray coating.

The estimated flat band potentials range between −0.5 V and −1.0 V (vs. RHE, pH 0); the flat band potentials for $CsNbWO_6$ and $CsTaWO_6$ fit with those reported in the literature.[16,112]

These results are supported by UV/vis measurements: since the crystal structure is identical for all compounds, the VB – consisting of O 2*p* states – should be located at the same potential. In combination with the identical bandgaps it can be concluded that the CB of all compounds is also located at nearly identical positions.

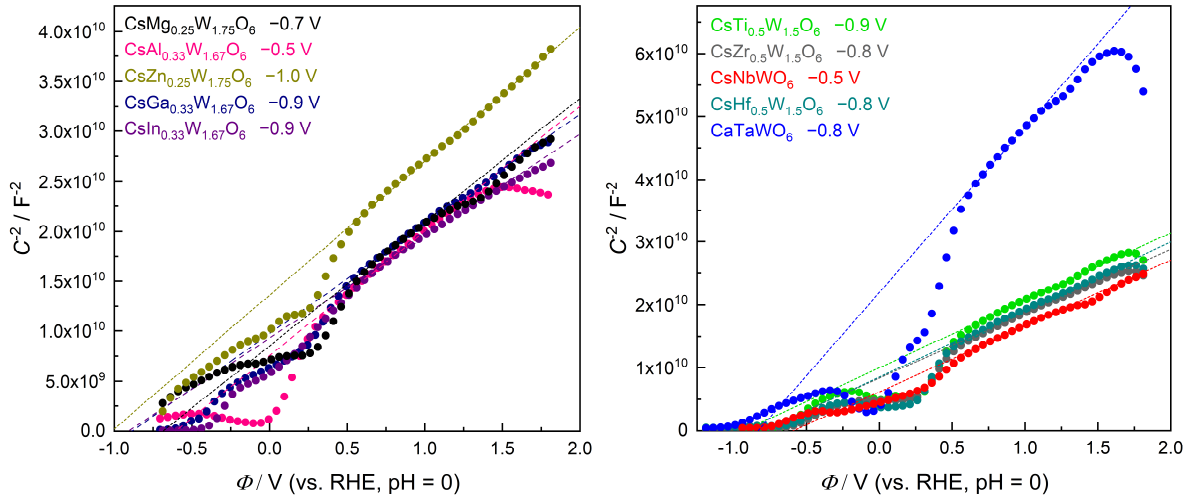

Figure 6.28: Mott-Schottky plots of $CsM_xW_{2-x}O_6$ for M^{n+} cations with d^0 or d^{10} electron configuration. Measurements were conducted in 0.1 mol L^{-1} Na_2SO_4 solution at pH 5.2 and at 1000 Hz.

The flat band potentials of $CsM_xW_{2-x}O_6$ with M^{n+} = Cr^{3+}, Fe^{3+}; Ni^{2+} and Cu^{2+} are in the same range as for the compounds depicted above (Figure 6.29, left). Sacrificial hydrogen evolution in solar light has been reported for $KFe_{0.33}W_{1.67}O_6$, indicating that the flat band potential of $CsFe_{0.33}W_{1.67}O_6$ is more negative than the potential for hydrogen evolution.[179] Only for M^{n+} = Mn^{2+} and Co^{2+} – which are also the compounds with the smallest bandgaps – the flat band potential is located at –0.2 V and –0.3 V, respectively. However, the Mott-Schottky plots of $CsMn_{0.25}W_{1.75}O_6$ and $CsCo_{0.25}W_{1.75}O_6$ are only linear in a relative small range compared to the other compounds, which makes determination of the flat band potential problematic.

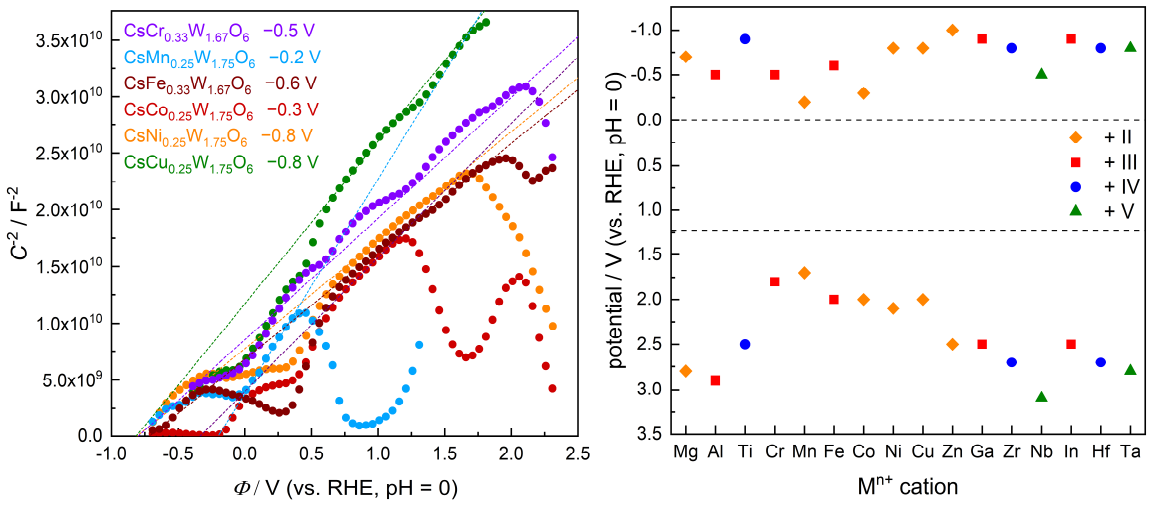

Figure 6.29: Mott-Schottky plots of $CsM_xW_{2-x}O_6$ for M^{n+} cations with d^n electron configuration (left) and overview of estimated band positions (right). Measurements for Mott-Schottky analysis were conducted in aqueous 0.1 mol L^{-1} Na_2SO_4 solution at pH 5.2 and at 1000 Hz.

Other methods to determine the flat band potential exist, however, these are based on photocurrents.[180] Measured photocurrents were below 1 µA – even with sodium sulphite Na_2SO_3 as sacrificial agent in the degassed electrolyte –, which is too small for a reasonable analysis.

The measured flat band potentials and bandgaps can be used to estimate the CB minimum and the VB maximum (Figure 6.29, right). All compounds should theoretically be suitable for photocatalytic water splitting, although the available overpotential for M^{n+} with d^n configuration is diminished. For $CsM_xW_{2-x}O_6$ with M^{n+} with d^0 or d^{10} electron configuration these values are highly similar, whereas a d^n electron configuration results in a less positive VB maximum. Since the crystal structure does not change, the potential of the O 2*p* states should also not have changed. The change of the VB originates thus more likely from the introduction of the partially occupied M 3*d* states; the transition from valence to conduction band would then be from M 3*d* to W 5*d*, which could drastically change the lifetime of photogenerated charge carriers. The kind of transition – direct or indirect – could also have changed.

The conclusion that the partially filled M 3*d* states are located above the O 2*p* states and thus result in a lowered bandgap are supported by calculations for MWO_4 (M = Mg^{2+}, Mn^{2+} and Zn^{2+}) with wolframite structure.[20] The Mn 3*d* states of $MnWO_4$ are located above the O 2*p* states and the energy difference between the Mn 3*d* and the W 5*d* states is 2.4 eV, which corresponds well with the measured bandgap of 2.72 eV. Moreover, the calculated energy difference between O 2*p* and W 5*d* states in $MnWO_4$ is 3.7 eV and highly similar to the measured bandgaps of 3.95 eV and 4.06 eV for $ZnWO_4$ and $MgWO_4$, respectively.

These calculations are supported by optical and ultraviolet photoelectron spectroscopy (UPS) measurements on MWO_4 (M = Mn^{2+}, Fe^{2+} and Ni^{2+}) single crystals.[181] The O 2*p* and M 3*d* states are hybridised in the VB, wherein the M 3*d* states form the VB maximum. On the other hand the CB minimum is composed of empty M 3*d* states in $NiWO_4$, but empty M 4*s* states in $FeWO_4$ and $MnWO_4$.

To summarise, optical and electronic properties depend on the electron configuration of M^{n+}. A d^0 or d^{10} electron configuration results in a bandgap of 3.5 ± 0.1 eV; the flat band potential is between −0.5 V and −1.0 V. If M^{n+} has partially filled d^n states, the bandgaps are between 1.9 eV and 2.9 eV and *d*–*d* transitions are visible at higher wavelengths. This bandgap reduction likely originates from the incorporation of M 3*d* states, which result in a raised VB maximum.

An overview of important material parameters – encompassing this and the two previous sections – is depicted in Table 6.1.

Table 6.1: Overview of important material parameters for $CsM_xW_{2-x}O_6$.

M^{n+}	a / Å	L_a / nm	η	A_{Bet} / $m^2\ g^{-1}$	E_g / eV	ϕ_{FB} / V
Mg^{2+}	10.3281 ± 0.0001	175 ± 15	5.6 ± 1.0	0.9	3.5	–0.7
Al^{3+}	10.2046 ± 0.0002	61 ± 14	10.2 ± 1.8	1.5	3.4	–0.5
Ti^{4+}	10.2775 ± 0.0001	127 ± 14	3.9 ± 1.0	1.0	3.4	–0.9
Cr^{3+}	10.2649 ± 0.0001	78 ± 2	8.4 ± 0.2	2.0	2.3	–0.5
Mn^{2+}	10.3560 ± 0.0001	148 ± 8	7.1 ± 0.3	0.8	2.0	–0.2
Fe^{3+}	10.2949 ± 0.0001	150 ± 9	2.7 ± 1.0	1.4	2.7	–0.6
Co^{2+}	10.3264 ± 0.0001	170 ± 11	4.7 ± 1.2	0.3	2.3	–0.3
Ni^{2+}	10.3081 ± 0.0001	292 ± 24	2.0 ± 0.9	0.5	2.9	–0.8
Cu^{2+}	10.3169 ± 0.0001	266 ± 15	2.2 ± 0.8	1.0	2.8	–0.8
Zn^{2+}	10.3331 ± 0.0001	135 ± 5	3.2 ± 0.6	2.1	3.5	–1.0
Ga^{3+}	10.25118 ± 0.0001	46 ± 2	10.6 ± 0.4	0.9	3.4	–0.9
Zr^{4+}	10.3758 ± 0.0006	14 ± 1	30.6 ± 1.8	2.5	3.5	–0.8
Nb^{5+}	10.3889 ± 0.0001	49 ± 4	6.6 ± 0.6	4.8	3.6	–0.5
In^{3+}	10.3846 ± 0.0001	76 ± 3	4.6 ± 0.9	1.0	3.4	–0.9
Hf^{4+}	10.3573 ± 0.0003	26 ± 1	45.4 ± 3.7	3.4	3.5	–0.8
Ta^{5+}	10.3945 ± 0.0001	23 ± 1	9.4 ± 1.5	3.8	3.6	–0.8

6.5 Photocatalytic Activity

The photocatalytic activity of $CsM_xW_{2-x}O_6$ for M^{n+} with d^0 or d^{10} electron configuration was evaluated by sacrificial hydrogen evolution under UV light irradiation (Figure 6.30). $CsNi_{0.25}W_{1.75}O_6$ and $CsCu_{0.25}W_{1.75}O_6$ were also included due to their comparatively large bandgap of 2.9 eV and 2.8 eV, respectively. Although all samples show hydrogen evolution without co-catalyst, the hydrogen amounts are generally low (0-2 h). Moreover, methanol alone – that is without photocatalyst – shows hydrogen evolution with a steady-state evolution rate of 45 µmol h^{-1} (Figure 10.22, appendix). The reason being the direct photolysis of methanol; UV light irradiation at 193 nm has been reported to result in the dissociation of methanol into an H atom and a methoxy radical.[182] Since light absorption and scattering are different for each sample, the hydrogen evolution by direct photolysis should also be different for each sample; therefore the above value cannot be simply subtracted for each sample. As a consequence, the hydrogen evolution in the first two hours will result from both photocatalysis and direct photolysis and no distinction is possible. However, after *in-situ* photochemical Rh deposition the photocatalytic activity increases considerably and the direct photolysis can be neglected (2-4 h). Some samples do not reach a steady-state level within these two hours and the hydrogen evolution rate is declining. The likely reason is the oxidation of co-catalyst, which has also been observed in

Pt nanoparticles.[183] Such a decline in hydrogen evolution has also been observed for mesoporous $CsTaWO_6$; however, the Rh amount was too miniscule for XPS measurements.[114] After deposition of Cr_2O_3 all samples achieve a steady-state level, but the hydrogen evolution is lower as compared to bare Rh as co-catalyst (4-6 h). The obvious reason is the blockade of the Rh surface by Cr_2O_3. After the lamp is switched off (6 h) the hydrogen evolution stops.

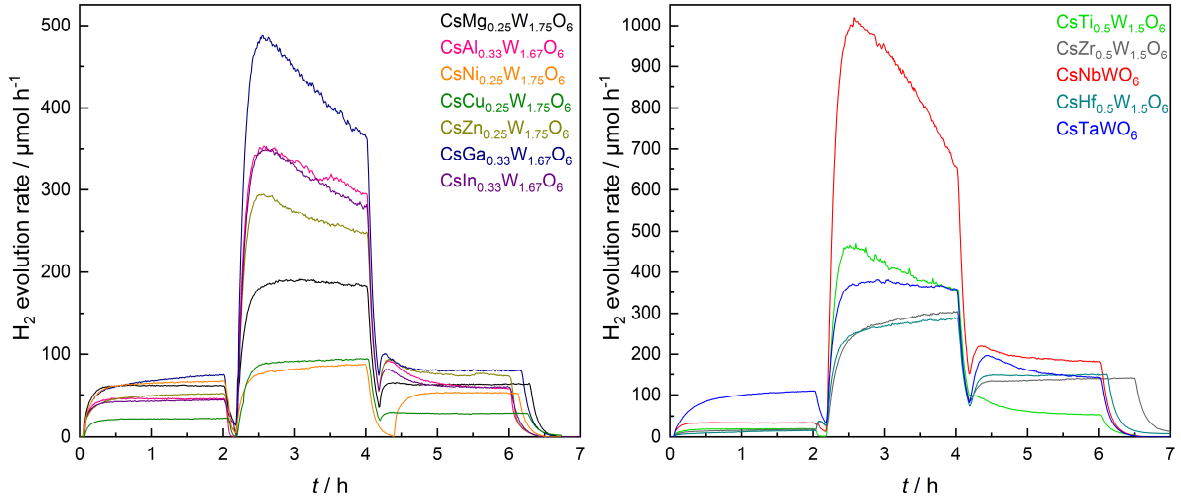

Figure 6.30: Hydrogen evolution of $CsM_xW_{2-x}O_6$ compounds with large bandgaps in water/methanol under UV light irradiation. 3 µmol Na_3RhCl_6 per mmol sample were added after 2 hours, after 4 h the same amount of K_2CrO_4 was added. After 6 h the lamp was finally switched off.

The hydrogen evolution rates of pure $CsM_xW_{2-x}O_6$ are barely above the hydrogen evolution rate of pure methanol and sometimes even below (Figure 6.31). Photodeposition of Rh as co-catalyst drastically increases the hydrogen evolution rate. The evolution rates of most samples are in a similar range with three exceptions: $CsNbWO_6$, $CsNi_{0.25}W_{1.75}O_6$ and $CsCu_{0.25}W_{1.75}O_6$. The rate of $CsNbWO_6$ is twice as high as most others. However, $CsNbWO_6$ has also the highest surface area of all samples (Table 6.1), which explains the higher photocatalytic activity. On the other hand, the hydrogen evolution rates of $CsNi_{0.25}W_{1.75}O_6$ and $CsCu_{0.25}W_{1.75}O_6$ are far lower than for other samples. This indicates that the incorporation of M^{n+} with partially filled *d* states actually lowers the photocatalytic activity. The most likely reason is that the changed transition from M 3*d* to W 5*d* – instead of O 2*p* to W 5*d* as for M^{n+} with d^0 or d^{10} electron configuration – results in shorter lifetimes for photogenerated charge carriers and thus in a lower photocatalytic activity. Moreover, ion exchange with Cu^{2+} in $KNbTeO_6$ has been reported to result in gap states that act as recombination centres.[58] Although $CsNi_{0.25}W_{1.75}O_6$ has the lowest surface area of all samples this cannot be the reason for the lower activity, since the surface areas of $CsCu_{0.25}W_{1.75}O_6$ and $CsTi_{0.5}W_{1.5}O_6$ are identical. However, the hydrogen evolution of $CsNi_{0.25}W_{1.75}O_6$ and $CsCu_{0.25}W_{1.75}O_6$ supports the negative flat band potential determined by Mott-Schottky plots (see section 6.4).

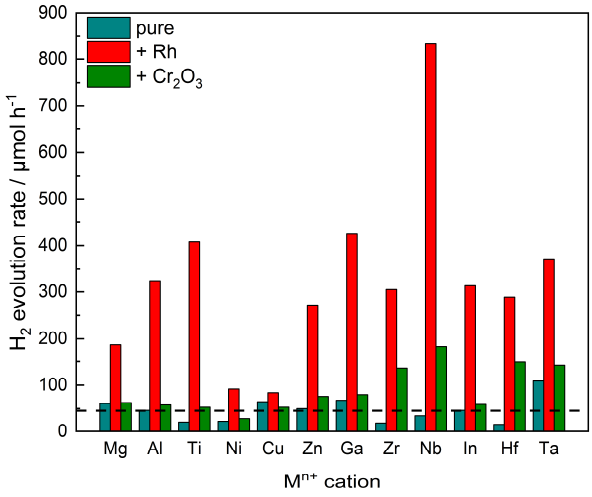

Figure 6.31: Overview of hydrogen evolution rates of $CsM_xW_{2-x}O_6$ with and without co-catalysts; the dashed line represents the hydrogen evolution rate of water/methanol without photocatalyst.

XRD patterns of the samples measured after photocatalytic measurements do not show any changes as compared to before; all samples are still phase pure and highly crystalline (Figure 10.23, appendix). Raman spectra also do not show any significant changes (Figure 10.24, appendix). All samples are greyish coloured afterwards due to co-catalyst deposition; the measured bandgaps do not show any changes – within the experimental error – as compared to before photocatalytic measurements (Figure 10.25, appendix).

$CsTi_{0.5}W_{1.5}O_6$ and $CsNbWO_6$ – with previously photodeposited Rh/Cr_2O_3 (see above) – were employed in pure water splitting (Figure 6.32, left). However, the detected gas amounts were barely above the limit of detection. The evolution transients of hydrogen and oxygen, respectively, do not seem to be correlated with each other and are also far from the ideal 2:1 ratio. Moreover, the detected hydrogen amounts were similar to those observed for pure water.

To compensate for the low activity of $CsM_xW_{2-x}O_6/Rh/Cr_2O_3$, iridium(IV) oxide IrO_2 was used as an additional co-catalyst for oxygen evolution: once as IrO_2 nanoparticles deposited on $CsMg_{0.25}W_{1.75}O_6$ and one once *via* photodeposition on $CsNbWO_6$ in a previous step. However, the $CsMg_{0.25}W_{1.75}O_6$ sample with IrO_2 nanoparticles only showed a short-lived oxygen evolution and no hydrogen evolution at all (Figure 6.32, right), whereas the $CsNbWO_6$ with photodeposited IrO_2 shows hydrogen evolution and a miniscule oxygen evolution. Nevertheless the oxygen amount is far too low for water splitting and could also result from an erratic background signal. The higher hydrogen evolution rate during the first 2.5 h results from the decomposition of organic impurities such as methanol residues from the previous experiment in water/methanol.

To conclude, $CsM_xW_{2-x}O_6$ defect-pyrochlores are not active in photocatalytic water splitting. The only reported water splitting for $CsM_xW_{2-x}O_6$ was by Ikeda *et al.* for $CsNbWO_6$ and

$CsTaWO_6$.[16] However, even with an 1 kW ultra-high pressure Hg lamp under reduced pressure and the addition of 1 mol L^{-1} CsOH only 19.7 µmol h^{-1} hydrogen and 8.8 µmol h^{-1} oxygen were reported for $CsTaWO_6$.

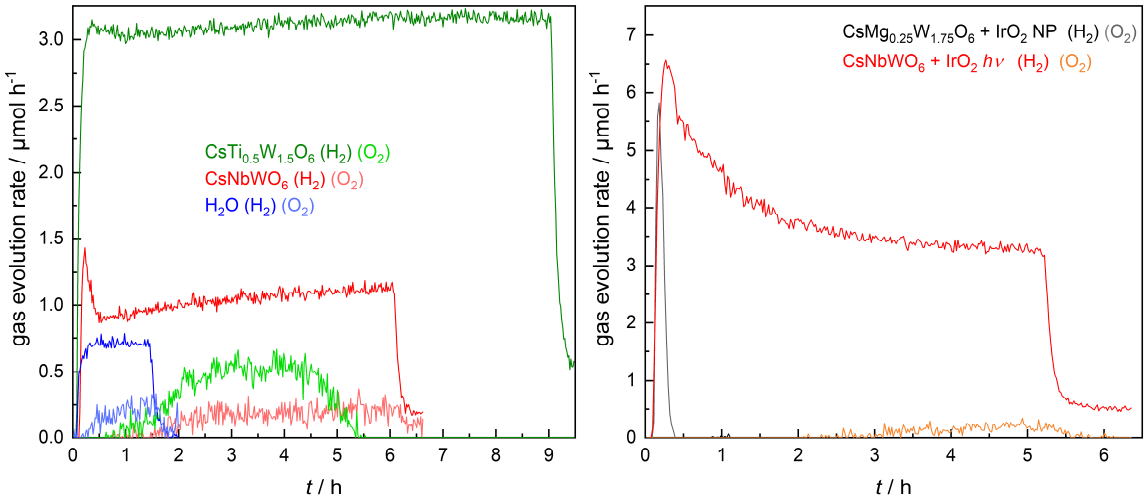

Figure 6.32: Gas evolution rates of water splitting experiments of selected samples without (left) and with (right) additional IrO_2 co-catalyst under UV light irradiation.

In order to be able to explain the inactivity in water splitting, transient absorption spectroscopy measurements were performed. The time constants τ of the fitted exponential decay functions can be used to estimate the lifetime of photogenerated excited states; the excited state in question is most likely W(V).[184] An exponential decay function may not necessarily be correct, *e. g.* the charge carrier dynamics in barium tantalates follow second order kinetics.[185] However, even if the actual kinetics do not follow the used exponential function, the obtained time constants can still be used to correlate changes in the elemental composition with the lifetimes of excited states, *i. e.* a larger time constant indicates longer-lived excited states, whereas a smaller time constant indicates shorter-lived excited states.

All four selected samples showed comparable ΔOD values in the range 450-650 nm, whereas signal intensity was declining above 600/650 nm (Figure 6.33 and Figure 10.26, appendix). Measurements at lower wavelengths were not possible due to intense sample fluorescence (Figure 10.27, appendix). As a compromise and for better comparableness, a wavelength of 500 nm was chosen for all samples.

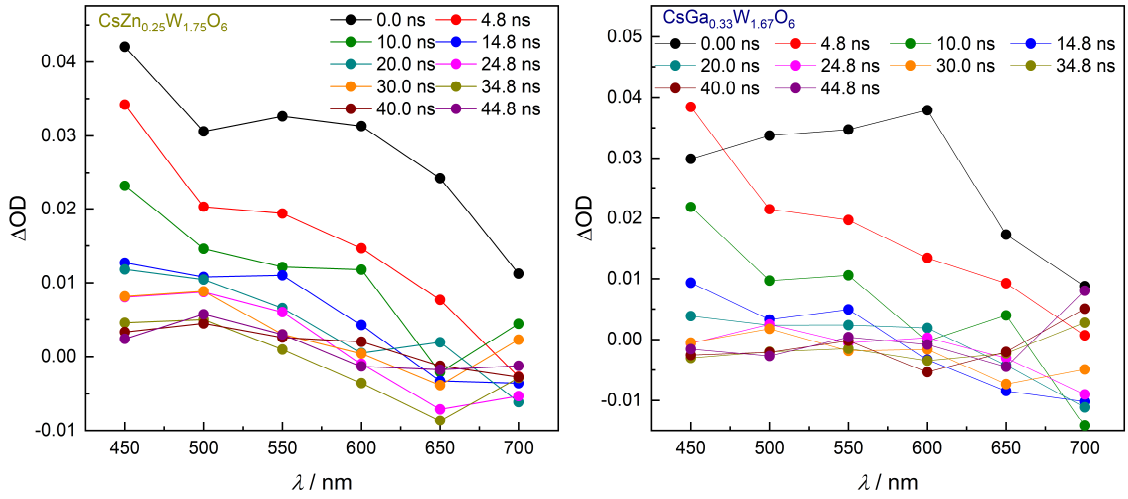

Figure 6.33: Transient absorption spectroscopy measurements at different wavelengths of $CsZn_{0.25}W_{1.75}O_6$ (left) and $CsGa_{0.33}W_{1.67}O_6$ (right). The excitation wavelength was 266 nm.

The transient absorption spectra of $CsZn_{0.25}W_{1.75}O_6$ and $CsGa_{0.33}W_{1.67}O_6$ can be well fitted with a one-phase exponential decay function (Figure 6.34); the obtained time constants are highly similar with 12.5 ± 0.2 ns and 9.3 ± 0.2 ns, respectively.

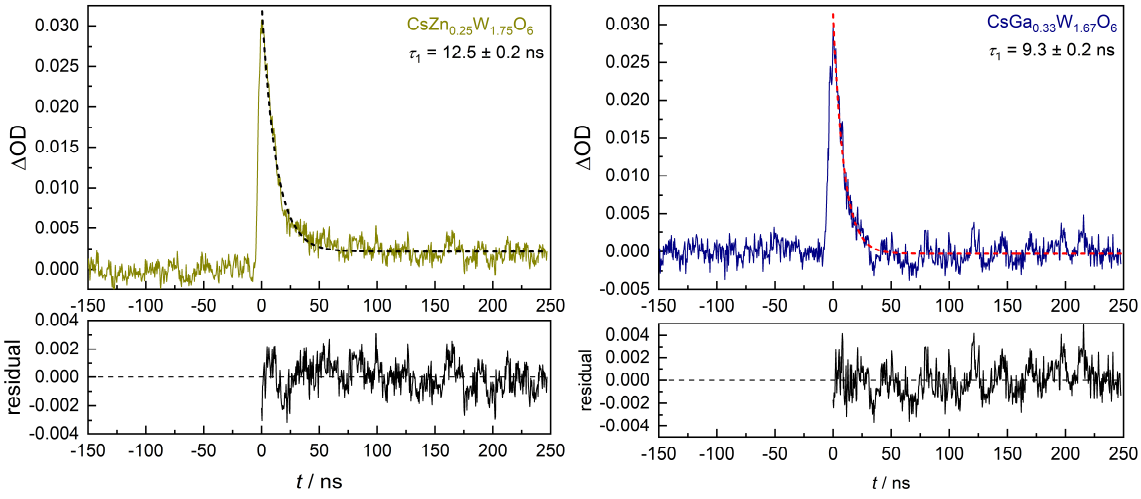

Figure 6.34: Transient absorption spectra of $CsZn_{0.25}W_{1.75}O_6$ (left) and $CsGa_{0.33}W_{1.67}O_6$ (right) fitted with an one-phase exponential decay function; the obtained time constants τ_1 are noted in the respective graphs. The excitation wavelength was 266 nm, the detection wavelength 500 nm.

The time constants obtained with a one-phase decay function for $CsMg_{0.25}W_{1.75}O_6$ and $CsNbWO_6$ are 13.8 ± 0.2 ns and 10.6 ± 0.2 ns, respectively (Figure 6.35).

Since all values are approximately 10 ns, it can be concluded that the influence of M^{n+} on charge carrier kinetics is negligible, provided that M^{n+} has a d^0 or d^{10}electron configuration. The

reason for this is that the VB to CB transition is from O 2*p* to W 5*d* without direct involvement of M^{n+} states.

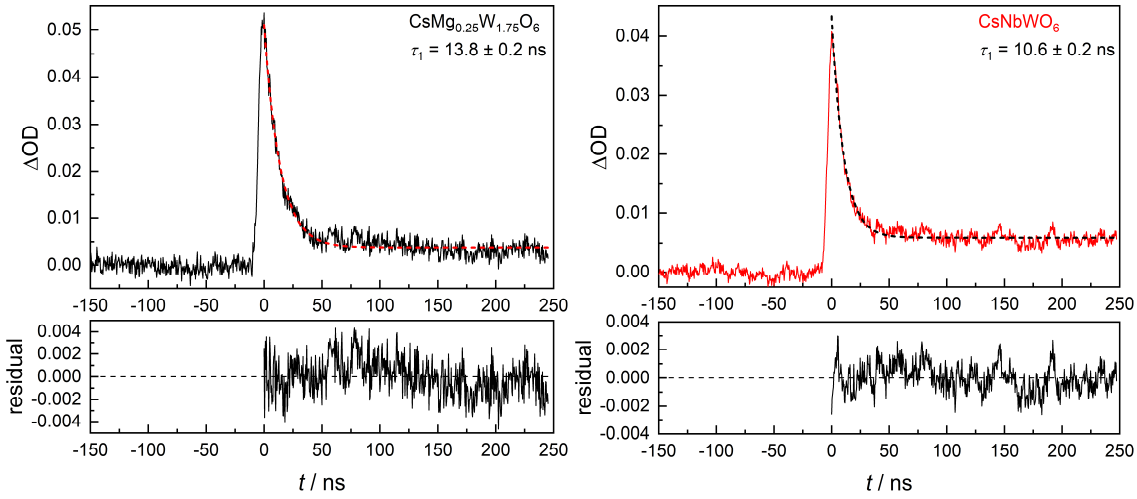

Figure 6.35: Transient absorption spectra of $CsMg_{0.25}W_{1.75}O_6$ (left) and $CsNbWO_6$ (right) fitted with an exponential decay function; the obtained time constants τ_1 are noted in the respective graphs. The excitation wavelength was 266 nm, the detection wavelength 500 nm.

Since $CsM_xW_{2-x}O_6$ compounds in which M^{n+} has partially occupied *d* states possess bandgaps in the visible light region, photocatalytic measurements have been performed in simulated solar light. However, even with addition of Rh as co-catalyst and methanol as sacrificial agent, no hydrogen could be detected (not shown). Since $CsNi_{0.25}W_{1.75}O_6$ and $CsCu_{0.25}W_{1.75}O_6$ have shown hydrogen evolution under UV light irradiation, these compounds should also be able to evolve hydrogen under simulated solar light irradiation. Additionally, sacrificial hydrogen evolution in solar light has been reported for $CsFe_{0.33}W_{1.67}O_6$.[179] XRD patterns and Raman spectra of the recovered samples show no signs of decomposition (Figure 10.28, appendix). UV/vis measurements also show no change of the *d*–*d* absorption bands or the bandgaps (Figure 10.29, appendix).

Transient absorption spectroscopy measurements were unsuccessful; the width of the measured peaks is close to the pulse duration of the excitation laser, thus precluding reliable estimation of time constants (Figure 6.36). Moreover, the signal-to-noise ratio is increased and the ΔOD values are an order of magnitude larger, indicating that the transient intensity I_T is also decreasing.

This could indicate that the lifetimes of photogenerated charge carriers in $CsM_xW_{2-x}O_6$ with M^{n+} cations with d^n electron configuration are far shorter than for M^{n+} cations with d^0 or d^{10} electron configuration. This is similar to the fast recombination that has been observed in α-Fe_2O_3: the decay half-time of α-Fe_2O_3 is only 3 ps compared to 6.2 ns for TiO_2.[186]

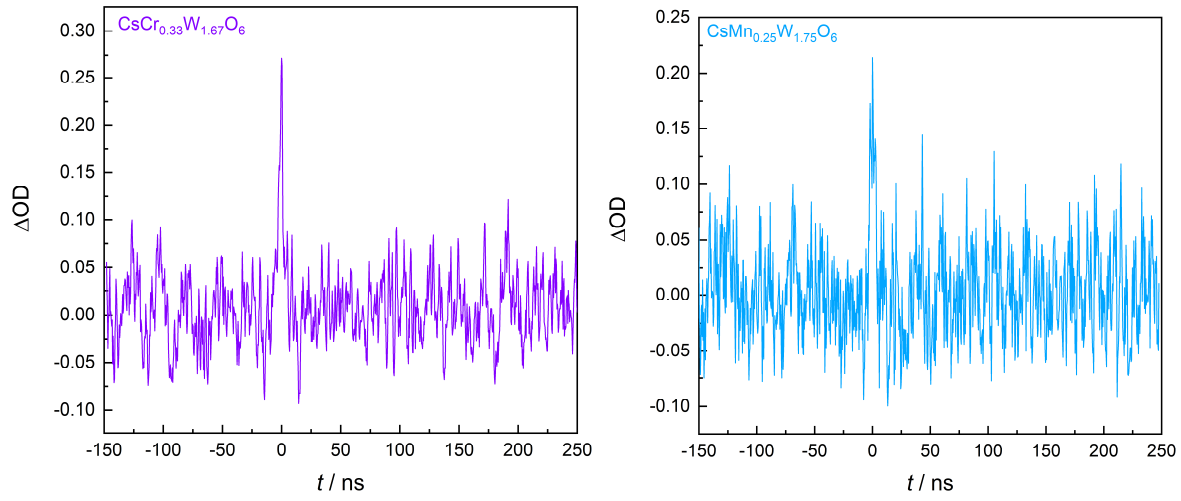

Figure 6.36: Transient absorption spectra of $CsCr_{0.33}W_{1.67}O_6$ (left) and $CsMn_{0.25}W_{1.75}O_6$ (right).

A reason for the inactivity in simulated solar light and the presumed shorter charge carrier lifetimes could be the existence of trap states. In $FeWO_4$ and $CoWO_4$ the occupied Fe 3*d* and Co 3*d* states are located near the VB maximum, whereas the empty Fe 3*d* and Co 3*d* states form the CB minimum.[187] Empty M^{n+} 3*d* states beneath the CB minimum could trap photogenerated electrons resulting in a fast recombination.

Another reason could be the existence of multiple oxidation states; especially Cr, Mn and Co have several stable oxidation states. These oxidation states can also act as trap states, *e. g.* Cr^{6+} states are located beneath the hydrogen evolution potential and can act as an electron trap.[57] On the other hand, Cr^{3+} in Cr and La co-doped $SrTiO_3$ acts as a trapping state for photogenerated holes and is oxidised to Cr^{6+} in the process.[188] Electrons excited from the Cr^{3+} states into the CB are also reported to be less reactive and shorter lived than compared to pure $SrTiO_3$. Also possible is a change of oxidation states upon irradiation.

Determination of the oxidation state of Cr, Mn, Fe, Co and Ni is highly problematic due to multiplet splitting – resulting in multiple overlapping peaks – and satellite peaks.[189] Even for the very similar compounds $FeCr_2O_4$ and $NiCr_2O_4$ the four respective five Cr $2p_{3/2}$ peaks are different.[189] XPS analysis is also hindered by the low amount of M^{2+} or Mn^{3+} in $CsM_xW_{2-x}O_6$, *i. e.* 2.8 at% and 3.7 at%, respectively. The detectable amounts are even lower, because sputter cleaning with argon was omitted, since argon sputtering can reduce metal oxides.[190,191] As a consequence, measured XP spectra show poor signal-to-noise ratio (Figure 6.37); accurate and reliable chemical state identification was not possible. Only for $CsCr_{0.33}W_{1.67}O_6$ a Cr(VI) signal at 579.5 eV could be observed, due to the large shift in binding energies of approximately 4 eV between Cr(III) and Cr(VI).[189]

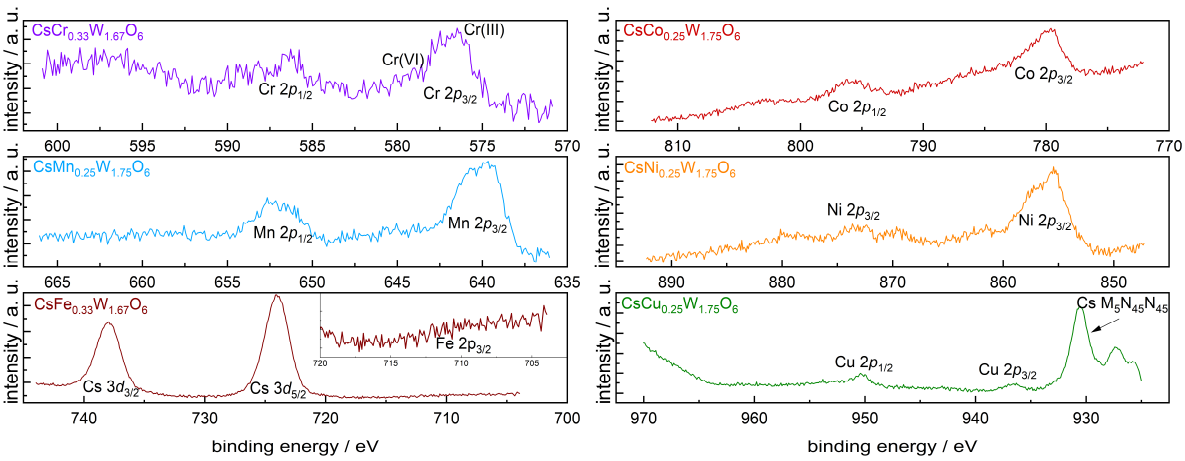

Figure 6.37: High-resolution XP spectra of M 2p region.

To summarise, $CsM_xW_{2-x}O_6$ compounds with M^{n+} with d^0 or d^{10} electron configuration are able to evolve hydrogen under UV light irradiation; the sample with the highest surface area also showed the highest photocatalytic activity. Sample characterisation after photocatalytic measurements showed no signs of decomposition. However, water splitting is not possible, presumably due to short lifetimes of charge carriers. Compounds in which M^{n+} has partially filled d^n states were inactive in sacrificial hydrogen evolution in simulated solar light irradiation. Transient absorption measurements with these samples were unsuccessful, which could indicate even shorter charge carrier lifetimes.

7 Crystal Structure and Defect-Chemistry of $ANbTeO_6$

7.1 Material Characterisation

Tellurium containing defect-pyrochlores with the composition $ANbTeO_6$ ($A = K^+$, Rb^+, Cs^+) are interesting materials due to their visible light absorbance (see section 2.3.3). However, their properties and photocatalytic activities have only been scarcely investigated yet (see section 2.3.4).

These materials have been synthesised *via* solid state reaction at 700 °C for 10 h according to formula 7.1:

$$A_2CO_3 + Nb_2O_5 + 2\ TeO_2 + O_2 \rightarrow 2\ ANbTeO_6 + CO_2\uparrow \qquad (7.1)$$

All three compounds are phase-pure and highly crystalline according to XRD patterns (Figure 7.1, left). The differences in relative intensities correspond well with the calculated patterns and appear to be solely caused by the different A cations (Figure 7.1, right).

The synthesis of $NaNbTeO_6$ has also been attempted; however, only a mixture of $NaNbO_3$ and $Na_2Te_2O_7$ was obtained (Figure 10.30, appendix). This may be caused the small size of Na^+ with 1.02 Å as opposed to the larger alkaline metal cations, *i. e.* K^+ with 1.38 Å, Rb^+ with 1.52 Å and Cs^+ with 1.67 Å (all for sixfold coordination).[150]

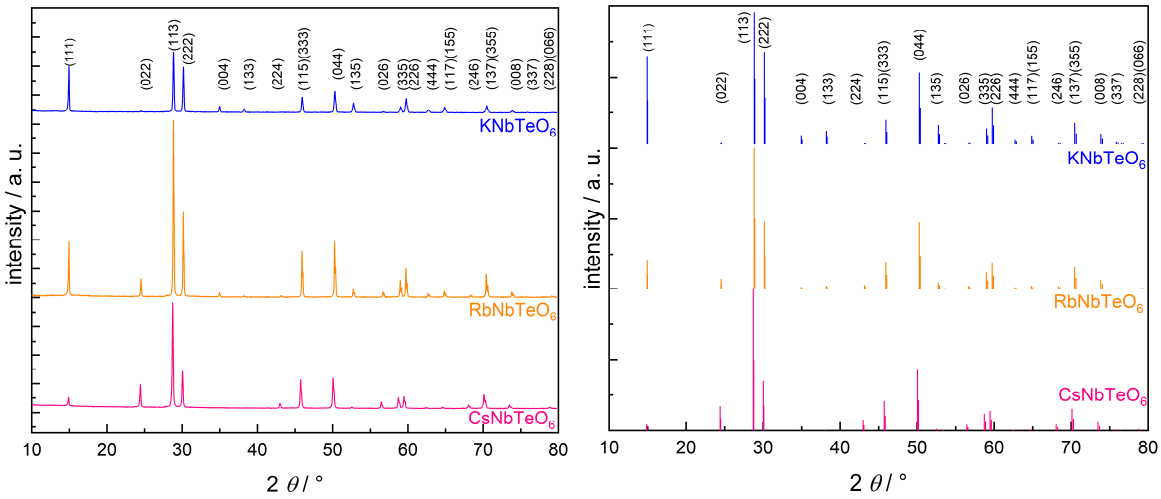

Figure 7.1: Measured (left) and calculated (right) XRD patterns of $ANbTeO_6$.

All three samples are intensely coloured: $KNbTeO_6$ is beige, $RbNbTeO_6$ brown and $CsNbTeO_6$ black (Figure 7.2, inset). The absorption edges of $KNbTeO_6$ and $RbNbTeO_6$ are located at 344 nm (Figure 7.2, left); the excitation of electrons from the VB into the CB is therefore not the reason for the visible light absorption. The colour of the samples stems from a pronounced

tailing that is increasing from $KNbTeO_6$ to $CsNbTeO_6$. Tauc-plots (Figure 7.2, right) show a bandgap of 3.4 eV for $KNbTeO_6$ and $RbNbTeO_6$; due to the intense tailing the bandgap for $CsNbTeO_6$ cannot be reliably estimated anymore. Misinterpretation of this tailing is likely responsible for the 2 eV bandgaps often reported for $KM_xTe_{2-x}O_6$ defect-pyrochlores.[25,65,117] The 3.4 eV bandgap and the colour of $KNbTeO_6$ are identical to reported values; however, no explanation of the colour is given therein.[58]

To check if these results are reproducible, the synthesis has been repeated at the same conditions. The absorption spectra of these samples are virtually identical to those of the first synthesis (Figure 10.31, appendix).

Occurrence of such tailings in UV/vis spectra has been observed both for doping and defects. Doping is rather unlikely in this case since all three samples have been prepared in the same way; inadvertent doping by impurities should thus result in similar visible light absorption. However, the clear trend between A and the magnitude of the tailing indicates an intrinsic property of the samples.

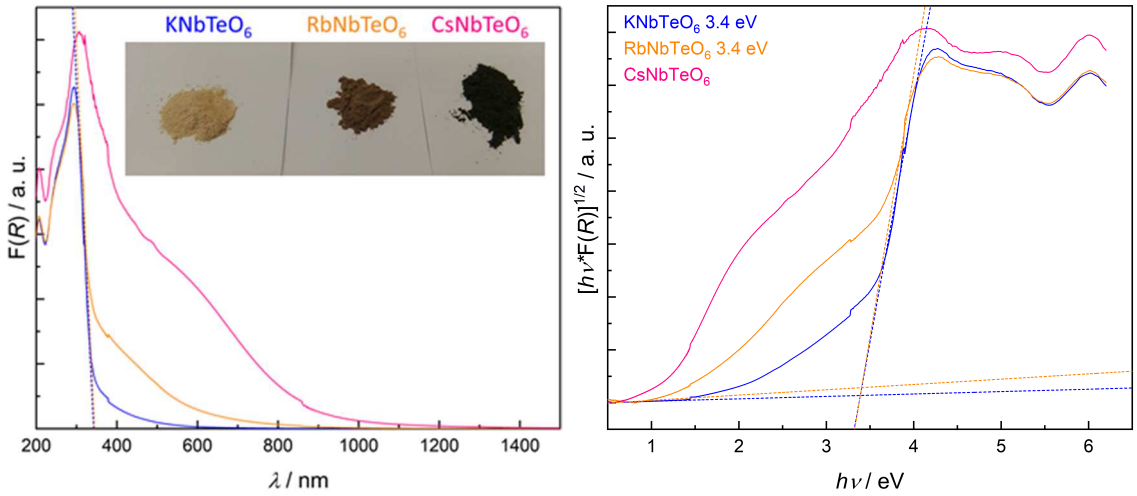

Figure 7.2: Kubelka-Munk absorption spectra (left) and Tauc-plots (right) for $ANbTeO_6$. The inset shows a photography of the samples.

In order to elucidate the origin of this tailing, XPS measurements have been performed to identify the chemical states present in the samples. XP spectra of the Te 3*d* region show three different Te signals for all three samples (Figure 7.3, left). These three signals are present in both the $3d_{5/2}$ and $3d_{3/2}$ peak, showing that these are genuine Te states and not an impurity with a coincidentally similar binding energy. These three signals can be attributed to Te(0) (573.3 eV, red), Te(IV) (575.7-576.1 eV, green) and Te(VI) (577.5 eV, brown).[192] XPS measurements have also been performed on Te reference compounds for verification of this assignment (Figure 7.3, right). These compounds also exhibit several different Te states. However,

the Te(0) signal of Te (573.1 eV), the Te(VI) signal of TeO_2 (576.3 eV) and the Te(VI) signal of $Te(OH)_6$ (577.0 eV) are conform well with the Te 3*d* signals for $ANbTeO_6$. For Te and TeO_2 an additional signal could be detected at 574.5 eV. Similar binding energies have been reported for Te(IV) containing glasses;[193] amorphous Te(IV) could be an intermediate between Te and TeO_2. The majority Te component in all three $ANbTeO_6$ samples is Te(IV), although the nominal oxidation state of Te in $ANbTeO_6$ is Te(VI). The Te(VI) signal is decreasing from $KNbTeO_6$ to $CsNbTeO_6$, while the Te(0) signal is increasing in the same order. Since elemental Te is a semiconductor with a bandgap of 0.335 eV,[194] the increasing Te(0) content is the likely reason for the increasing visible light absorption from $KNbTeO_6$ to $CsNbTeO_6$. Since the (calculated) bandgaps of the different TeO_2 polymorphs are approximately 3 eV,[195] it is unlikely that Te(IV) would result in such intense visible light absorption. Waehayee *et al.* found only one signal for $KNbTeO_6$ – and ion exchanged derivatives –; the binding energies of 576.4-576.8 eV fit rather well to the Te(IV) signal in $KNbTeO_6$ (576.2 eV), but have been erroneously ascribed to Te(VI).[58] A method to investigate if these defect states are limited to the surface or are also present in the bulk volume would be Te L_3-edge XANES.[109]

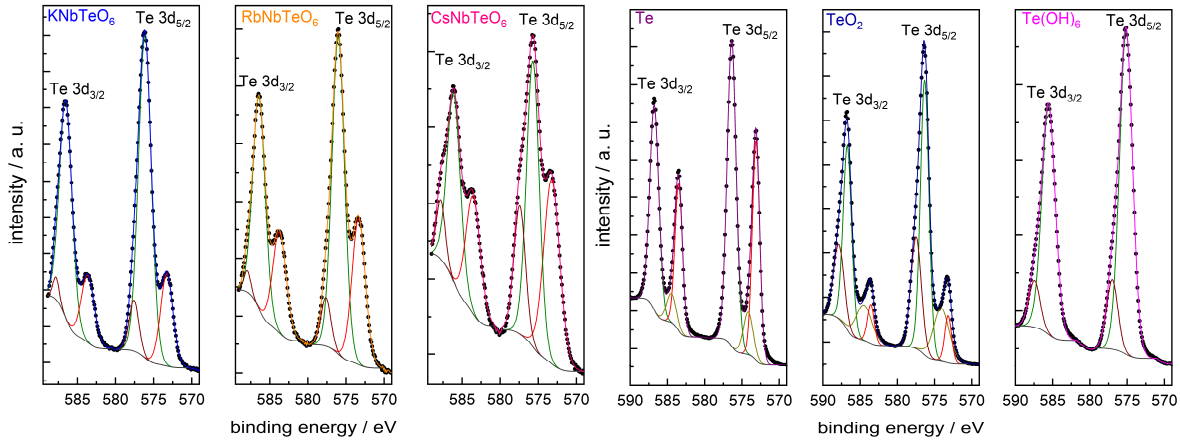

Figure 7.3: High resolution XPS of the Te 3*d* region for $ANbTeO_6$ (left) and Te reference compounds (right). Signals attributed to Te(0) are depicted in red, Te(IV) in green and Te(VI) in brown.

The O 1*s* spectra also give valuable information about the occurrence of defects. Peak fitting reveals that each sample consists of three different oxygen species (Figure 7.4, left) with mean binding energy values of 529.9 eV, 531.1 eV and 532.9 eV. A binding energy of 529.9 eV (red) is rather typical for lattice oxide anions of transition metal oxides.[196] The 531.1 eV middle signal (green) could be either ascribed to hydroxides or ionised oxygen species to compensate deficiencies in the subsurface of transition metal oxides.[196] However, newer results on NiO attribute this signal to defective oxygen – that is oxygen atoms located near defects – and not to hydroxides.[197] The 532.9 eV (brown) signal can be assigned to loosely adsorbed oxygen compounds, such as water molecules.[196,198] The intensity of the defective oxygen signal is

increasing from $KNbTeO_6$ to $CsNbTeO_6$, while the signal belonging to lattice oxygen is decreasing (Figure 7.4, right). For $RbNbTeO_6$ and $CsNbTeO_6$ the defective oxygen signal is actually more intense than the lattice oxygen signal, indicating a high prevalence of defects. The abundance of Te(IV) and Te(0) defects – Te''_{Te} and Te''''_{Te} in Kröger-Vink notation – requires the formation of oxygen vacancies $V^{\bullet\bullet}_O$ to ensure charge neutrality.

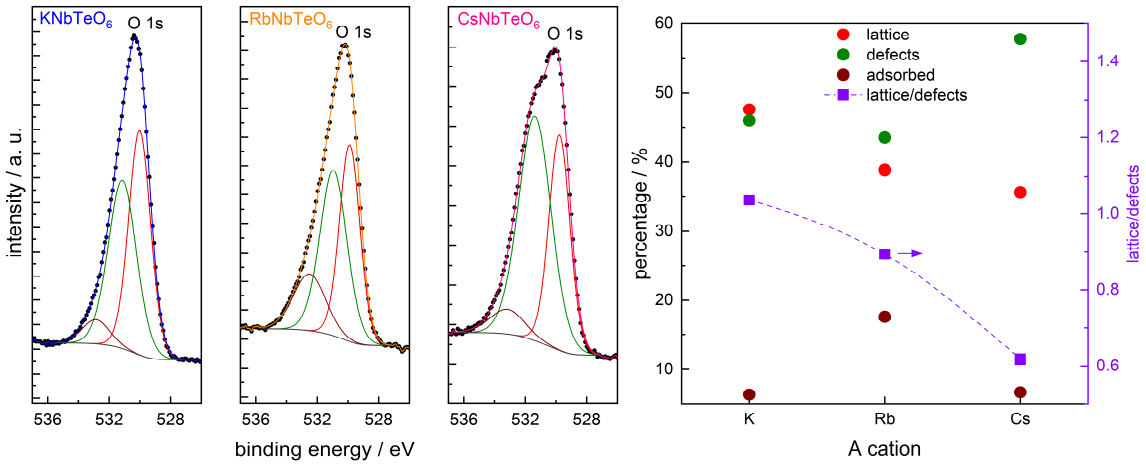

Figure 7.4: High resolution XPS of the O 1*s* region (left) and relative distribution of O 1*s* species.

The high amount of defects – especially in $CsNbTeO_6$ – can also be seen in the XPS of the A cations and in the Nb 3*d* region. While both the K 2*p* and Rb 3*d* spectra consist of only one signal (Figure 7.5, left), the Cs 3*d* region shows two different signals (723.8 eV (red) and 725.1 eV (green)); both can be assigned to Cs(I).[199,200] The Rb 3*d* region overlaps with the minor Te 4*p* signal; however, peak fitting is not impaired by this overlap.

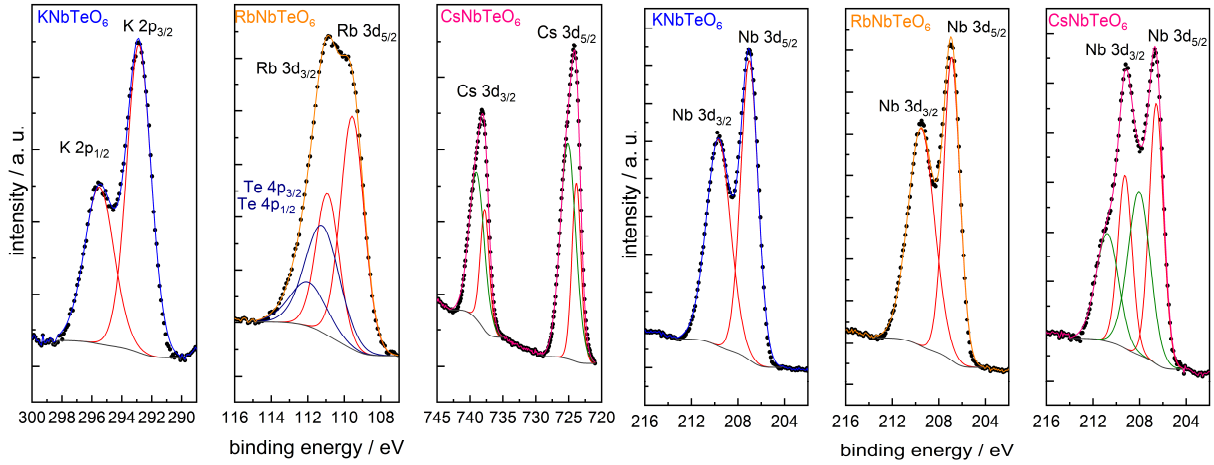

Figure 7.5: High resolution XPS of K 2*p*, Rb 3*d* and Cs 3*d* (left) and Nb 3*d* (right).

The spectra of the Nb 3*d* regions also show one signal for $KNbTeO_6$ and $RbNbTeO_6$ and two for $CsNbTeO_6$ (Figure 7.5, right); both signals (206.6 eV (red) and 208.0 eV (green)) can be

assigned to Nb(V).[201,202] These two different signals for $CsNbTeO_6$ – both for Cs 3*d* and Nb 3*d* – indicate two different chemical environments in this sample, likely as a result of the large amount of defects.

The elemental compositions of these samples have been determined by EDX and XPS (Table 7.1). The different analysis depth of these two techniques can be used to distinguish between surface and bulk volume composition. While the bulk volume compositions match well with the theoretical values, the surface compositions reveal either an A and Te surplus or a Nb deficiency. However, a Nb deficiency is more likely, since the A and Nb amounts for $RbNbTeO_6$ and $CsNbTeO_6$ are nearly identical. Moreover, survey XPS scans revealed no impurities (Figure 10.32, appendix). Since the discrepancy between both elemental compositions is strongest for $KNbTeO_6$, the different surface composition cannot explain the increasing amount of defects from $KNbTeO_6$ to $CsNbTeO_6$.

Table 7.1: Elemental composition of $ANbTeO_6$ compounds as determined by EDX and XPS. All values have been normalised to Nb = 1.

sample	A	Nb	Te	O	method
$KNbTeO_6$	0.89	1	0.99	6.88	EDX
	1.91	1	2.47	9.89	XPS
$RbNbTeO_6$	1.00	1	1.09	6.49	EDX
	1.67	1	1.65	8.00	XPS
$CsNbTeO_6$	1.05	1	1.24	6.88	EDX
	1.76	1	1.79	8.55	XPS

Although the nominal oxidation state of Te in $ANbTeO_6$ is +VI, the used precursor for the synthesis is TeO_2 with a Te oxidation state of +IV. This has been done because Tellurium(VI) oxide TeO_3 decomposes before the synthesis temperature of 700 °C. The decomposition reaction occurs in two steps: TeO_3 is starting to decompose at 475 °C to the Te(IV,VI) mixed valence oxide Te_2O_5 (formula 7.2).[203]

$$2\ TeO_3 \rightarrow Te_2O_5 + \tfrac{1}{2} O_2 \uparrow \qquad (7.2)$$

This intermediate oxide further decomposes between 540-615 °C to TeO_2 (formula 7.3).[203]

$$Te_2O_5 \rightarrow 2\ TeO_2 + \tfrac{1}{2} O_2 \uparrow \qquad (7.3)$$

To investigate if the initial Te oxidation state has an influence on the defect formation in $ANbTeO_6$, the synthesis was repeated with telluric acid $Te(OH)_6$ instead of TeO_2. Telluric acid first dehydrates and then also decomposes to TeO_2; however, the decomposition mechanism is far more complex and for this reason not depicted herein.[203] The synthesis – performed at

the same temperature and for the same time as with TeO_2 – also results in phase pure materials (Figure 10.33, left, appendix). The absorption spectra are largely similar to those $ANbTeO_6$ samples synthesised with TeO_2 (Figure 7.1, left). The largest difference can be observed for $CsNbTeO_6$; the visible light absorption is less intense if $Te(OH)_6$ is used in the synthesis. Due to the less intense absorption, the absorption edge of $CsNbTeO_6$ can be better observed. The absorption edge – and therefore the bandgap – is identical for all three materials. To conclude, the initial Te oxidation state does not significantly affect the visible light absorption and thus the defect formation.

The synthesis of $ANbTeO_6$ was furthermore repeated in pure oxygen instead of air in an attempt to supress the formation of Te(IV) and Te(0) (Figure 7.6, right). The visible light absorption of these samples is slightly more intense than of those samples synthesised in air, indicating a higher amount of Te(IV) and Te(0) present in these samples. That a higher oxygen content results in a larger amount of reduced Te species is counterintuitive and has to be investigated further. While $KNbTeO_6$ and $RbNbTeO_6$ are phase pure, the XRD pattern of $CsNbTeO_6$ shows small amounts of $Cs_2Te_2O_{12}$ (Figure 10.33, right, appendix).

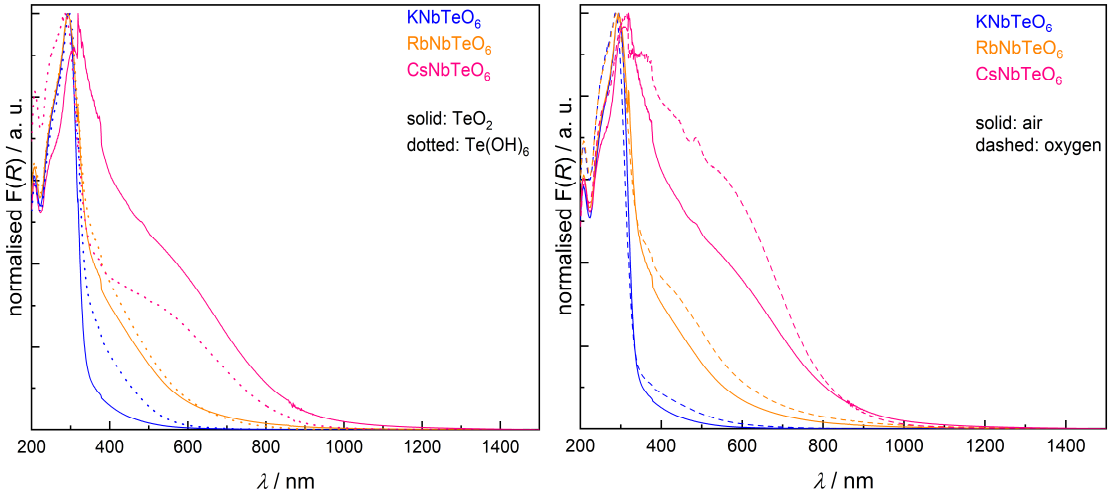

Figure 7.6: Kubelka-Munk absorption spectra of $ANbTeO_6$ synthesises with $Te(OH)_6$ and TeO_2 (left) and of $ANbTeO_6$ synthesised in pure oxygen instead of air (right).

To elucidate the origin of the defects, Rietveld refinements have been conducted to find a correlation between defects and potential distortions of the crystal structure; the calculated patterns conform well to the experimental ones (Figure 7.7).

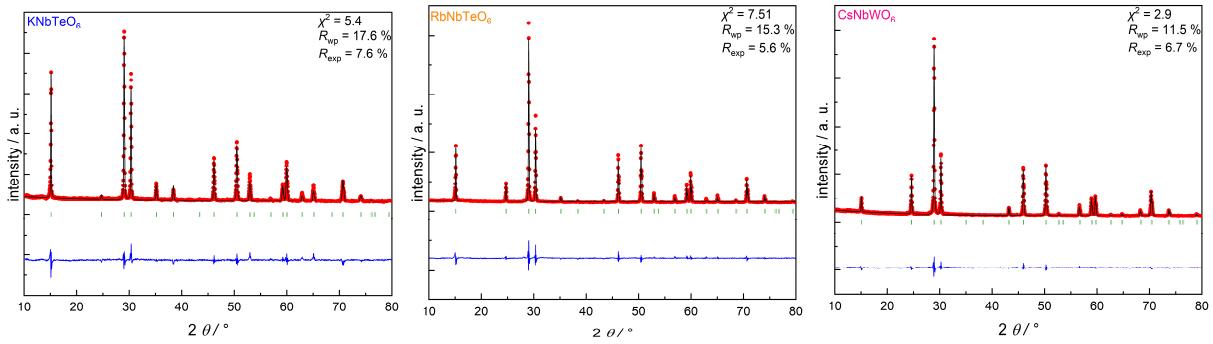

Figure 7.7: Rietveld refinements of $KNbTeO_6$ (left), $RbNbTeO_6$ (middle) and $CsNbTeO_6$ (right).

Lattice constants are increasing from $KNbTeO_6$ to $CsNbTeO_6$; however, the lattice constant of $CsNbTeO_6$ is far larger than these of $KNbTeO_6$ or $RbNbTeO_6$ (Figure 7.8, left). This particular increase is also visible if the lattice constant is plotted against the ionic radius of the A cations (Figure 7.8, right), indicating that the larger lattice constant of $CsNbTeO_6$ cannot be solely explained by the larger size of the Cs^+ cation. The crystallite sizes differ between 150 to 325 nm and are uncorrelated with A (Figure 7.8, left).

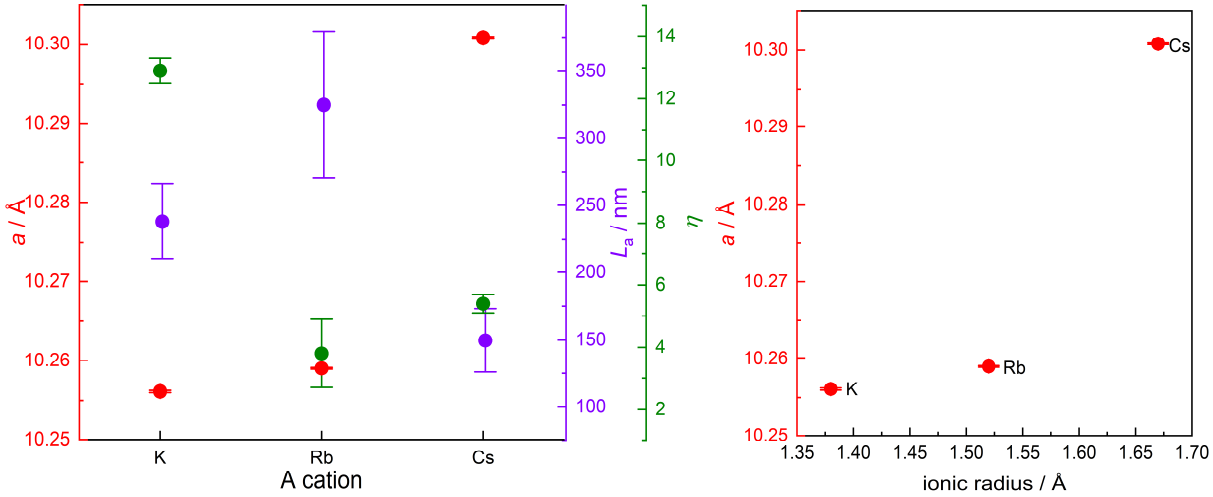

Figure 7.8: Overview between lattice constants, crystallite sizes and strain parameters for $ANbTeO_6$ compounds (left). Correlation between lattice constant and ionic radius of A (right).

The strain parameter for $KNbTeO_6$ is far larger than those of $RbNbTeO_6$ and $CsNbTeO_6$. A possible explanation could be the incorporation of water molecules into the hexagonal channels of the defect-pyrochlore crystal structure, which has been shown for $KNbWO_6$ and $KTaWO_6$.[23,83,102] Rietveld refinements for both dried and water vapour saturated $KNbTeO_6$ (Figure 7.9) do not show any differences in relative intensities, which indicates that the composition of the unit cell does not change and water molecules are not incorporated. The broad signal between 15-20° results from the polycarbonate dome of the same sample holder, which

has been used to prevent exposure of the sample to ambient humidity. Moreover, the change of lattice parameters is only 0.0045 Å, which is far less than for $KTaWO_6$ (see section 5.2) and likely results from experimental error. Additionally, if water molecules would be present in the unit cell, Rietveld refinements would not be as satisfactory as those depicted in Figure 7.9. Neutron powder diffraction by Mayer *et al.* also showed no water incorporation for $KNbTeO_6$ and $KSbWO_6$.[87] This is presumed to be due to the higher covalence of the main group elements Sb and Te.

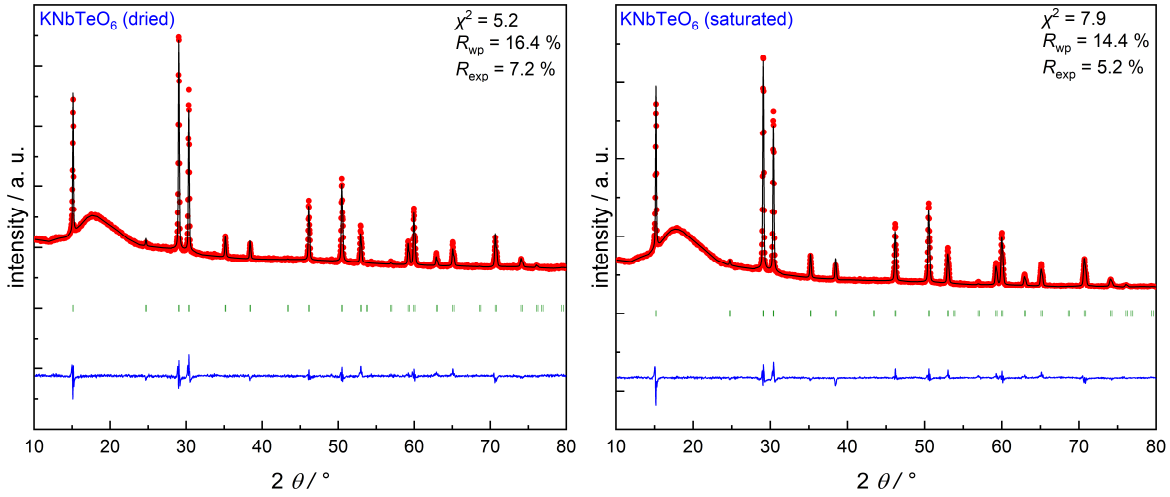

Figure 7.9: Rietveld refinements for dried $KNbTeO_6$ (left) and water vapour saturated $KNbTeO_6$ (right).

Evaluation of distances and angles of the refined crystal structures reveals a distortion, whose magnitude depends on the A cation. The distances between the A cations and their coordinating oxygen anions are expectedly increasing with an increasing size of A (Figure 7.10, left). The distances between Nb/Te cations – located in the centre of the octahedra – and the oxygen anions at the vertices are slightly decreasing from $KNbTeO_6$ to $CsNbTeO_6$. The increasing size of the A cations in the hexagonal channels seem to result in a compression of the octahedral framework. Assuming an ideal octahedron, the oxygen atoms – located at the vertices – should have an identical distance to all adjoining oxygen atoms. However, two different O-O distances are obtained for every sample; the difference between those two is 0.4024 Å for $KNbTeO_6$, 0.2304 Å for $RbNbTeO_6$ and 0.1397 Å for $CsNbTeO_6$. The angles present in the octahedra also show a distortion (Figure 7.10, right). In an ideal octahedron the angles O-Nb/Te-O (vertex-centre-vertex) and O-O-O (vertex-vertex-vertex) should be 90° and 60°, respectively. Due to a shift of the oxygen atoms, some angles in a single octahedron are smaller while others are wider. The difference between the angles in a single octahedron is diminishing from $KNbTeO_6$ to $CsNbTeO_6$. Also increasing with A is the Nb/Te-O-Nb/Te (centre-connecting vertex-centre) angle, resulting in larger channels. The measured angle of 129° for $KNbTeO_6$ deviates from the 138° reported in the literature.[87] The narrower channels compared to $KNbWO_6$,

whose Nb/W-O-Nb/W angle is reported to be 143°,[87] could be a reason why water molecule incorporation does not occur for $KNbTeO_6$.

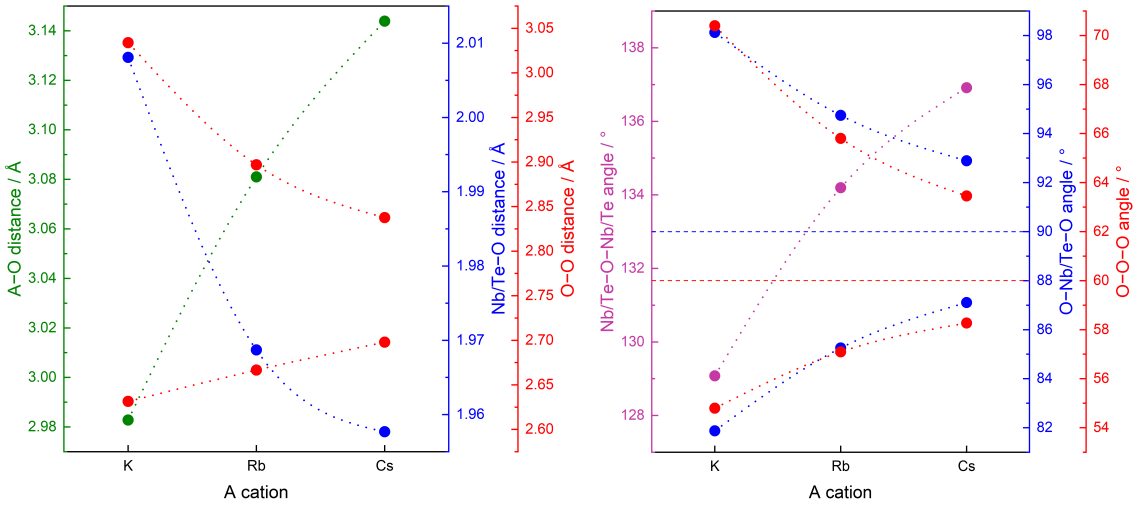

Figure 7.10: Distances (left) and angles (right) for $ANbTeO_6$ compounds. Horizontal dashed lines represent angles in an ideal octahedron.

The resulting differences in the octahedra – especially in the upper-left and lower-right planes – can be seen in Figure 7.11.

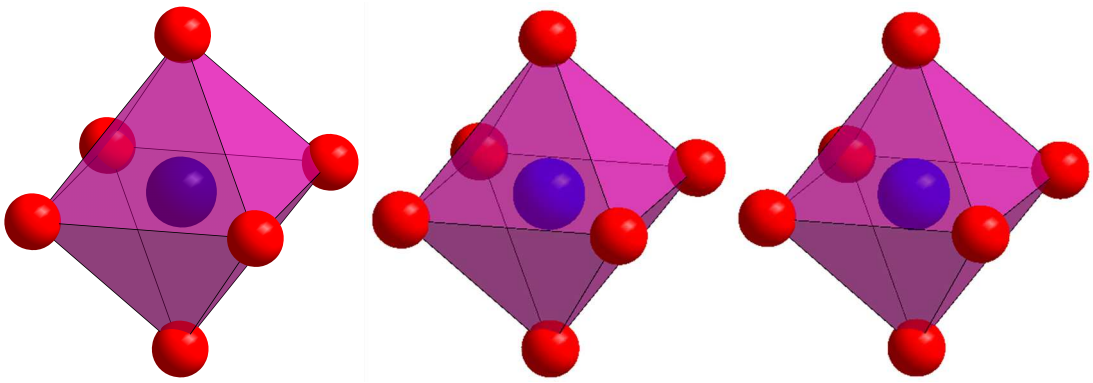

Figure 7.11: Nb/Te-O_6 octahedra for $KNbTeO_6$ (left), $RbNbTeO_6$ (middle) and $CsNbTeO_6$ (right).

To summarise, Rietveld refinements reveal a distortion of the crystal structure that is decreasing from $KNbTeO_6$ to $CsNbTeO_6$. However, the amount of defects – as shown by UV/vis spectroscopy and XPS – is increasing in reverse order. The distortion of the crystal structure results in strain, which can be diminished by the formation of defects. This may explain, why the sample with the highest amount of defects has the smallest crystal structure distortion and vice versa.

The Raman spectra of all three samples show the same bands (Figure 7.12, left); band assignment has been done according to Maczka *et al.*[153] The A_{1g} mode (500 cm^{-1}) stems from the symmetric stretching of the NbO_6/TeO_6 octahedra and is the most intense band for all

samples.[92] The relative intensities of the Raman modes below 250 cm^{-1} are vastly different for all three samples. These bands result from bending modes of NbO_6/TeO_6 coupled with translation modes of A and Nb/Te.[92] The mobility of the three A cations in the hexagonal channels is different for each A cation, resulting in more or less intense Raman bands. $RbNbTeO_6$ and $CsNbTeO_6$ also show an intense band at 780 and 790 cm^{-1}, respectively, with a strong shoulder at higher wavenumbers.

These bands have first been ascribed to second-order Raman scattering;[92] the temperature dependence of these bands, however, excludes second-order Raman scattering.[153] Raman bands at similar wavenumbers have been observed for $R_2Ti_2O_7$ pyrochlores (R = Y^{3+}, Gd^{3+}, Dy^{3+}).[178] Cation antisite defects have been reported to result in a rearrangement of the oxygen sublattice and low coordinated Ti^{4+} cations, which in turn result in lower Ti–O distances. Cation antisite defects are by definition not possible in $AM_xM'_{2-x}O_6$ defect-pyrochlores, since M and M' are already occupying the same site and A cations are far too large to occupy this site. Instead these bands belong to stretching modes of shorter than normal Nb–O or Te–O bonds, which result from vacancies in the centre of the octahedra.[153] These vacancies are more predominant in $RbNbTeO_6$ and $CsNbTeO_6$, which is in accordance with UV/vis spectroscopy and XPS.

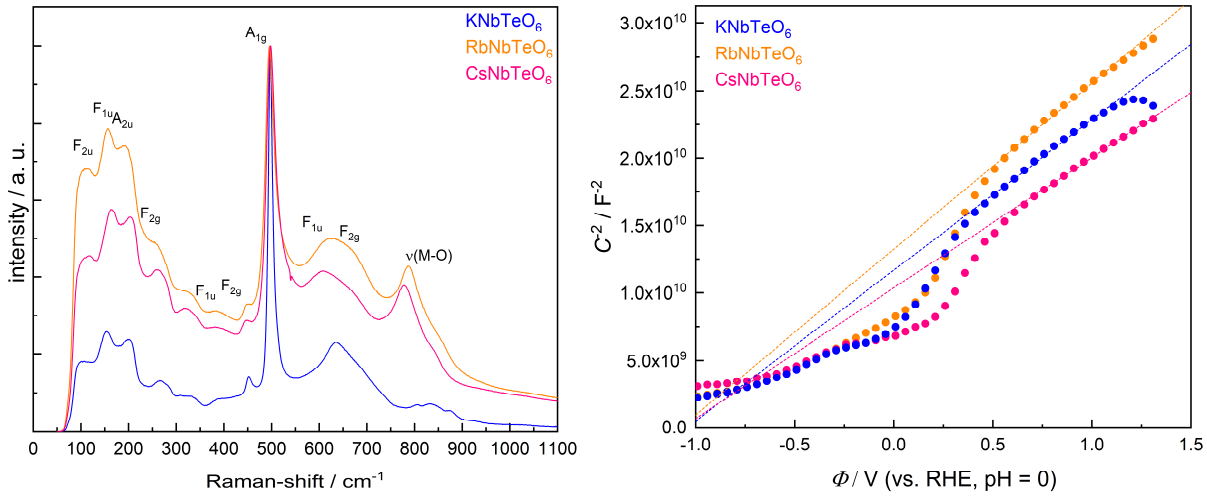

Figure 7.12: Raman spectra (left) and Mott-Schottky plots (right) of $ANbTeO_6$ compounds.

Mott-Schottky analysis has been performed to check if these materials are suitable for photocatalytic hydrogen evolution (Figure 7.12, right). The positive slopes of the curves imply n-type semiconducting behaviour for $ANbTeO_6$ materials. The slopes of all three curves are almost identical; the charge carrier concentrations should also be nearly identical. However, calculation of the charge carrier concentration requires the relative permittivity of these materials to be known, which is not the case. The flat band potentials are located at approximately –0.8 V, which makes these materials suitable for hydrogen evolution. The flat

band potential is similar to these of tungsten-based defect-pyrochlores (see sections 5.5 and 6.4). The crystal structure and therefore the position of the oxygen atoms are identical in all defect-pyrochlore materials; the VB – consisting of O 2*p* states – should thus be located at the same potential. Since the bandgaps of $ANbTeO_6$ materials are also similar to those of $KTaWO_6$ and $CsM_xW_{2-x}O_6$ (for M^{n+} cations with d^0 or d^{10} electron configuration), the CB should also be located at a similar potential. Moreover, calculations revealed that the CB minimum consists mainly of Nb 4*d* and O 2*p* states, whereas Te states form the upper CB.[58]

The photocatalytic activity depends on the surface area. The BET surface areas have been measured with krypton physisorption and are 0.7 $m^2\ g^{-1}$ for $KNbTeO_6$ and $CsNbTeO_6$ and 0.6 $m^2\ g^{-1}$ for $RbNbTeO_6$. The small surface areas are a consequence of the high temperatures necessary for solid state reaction and the absence of any porogen or surfactant.

The morphology of $KNbTeO_6$ has been investigated with SEM (Figure 7.13). SEM images of $KNbTeO_6$ show mostly octahedra with a smooth surface. Contrary to that, $RbNbTeO_6$ and $CsNbTeO_6$ are consisting of irregularly shaped particles; these are far more agglomerated than for $KNbTeO_6$.

A summary of important material parameters is depicted in Table 7.2.

Table 7.2: Summary of material parameters of $ANbTeO_6$.

sample	a / Å	L_a / nm	η	E_g / eV	ϕ_{FB} / V	A_{BET} / $m^2\ g^{-1}$
$KNbTeO_6$	10.2561	238 ± 28	12.9 ± 0.4	3.4	–0.8	0.7
$RbNbTeO_6$	10.2590	325 ± 54	3.8 ± 1.1	3.4	–0.9	0.6
$CsNbTeO_6$	10.3008	150 ± 24	5.4 ± 0.3	3.4	–0.7	0.7

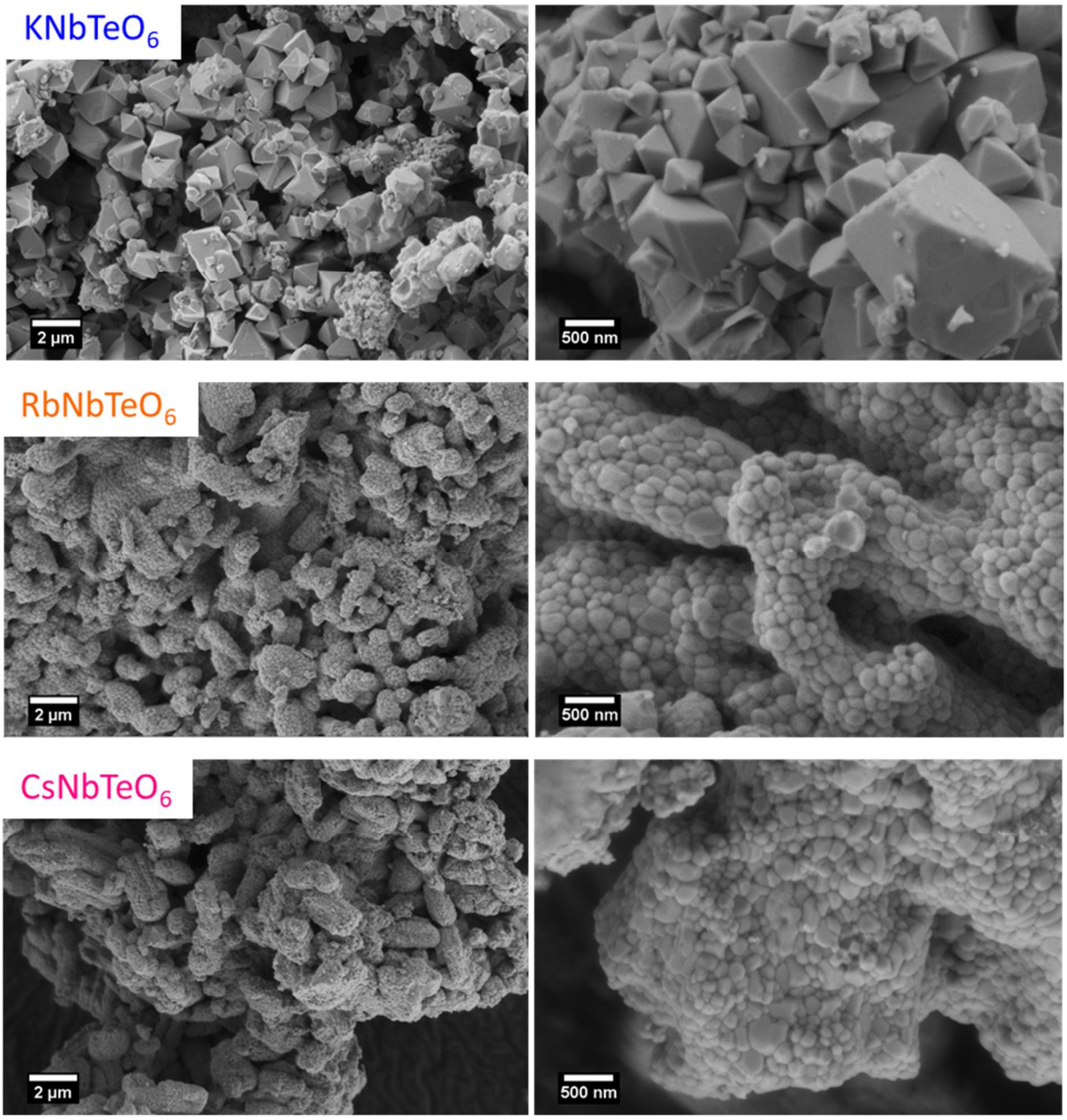

Figure 7.13: SEM images of $KNbTeO_6$ (top), $RbNbTeO_6$ (middle) and $CsNbTeO_6$ (bottom).

7.2 Photocatalytic Activity

All three samples showed hydrogen evolution under UV irradiation (Figure 7.14, left). At approximately 30 minutes the hydrogen evolution rate seems to approach a steady-state level. However, the rate is then sharply increasing, but subsequently declines slowly over the course of six hours. A true steady-state level is never reached. The sharp increase suggests a change of the samples upon irradiation and that a more active state is formed. The gradual decline hints at a slow, but constant decomposition of the samples. Although the detector settings of

the used mass spectrometer were identical for all three samples, the signal-to-noise ratio vastly differs. To exclude a faulty detector, the software and detector were stopped and restarted (the resulting gap in the data of roughly one minute can be neglected) with no effect during the $RbNbTeO_6$ measurement. The different signal-to-noise ratios seem to be intrinsic to the measured samples.

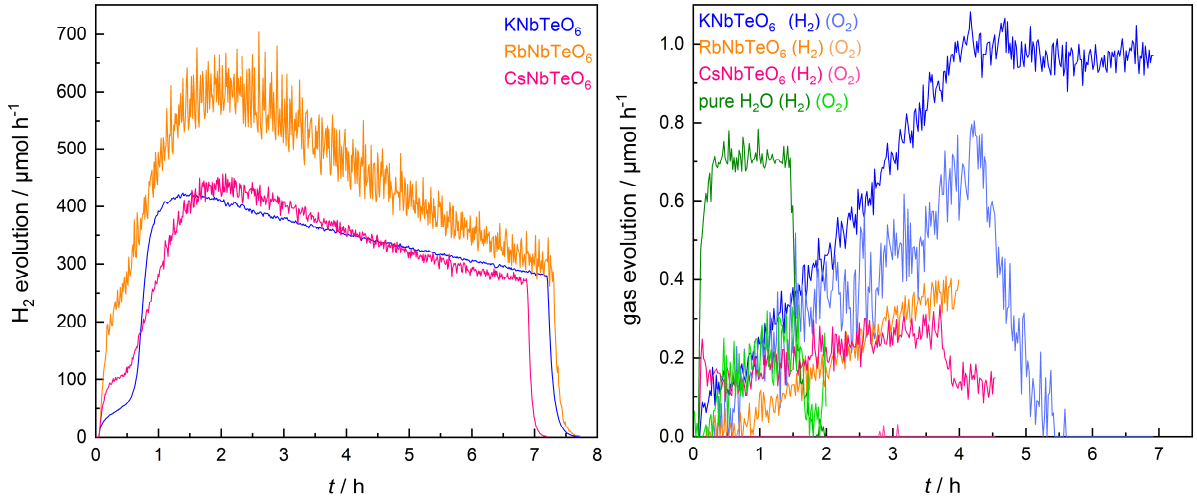

Figure 7.14: Hydrogen evolution of $ANbTeO_6$ with Rh in water/methanol under UV light irradiation (left) and water splitting of pure water and $ANbTeO_6$ with Rh/Cr_2O_3 in water under UV light irradiation (right).

Overall water splitting was attempted with $ANbTeO_6$ with previously photodeposited Rh/Cr_2O_3 as co-catalyst (Figure 7.14, right). The detected amounts of hydrogen and oxygen are barely above the limit of detection; this is also the most likely reason why hydrogen and oxygen are not in a 2:1 ratio. Irradiation without any photocatalyst present also resulted in the evolution of hydrogen and oxygen – the likely reason is the direct photolysis of water. Due to the nearly identical amounts, the evolved hydrogen and oxygen more likely originate from photolysis instead of photocatalysis.

Photocatalytic hydrogen evolution in simulated solar light did not result in the formation of hydrogen (not shown). The high bandgap of 3.4 eV would preclude photocatalysis in solar light, although there is a literature report about sacrificial hydrogen evolution with $KTaTeO_6$ in actual solar light.[25] However, these results are highly questionable, since an amount of hydrogen of approximately 100 µmol h^{-1} g^{-1} is already reported for 0 h.[25]

To conclude, $ANbTeO_6$ may be active in sacrificial hydrogen evolution but changes in (at least) two different pathways upon irradiation with UV light and is not active in overall water splitting. $ANbTeO_6$ also did not show any activity in sacrificial hydrogen evolution in simulated solar light.

7.3 Material Characterisation after Light Irradiation

Extensive postcatalytic characterisation has been performed to elucidate the changes in hydrogen evolution shown above. XRD patterns of $ANbTeO_6$ samples after photocatalytic hydrogen evolution show the same phase-purity and high crystallinity as prior to irradiation (Figure 7.15, left). SEM images also do not show any change in morphology (Figure 10.34, appendix). UV/vis spectroscopy reveals that the visible light absorption has changed after irradiation, indicating a change of the defects present in these samples (Figure 7.15, right). Raman spectra show small changes in relative intensities (Figure 10.35, appendix); however, these changes do not correlate with the changes observed in the UV/vis spectra.

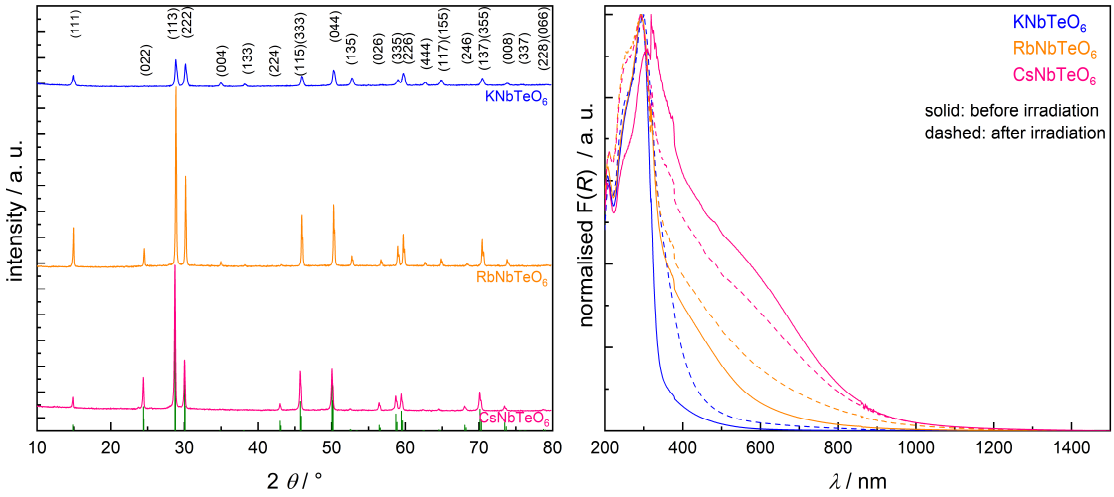

Figure 7.15: XRD patterns after photocatalysis (left) and Kubelka-Munk absorption spectra of $ANbTeO_6$ before and after photocatalysis (right).

XPS measurements have been performed to investigate changes of surface and defects. The surface composition after irradiation is deficient on Te and especially A cations, which is in contrast to the Nb deficiency before irradiation (Table 7.3).

Table 7.3: Elemental compositions (normalised to Nb = 1) before and after irradiation.

	before irradiation				after irradiation				
sample	**A**	**Nb**	**Te**	**O**	**A**	**Nb**	**Te**	**O**	**method**
$KNbTeO_6$	0.89	1	0.99	6.88	0.79	1	0.97	6.95	EDX
	1.91	1	2.47	9.89	0.27	1	0.86	4.20	XPS
$RbNbTeO_6$	1.00	1	1.09	6.49	0.86	1	1.06	6.71	EDX
	1.67	1	1.65	8.00	0.16	1	0.65	2.93	XPS
$CsNbTeO_6$	1.05	1	1.24	6.88	0.84	1	1.09	6.95	EDX
	1.76	1	1.79	8.55	0.36	1	0.71	2.95	XPS

This can only be explained by the dissolution of A and Te cations. The photogenerated charge carriers seem to react with the surface itself rather than the adsorbed water molecules, resulting in the dissolution of A and Te cations. The presence of methanol as a hole scavenger suggests a reductive photocorrosion. Additionally, the lower O content on the surface suggests a general reduction of the surface. In contrast to the XPS results, the EDX measurements only reveal a slight reduction of A – that is due to dissolution of the only loosely bound A cations. The distinctive difference between bulk and surface compositions proves that the photocorrosion is limited to the surface. This also explains why XRD and SEM did not show any changes.

High resolution XP spectra of the Te 3*d* region reveal that Te(0) is now the most abundant Te state for all three samples and not Te(IV) as before irradiation (Figure 7.16, left). This is further evidence that the photocorrosion is reductive and not oxidative. The same additional signal at 574.5 eV as for Te and TeO_2 (Figure 7.3, right) has also been observed. As mentioned above, the binding energy is similar to that of TeO_2 glasses;[193] amorphous Te(IV) could be an intermediate between Te(IV) and Te(0). Since this signal has not been observed for pristine $ANbTeO_6$, the thermal and photoinduced reduction pathways seem to be different.

The Nb 3*d* spectra reveal a new signal at 204.5 eV or 204.8 eV (Figure 7.16, right) that could either be Nb(II) or Nb(IV) states. For identification of this state, literature values for the binding energies of niobium(II) oxide NbO and niobium(IV) oxide NbO_2 have been used. The reported binding energies for NbO are 203.7 eV, 203.8 eV and 204.7 eV, whereas the binding energies reported for NbO_2 are 205.7 eV, 206.1 eV, 206.4 eV and 207.6 eV (all respective to a C 1*s* signal at 284.8 eV).[204–207] The measured values fit rather well to those reported for NbO, indicating that a Nb(II) state forms during irradiation. This emerging state could be also a reason for the sharp increase in hydrogen evolution, since charge carriers which are trapped at Nb(II) could not recombine.

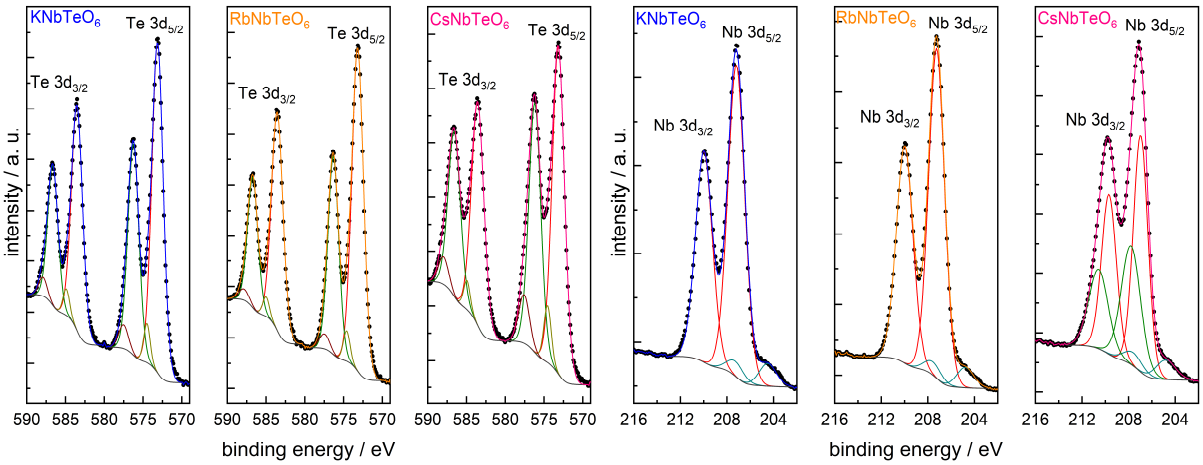

Figure 7.16: High resolution XPS of Te 3*d* states (left) and Nb 3*d* states (right) after irradiation. Signals attributed to Te(0) are depicted in red, Te(IV) in green and Te(VI) in brown. Signals attributed to Nb(V) are depicted in red or green and Nb(II) in cyan.

The O 1*s* signals of all three samples are the same as before irradiation; however, their relative intensities have changed (Figure 7.17, left). The signal corresponding to lattice oxygen has been increased, while the defective oxygen signal has been decreased (Figure 7.17, right). Moreover, the ratio of lattice/defect signal – that originally has been decreasing from $KNbTeO_6$ to $CsNbTeO_6$ – is identical for all three samples. No change could be observed in the high resolution XP spectra of the A cations (Figure 10.36, appendix).

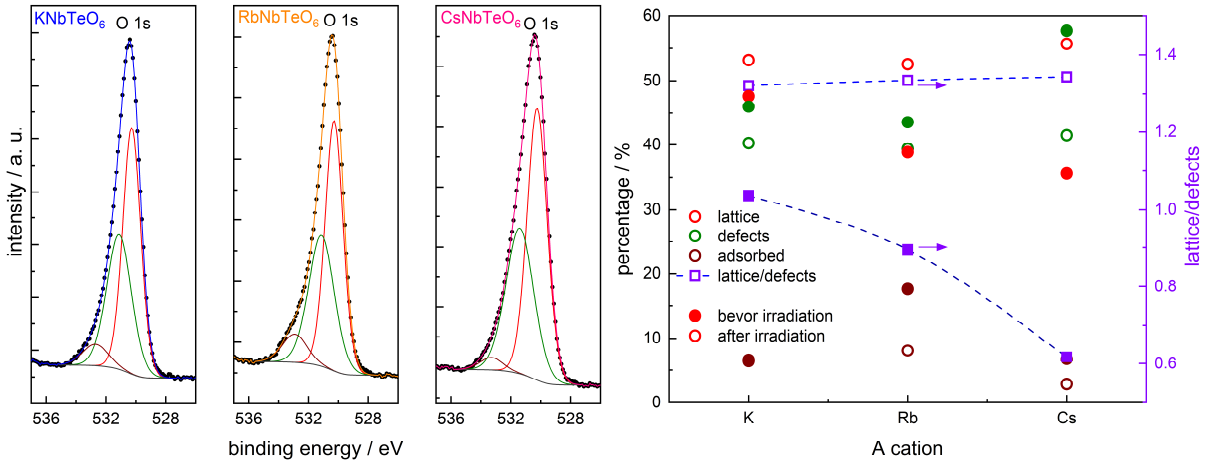

Figure 7.17: High resolution XPS of O 1*s* (left) and overview of O 1*s* states before and after irradiation (right).

To summarise, $ANbTeO_6$ suffers from reductive surface decomposition with a drastically changed surface composition. After irradiation Te(0) is the predominant Te species for all three samples and Nb(II) states could be detected.

8 Conclusion

Ion exchange with Sn^{2+} is considered a promising way to reduce the bandgap of metal oxides to make them photocatalytically active in visible light. $KTaWO_6$ was found to incorporate water molecules into the hexagonal channels of the defect-pyrochlore crystal structure. These water molecules greatly facilitate Sn^{2+} ion exchange compared to $CsTaWO_6$, which shows no water incorporation; the Sn^{2+} exchange reduces the bandgap from 3.6 eV to 2.2 eV. Theoretical calculations showed that the bandgap reduction does not purely result from the introduction of Sn^{2+} – as previously believed – but is indeed a cooperative effect requiring both Sn^{2+} ions and the coordination of a small molecule – such as water or methanol – to Sn^{2+}. Ion exchange may change the nature of the VB to CB transition from indirect to direct – or vice versa. Ion exchange in aqueous media results in the formation of a tin oxide layer on the semiconductor surface due to hydrolysis. A method to unambiguously determine the Sn oxidation state was developed using both photoelectron and Auger signals. Surface Sn^{2+} is easily oxidised to Sn^{4+} independent of the ion exchange conditions. Photocatalysis in visible light was not successful since Sn^{2+} is prone to photooxidation, therefore increasing the bandgap again.

A method to directly synthesise $TaWO_{5.5}$ at low temperatures *via* hydrothermal treatment was found.

A wide range of $CsM_xW_{2-x}O_6$ defect-pyrochlores – some of them previously unknown – were synthesised, characterised and employed in photocatalytic hydrogen evolution experiments. The solid solution crystal structure enables the incorporation of many different M^{n+} cations – from M^{2+} up to M^{5+} – without changing the structure, provided that the ionic radius of M^{n+} is in a certain range. The bandgap and band positions of all compounds with d^0 and d^{10} configuration of M^{n+} are very similar, since the band transition is dominated by O and W orbitals. This gives the opportunity to elucidate if certain M^{n+} ions are intrinsically better suited for photocatalysis without the error source of different crystal or band structures. Sacrificial hydrogen evolution experiments showed that photocatalytic activity is determined mainly by surface area and not M^{n+}. Using M^{n+} cations with partly filled *d* levels – such as Mn^{2+}, Cr^{3+}, Fe^{3+}, Co^{2+}, Ni^{2+} or Cu^{2+} – allows to reduce the bandgap to 2.1 eV at the most. However, this seems to drastically reduce the lifetime of the photogenerated charge carriers. These samples did not show any sacrificial hydrogen evolution in simulated solar light.

The origin of the visible light absorption of $ANbTeO_6$ (A = K^+, Rb^+ and Cs^+) could be traced to Te(IV) and Te(0) defects instead of a low bandgap as presumed in literature. The degree of crystal structure distortion depends on the A^+ cation. UV light irradiation results in reductive

photocorrosion of the sample surface followed by declining hydrogen evolution rates. Combined with the rarity – and therefore considerable price – of Te, it can be concluded that Te is not a suitable element for photocatalysis.

Although photocatalytic water splitting in visible light was ultimately not achieved, the gained knowledge in this work could be useful in developing new photocatalytic materials.

9 Outlook

The information gained on Sn^{2+} exchange in defect-pyrochlores – both theoretical and experimental – should also be applicable to other materials that are suitable for ion exchange, such as layered structures. Despite the susceptibility towards photooxidation, $Sn_xK_{1-2x}TaWO_6$ materials could be suitable for other applications. One possibility would be to use the change of the optical properties upon water incorporation as a material for humidity sensors. Using a protective layer to prevent surface oxidation – such as TiO_2 by atomic layer deposition – is a promising strategy to employ these materials in photocatalysis, *e. g.* NiO_x has been used successfully as a protective layer for α-$SnWO_4$.[39]

Proton exchanging $KTaWO_6$ results in $HTaWO_6 \cdot H_2O$, which can be used as proton conductor or solid acid catalyst.[96] Nanoparticles would be convenient due to their large surface area. Using the synthesis developed by Weller *et al*. would also result in a mesoporous material with high surface area and good mass transport properties.[116]

$CsM_xW_{2-x}O_6$ materials can be considered as isolated M^{n+} cations coordinated by oxygen in a matrix of WO_6 octahedra. This would make them interesting as pseudo single atom catalysts, since many transition metal cations are catalytically active. Their advantage would be that the active sites cannot sinter together and thus deactivate.

Another promising possibility would be the combination of a redox active M^{n+} cation – such as Mn^{2+} or Co^{2+} – and the substitution of Cs^+ with Li^+ as the alkaline metal cation located in the channels. Such a material would be an interesting electrode material for lithium ion batteries.

Transient absorption measurements in different atmospheres – inert or sacrificial agent-filled – combined with (or without) co-catalysts would be a versatile technique to investigate the charge carrier dynamics in $CsM_xW_{2-x}O_6$ materials in order to develop strategies to elongate their lifetimes.

The information gained on the defects and photocorrosion of $ANbTeO_6$ should also be applicable to other Te^{6+} containing materials.

10 Appendix

10.1 Additional Figures for Section 5

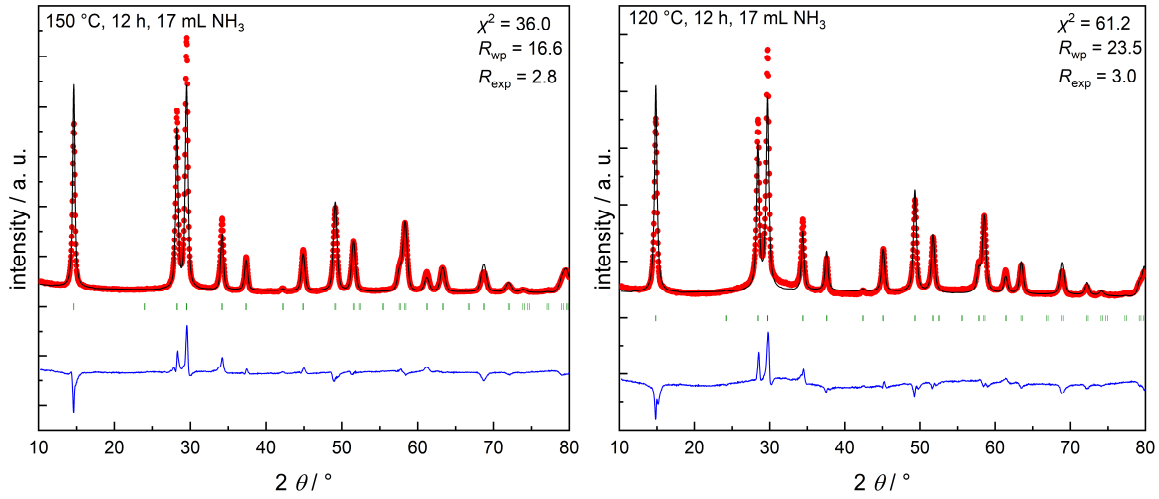

Figure 10.1: Rietveld refinements for two selected $KTaWO_6$ samples. Attempts to refine anisotropic thermal displacement parameters, atomic positions and occupancies only resulted in nonsensical values.

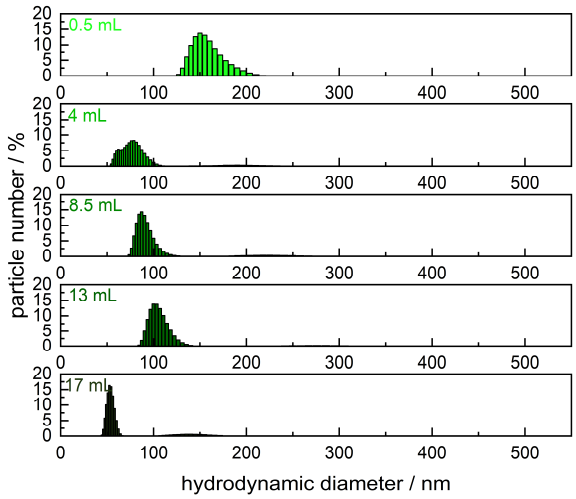

Figure 10.2: Particle size distributions for $KTaWO_6$ nanoparticles synthesised with different ammonia amounts.

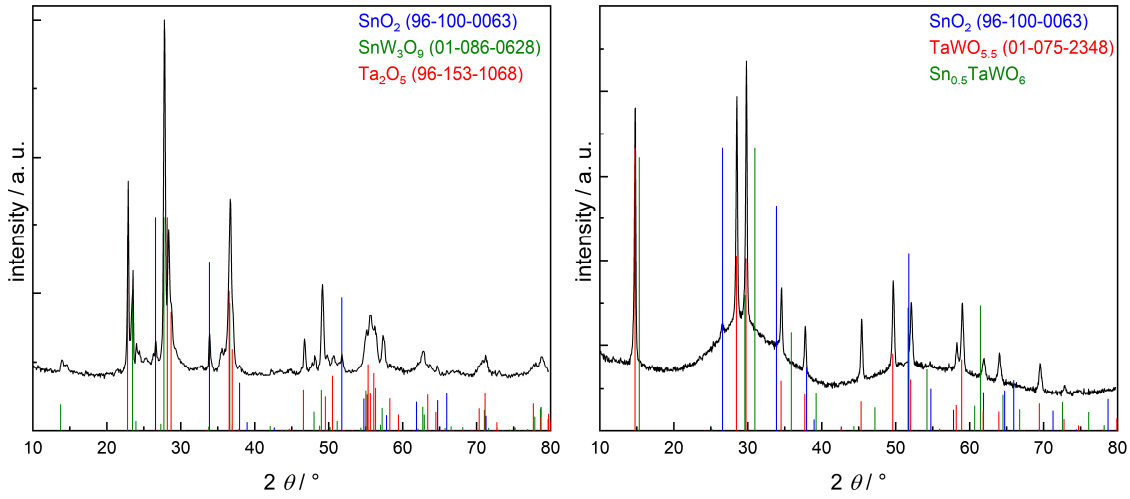

Figure 10.3: XRD patterns of the attempted synthesis of $Sn_{0.5}TaWO_6$ *via* solid-state reaction (left) and hydrothermal treatment (right).

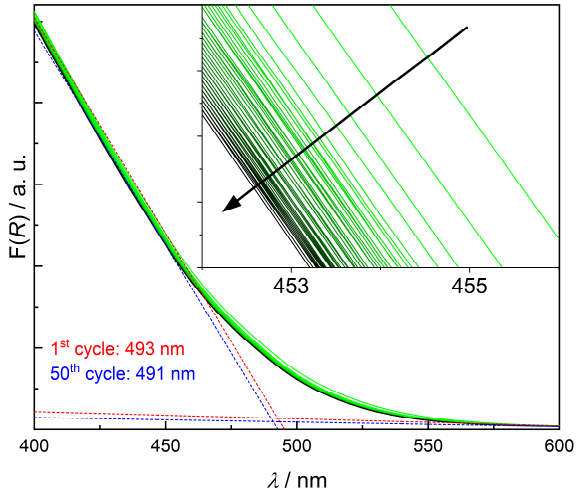

Figure 10.4: Kubelka-Munk absorption spectra of $Sn_xK_{1-2x}TaWO_6$. The dried sample – already within the sample holder – was taken out of the drying oven and directly placed into the spectrometer. The arrow indicates the chronological progression of the measurement cycles; each cycle lasted 54 seconds.

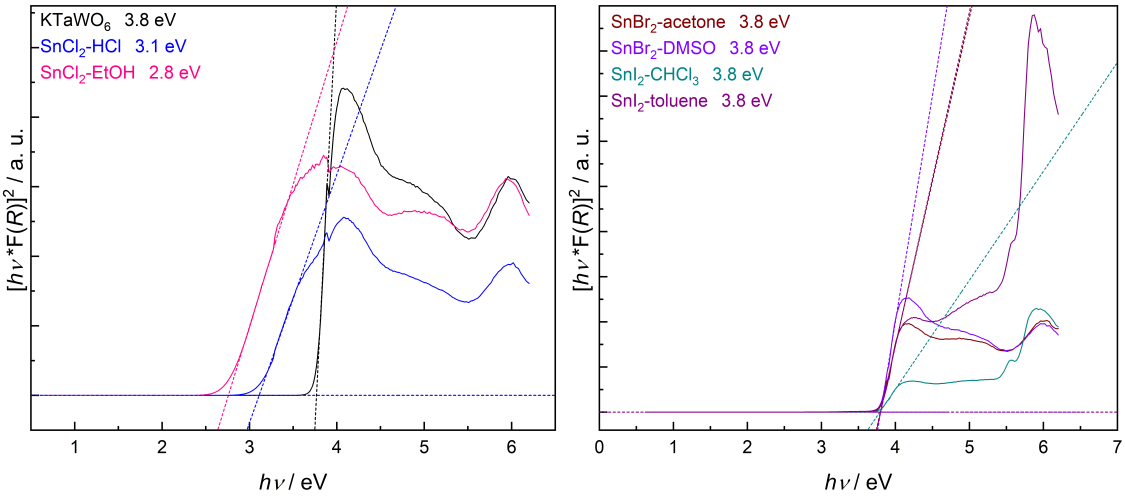

Figure 10.5: Tauc plots for direct bandgaps for samples exchanged with $SnCl_2$ (left) and $SnBr_2$ or SnI_2 (right).

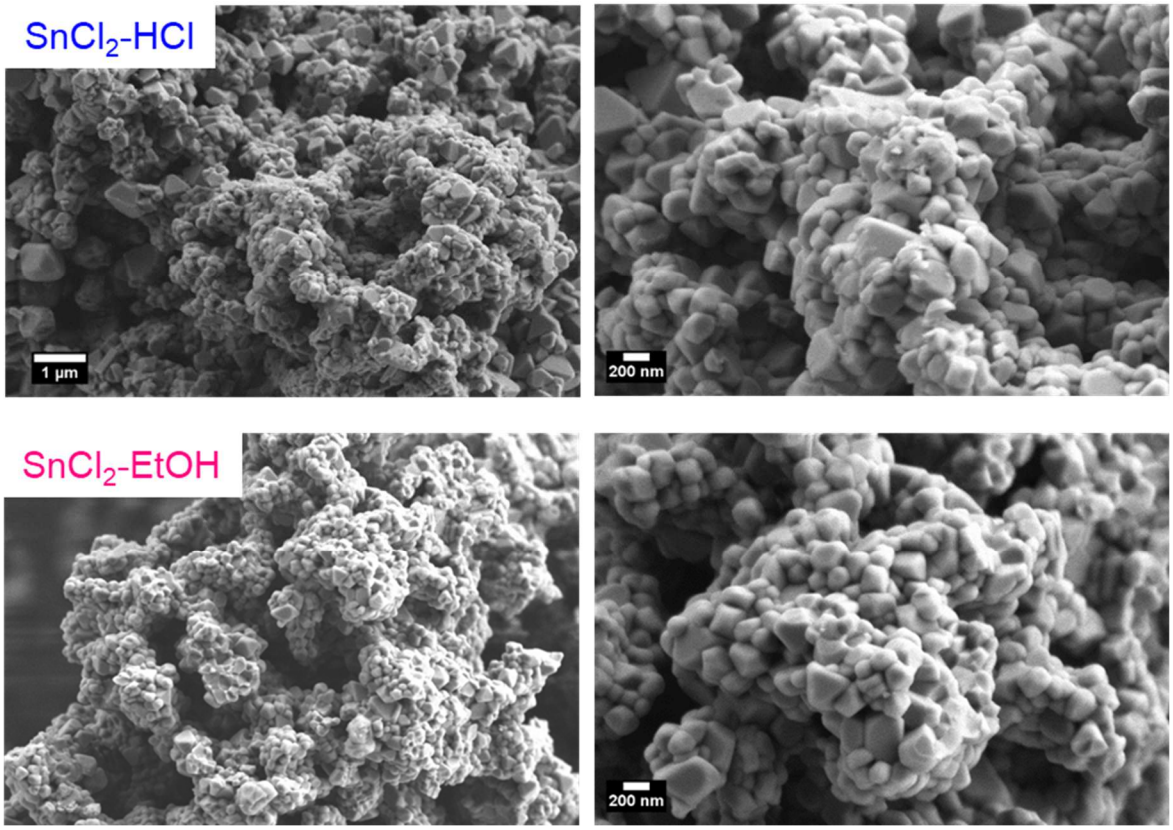

Figure 10.6: SEM images of the $SnCl_2$-HCl (top) and $SnCl_2$-EtOH (bottom) samples.

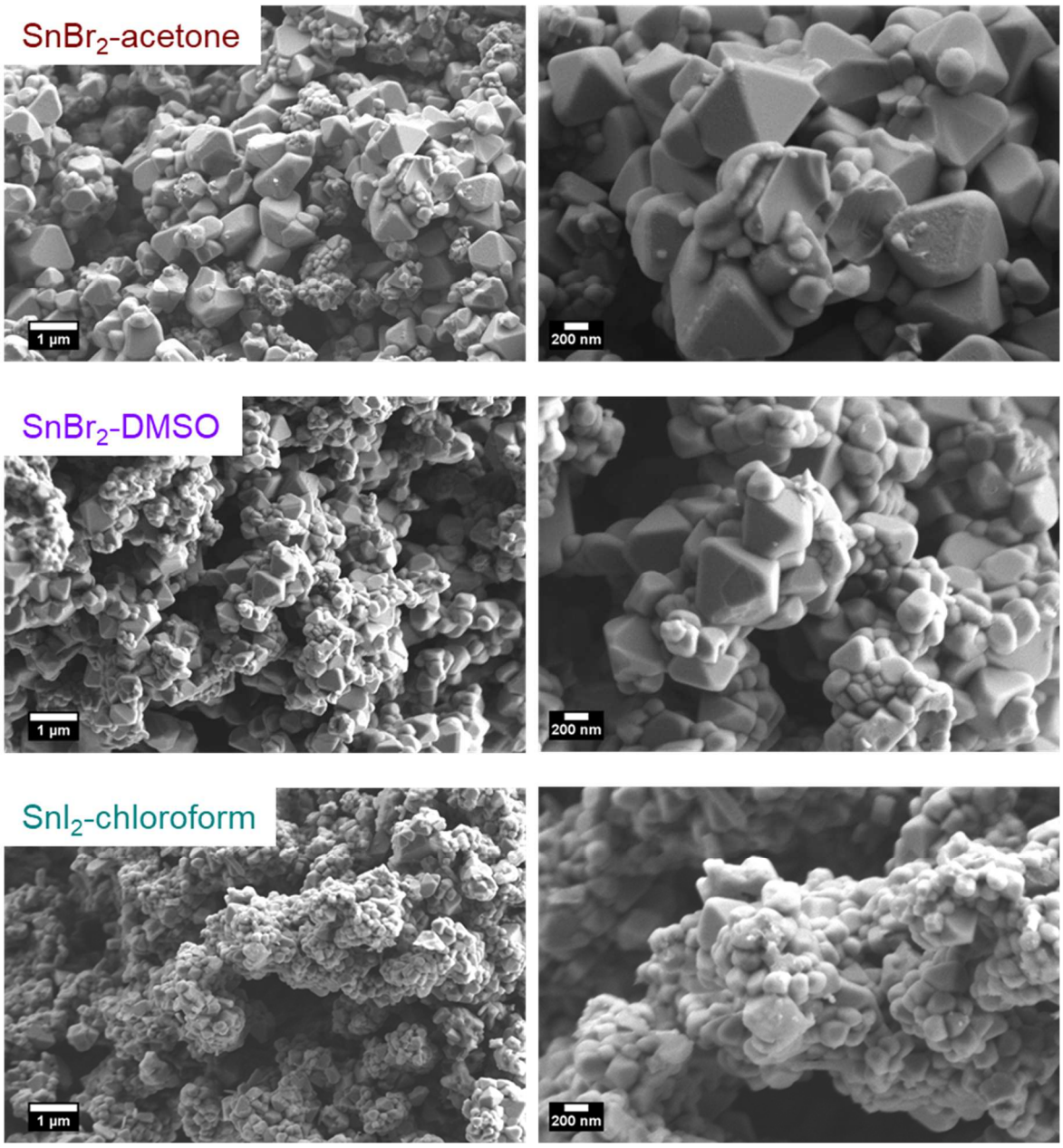

Figure 10.7: SEM images of the $SnBr_2$-acetone (top), $SnBr_2$-DMSO (middle) and SnI_2-chloroform (bottom) samples.

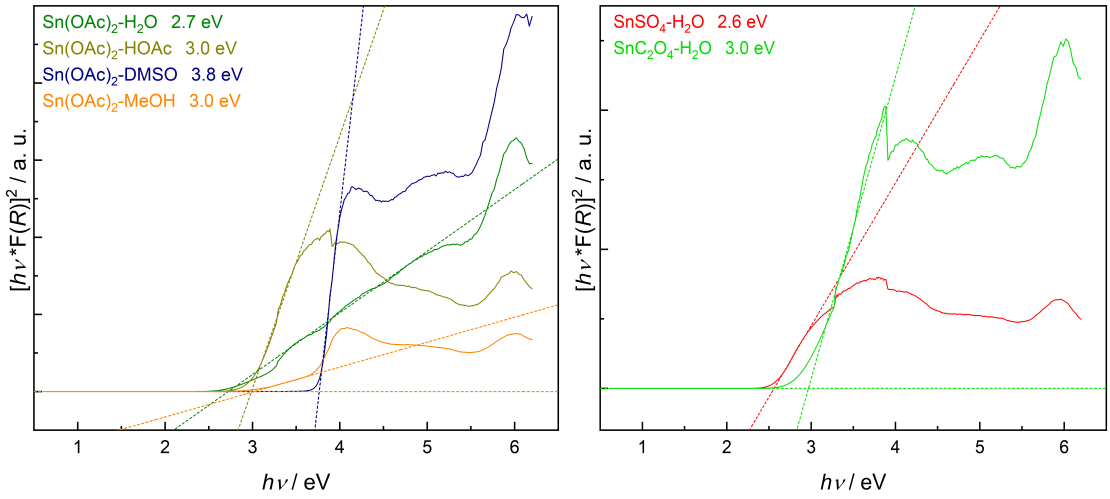

Figure 10.8: Tauc plots for direct bandgaps for samples exchanged with $Sn(OAc)_2$ (left) and $SnSO_4$ or SnC_2O_4 (right).

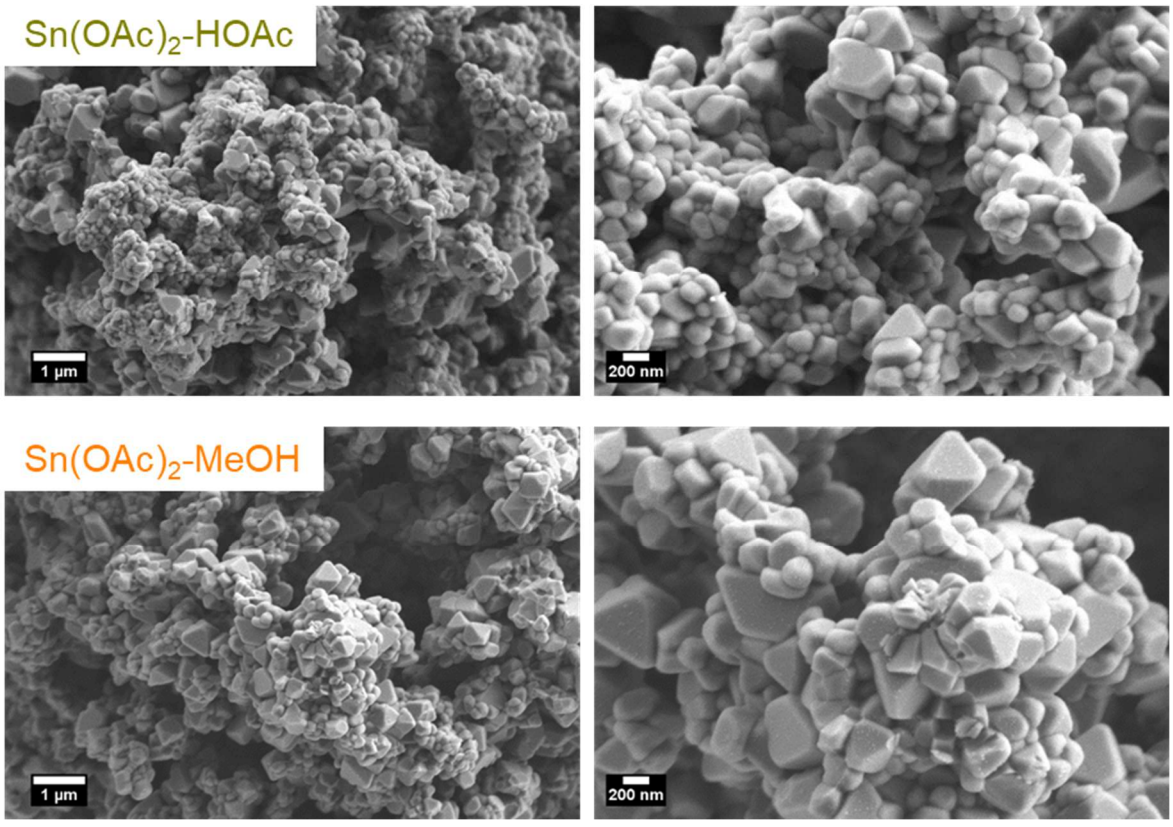

Figure 10.9: SEM images of $Sn(OAc)_2$-HOAc (top) and $Sn(OAc)_2$-MeOH (bottom) samples.

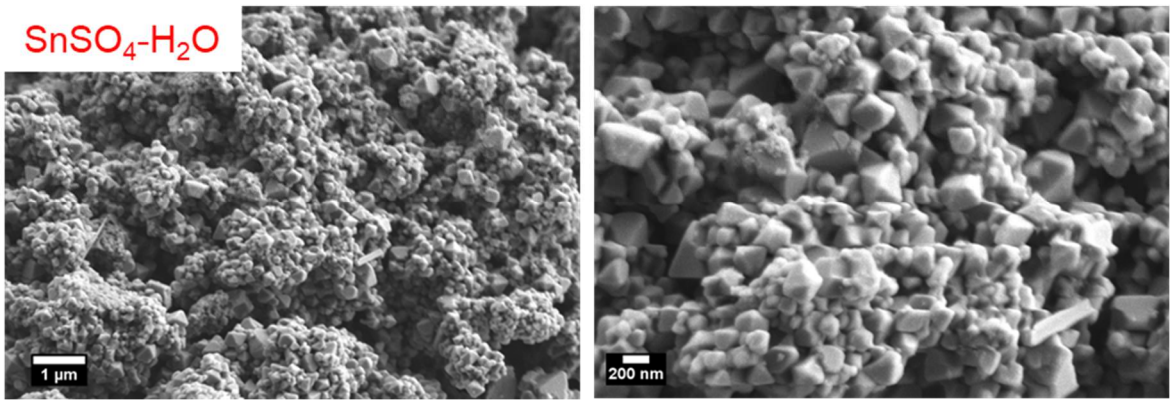

Figure 10.10: SEM images of the $SnSO_4$-H_2O sample.

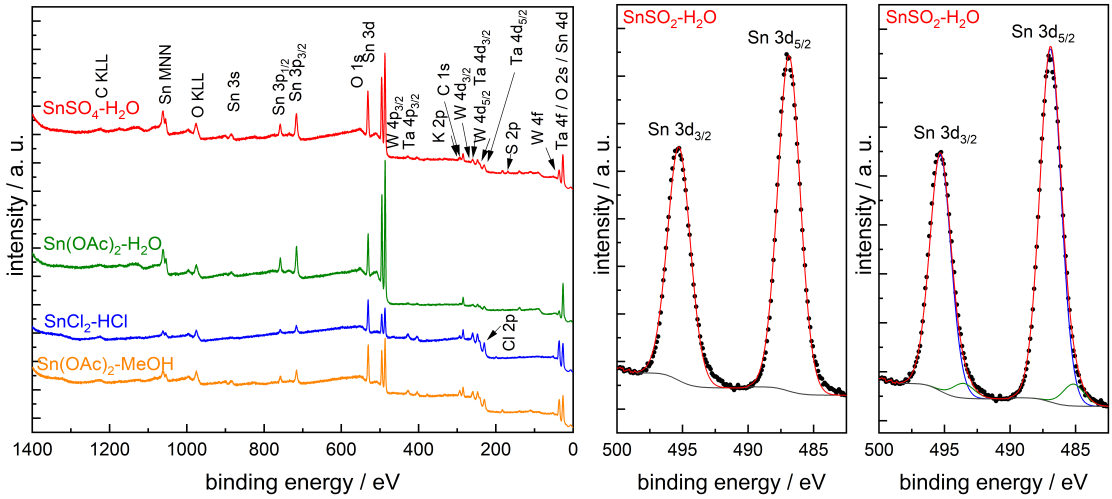

Figure 10.11: XPS survey spectra (left) and fittings attempts with one component (middle) and two components (right) for the Sn 3*d* signals of the $SnSO_4$-H_2O sample.

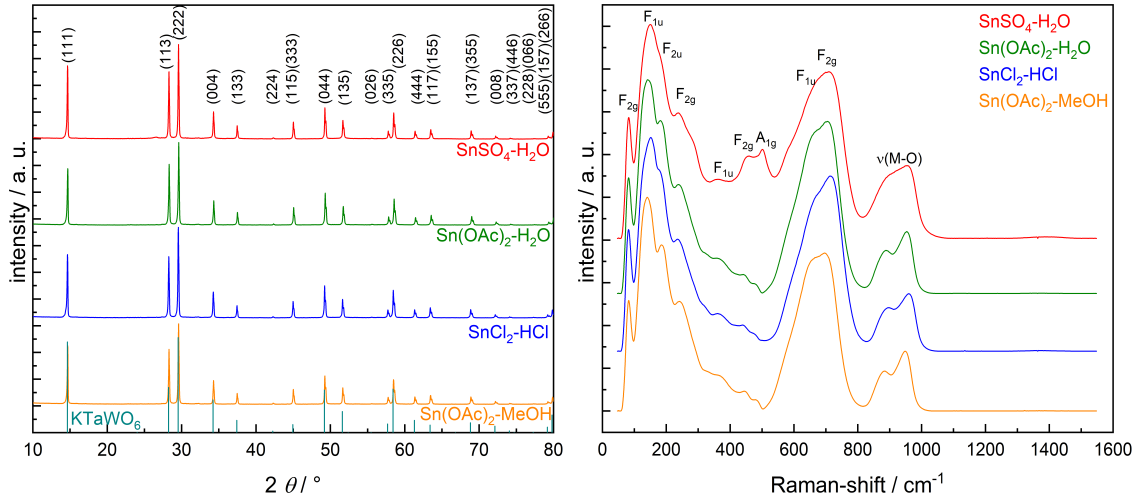

Figure 10.12: XRD patterns (left) and Raman spectra (right) of the samples after UV light irradiation.

10.2 Additional Figures for Section 6

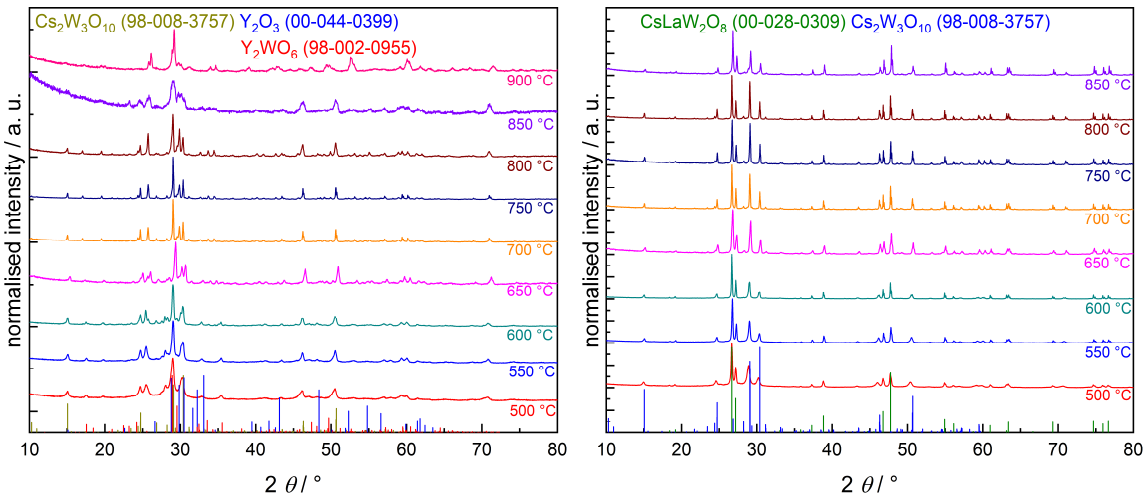

Figure 10.13: XRD patterns of the attempted synthesis of $CsY_{0.33}W_{1.67}O_6$ (left) and $CsLa_{0.33}W_{1.67}O_6$ (right).

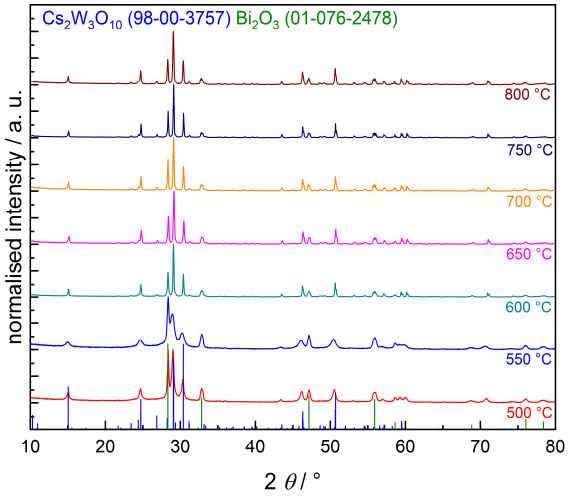

Figure 10.14: XRD patterns of the attempted synthesis of $CsBi_{0.33}W_{1.67}O_6$.

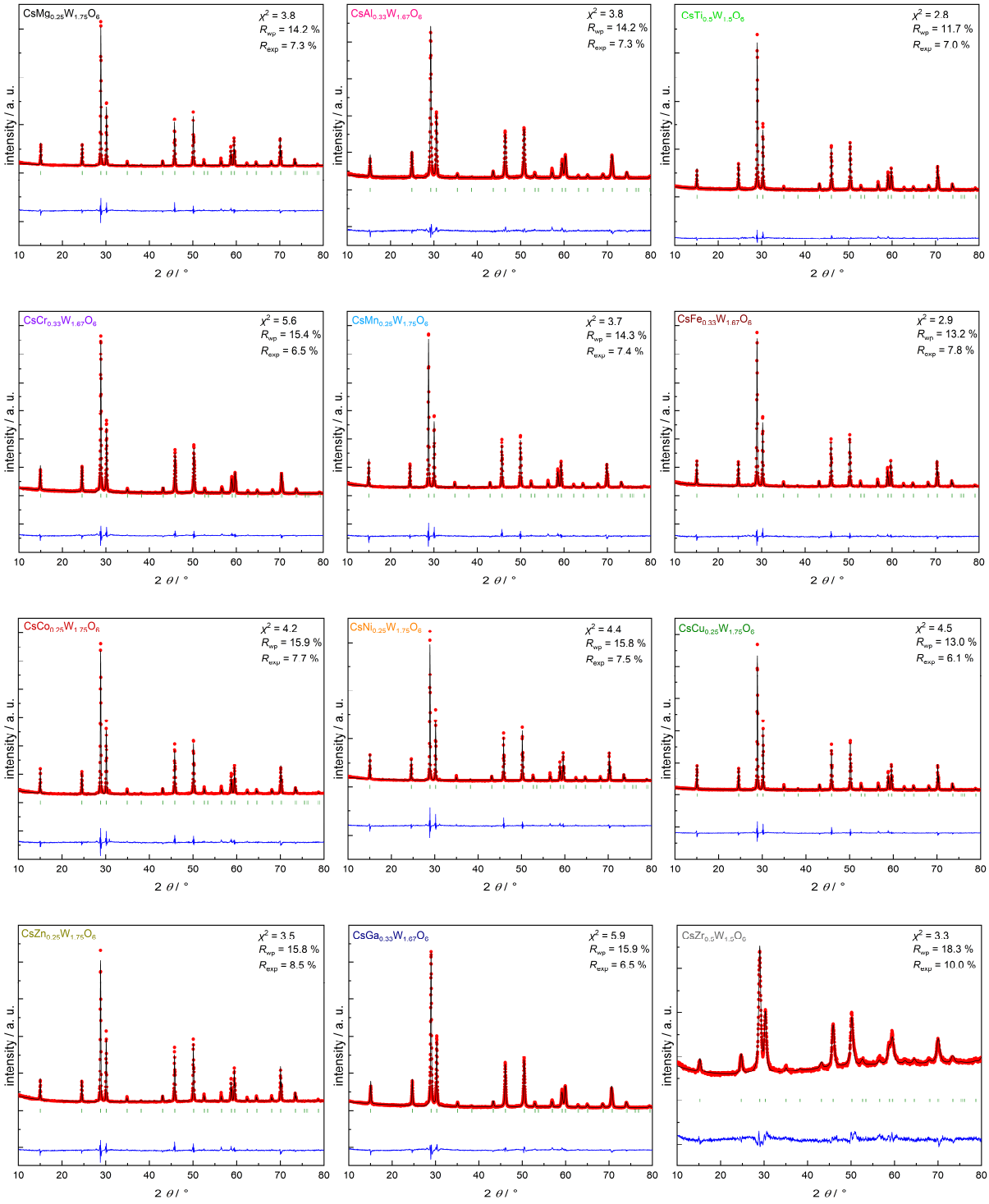

Figure 10.15: Rietveld refinements of phase pure $CsM_xW_{2-x}O_6$ compounds. All but one samples have been calcined at 800 °C for 10 h; $CsZr_{0.5}W_{1.5}O_6$ has been calcined at 600 °C instead to avoid thermal decomposition.

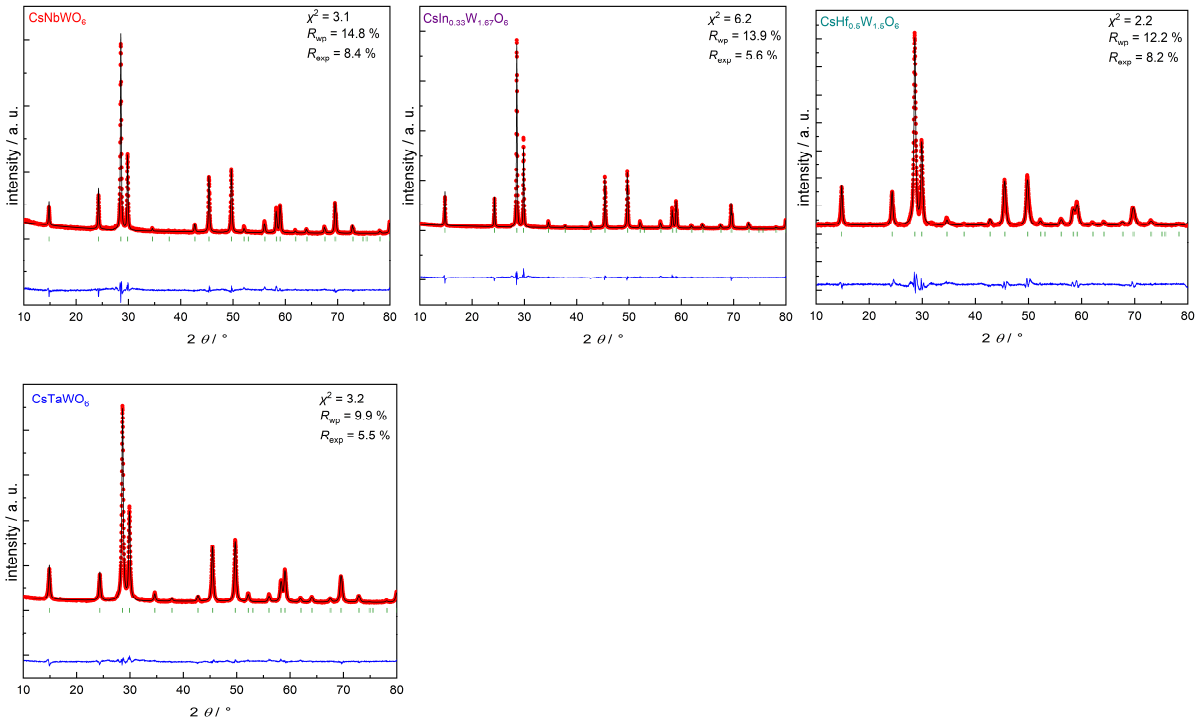

Figure 10.16: Rietveld refinement of phase pure $CsM_xW_{2-x}O_6$ compounds. All but one samples have been calcined at 800 °C for 10 h; $CsHf_{0.5}W_{1.5}O_6$ has been calcined at 600 °C instead to avoid thermal decomposition.

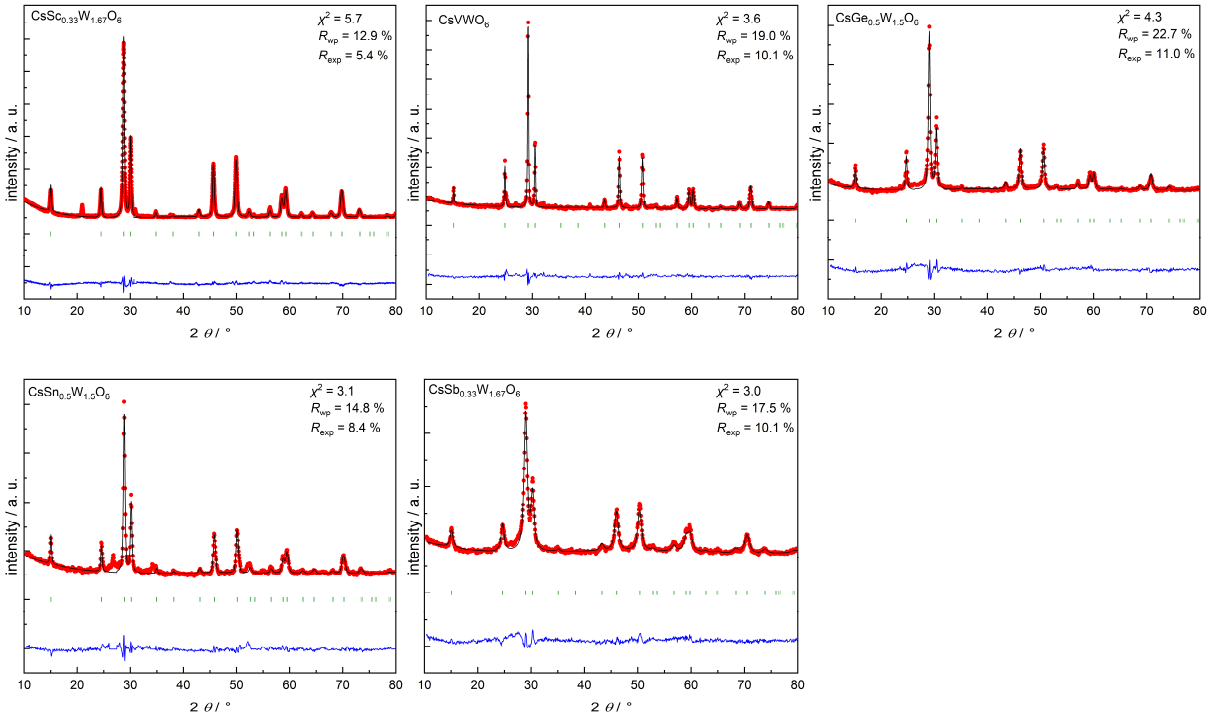

Figure 10.17: Rietveld refinement of not phase pure $CsM_xW_{2-x}O_6$ compounds. Reflections belonging to impurities have been excluded if necessary. $CsSc_{0.33}W_{1.67}O_6$ and $CsSn_{0.5}W_{1.5}O_6$ have been calcined at 800 °C, $CsSb_{0.33}W_{1.67}O_6$ and $CsGe_{0.5}W_{1.5}O_6$ and $CsVWO_6$ at 500 °C.

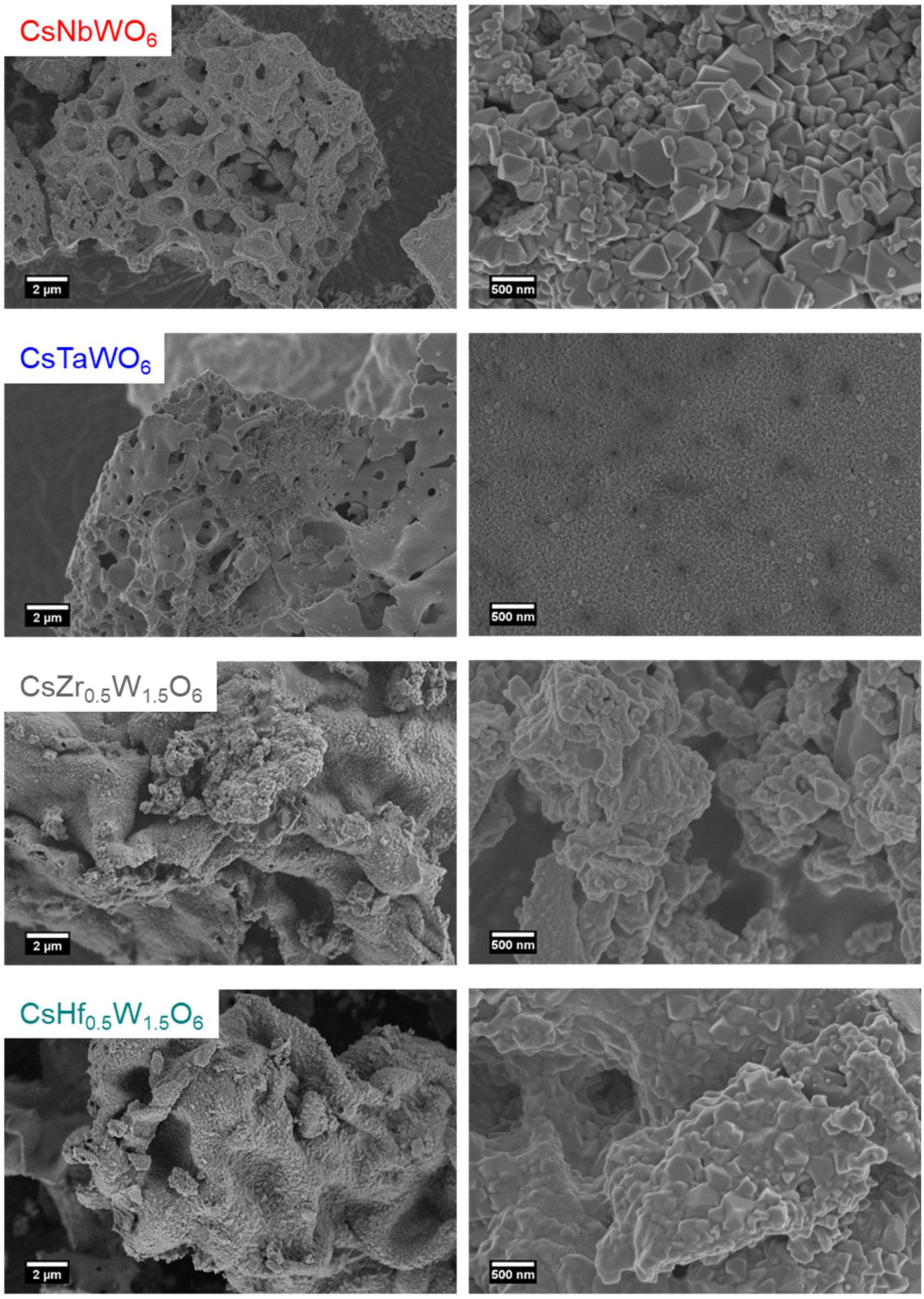

Figure 10.18: SEM images of $CsM_xW_{2-x}O_6$ samples.

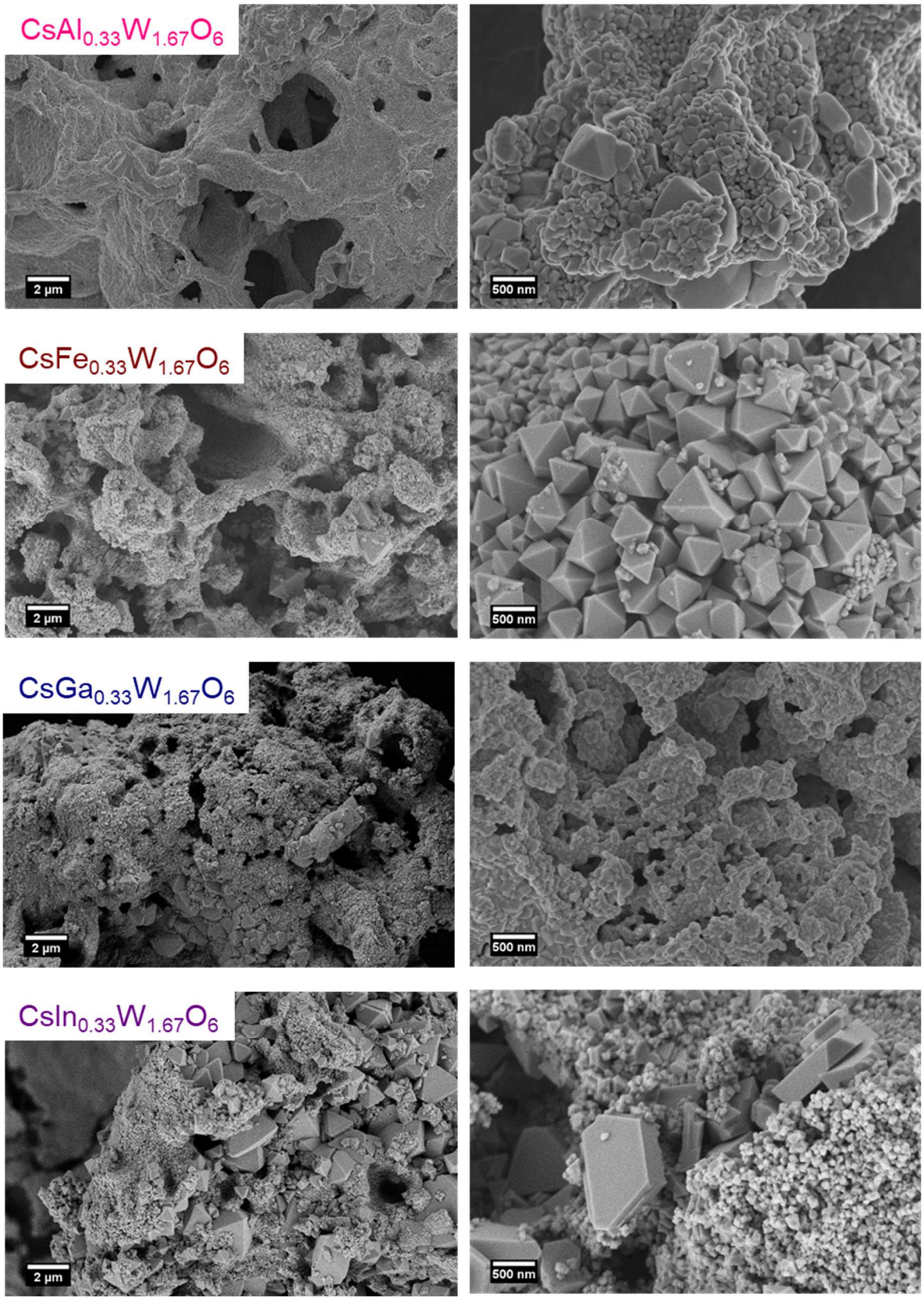

Figure 10.19: SEM images of $CsM_xW_{2-x}O_6$ samples.

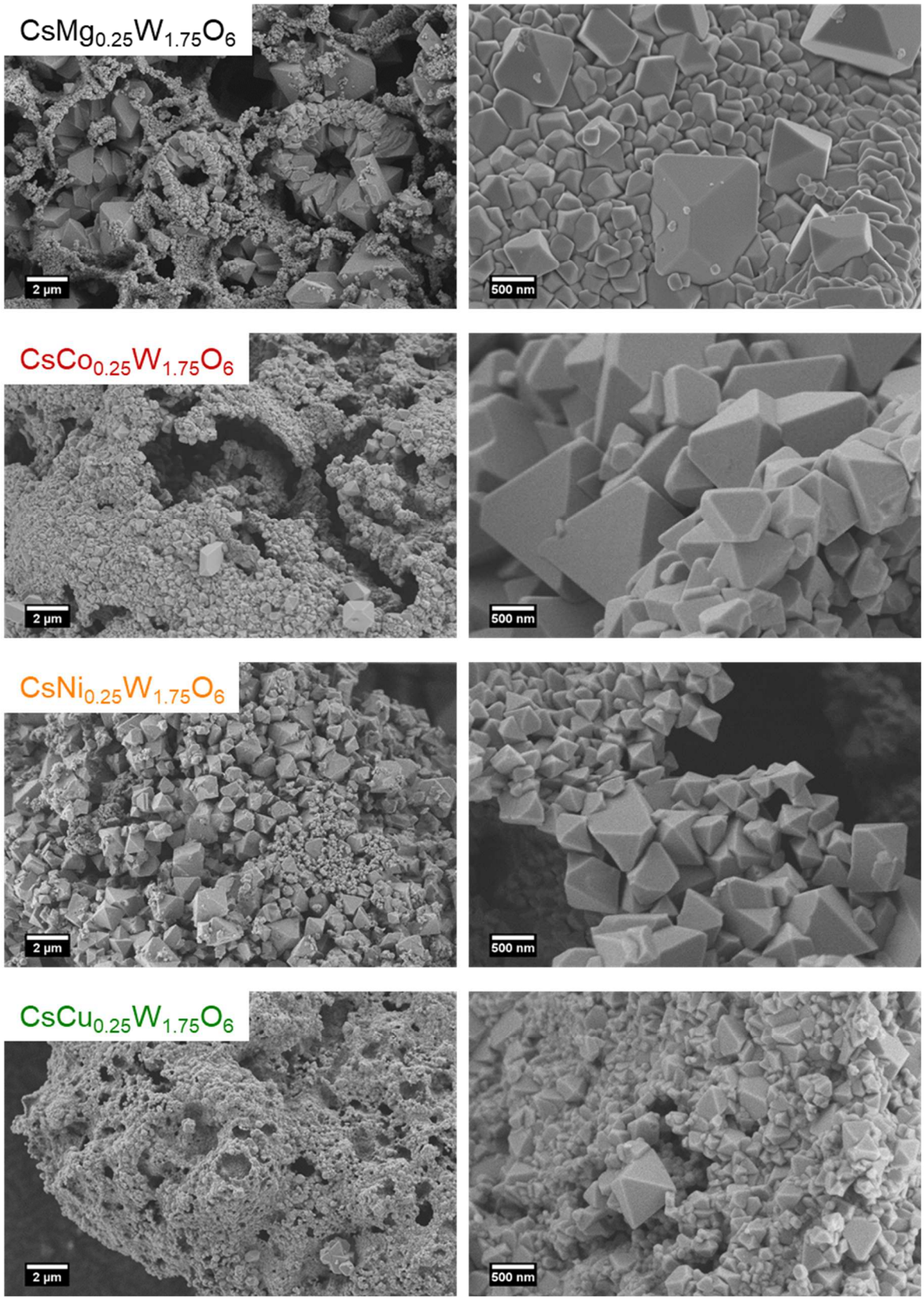

Figure 10.20: SEM images of $CsM_xW_{2-x}O_6$ samples.

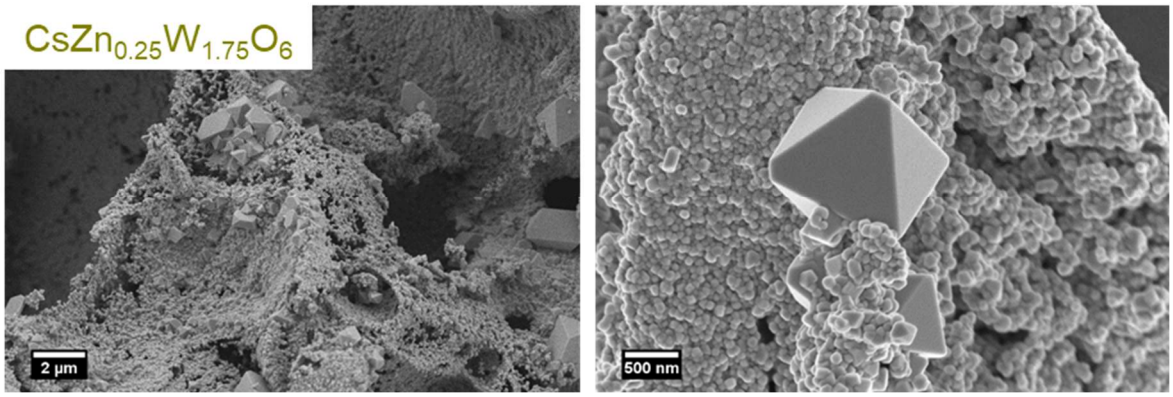

Figure 10.21: SEM images of $CsZn_{0.25}W_{1.75}O_6$.

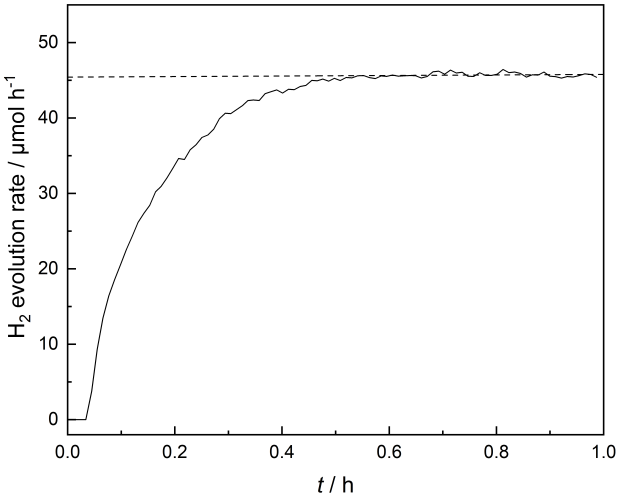

Figure 10.22: hydrogen evolution rate of a methanol/water mixture under UV light irradiation.

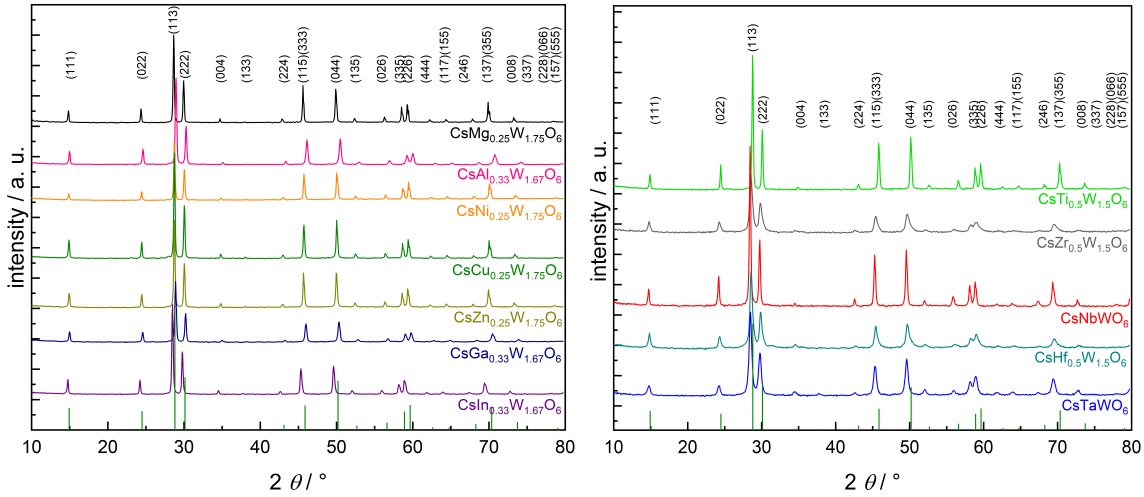

Figure 10.23: XRD patterns of $CsM_xW_{2-x}O_6$ samples after UV light irradiation.

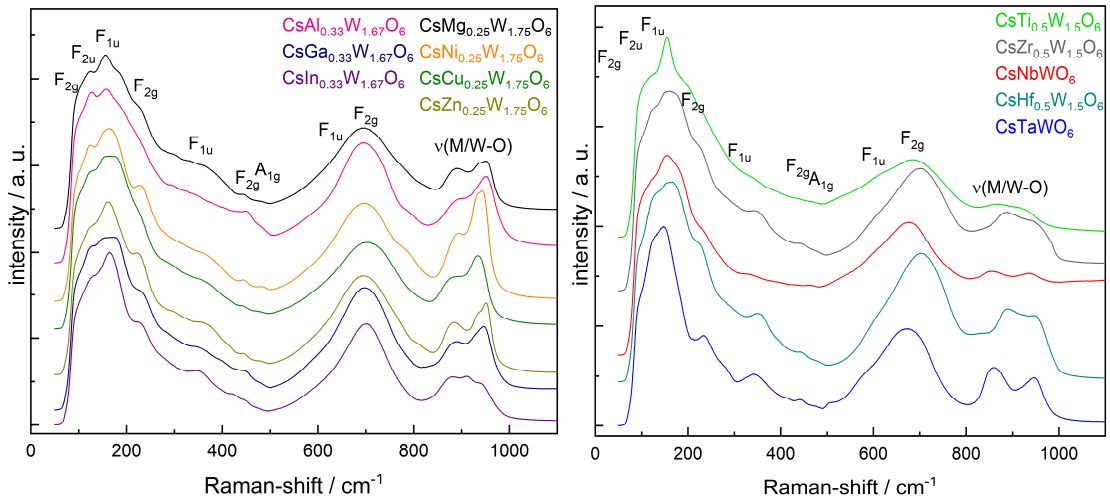

Figure 10.24: Raman spectra of $CsM_xW_{2-x}O_6$ samples after UV light irradiation.

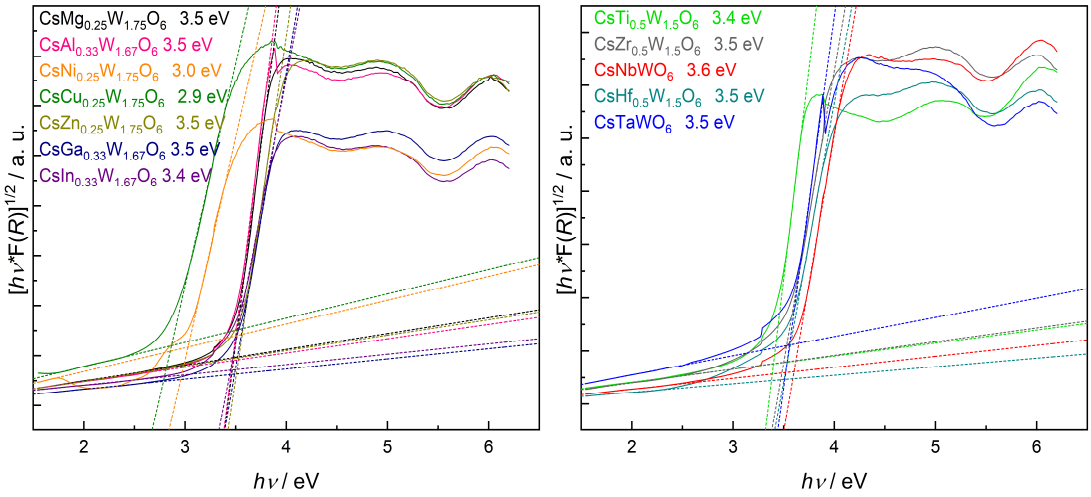

Figure 10.25: Tauc plots of $CsM_xW_{2-x}O_6$ samples after UV light irradiation.

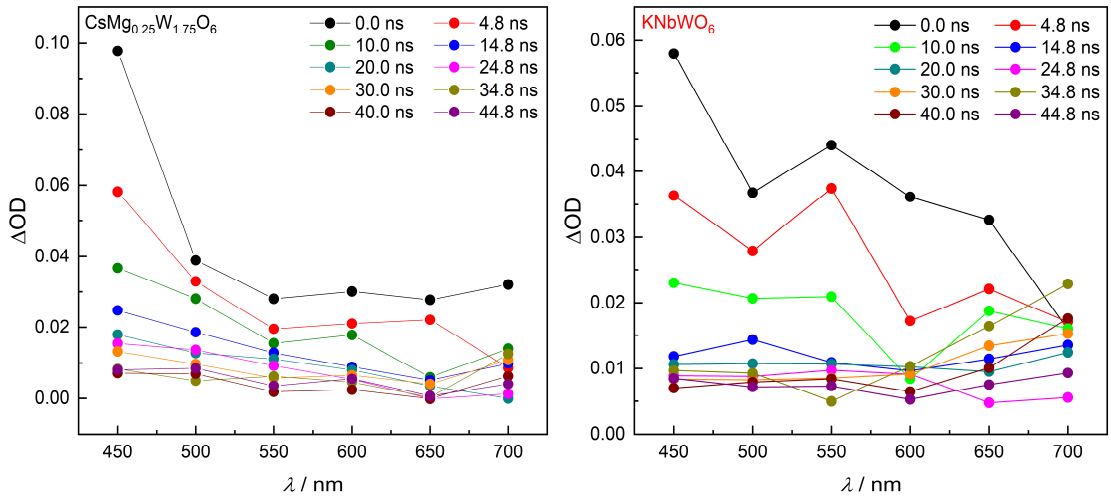

Figure 10.26: Transient absorption spectroscopy measurements at different wavelengths of $CsMg_{0.25}W_{1.75}O_6$ (left) and $CsNbWO_6$ (right). Excitation wavelength was 266 nm.

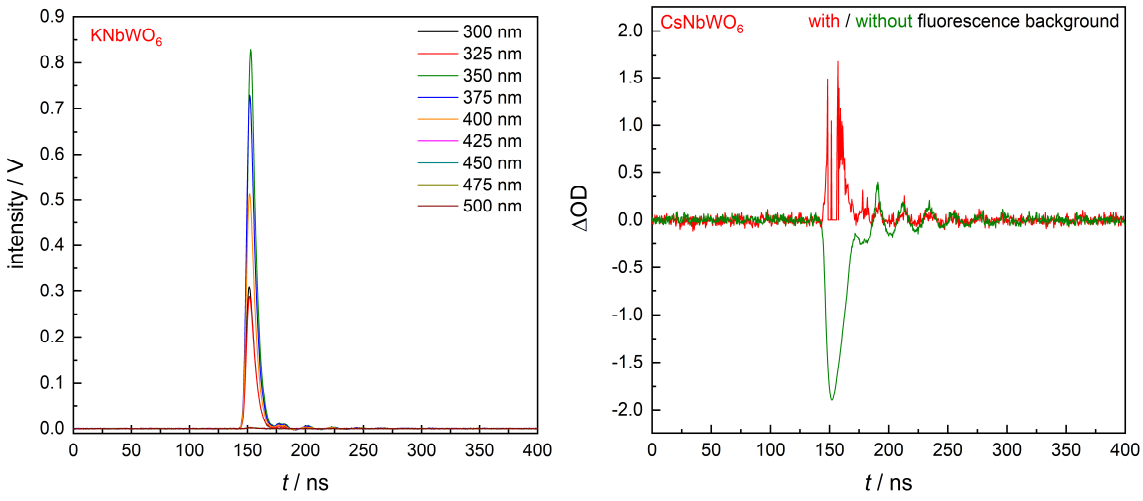

Figure 10.27: Fluorescence signals at different wavelengths (left) and transient absorption measurements at 400 nm (right) of $KNbWO_6$. Excitation wavelength was 266 nm.

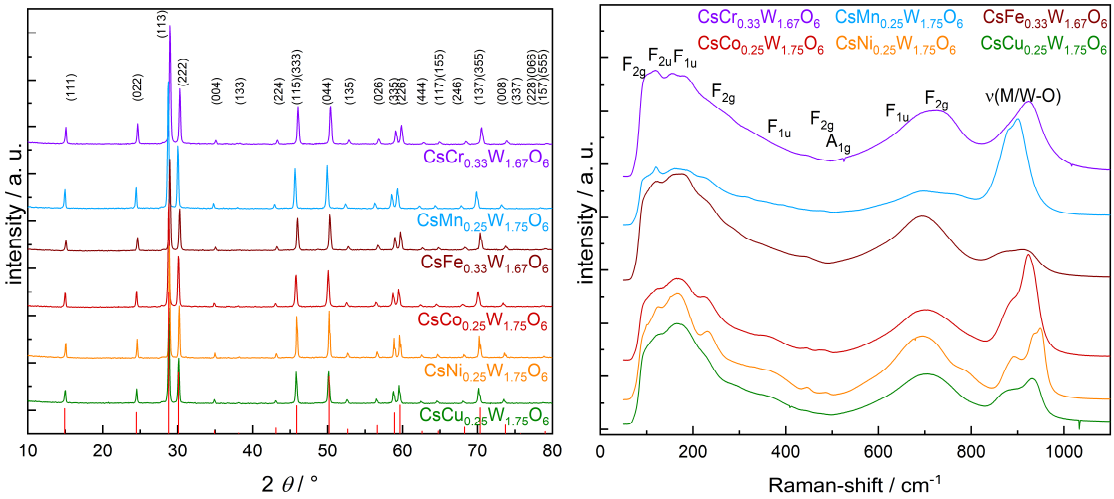

Figure 10.28: XRD patterns (left) and Raman spectra (right) of $CsM_xW_{2-x}O_6$ after simulated solar light irradiation.

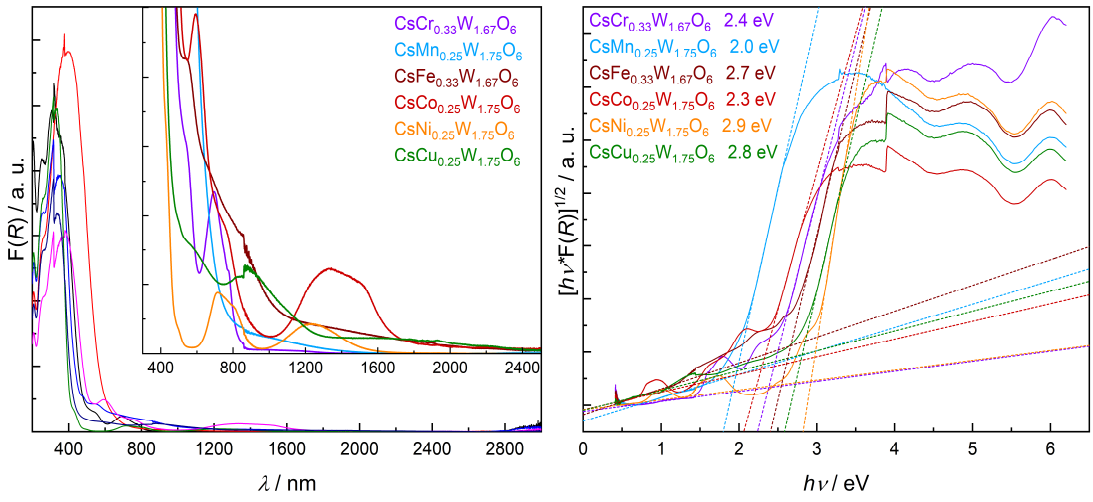

Figure 10.29: Kubelka-Munk absorption spectra (left) and Tauc plots (right) of $CsM_xW_{2-x}O_6$ after simulated solar light irradiation.

10.3 Additional Figures for Section 7

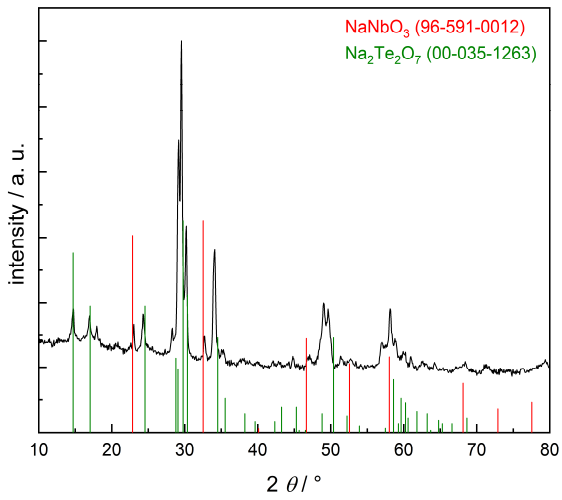

Figure 10.30: XRD pattern of the attempted synthesis of $NaNbTeO_6$.

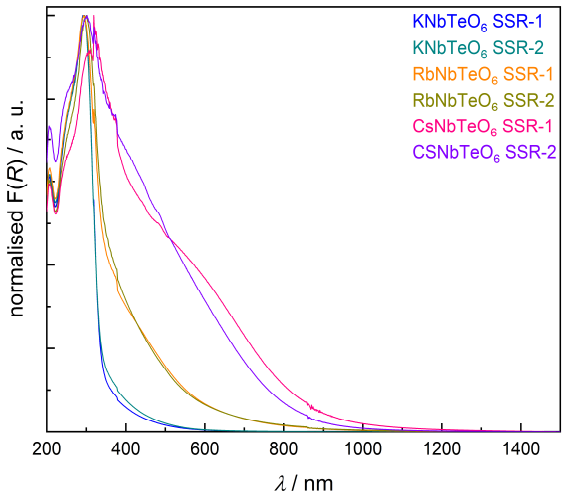

Figure 10.31: Kubelka-Munk absorption spectra of $ANbTeO_6$; SSR-1 and SSR-2 indicate the first synthesis and the second synthesis.

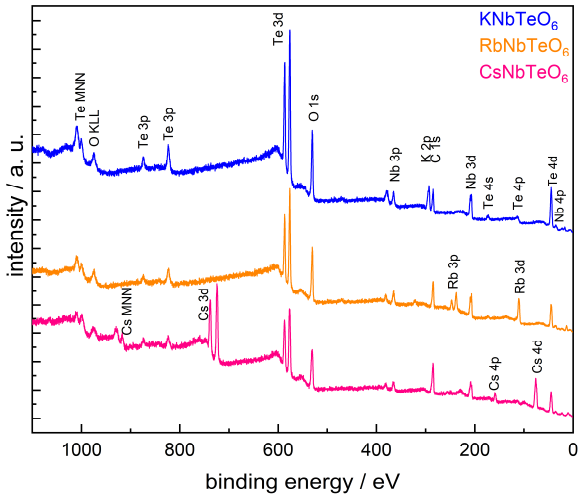

Figure 10.32: XPS survey scans of $ANbTeO_6$.

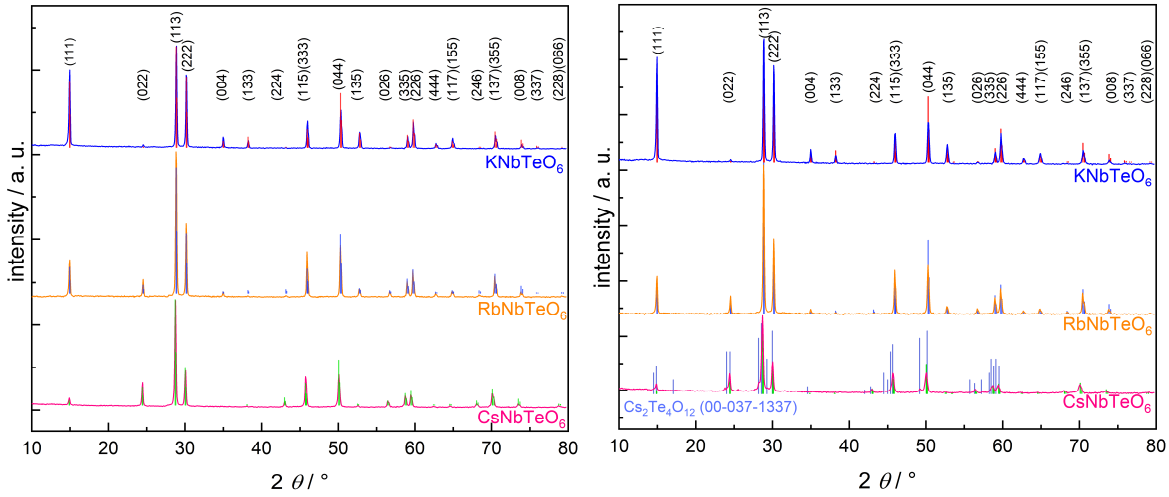

Figure 10.33: XRD patterns of $ANbTeO_6$ synthesised with $Te(OH)_6$ instead of TeO_2 (left) and of $ANbTeO_6$ synthesised in pure oxygen instead of air (right).

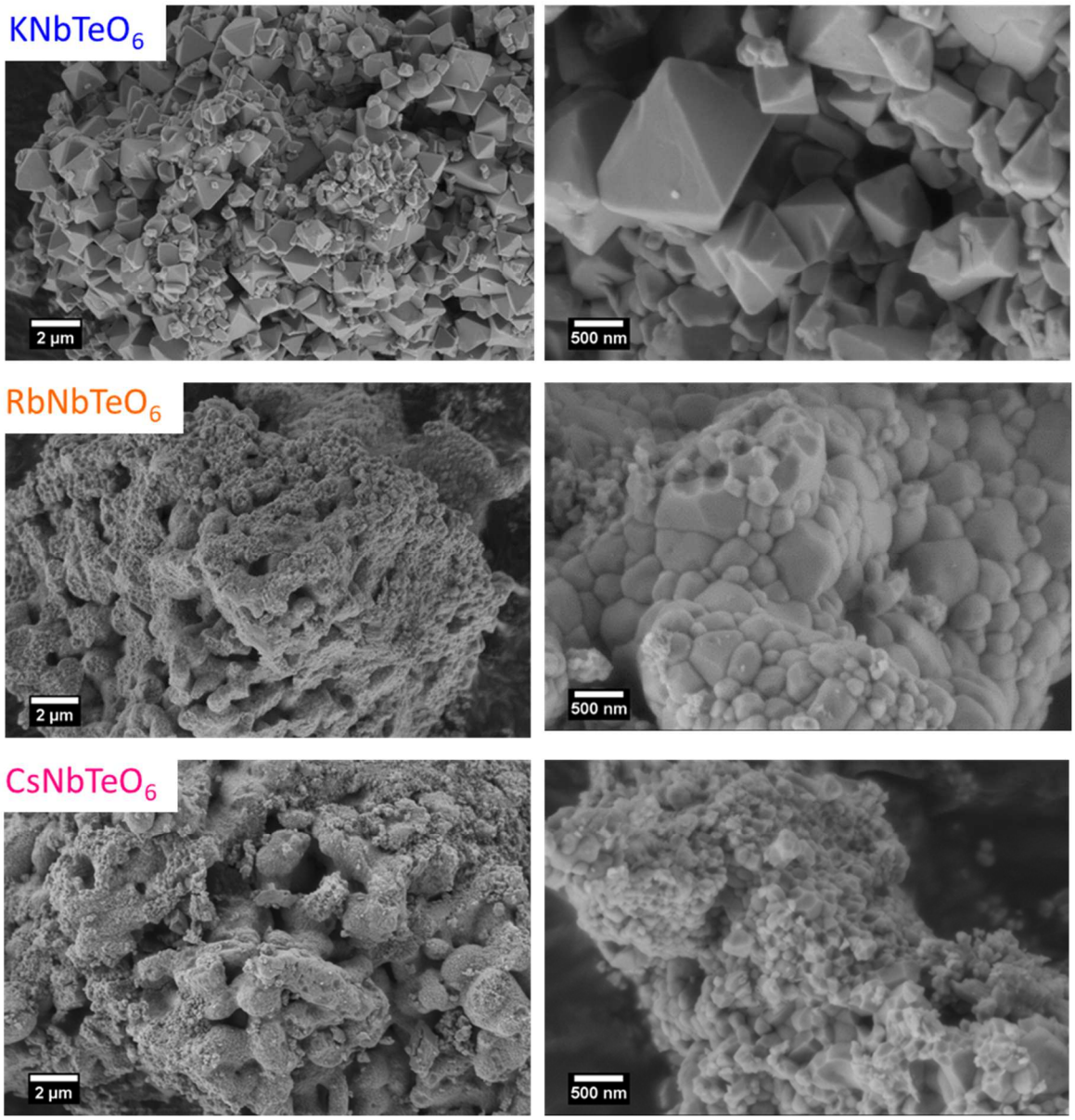

Figure 10.34: SEM images of $ANbTeO_6$ after irradiation.

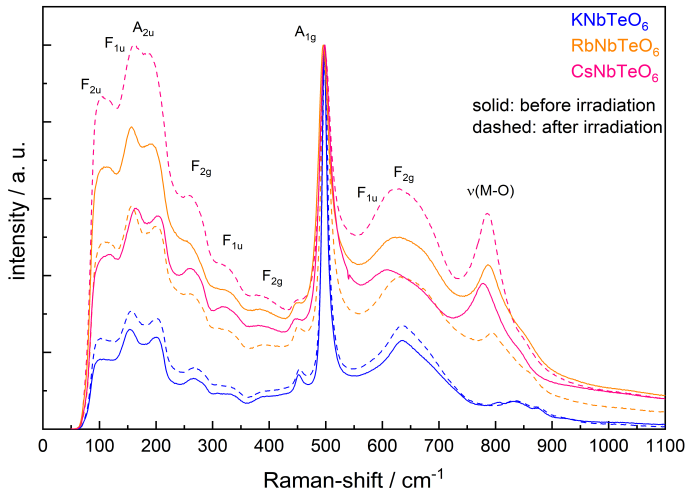

Figure 10.35: Raman spectra of $ANbTeO_6$ before and after irradiation.

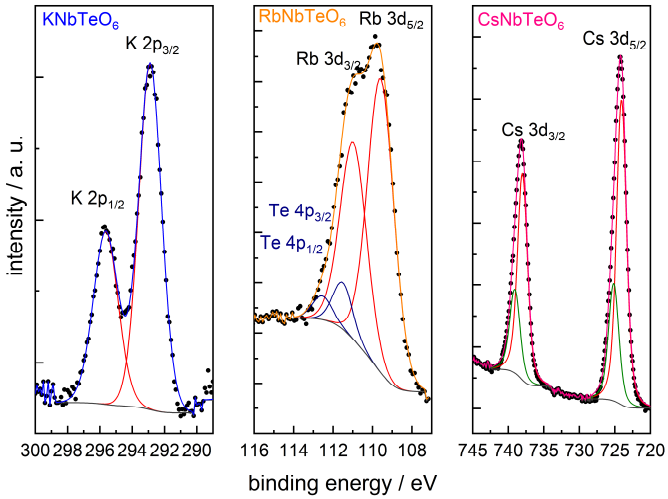

Figure 10.36: High resolution XPS of A cations of $ANbTeO_6$ after irradiation.

11 References

[1] N. S. Lewis, D. G. Nocera, *Proc. Natl. Acad. Sci. U. S. A.* **2006**, *103*, 15729–15735.

[2] R. Perez, M. Perez, *SHC Solar Update* **2015**, 4–6.

[3] A. Fujishima, K. Honda, *Nature* **1972**, *238*, 37–38.

[4] S. Banerjee, S. C. Pillai, P. Falaras, K. E. O'Shea, J. A. Byrne, D. D. Dionysiou, *J. Phys. Chem. Lett.* **2014**, *5*, 2543–2554.

[5] C. Zachäus, F. F. Abdi, L. M. Peter, R. van de Krol, *Chem. Sci.* **2017**, *8*, 3712–3719.

[6] P. S. Bassi, Gurudayal, L. H. Wong, J. Barber, *Phys. Chem. Chem. Phys.* **2014**, *16*, 11834–11842.

[7] M. A. Subramanian, R. Subramanian, A. Clearfield, *Solid State Ionics* **1985**, *15*, 15–19.

[8] D. Babel, G. Pausewang, W. Viebahn, *Z. Naturforsch., B J. Chem. Sci.* **1967**, *22*, 1219–1220.

[9] G. Le Flem, R. Salmon, *C. R. Seances Acad. Sci., Ser. C* **1970**, *271*, 1182–1184.

[10] M. L. Veiga, A. Jerez, M. Gaitán, C. Pico, *Thermochim. Acta* **1988**, *124*, 25–33.

[11] A. Castro, I. Rasines, X. M. Turrillas, *J. Solid State Chem.* **1989**, *80*, 227–234.

[12] T. Kar, R. N. P. Choudhary, *J. Phys. Chem. Solids* **2001**, *62*, 1149–1161.

[13] T. Kar, R. N. P. Choudhary, *Mater. Sci. Eng., B* **2002**, *90*, 224–233.

[14] N. G. Chernorukov, A. V. Knyazev, N. Y. Kuznetsova, S. N. Golubev, *Russ. J. Inorg. Chem.* **2008**, *53*, 1303–1310.

[15] T. Siritanon, G. Laurita, R. T. Macaluso, J. N. Millican, A. W. Sleight, M. A. Subramanian, *Chem. Mater.* **2009**, *21*, 5572–5574.

[16] S. Ikeda, T. Itani, K. Nango, M. Matsumura, *Catal. Lett.* **2004**, *98*, 229–233.

[17] Y. Hosogi, Y. Shimodaira, H. Kato, H. Kobayashi, A. Kudo, *Chem. Mater.* **2008**, *20*, 1299–1307.

[18] Y. Hosogi, H. Kato, A. Kudo, *J. Phys. Chem. C* **2008**, *112*, 17678–17682.

[19] S. Uma, J. Singh, V. Thakral, *Inorg. Chem.* **2009**, *48*, 11624–11630.

[20] S. Dey, R. A. Ricciardo, H. L. Cuthbert, P. M. Woodward, *Inorg. Chem.* **2014**, *53*, 4394–4399.

[21] S. Garía-Martin, M. L. Veiga, A. Jerez, M. Gaitán, C. Pico, *J. Chem. Soc., Dalt. Trans.* **1988**, 2141–2144.

[22] T. Weller, L. Specht, R. Marschall, *Nano Energy* **2017**, *31*, 551–559.

[23] M. Weiss, R. Marschall, *Nanoscale* **2018**, *10*, 9691–9697.

[24] M. Weiss, T. Bredow, R. Marschall, *Chem. Eur. J.* **2018**, *24*, 18535–18543.

[25] P. Venkataswamy, C. S. Reddy, R. Gundeboina, G. Sadanandam, N. K. Veldurthi, M. Vithal, *Electron. Mater. Lett.* **2018**, *14*, 446–460.

[26] M. Weiss, B. Wirth, R. Marschall, *Inorg. Chem.* **2020**, *59*, 8387–8395.

[27] T. R. Karl, K. E. Trenberth, *Science* **2003**, *302*, 1719–1723.

[28] *BP Statistical Review of World Energy 2019*, **2019**.

[29] A. F. Ghoniem, *Prog. Energy Combust. Sci.* **2011**, *37*, 15–51.

[30] S. Ardo, D. Fernandez Rivas, M. A. Modestino, V. Schulze Greiving, F. F. Abdi, E. Alarcon Llado, V. Artero, K. Ayers, C. Battaglia, J.-P. Becker, et al., *Energy Environ. Sci.* **2018**, *11*, 2768–2783.

[31] R. van de Krol, B. A. Parkinson, *MRS Energy Sustain.* **2017**, *4*, E13.

[32] F. E. Osterloh, *ACS Energy Lett.* **2017**, *2*, 445–453.

[33] Z. Wang, L. Zhang, T. U. Schülli, Y. Bai, S. A. Monny, A. Du, L. Wang, *Angew. Chem. Int. Ed.* **2019**, *58*, 17604–17609.

[34] R. Abe, *J. Photochem. Photobiol., C* **2010**, *11*, 179–209.

[35] C. Y. Toe, Z. Zheng, H. Wu, J. Scott, R. Amal, Y. H. Ng, *Angew. Chem.* **2018**, *130*, 13801–13805.

[36] K. Kirchberg, R. Marschall, *Sustainable Energy Fuels* **2019**, *3*, 1150–1153.

[37] A. Bloesser, R. Marschall, *ACS Appl. Energy Mater.* **2018**, *1*, 2520–2525.

[38] P. Voepel, M. Weiss, B. M. Smarsly, R. Marschall, *J. Photochem. Photobiol., A* **2018**, *366*, 34–40.

[39] M. Kölbach, I. J. Pereira, K. Harbauer, P. Plate, K. Höflich, S. P. Berglund, D. Friedrich, R. van de Krol, F. F. Abdi, *Chem. Mater.* **2018**, *30*, 8322–8331.

[40] Y. Shiga, N. Umezawa, N. Srinivasan, S. Koyasu, E. Sakai, M. Miyauchi, *Chem. Commun.* **2016**, *52*, 7470–7473.

[41] S. Lukic, J. Menze, P. Weide, G. W. Busser, M. Winterer, M. Muhler, *ChemSusChem* **2017**, *10*, 4190–4197.

[42] D. Chen, Z. Wang, T. Ren, H. Ding, W. Yao, R. Zong, Y. Zhu, *J. Phys. Chem. C* **2014**, *118*, 15300–15307.

[43] F. Amano, E. Ishinaga, A. Yamakata, *J. Phys. Chem. C* **2013**, *117*, 22584–22590.

[44] T. Ohno, K. Sarukawa, M. Matsumura, *New J. Chem.* **2002**, *26*, 1167–1170.

[45] J. Schneider, D. W. Bahnemann, *J. Phys. Chem. Lett.* **2013**, *4*, 3479–3483.

[46] J. Ran, J. Zhang, J. Yu, M. Jaroniec, S. Z. Qiao, *Chem. Soc. Rev.* **2014**, *43*, 7787–7812.

[47] R. Li, H. Han, F. Zhang, D. Wang, C. Li, *Energy Environ. Sci.* **2014**, *7*, 1369–1376.

[48] K. Wenderich, G. Mul, *Chem. Rev.* **2016**, *116*, 14587–14619.

[49] K. Maeda, K. Teramura, D. Lu, N. Saito, Y. Inoue, K. Domen, *Angew. Chem. Int. Ed.* **2006**, *45*, 7806–7809.

[50] K. Maeda, K. Teramura, D. Lu, N. Saito, Y. Inoue, K. Domen, *J. Phys. Chem. C* **2007**, *111*, 7554–7560.

[51] G. W. Busser, B. Mei, A. Pougin, J. Strunk, R. Gutkowski, W. Schuhmann, M. G. Willinger, R. Schlögl, M. Muhler, *ChemSusChem* **2014**, *7*, 1030–1034.

[52] J. Soldat, G. W. Busser, M. Muhler, M. Wark, *ChemCatChem* **2016**, *8*, 153–156.

[53] D. E. Scaife, *Sol. Energy* **1980**, *25*, 41–54.

[54] H. Tong, S. Ouyang, Y. Bi, N. Umezawa, M. Oshikiri, J. Ye, *Adv. Mater.* **2012**, *24*, 229–251.

[55] T. Umebayashi, T. Yamaki, H. Itoh, K. Asai, *J. Phys. Chem. Solids* **2002**, *63*, 1909–1920.

[56] W. Choi, A. Termin, M. R. Hoffmann, *J. Phys. Chem.* **1994**, *98*, 13669–13679.

[57] D. Wang, J. Ye, T. Kako, T. Kimura, *J. Phys. Chem. B* **2006**, *110*, 15824–15830.

[58] A. Waehayee, P. Watthaisong, S. Wannapaiboon, N. Chanlek, H. Nakajima, J. Wittayakun, S. Suthirakun, T. Siritanon, *Catal. Sci. Technol.* **2020**, *10*, 978–992.

[59] S. Ouyang, J. Ye, *J. Am. Chem. Soc.* **2011**, *133*, 7757–7763.

[60] I. S. Cho, C. H. Kwak, D. W. Kim, S. Lee, K. S. Hong, *J. Phys. Chem. C* **2009**, *113*, 10647–

10653.

[61] J. Boltersdorf, B. Zoellner, C. M. Fancher, J. L. Jones, P. A. Maggard, *J. Phys. Chem. C* **2016**, *120*, 19175–19188.

[62] J. Boltersdorf, I. Sullivan, T. L. Shelton, Z. Wu, M. Gray, B. Zoellner, F. E. Osterloh, P. A. Maggard, *Chem. Mater.* **2016**, *28*, 8876–8889.

[63] S. Katayama, H. Hayashi, Y. Kumagai, F. Oba, I. Tanaka, *J. Phys. Chem. C* **2016**, *120*, 9604–9611.

[64] R. R. Jitta, R. Guje, N. K. Veldurthi, S. Prathapuram, R. Velchuri, V. Muga, *J. Alloys Compd.* **2015**, *618*, 815–823.

[65] R. Guje, R. Gundeboina, J. R. Reddy, N. K. Veldurthi, S. Kurra, M. Vithal, *Photochem. Photobiol.* **2016**, *92*, 223–230.

[66] M. Rochkind, S. Pasternak, Y. Paz, *Molecules* **2015**, *20*, 88–110.

[67] X. Zeng, Y. Chen, S. Jiao, Z. Fang, B. Wang, G. Pang, S. Feng, *New J. Chem.* **2018**, *42*, 5753–5758.

[68] J. Shi, L. Ma, P. Wu, Z. Zhou, P. Guo, S. Shen, D. Jing, L. Guo, *Nano Res.* **2012**, *5*, 576–583.

[69] J. Shi, L. Ma, P. Wu, Z. Zhou, J. Jiang, X. Wan, D. Jing, L. Guo, *ChemCatChem* **2012**, *4*, 1389–1396.

[70] H. G. Kim, O. S. Becker, J. S. Jang, S. M. Ji, P. H. Borse, J. S. Lee, *J. Solid State Chem.* **2006**, *179*, 1214–1218.

[71] J. Boltersdorf, T. Wong, P. A. Maggard, *ACS Catal.* **2013**, *3*, 2943–2953.

[72] A. Mukherji, R. Marschall, A. Tanksale, C. Sun, S. C. Smith, G. Q. Lu, L. Wang, *Adv. Funct. Mater.* **2011**, *21*, 126–132.

[73] J. Sun, X. Zhao, H. Sun, W. Fan, *J. Solid State Chem.* **2012**, *194*, 352–360.

[74] R. Marschall, A. Mukherji, A. Tanksale, C. Sun, S. C. Smith, L. Wang, G. Q. M. Lu, *J. Mater. Chem.* **2011**, *21*, 8871–8879.

[75] L. Liu, L. Li, Q. Li, C. Sun, *Journal of Materiomics* **2017**, *3*, 71–76.

[76] P. Wang, B. Huang, Y. Dai, M. H. Whangbo, *Phys. Chem. Chem. Phys.* **2012**, *14*, 9813–9825.

[77] J. Willkomm, K. L. Orchard, A. Reynal, E. Pastor, J. R. Durrant, E. Reisner, *Chem. Soc. Rev.* **2016**, *45*, 9–23.

[78] D. G. Fukina, E. V. Suleimanov, R. P. Yavetskiy, G. K. Fukin, A. V. Boryakov, E. N. Borisov, E. V. Borisov, S. I. Surodin, N. V. Saharov, *J. Solid State Chem.* **2016**, *241*, 64–69.

[79] M. Ohtaki, S. Miyaishi, *J. Electron. Mater.* **2013**, *42*, 1299–1302.

[80] K. R. Whittle, G. R. Lumpkin, S. E. Ashbrook, *J. Solid State Chem.* **2006**, *179*, 512–521.

[81] G. J. Thorogood, B. J. Kennedy, V. K. Peterson, M. M. Elcombe, G. J. Kearley, J. V. Hanna, V. Luca, *J. Solid State Chem.* **2009**, *182*, 457–464.

[82] K. Mizuta, M. Ohtaki, *J. Electron. Mater.* **2016**, *45*, 1695–1699.

[83] P. W. Barnes, P. M. Woodward, Y. Lee, T. Vogt, J. A. Hriljac, *J. Am. Chem. Soc.* **2003**, *125*, 4572–4579.

[84] A. V. Knyazev, N. G. Chernorukov, N. N. Smirnova, N. Y. Kuznetsova, A. V. Markin, *Thermochim. Acta* **2008**, *470*, 47–51.

[85] N. G. Chernorukov, A. V. Knyazev, N. Y. Kuznetsova, I. V. Ladenkov, *Phys. Solid State* **2011**, *53*, 292–298.

[86] A. V. Knyazev, M. Maczka, N. Y. Kuznetsova, *Thermochim. Acta* **2010**, *506*, 20–27.

[87] S. F. Mayer, H. Falcón, M. T. Fernández-Díaz, J. A. Alonso, *Crystals* **2018**, *8*, 368.

[88] Y. N. Han, S. Jiao, M. Xu, G. Pang, S. Feng, *RSC Adv.* **2014**, *4*, 14357–14360.

[89] Y. N. Han, S. Jiao, M. Xu, Y. Xu, G. Pang, S. Feng, *RSC Adv.* **2014**, *4*, 24142–24146.

[90] T. Kar, R. N. P. Choudhary, *J. Phys. Chem. Solids* **1999**, *60*, 673–679.

[91] C. Tagusagawa, A. Takagaki, S. Hayashi, K. Domen, *J. Phys. Chem. C* **2009**, *113*, 7831–7837.

[92] M. Mączka, A. V. Knyazev, N. Y. Kuznetsova, M. Ptak, L. Macalik, *J. Raman Spectrosc.* **2011**, *42*, 529–533.

[93] R. M. Biefeld, M. A. Butler, L. J. Azevedo, *Solid State Commun.* **1981**, *38*, 1125–1128.

[94] D. Groult, J. Pannetier, B. Raveau, *J. Solid State Chem.* **1982**, *41*, 277–285.

[95] R. Hinrichs, G. Tomandl, J. A. H. da Jornada, *Solid State Ionics* **1995**, *77*, 257–262.

[96] N. Binesh, V. Bhat, S. V. Bhat, *Solid State Ionics* **1996**, *86–88*, 665–668.

[97] D. Kowalska, E. Piskorska-Hommel, A. Majchrowski, M. Wołcyrz, *J. Solid State Chem.* **2019**, *276*, 146–151.

[98] F. X. Zhang, C. L. Tracy, J. Shamblin, R. I. Palomares, M. Lang, S. Park, C. Park, S. Tkachev, R. C. Ewing, *RSC Adv.* **2016**, *6*, 94287–94293.

[99] R. J. Cava, R. S. Roth, T. Siegrist, B. Hessen, J. J. Krajewski, W. F. Peck, *J. Solid State Chem.* **1993**, *103*, 359–365.

[100] D. Hirai, M. Bremholm, J. M. Allred, J. Krizan, L. M. Schoop, Q. Huang, J. Tao, R. J. Cava, *Phys. Rev. Lett.* **2013**, *110*, 166402.

[101] S. V. Streltsov, I. I. Mazin, R. Heid, K. P. Bohnen, *Phys. Rev. B* **2016**, *94*, 241101.

[102] D. W. Murphy, R. J. Cava, K. Rhyne, R. S. Roth, A. Santoro, S. M. Zahurak, J. L. Dye, *Solid State Ionics* **1986**, *18–19*, 799–801.

[103] G. Rodríguez-Gattorno, L. F. del Castillo, E. Torres-García, *Thermochim. Acta* **2005**, *435*, 176–180.

[104] C. A. Perottoni, J. A. H. da Jornada, *Phys. Rev. Lett.* **1997**, *78*, 2991–2994.

[105] S.-H. Choe, C.-J. Yu, M. Choe, Y.-H. Kye, Y.-N. Han, G. Pang, *Phys. Rev. B* **2020**, *102*, 035131.

[106] J. A. Alonso, S. Mayer, H. Falcón, X. Turrillas, M. T. Fernández-Díaz, *Crystals* **2017**, *7*, 24.

[107] A. V. Knyazev, W. Paraguassu, A. G. Blokhina, M. I. Lelet, S. S. Knyazeva, G. B. Corrêa Junior, *J. Chem. Thermodyn.* **2017**, *107*, 26–36.

[108] J. Li, T. Siritanon, J. K. Stalick, A. W. Sleight, M. A. Subramanian, *Inorg. Chem.* **2011**, *50*, 5747–5754.

[109] A. Waehayee, N. Chanlek, P. Kidkhunthod, H. Nakajima, S. Suthirakun, T. Siritanon, *Phys. Rev. B* **2019**, *100*, 045132.

[110] C. Sun, A. Mukherji, G. Liu, L. Wang, S. C. Smith, *Chem. Phys. Lett.* **2011**, *501*, 427–430.

[111] G. Ravi, P. Shrujana, S. Palla, J. R. Reddy, R. Guje, R. Velchuri, M. Vithal, *Micro Nano Lett.* **2014**, *9*, 11–15.

[112] L. Schwertmann, A. Grünert, A. Pougin, C. Sun, M. Wark, R. Marschall, *Adv. Funct. Mater.* **2015**, *25*, 905–912.

[113] L. Schwertmann, M. Wark, R. Marschall, *RSC Adv.* **2013**, *3*, 18908–18915.

[114] M. Weiss, S. Waitz, R. Ellinghaus, T. Weller, R. Marschall, *RSC Adv.* **2016**, *6*, 79037–79042.

[115] T. Weller, J. Sann, R. Marschall, *Adv. Energy Mater.* **2016**, *6*, 1600208.

[116] T. Weller, L. Deilmann, J. Timm, T. S. Dörr, P. A. Beaucage, A. S. Cherevan, U. B. Wiesner, D. Eder, R. Marschall, *Nanoscale* **2018**, *10*, 3225–3234.

[117] R. Guje, G. Ravi, S. Palla, K. N. Rao, M. Vithal, *Mater. Sci. Eng., B* **2015**, *198*, 1–9.

[118] K. Kirchberg, A. Becker, A. Bloesser, T. Weller, J. Timm, C. Suchomski, R. Marschall, *J. Phys. Chem. C* **2017**, *121*, 27126–27138.

[119] A. Bloesser, P. Voepel, M. O. Loeh, A. Beyer, K. Volz, R. Marschall, *J. Mater. Chem. A* **2018**, *6*, 1971–1978.

[120] P. Voepel, B. M. Smarsly, *Z. Anorg. Allg. Chem.* **2017**, *643*, 3–13.

[121] D. Zhao, J. Feng, Q. Huo, N. Melosh, G. H. Fredrickson, B. F. Chmelka, G. D. Stucky, *Science* **1998**, *279*, 548–552.

[122] F. Schüth, *Angew. Chem.* **2003**, *115*, 3730–3750.

[123] M. Juelsholt, T. L. Christiansen, K. M. Ø. Jensen, *J. Phys. Chem. C* **2019**, *123*, 5110–5119.

[124] A. E. Danks, S. R. Hall, Z. Schnepp, *Mater. Horizons* **2016**, *3*, 91–112.

[125] W. Wen, J. M. Wu, *RSC Adv.* **2014**, *4*, 58090–58100.

[126] A. Rabenau, *Angew. Chem.* **1985**, *97*, 1017–1032.

[127] F. Parrino, S. Livraghi, E. Giamello, L. Palmisano, *Angew. Chem.* **2018**, *130*, 10862–10866.

[128] T. Bredow, A. R. Gerson, *Phys. Rev. B* **2000**, *61*, 5194–5201.

[129] C. Wessel, C. Reimann, A. Müller, D. Weber, M. Lerch, T. Ressler, T. Bredow, R. Dronskowski, *J. Comput. Chem.* **2012**, *33*, 2102–2107.

[130] R. Dovesi, A. Erba, R. Orlando, C. M. Zicovich-Wilson, B. Civalleri, L. Maschio, M. Rérat, S. Casassa, J. Baima, S. Salustro, et al., *Wiley Interdiscip. Rev. Comput. Mol. Sci.* **2018**, *8*, e1360.

[131] B. Metz, H. Stoll, M. Dolg, *J. Chem. Phys.* **2000**, *113*, 2563–2569.

[132] M. F. Peintinger, D. V. Oliveira, T. Bredow, *J. Comput. Chem.* **2013**, *34*, 451–459.

[133] D. Andrae, U. Häußermann, M. Dolg, H. Stoll, H. Preuß, *Theor. Chim. Acta* **1990**, *77*, 123–141.

[134] A. R. Stokes, A. J. C. Wilson, *Math. Proc. Cambridge Philos. Soc.* **1942**, *38*, 313–322.

[135] H. M. Rietveld, *J. Appl. Crystallogr.* **1969**, *2*, 65–71.

[136] J. Rodríguez-Carvajal, *Phys. B Phys. Condens. Matter* **1993**, *192*, 55–69.

[137] P. Thompson, D. E. Cox, J. B. Hastings, *J. Appl. Crystallogr.* **1987**, *20*, 79–83.

[138] B. H. Toby, *Powder Diffr.* **2006**, *21*, 67–70.

[139] T. H. de Keijser, J. I. Langford, E. J. Mittemeijer, A. B. P. Vogels, *J. Appl. Crystallogr.* **1982**, *15*, 308–314.

[140] J. G. M. van Berkum, R. Delhez, T. H. de Keijser, E. J. Mittemeijer, *Acta Crystallogr., Sect. A: Found. Crystallogr.* **1996**, *52*, 730–747.

[141] A. R. Stokes, A. J. C. Wilson, *Proc. Phys. Soc.* **1944**, *56*, 174–181.

[142] C. D. Wagner, *Faraday Discuss. Chem. Soc.* **1975**, *60*, 291–300.

[143] S. W. Gaarenstroom, N. Winograd, *J. Chem. Phys.* **1977**, *67*, 3500–3506.

[144] M. C. Biesinger, L. W. M. Lau, A. R. Gerson, R. S. C. Smart, *Phys. Chem. Chem. Phys.* **2012**, *14*, 2434–2442.

[145] J. Tauc, R. Grigorovici, A. Vancu, *Phys. Status Solidi B* **1966**, *15*, 627–637.

[146] M. Thommes, K. Kaneko, A. V. Neimark, J. P. Olivier, F. Rodriguez-Reinoso, J. Rouquerol, K.

S. W. Sing, *Pure Appl. Chem.* **2015**, *87*, 1051–1069.

[147] Y. Zhao, E. A. Hernandez-Pagan, N. M. Vargas-Barbosa, J. L. Dysart, T. E. Mallouk, *J. Phys. Chem. Lett.* **2011**, *2*, 402–406.

[148] A. Iwase, H. Kato, A. Kudo, *Chem. Lett.* **2005**, *34*, 946–947.

[149] K. Gelderman, L. Lee, S. W. Donne, *J. Chem. Educ.* **2007**, *84*, 685–688.

[150] R. D. Shannon, *Acta Crystallogr., Sect. A: Cryst. Phys., Diffr., Theor. Gen. Crystallogr.* **1976**, *32*, 751–767.

[151] S. Y. Venyaminov, F. G. Prendergast, *Anal. Biochem.* **1997**, *248*, 234–245.

[152] P. F. McMillan, R. L. Remmele Jr., *Am. Mineral.* **1986**, *71*, 772–778.

[153] M. Mączka, A. V. Knyazev, A. Majchrowski, J. Hanuza, S. Kojima, *J. Phys.: Condens. Matter* **2012**, *24*, 195902.

[154] A.-D. Li, J.-Z. Kong, H.-F. Zhai, J.-B. Cheng, H. Li, D. Wu, *J. Am. Ceram. Soc.* **2009**, *92*, 1959–1965.

[155] L. E. Brus, *J. Chem. Phys.* **1984**, *80*, 4403–4409.

[156] J. A. Bearden, *Rev. Mod. Phys.* **1967**, *39*, 78–124.

[157] R. D. Shannon, C. T. Prewitt, *Acta Crystallogr., Sect. B: Struct. Crystallogr. Cryst. Chem.* **1969**, *25*, 925–946.

[158] Y. Q. Guo, R. Q. Tan, X. Li, J. H. Zhao, Z. L. Luo, C. Gao, W. J. Song, *CrystEngComm* **2011**, *13*, 5677–5680.

[159] X. Chen, M. Grandbois, *J. Raman Spectrosc.* **2013**, *44*, 501–506.

[160] M. Krivec, R. Dillert, D. W. Bahnemann, A. Mehle, J. Štrancar, G. Dražić, *Phys. Chem. Chem. Phys.* **2014**, *16*, 14867–14873.

[161] J. D. Donaldson, W. Moser, W. B. Simpson, *J. Chem. Soc.* **1964**, 5942–5947.

[162] R. M. Cigala, F. Crea, C. De Stefano, G. Lando, D. Milea, S. Sammartano, *Geochim. Cosmochim. Acta* **2012**, *87*, 1–20.

[163] D. Shuttleworth, *J. Phys. Chem.* **1980**, *84*, 1629–1634.

[164] J. C. C. Fan, J. B. Goodenough, *J. Appl. Phys.* **1977**, *48*, 3524–3531.

[165] T. Hashemi, C. A. Hogarth, F. Golestani-Fard, *J. Mater. Sci.* **1988**, *23*, 2645–2648.

[166] X. Cao, L. Cao, W. Yao, X. Ye, *Surf. Interface Anal.* **1996**, *24*, 662–666.

[167] M. A. Stranick, A. Moskwa, *Surf. Sci. Spectra* **1993**, *2*, 45–49.

[168] M. A. Stranick, A. Moskwa, *Surf. Sci. Spectra* **1993**, *2*, 50–54.

[169] S. Süzer, *Pure Appl. Chem.* **1997**, *69*, 163–168.

[170] L. Kövér, Z. Kovacs, R. Sanjines, G. Moretti, I. Cserny, G. Margaritondo, J. Palinkas, H. Adachi, *Surf. Interface Anal.* **1995**, *23*, 461–466.

[171] K. Schenk-Meuser, H. Duschner, *Fresenius. J. Anal. Chem.* **1997**, *358*, 265–267.

[172] A. W. C. Lin, N. R. Armstrong, T. Kuwana, *Anal. Chem.* **1977**, *49*, 1228–1235.

[173] L. Kövér, G. Moretti, Z. Kovács, R. Sanjinés, I. Cserny, G. Margaritondo, J. Pálinkás, H. Adachi, *J. Vac. Sci. Technol. A* **1995**, *13*, 1382–1388.

[174] J. F. Moulder, W. F. Stickle, P. E. Sobol, K. D. Bomben, *Handbook of X-Ray Photoelectron Spectroscopy*, Physical Electronics Inc., Eden Prairie, **1995**.

[175] K. Domen, A. Kudo, M. Shibata, A. Tanaka, K.-I. Maruya, T. Onishi, *J. Chem. Soc. Chem.*

Commun. **1986**, 1706–1707.

[176] M. Hervieu, B. Raveau, *C. R. Seances Acad. Sci., Ser. C* **1970**, *271*, 1568–1570.

[177] N. A. Asryan, A. S. Alikhanyan, G. D. Nipan, *Inorg. Mater.* **2004**, *40*, 626–631.

[178] M. L. Sanjuán, C. Guglieri, S. Díaz-Moreno, G. Aquilanti, A. F. Fuentes, L. Olivi, J. Chaboy, *Phys. Rev. B* **2011**, *84*, 104207.

[179] G. Ravi, S. Palla, N. K. Veldurthi, J. R. Reddy, A. Hari Padmasri, M. Vithal, *Int. J. Hydrogen Energy* **2014**, *39*, 15352–15361.

[180] A. Hankin, F. E. Bedoya-Lora, J. C. Alexander, A. Regoutz, G. H. Kelsall, *J. Mater. Chem. A* **2019**, *7*, 26162–26176.

[181] T. Ejima, T. Banse, H. Takatsuka, Y. Kondo, M. Ishino, N. Kimura, M. Watanabe, I. Matsubara, *J. Lumin.* **2006**, *119–120*, 59–63.

[182] S. Satyapal, J. Park, R. Bersohn, B. Katz, *J. Chem. Phys.* **1989**, *91*, 6873–6879.

[183] R. Arrigo, M. Hävecker, M. E. Schuster, C. Ranjan, E. Stotz, A. Knop-Gericke, R. Schlögl, *Angew. Chem. Int. Ed.* **2013**, *52*, 11660–11664.

[184] D. Hollmann, O. Merka, L. Schwertmann, R. Marschall, M. Wark, A. Brückner, *Top. Catal.* **2015**, *58*, 769–775.

[185] J. Schneider, K. Nikitin, M. Wark, D. W. Bahnemann, R. Marschall, *Phys. Chem. Chem. Phys.* **2016**, *18*, 10719–10726.

[186] S. R. Pendlebury, X. Wang, F. Le Formal, M. Cornuz, A. Kafizas, S. D. Tilley, M. Grätzel, J. R. Durrant, *J. Am. Chem. Soc.* **2014**, *136*, 9854–9857.

[187] S. Rajagopal, V. L. Bekenev, D. Nataraj, D. Mangalaraj, O. Y. Khyzhun, *J. Alloys Compd.* **2010**, *496*, 61–68.

[188] F. Ichihara, F. Sieland, H. Pang, D. Philo, A.-T. Duong, K. Chang, T. Kako, D. W. Bahnemann, J. Ye, *J. Phys. Chem. C* **2020**, *124*, 1292–1302.

[189] M. C. Biesinger, B. P. Payne, A. P. Grosvenor, L. W. M. Lau, A. R. Gerson, R. S. C. Smart, *Appl. Surf. Sci.* **2011**, *257*, 2717–2730.

[190] M. Fondell, M. Gorgoi, M. Boman, A. Lindblad, *J. Electron Spectros. Relat. Phenomena* **2018**, *224*, 23–26.

[191] D. F. Mitchell, G. I. Sproule, M. J. Graham, *Surf. Interface Anal.* **1990**, *15*, 487–497.

[192] M. K. Bahl, R. L. Watson, K. J. Irgolic, *J. Chem. Phys.* **1977**, *66*, 5526–5535.

[193] B. V. R. Chowdari, P. Pramoda Kumari, *J. Non-Cryst. Solids* **1996**, *197*, 31–40.

[194] H. G. Junginger, *Solid State Commun.* **1967**, *5*, 509–511.

[195] S. Moufok, L. Kadi, B. Amrani, K. D. Khodja, *Results Phys.* **2019**, *13*, 102315.

[196] J. C. Dupin, D. Gonbeau, P. Vinatier, A. Levasseur, *Phys. Chem. Chem. Phys.* **2000**, *2*, 1319–1324.

[197] B. P. Payne, M. C. Biesinger, N. S. McIntyre, *J. Electron Spectros. Relat. Phenomena* **2009**, *175*, 55–65.

[198] J. H. Linn, W. E. Swartz Jr., *Appl. Surf. Sci.* **1984**, *20*, 154–166.

[199] W. E. Morgan, J. R. van Wazer, W. J. Stec, *J. Am. Chem. Soc.* **1973**, *95*, 751–755.

[200] G. Ebbinghaus, A. Simon, *Chem. Phys.* **1979**, *43*, 117–133.

[201] F. Garbassi, J. C. J. Bart, G. Petrini, *J. Electron Spectros. Relat. Phenomena* **1981**, *22*, 95–107.

[202] Y. Baba, T. A. Sasaki, *Surf. Interface Anal.* **1984**, *6*, 171–173.

[203] M. A. K. Ahmed, H. Fjellvag, A. Kjekshus, *J. Chem. Soc., Dalt. Trans.* **2000**, 4542–4549.

[204] M. K. Bahl, *J. Phys. Chem. Solids* **1975**, *36*, 485–491.

[205] R. Fontaine, R. Caillat, L. Feve, M. J. Guittet, *J. Electron Spectros. Relat. Phenomena* **1977**, *10*, 349–357.

[206] Z. Weibin, W. Weidong, W. Xueming, C. Xinlu, Y. Dawei, S. Changle, P. Liping, W. Yuying, B. Li, *Surf. Interface Anal.* **2013**, *45*, 1206–1210.

[207] D. D. Sarma, C. N. R. Rao, *J. Electron Spectros. Relat. Phenomena* **1980**, *20*, 25–45.

12 Lists of Scientific Contributions, Tables, Figures, Abbreviations and Symbols

12.1 Scientific Contributions

12.1.1 Peer-Reviewed Journals

- M. Weiss, S. Waitz, R. Ellinghaus, T. Weller, R. Marschall
  "Highly mesoporous $CsTaWO_6$ *via* hard-templating for photocatalytic hydrogen production", *RSC Adv*. **2016**, *6*, 79037-79042. (not part of this work)

- M. Weiss, R. Marschall
  "Synthesis of hydrated $KTaWO_6$ nanoparticles and Sn(II) incorporation for visible light absorption", *Nanoscale* **2018**, *10*, 9691-9697.

- M. Weiss, T. Bredow, R. Marschall
  "The Influence of Tin(II) Incorporation on Visible Light Absorption and Photocatalytic Activity in Defect-Pyrochlores", *Chem. Eur. J.* **2018**, *24*, 18535-18543.

- M. Weiss, B. Wirth, R. Marschall
  "Photoinduced Defect and Surface Chemistry of Niobium Tellurium Oxides $ANbTeO_6$ (A = K, Rb, Cs) with Defect-Pyrochlore Structure", *Inorg. Chem.* **2020**, DOI: 10.1021/acs.inorgchem.0c00811.

- N. Dengo, A. F. de Fazio, M. Weiss, R. Marschall, P. Dolcet, M. Fanetti, S. Gross
  "Thermal Evolution of ZnS Nanostructures: Effect of Oxidation Phenomena on Structural Features and Photocatalytical Performances", *Inorg. Chem*. **2018**, *57*, 13104-13114.

- P. Voepel, M. Weiss. B. M. Smarsly, R. Marschall
  "Photocatalytic activity of multiphase TiO_2(B)/anatase nanoparticle heterojunctions prepared from ionic liquids", *J. Photochem. Photobiol. A* **2018**, *366*, 34-40.

- S. D. Yambem, J. Timm, M. Weiss, A. K. Pandey, R. Marschall
  "Sulfonated Mesoporous Silica as Proton Exchange Layer in Solid State Organic Transistor", *Adv. Electron. Mater*. **2017**, *3*, 1700316.

12.1.2 Conference Contributions

- M. Weiss, S. Waitz, R. Ellinghaus, T. Weller, R. Marschall
  "Highly mesoporous $CsTaWO_6$ via hard-templating for photocatalytic hydrogen production", 29. Deutsche Zeolith Tagung, 01.03.2017-03.03.2017, Frankfurt am Main, Germany, poster contribution.

- M. Weiss, R. Marschall
  "Photocatalytic Hydrogen Production using Tin-Exchanged Materials", 6th International Conference on Semiconductor Photochemistry, 11.09.2017-14.09.2017, Oldenburg, Germany, poster contribution.

- M. Weiss, R. Marschall
  "Sn(II) exchange for visible light absorption of $KTaWO_6$ with defect-pyrochlore structure", 19th International Symposium on the Reactivity of Solids, 15.07.2018-18.07.2018, Bayreuth, Germany, poster contribution.

- M. Weiss, R. Marschall
  "Sn(II) exchange for visible light absorption of $KTaWO_6$ with defect-pyrochlore structure", 22nd International Conference on Photochemical Conversion and Storage of Solar Energy, 29.07.2018-03.08.2018, Hefei, People's Republic of China, poster contribution, ACS Applied Energy Materials best poster award.

- M. Weiss, T. Bredow, R. Marschall
  "Towards visible light absorption for photocatalyis by Sn(II) incorporation into defect pyrochlores", 118th General Assembly of the German Bunsen Society for Physical Chemistry, 30.05.2019-01.06.2019, Jena, Germany, poster contribution.

- M. Weiss, T. Bredow, R. Marschall
  "Visible light absorption for photocatalysis by tin(II) incorporation into defect-pyrochlores – creating new visible light absorbing photocatalysts", 7th International Conference on Semiconductor Photochemistry, 11.09.2019-14.09.2019, Milano, Italy, oral contribution.

12.2 List of Tables

12.3 List of Figures

12.4 List of Abbreviations

as-syn.	as synthesised
a. u.	arbitrary units
BET	Brunauer-Emmett-Teller
CB	conduction band
COD	Crystallography Open Database
DLS	dynamic light scattering
DMSO	dimethyl sulfoxide
DOS	density of states
DR	diffuse reflectance
DRIFT	diffuse reflectance infrared Fourier transform spectroscopy
DTG	differential thermogravimetric analysis
EDTA	ethylenediaminetetraacetic acid
EDX	energy dispersive X-ray (spectroscopy)
eq.	equivalents
EtOH	ethanol
FTO	fluorine doped tin oxide
GC	gas chromatography

HOAc	acetic acid
HS	high-spin
ICSD	Inorganic Crystal Structure Database
IR	infrared
MeOH	methanol
MS	mass spectrometry
NHE	normal hydrogen electrode
NIST	National Institute of Standards and Technologies
OAC^-	acetate anion
OD	optical density
sccm	standard cubic centimetre per minute
SEM	scanning electron microscopy
s. o.	spin only
SQUID	superconducting quantum interference device
TCD	thermal conductivity detector
TEM	transmission electron microscopy
TGA	thermogravimetric analysis
TWy	terawatt year
UPS	ultraviolet photoelectron spectroscopy
UV	ultraviolet
VB	valence band
vis	visible
XANES	X-ray near edge absorption spectroscopy
XPS	X-ray photoelectron spectroscopy
XRD	X-ray diffraction

12.5 List of Symbols

symbol	unit	description
a	Å	lattice constant
A	m^2	(surface) area
A/V	m^{-1}	surface-area-to-volume ratio
A_{BET}	$m^2\ g^{-1}$	BET area
A_{hkl}	$Å^{-1}$, nm^{-1}	area of a hkl reflection
B	$Å^2$	isotropic thermal displacement parameter
c_{rel}	%	relative concentration
C	F	capacitance
e	C	elemental constant
$E_{binding}$	eV	binding energy
E_F	eV	Fermi-Energie
E_g	eV	bandgap

symbol	unit	description
E_{kin}	eV	kinetic energy
f	Hz	frequency
F(R)	a. u.	Kubelka-Munk function
h	J s	Planck constant
H_{hkl}	a. u.	height of a hkl reflection
hv	eV	photon energy
I_0	mV	probe intensity
I_t	mV	pump and probe intensity
$K00$, $K41$, $K61$, $K81$		size parameters for Rietveld refinement
k_B	J K^{-1}	Boltzmann constant
L_a	nm	average crystallite size
L_{hkl}	nm	crystallite size corresponding to a hkl reflection
N_D	m^{-3}	donor density
p	Pa	pressure
p_0	Pa	saturation pressure
r	µmol h^{-1}	molar gas evolution rate
R	J mol^{-1} K^{-1}	gas constant
R_{exp}	%	expected R-factor (Rietveld refinement)
R_{wp}	%	weighted R-factor (Rietveld refinement)
S	$Å^{-1}$, nm^{-1}	scattering vector
Str_i i = 1-8		strain parameters for Rietveld refinement
T	K	absolute temperature
t	ns, h	time
U, X, W		Gaussian parameters for Rietveld refinement
V	m^3	volume
$\dot{V}$	m^3 h^{-1}	volume flow
V_X	n. a.	vacancy on site of X (Kroeger-Vink notation)
w_i	a. u.	weight (Rietveld refinement)
X, Y		Lorentzian parameters for Rietveld refinement
x, y, z		fractal atom coordinates
$y_{c,i}$	a. u.	calculated intensity (Rietveld refinement)
$y_{o,i}$	a. u.	observed intensity (Rietveld refinement)
Z_i	Ω	imaginary impedance
α	eV	Auger parameter
α'	eV	modified Auger parameter
β_{hkl}	$Å^{-1}$, nm^{-1}	integral breadth of a hkl reflection
ΔOD		change in absorption
$\Delta OD_{initial}$		starting value in exponential decay function
ΔOD_{offset}		offset value in exponential decay function
ΔG	kJ mol^{-1}	change of free enthalpy
ε		relative permittivity
ε_0	F m^{-1}	vacuum permittivity
ζ	mV	Zeta potential
η		strain
θ	°	Bragg Angle
ϑ	°C	temperature
λ	Å, nm	wavelength
μ		effective Magnetic moment
μ_B	J T^{-1}	Bohr magneton

symbol	unit	description
ν	s^{-1}	frequency
$\bar{\nu}$	cm^{-1}	wave number
σ	a. u.	standard uncertainty (Rietveld refinement)
τ	ns	time constant of exponential decay function
ϕ	V	potential
ϕ_{FB}	V	flat band potential
χ^2		“goodness of fit” (Rietveld refinement)

13 Versicherungen und Erklärungen

- §8 Satz 2 Nr. 3 Promotionsordnung für die Fakultät für Biologie, Chemie und Geowissenschaften
  Ich versichere hiermit eidesstattlich, dass ich die vorliegende Arbeit selbstständig verfasst und keine anderen als die von mir angegebenen Quellen und Hilfsmittel benutzt habe.

- §8 Satz 2 Nr. 3 Promotionsordnung für die Fakultät für Biologie, Chemie und Geowissenschaften
  Ich erkläre hiermit, dass ich diese Dissertation nicht bereits zur Erlangung eines akademischen Grades eingereicht habe und ich nicht bereits diese oder eine andere gleichartige Doktorprüfung endgültig nicht bestanden habe.

- §8 Satz 2 Nr. 4 Promotionsordnung für die Fakultät für Biologie, Chemie und Geowissenschaften
  Ich erkläre hiermit, dass ich die Hilfe von gewerblichen Promotionsberatern und –vermittlern oder ähnlichen Dienstleistern weder bisher in Anspruch genommen habe noch zukünftig in Anspruch nehmen werde.

- §8 Satz 2 Nr. 7 Promotionsordnung für die Fakultät für Biologie, Chemie und Geowissenschaften
  Ich erkläre mein Einverständnis, dass die elektronische Fassung der Dissertation unter Wahrung meiner Urheberrechte und des Datenschutzes einer gesonderten Überprüfung unterzogen werden kann.

- §8 Satz 2 Nr. 8 Promotionsordnung für die Fakultät für Biologie, Chemie und Geowissenschaften
  Ich erkläre, dass bei Verdacht wissenschaftlichen Fehlverhaltens Ermittlungen durch universitätsinterne Organe der wissenschaftlichen Selbstkontrolle stattfinden können.

Bayreuth, den _____ _____

Morten Weiß